XX COURSE OF PHILOSOPHY DOCTORATE IN
STRUCTURAL AND GEOTECHNICAL ENGINEERING
University of Rome "Tor Vergata"

MODELS AND FINITE ELEMENT METHODS FOR POROUS MEDIA SUBJECTED TO LOCALIZED STRAINS

a dissertation submitted in partial fulfillment of the requirements for the degree of
Doctor of Philosophy
by

Andrea Abati

PhD Course Coordinator

Prof. Ing. Franco Maceri

Tutor

Prof. Ing. Carlo Callari

Department of Civil Engineering

February 2008

Sommario

In questa tesi si presenta una teoria termodinamica per continui porosi multi-fase basata sul lavoro di Biot e la relativa formulazione numerica mediante elementi finiti non convenzionali che consentono di modellare fenomeni di localizzazione delle deformazioni. In una prima fase si ricava una forma generale per le relazioni iperelastiche incrementali. Si ottengono quindi espressioni particolari per gli operatori iperelastici tangenti utilizzando argomenti tipici della teoria delle miscele. Si verifica la compatibilità di tali operatori con la suddetta teoria termodinamica utilizzando le condizioni di simmetria e di Maxwell. Fra i principali risultati della trattazione considerata vi è una semplice espressione della dissipazione, che sarà utilizzata in un approccio multi-scala alla localizzazione delle deformazioni.

Si considera quindi una formulazione agli elementi finiti del modello costitutivo ottenuto, concentrando l'attenzione sulla linearizzazione del sistema risolvente. Tra le possibili fonti di non-linearità, si considerano anche quelle dovute a condizioni al contorno unilatere sul flusso fluido, introdotte per modellare efficacemente l'interfaccia tra mezzo poroso e atmosfera. Si analizzano semplici esempi numerici monodimensionali, allo scopo di valutare le prestazioni numeriche delle tecniche di regolarizzazione di tipo penalty e Lagrangiano aumentato utilizzate. In tali esempi si evidenzia anche l'analogia formale e numerica tra problemi di filtrazione con vincoli unilateri e problemi di contatto in assenza di attrito. Si prendono inoltre in considerazione altre situazioni di interesse pratico, come la propagazione di un fronte di saturazione in uno strato di terreno e la parziale saturzione in una diga di calcestruzzo a gravità.

Per modellare meccanismi dissipativi localizzati, si analizza la presenza di discontinuità negli spostamenti e nei flussi fluidi nel caso di mezzi porosi multi-fase. Nel corrispondente metodo agli elementi finiti, l'insorgere di tali discontinuità è simulato mediante "enhancement" locale delle funzioni interpolanti. Infine, si presentano i risultati della simulazione numerica di una prova di compressione piana su un mezzo poroso parzialmente saturo. Tale simulazione consente di evidenziare tutte le caratteristiche delle formulazioni teoriche e numeriche presentate in questa tesi.

Abstract

In this thesis we present a thermodynamic theory for multiphase porous continua based on Biot work and the corresponding numerical formulation by non-standard finite element methods modelling strain localization phenomena. Firstly, a general form of hyperelastic rate equations is provided. Particular expressions for hyperelastic tangent operators are then obtained by using arguments typically employed in the mixture theory. The compatibility of such operators with the aforementioned thermodynamic theory is then investigated by means of symmetry and Maxwell conditions. Among the main results of the presented formulation there is a simple expression for dissipation, that will be used in a multi-scale approach to the localization of deformations in multiphase solids.

A finite element formulation of this constitutive model is then presented, focusing the attention on the linearization of the resulting solving system. Among the different sources of non-linearity, also the ones due to unilateral boundary conditions on the fluid flow are considered. Such boundary conditions are introduced to effectively model the interface between the porous solid and the atmosphere. In order to investigate numerical performance of penalty and augmented Lagrangian regularization techniques employed herein, simple one-dimensional numerical examples are considered. In these examples, both the numerical and formal analogies between seepage problems with unilateral constraints and frictionless contact problems are pointed out. Further situations of practical interest are considered, as the propagation of a saturation front in a soil sample and the partial saturation of a concrete gravity dam.

To model localized dissipative mechanisms, we analyze the presence of discontinuities in displacements and fluid flows. In the corresponding finite element method, the appearance of these discontinuities is simulated by local enhancement of interpolating functions. Finally, results of the numerical simulation of a plain strain compression test on a partially saturated porous solid are presented. This simulation allows us to point out all the features of theoretical and numerical formulations presented in this thesis.

Acknowledgements

Firstly, I wish to thank my tutor, Prof. Carlo Callari for his guidance and support throughout my Ph.D. studies. I am sure I could not have ever completed this work without his precious and punctual support in studying mechanics of porous continua and finite element methods. Furthermore, not only he has introduced me in these research topics, but also he has often advised me in academic and everyday life.

I am also very grateful to Prof. Franco Maceri for giving me the chance to make this fulfilling experience and helping me in several occasions.

The strong discontinuity analysis presented in this thesis is a joint work with Prof. Francisco Armero. I thank him for his thoroughness in answering our questions.

I thank Prof. Giulio Maier and the other participants to the research project: "Diagnostic analyses and safety assessment of existing concrete dams (PRIN 2004)", which has partially supported this research.

I wish to acknowledge Prof. Bernhard A. Schrefler and his co-workers, Francesco Pesavento, Lorenzo Sanavia and Stefano Secchi, for their fundamental suggestions in theoretical treatment of multiphase continua.

I am also grateful to Prof. Paolo Bisegna, for introducing me in continuum mechanics and for many useful discussions helping me in this work, and to Prof. Paolo Podio-Guidugli, who has introduced me in continuum thermodynamics.

I thank my officemates Francesco Ascione, Meriem Debbabi and, in particular, Federica Caselli. I also thank the other friends of the Department of Civil Engineering of the University of Rome "Tor Vergata": Maurizio Cangelli, Antonella Di Chiara, Serena Maniccia, Federico Tocchetti, Giuseppe Tomassetti and Giuseppe Vairo.

I am sincerely grateful to my family and in particular, to my brothers, Francesco and Lorenzo, to my aunt Laura and to my grandmother Giuseppina for giving me love and support in the most difficult moments. For the same reason, I want to thank Serena, who knows my worst faults and, nevertheless, she has not run away yet.

Finally, I want to dedicate this work to my parents, Rosetta and Massimo. I owe them everything and, whatever I do, I know they will keep on being proud of me.

Table of contents

Introduction

Motivation

Theory of porous media is known as a powerful tool in solving problems of interest in many fields of applied sciences, for example in engineering problems involving strong interactions between structures and ground, such as dams during construction and reservoir operations, or underground openings excavated under a water table. In this context, also shakedown analysis in fully saturated porous solids [49] have been performed. Furthermore, theory of porous media can be also successfully applied in many other fields, such as in petroleum and mining engineering or in the analysis of regional subsidence due to extracting activities [95]. Porous media laws can be effectively employed also in concrete modelling, for example in evaluating the effects of high temperatures [73], shrinkage, creep [72] and alkali-silicate reactions [53, 145]. Also biomechanics problems have been investigated by means of poro-elasticity [57, 69]. Further applications can be found in the safety assessment of nuclear waste disposal in porous media [75]. Recently, the need to reduce emissions has motivated the research employing porous media concepts on injection and storage of carbon dioxide in depleted aquifers and hydrocarbon reservoirs [115].

In many applications, the mechanical response of multiphase porous media can be modelled by neglecting the coupling with fluid flows taking place in the porous network, thus allowing the use of tools typically employed in classical continuum mechanics. For example, this simplifying assumption is reasonable when very different time scales characterize evolutions of mechanical and hydraulic problems [28]. In Civil

Engineering, these two situations are often indicated as *drained* and *undrained* conditions. Of course, these two *limit* approaches are not satisfying in those frequent cases where evolution times of mechanical and fluid problems are comparable. Effective theories for porous media are then required to effectively model both the mutual *couplings* between mechanical and hydraulic problems.

Even if the aforementioned limit hypotheses are removed, usually the simplifying assumption of pores saturated by a single fluid, liquid or gas, is kept. Anyway, there are many situations where this assumption is shown to be ineffective: for example, when the portion above the water table cannot be considered completely dry or when a multiphase flow characterizes the porous network.

A further crucial task is to effectively model failure phenomena localized in sliding or fracture surfaces frequently observed in multiphase porous media. The resulting collapse mechanisms are coupled with fluid flow fields and play a fundamental role in observed failure events. For example, during excavation of shallow tunnels, "shear bands" can propagates from the cavity up to the ground surface, thus leading to the collapse of the tunnel roof or of the excavation face. Even more catastrophic events have been registered in dam engineering, involving localized failure phenomena induced by interaction between the solid skeleton and interstitial pore-pressures, in the abutments, as in Malpasset Dam, or in the reservoir banks, as in Vajont Dam. Unfortunately, standard finite element methods are not suitable for localization analysis, as they show great difficulties in reproducing the concentration of strains. We denote as "standard" the finite element formulations implementing rate-independent plasticity models of the local continuum. Localized solutions eventually obtained with these conventional methods are unacceptably dependent on the adopted discretization in terms of mesh size and alignment [107, 144]. Such a pathological mesh dependence is due to the lack of a characteristic length in the constitutive model [79, 105, 113, 139], leading to an ill-posed problem in presence of softening and/or non associated evolution laws. A number of non-standard techniques has been proposed to regularize the problem, like viscous [100], high-gradient [50], non-local [17] and Cosserat [61] models. The main goal of some of these approaches is to introduce small-scale lengths that are able

to objectively characterize localized dissipative mechanisms along shear bands. These small-scale effects can be effectively incorporated in a classical local continuum framework by the strong discontinuity approach [129], a non-standard numerical technique that allows to model the appearance of discontinuous displacement fields and that can be viewed in the more general context of assumed strain enhanced finite element methods [130]. More recently, the strong discontinuity concept has been considered in the so-called extended finite element framework [136]. A comprehensive review on strong discontinuity approaches can be found in [98] together with numerical examples on two and three-dimensional problems. The strong discontinuity approach has been also employed in problems involving fully saturated porous continua [9, 33, 34] in the assumed strain enhanced finite element framework. The final goal of this thesis is to extend the latter approach to the partially saturated case.

Objectives

The final objective of this thesis is a constitutive theory for multiphase media, developed in a thermodynamic macroscopic framework and able to model possible localized failure phenomena by the strong discontinuity approach. This goal is attained by the following intermediate steps.

- Hyperelastic constitutive equations are provided in a thermodynamic macroscopic framework based on Biot work in terms of tangent operators obtained by using arguments typically employed in mixture theories.

- A finite element implementation of the aforementioned hyperelastic constitutive equation is developed in order to effectively model the reversible response in multiphase continua.

- Interfaces between porous solid and atmosphere are properly modelled as unilateral boundary conditions, to effectively employ the constitutive theory and the relative finite element implementation to problems of interest in engineering.

- An extension to irreversible phenomena of the aforementioned constitutive model is obtained in the general framework of additive elasto-plastic decompositions of strains and fluid mass contents.

- A simple expression for dissipation is obtained and employed in a multi-scale approach to the localization of deformations in multiphase solids by the strong discontinuity approach.

The main results reported in the present thesis are presented by Abati and Callari [3], Callari and Abati [31, 32], Callari, Armero and Abati [37].

Dissertation overview

An outline of this thesis is as follows. In Chapter 1, governing equations for a three-phase porous continuum are developed in a macroscopic thermodynamic framework. Based on Biot theory [18, 54], a general rate form for hyperelastic relations is obtained in terms of tangent operators (solid skeleton elastic tensor, coupling tensors, storage modulus). Possible particular forms for these operators are obtained, based on tools typically employed in alternative approaches as mixture theories [60, 95, 119]. The compatibility of the so-obtained operators with the aforementioned macroscopic thermodynamical framework is investigated following the classical arguments introduced by Coleman and Noll [52]. Such a thermodynamic framework leads to simple expressions for the Clausius-Duhem inequality which can be easily employed in the multi-scale approach to strain localization proposed in Chapter 4.

In Chapter 2, we present a finite element method discretization of the differential problem resulting from governing equations presented in Chapter 1. Quasi-static conditions and the infinitesimal deformation hypothesis are assumed in the numerical formulation. The discretization in the time domain is obtained by the Backward-Euler implicit scheme: the resulting highly non-linear solving system is solved by a standard Newton-Raphson iterative procedure and a particular attention is payed on the linearization process. Numerical examples are presented to validate the considered

poro-elastic model and to assess the performance of the numerical formulation. In particular, a benchmark problem involving the desaturation of a sand column is simulated. As a well-known severe test, we consider the propagation of a saturation front in an initially dry solid. Finally, the formulation is applied to a problem of interest for dam engineering.

In Chapter 3, the theoretical treatment and numerical formulation of boundary conditions commuting between "imposed pressure" and "imposed flow" types, depending on the system response evolution, are presented. This kind of boundary conditions effectively models interfaces between porous solid and atmosphere in many situations of practical interest, e.g. the surfaces of dam abutments, reservoir banks, slope, underground openings, only to cite few cases. In these situations, the geometric locus of zero pore pressure intersects the boundary in contact with atmosphere. Different responses are typically observed on the two boundary portions located above and below this intersection: the interstitial pressure is lower than the atmospheric value in the upper part and an outflow is observed in the remaining portion. The locus of zero fluid pressure is not a priori known and it evolves with time in presence of unsteady fluid flow. Therefore, in the analysis of these interfaces between porous solid and atmosphere, the boundary condition to be applied may change between the two aforementioned types during problem evolution. These boundary conditions can be considered in the more general framework of unilateral constraints, leading to a more effective numerical formulation, especially for those frequent situations where large boundary regions are almost instantaneously subjected to a switch of condition type. Two numerical techniques, the penalty and the augmented Lagrangian method, typically employed in contact mechanics [14, 92, 151, 153], are here introduced to treat fluid-flow unilateral boundaries in the finite element formulation for coupled unsaturated porous solids presented in Chapter 2 and the performance of such regularization techniques is thoroughly investigated by representative numerical examples.

Finally, an analysis of strong discontinuities in partially-saturated porous solids is considered in Chapter 4. The analysis considers discontinuous displacement fields and corresponding singular distributions of strain, as well as singular distributions of fluid

contents corresponding to discontinuous flows of gaseous and liquid phases, modelling their accumulation and/or drainage in the localized failures of interest. The constitutive model presented in Chapter 1 provides the proper framework for the extension of the results presented in [33, 34] for the fully saturated case. In the multi-scale context introduced firstly in [8], the small-scale problem is defined by the localized mass balances of liquid and gas contents, both related to singular dilatancy of the discontinuity, besides the mechanical response driven by the assumed effective traction. This requires the consideration of the proper pore pressures and saturation degrees on the discontinuity. This small-scale problem is then connected to the large-scale coupled problem through a weak equilibrium statement between this traction and the stresses in the bulk. A main feature of the proposed method is the direct approximation of this equation by finite elements enhanced with singular fields of strain and fluid contents. These enhancements are kept local at the element level, allowing the static condensation of the different enhanced parameters and, hence, a simple and very efficient numerical implementation in existing finite element codes. Different numerical simulations that illustrate the range of application of the developed models and the performance of the new finite element methods are then presented.

1

Hyperelastic constitutive equations

1.1 Introduction

Equations governing the evolution of a three-phase porous continuum are developed in this chapter with a macroscopic approach. In macroscopic theories, balance equations are obtained regarding the multiphase medium as a system of overlapping continua filling the whole volume with a reduced density. At each time, this volume is identified by the current configuration of the solid skeleton (Fig. 1.1).

A connection between balances characterizing the response of multiphase continua at macroscopic and microscopic scales can be obtained by the use of alternative approaches, as averaging [95, 119] or homogenization [44, 62] techniques. Nevertheless, in this work we are concerned only with the macroscopic scale. In particular, the macroscopic approach based on the Biot work [18, 54] and mixture theories developed by means of the volume fraction concept [23, 55, 60, 82] are considered herein in developing a hyperelastic constitutive model that is thermodynamically consistent.

In developments that follow, macroscopic thermodynamics based on Biot theory are considered in obtaining a general rate form for hyperelastic relations in terms of tangent operators (solid skeleton elastic tensor, coupling tensors, storage modulus). In this framework, the porous continuum can be viewed as an open system exchanging fluids with the environment. Only one free energy potential is considered for the whole

porous continuum. Symmetry and Maxwell conditions are then written in terms of this unique potential. Coupling and storage parameters appearing in the aforementioned hyperelastic rate equations are obtained independently herein following arguments typically employed in mixture theories. The thermodynamic consistency of these equations is then investigated by the use of symmetry and Maxwell conditions obtained in the aforementioned macroscopic framework. Therefore, the thermodynamic macroscopic approach presented herein is to be contrasted with the other ones based on Biot theory, where symmetry and Maxwell conditions are explicitly enforced in deriving particular forms of hyperelastic tangent operators, as in [54, 56, 97].

Since in this work phase interfaces are neglected in mass and energy balances, we prove that the total stress decomposition proposed by Bishop [21] is thermodynamically consistent only if fluid pressure contributions are weighted by saturation degrees, consistently with other approaches disregarding interfacial phenomena [23, 77, 82, 94]. On the other hand, it is often argued that a proper constitutive theory for multiphase solids should take into account the presence of menisci at phase interfaces, the so-called "contractile skin" [70]. In particular, the explicit consideration of such interfacial phenomena can play a crucial role in problems characterized by very low values of liquid saturation degree. We refer to the thermodynamical treatment proposed by Gray and Schrefler [76] and applied in [72] to model high-temperature response of concrete, showing that a measure of the solid surface fraction in contact with each fluid is to be used as the weighting function of fluid pressure contributions in stress decomposition equation.

We remark that among the main features of the approach proposed herein is the consideration of a thermodynamic framework employing the same primary variables (solid-skeleton displacements and fluid pressures) normally employed in formulating initial and boundary value problems and relative finite element approximations in multiphase porous continua. As a further result, the Clausius-Duhem dissipation inequality takes a simple expression that can be used in the multi-scale approach to strain localization phenomena in unsaturated porous media presented in Chapter 4, extending the results reported in [9, 33, 34] for the fully saturated case.

In subsequent developments we indicate as "unsaturated" or "partially saturated"

those situations where the porous space is filled by more than one fluid phase. An outline of this chapter is as follows. In Section 1.2 fluid mass balances are written in terms of fluid mass content rates by the use of the overlapping continua concept and assuming exact kinematics for the solid skeleton as well as for both fluids. Infinitesimal deformations of the solid skeleton are then assumed in the following. In Section 1.3 a general rate form for hyperelastic equations is obtained for quasi-static processes in a macroscopic framework developed for thermodynamically open continua. Therefore, we write in a general form symmetry and Maxwell relations, that can be viewed as admissibility conditions for the particular forms of tangent operators obtained by the use of mixture theory concepts in Section 1.4. Two different classes of hyperelastic tangent operators are considered, as a consequence of two different constitutive hypotheses on saturation degree models. In particular, if we assume a realistic dependency of saturation degrees on the porosity, the obtained tangent operators are proved to be consistent with the effective stress equation proposed by Lewis and Schrefler [94]. On the other hand, if the simplifying assumption of saturation degrees depending only on capillary pressure is considered, an approximated rate form of the aforementioned effective stress equation is to be employed to ensure thermodynamical consistency. Such a simplified version of the Lewis-Schrefler stress is coincident with the one proposed by Coussy [54].

Finally, it is shown how the presented thermodynamical framework leads to an expression for the total mechanical power which includes as a particular case the one proposed by Houlsby [80].

The main results reported in the present chapter are also presented by Callari and Abati [31].

1.2 Fluid mass balance

As typically assumed in macroscopic theories, the solid skeleton and the fluid phases filling the porous space are treated as overlapping continua and continuum mechanics arguments are then employed in the developments that follows to obtain the equations governing the porous solid.

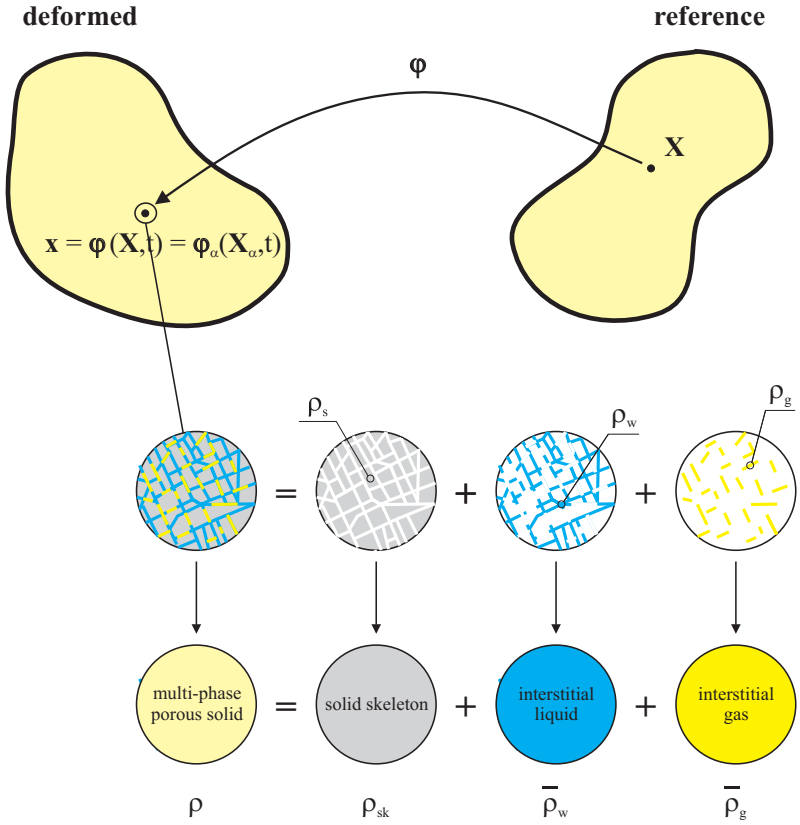

Figure 1.1: Reference and current configurations of a porous solid: superposition of equivalent continua [1]

The reference configuration of the porous continuum is identified with a spatial domain $\Omega \subset \mathbb{R}^{n_{\text{dim}}}$ for $n_{\text{dim}} = 1, 2$ or 3, the spatial dimension of the problem. The current configuration of this porous solid is characterized by the solid-skeleton deformation $\boldsymbol{\varphi} : \Omega \times [0, T] \to \mathbb{R}^{n_{\text{dim}}}$ for the considered time interval T. We denote by $\mathbf{x} = \boldsymbol{\varphi}(\mathbf{X}, t)$ the position at time instant t of the solid-skeleton particle $\mathbf{X} \in \Omega$. The deformation gradient and the corresponding Jacobian are defined by

$$\mathbf{F} := \text{Grad}\, \boldsymbol{\varphi} \qquad \text{and} \qquad J := \det \mathbf{F} > 0 \tag{1.1}$$

respectively, where $\text{Grad}(\cdot)$ denotes the material gradient with respect to the reference coordinates $\mathbf{X}$.

In the macroscopic approach considered herein, the generic fluid phase α is characterized in terms of the so-called "reduced" density $\bar{\rho}_\alpha$, measuring the mass of fluid α per unit current volume of the porous solid. Therefore, in addition to solid-skeleton,

all the considered fluid phases are assumed to be present with their reduced densities $\bar{\rho}_\alpha(\mathbf{x},t)$ at any position $\mathbf{x}$ in the deformed configuration of the porous solid $\boldsymbol{\varphi}(\Omega)$. In other words, $\mathbf{x}$ is the current position of a particle of fluid α initially located at $\mathbf{X}_\alpha$ and subjected to a motion $\boldsymbol{\varphi}_\alpha(\mathbf{X}_\alpha,t)$. The material time derivatives with respect to solid-skeleton and α-fluid motions are defined as

$$\frac{d(\cdot)}{dt} := \left.\frac{\partial(\cdot)}{\partial t}\right|_{\mathbf{X}} =: \dot{(\cdot)} \qquad \text{and} \qquad \frac{d_\alpha(\cdot)}{dt} := \left.\frac{\partial(\cdot)}{\partial t}\right|_{\mathbf{X}_\alpha} \tag{1.2}$$

to measure the time variations associated with fixed material particles of solid skeleton and fluid α, respectively. These material time derivatives can be calculated for the spatial field of reduced density $\bar{\rho}_\alpha(\mathbf{x},t)$, leading to:

$$\dot{\bar{\rho}}_\alpha = \frac{\partial \bar{\rho}_\alpha}{\partial t} + \nabla\bar{\rho}_\alpha \cdot \mathbf{v} \qquad \text{and} \qquad \frac{d_\alpha \bar{\rho}_\alpha}{dt} = \frac{\partial \bar{\rho}_\alpha}{\partial t} + \nabla\bar{\rho}_\alpha \cdot \mathbf{v}_\alpha \tag{1.3}$$

for the spatial velocities $\mathbf{v} := \dot{\boldsymbol{\varphi}} \circ \boldsymbol{\varphi}^{-1}$ and $\mathbf{v}_\alpha := \dot{\boldsymbol{\varphi}}_\alpha \circ \boldsymbol{\varphi}_\alpha^{-1}$ of solid skeleton and fluid α, respectively. In (1.3) we have denoted by "$\nabla(\cdot)$" the gradient operator with respect to spatial coordinates $\mathbf{x}$ and by "$\cdot$" the standard Euclidean inner product between vectors in $\mathbb{R}^{n_{\text{dim}}}$. From (1.3), the following relation between material time derivatives with respect to solid skeleton and fluid motion is obtained:

$$\frac{d_\alpha \bar{\rho}_\alpha}{dt} = \dot{\bar{\rho}}_\alpha + \nabla\bar{\rho}_\alpha \cdot (\mathbf{v}_\alpha - \mathbf{v}) \tag{1.4}$$

An arbitrary region included in the current configuration $\boldsymbol{\varphi}(\Omega)$ of the porous solid can be identified with the deformed configuration $\boldsymbol{\varphi}_\alpha(\mathcal{P}_\alpha)$ of a material fluid region $\mathcal{P}_\alpha$ according to motion $\boldsymbol{\varphi}_\alpha$. The mass of fluid α contained in this region is

$$I_\alpha := \int_{\boldsymbol{\varphi}_\alpha(\mathcal{P}_\alpha)} \bar{\rho}_\alpha \, dv \tag{1.5}$$

for the elemental deformed volume dv. Applying the Reynolds transport theorem, the material time derivative of integral (1.5) can be expressed as

$$\frac{d_\alpha I_\alpha}{dt} = \int_{\boldsymbol{\varphi}_\alpha(\mathcal{P}_\alpha)} \left(\frac{d_\alpha \bar{\rho}_\alpha}{dt} + \bar{\rho}_\alpha \, \text{div}\, \mathbf{v}_\alpha \right) \, dv \tag{1.6}$$

where we have denoted by "div$(\cdot)$" the divergence operator with respect to spatial coordinates $\mathbf{x}$. Relation (1.4) between material time derivatives is substituted in (1.6)

and the following equation is obtained after some manipulation:

$$\frac{d_\alpha I_\alpha}{dt} = \int_{\boldsymbol{\varphi}_\alpha(\mathcal{P}_\alpha)} (\dot{\bar{\rho}}_\alpha + \bar{\rho}_\alpha \mathrm{div}\, \mathbf{v})\, dv + \int_{\boldsymbol{\varphi}_\alpha(\mathcal{P}_\alpha)} \mathrm{div}\, \mathbf{q}_\alpha \; dv \tag{1.7}$$

where

$$\mathbf{q}_\alpha := \bar{\rho}_\alpha(\mathbf{v}_\alpha - \mathbf{v}) \tag{1.8}$$

is the mass flow of fluid α in the porous solid, that is, the relative velocity of fluid mass with respect to solid skeleton.

Under the assumptions that no sources of fluid exist and that no mass is exchanged between all the considered phases, the mass balance for fluid α is given by imposing $d_\alpha I_\alpha/dt = 0$ in (1.7). In view of the arbitrary choice of $\boldsymbol{\varphi}_\alpha(\mathcal{P}_\alpha)$, such a mass balance can be written in local form:

$$\dot{\bar{\rho}}_\alpha + \bar{\rho}_\alpha d_v = -\mathrm{div}\, \mathbf{q}_\alpha \tag{1.9}$$

where, denoting by $\mathbf{1}$ the second-order symmetric identity tensor in $\mathbb{R}^{n_{\mathrm{dim}}}$ and by "$\nabla^s(\cdot)$" the symmetric part of spatial gradient, we have introduced the trace $d_v := \mathbf{d} : \mathbf{1}$ of spatial strain rate $\mathbf{d} := \nabla^s \mathbf{v}$.

Following [19], [114] and [55], balance equation (1.9) can be written in terms of fluid mass content function $M_\alpha : \Omega \times [0, T] \to \mathbb{R}$, defined as the mass of fluid α per unit reference volume of the porous solid:

$$M_\alpha := J\bar{\rho}_\alpha \tag{1.10}$$

for the solid-skeleton Jacobian $(1.1)_2$, measuring the ratio between the current and the initial volume of the porous continuum. As a consequence of relation

$$\dot{J} = J d_v \tag{1.11}$$

the material time derivative of fluid content (1.10) combined with (1.9) leads to:

$$\dot{M}_\alpha = -J\mathrm{div}\, \mathbf{q}_\alpha \tag{1.12}$$

In the range of infinitesimal deformations of solid skeleton, fluid-mass balance equation (1.12) reads:

$$\dot{M}_\alpha = -\mathrm{div}\, \mathbf{q}_\alpha \tag{1.13}$$

1.3 Macroscopic thermodynamics of three-phase porous solids

The main features of a macroscopic thermodynamic framework for multiphase porous continua is presented in the following sections. A detailed analysis can be found in [54]. We consider isothermal and quasi-static processes as well as infinitesimal deformations of the solid skeleton. On the other hand, a non-linearized kinematics is employed for the fluid phases. We assume the fluid mixture filling the porous space as composed by two immiscible fluid phases, namely a gaseous phase g and a liquid phase w.

1.3.1 Energy balance

At the macro-scale, the porous solid can be viewed as a thermodynamic open system, exchanging fluids with the environment. Therefore, denoting by dV and dA the elemental material volume and area, respectively, the internal energy balance for an arbitrary region $\mathcal{P}$ included in the porous continuum Ω can be written as:

$$\int_{\mathcal{P}} \dot{e}_i \, dV + \sum_{\alpha=w,g} \int_{\partial\mathcal{P}} e_{i_m\alpha} \mathbf{q}_\alpha \cdot \mathbf{n} \, dA = P_{e,u} + P_{e,q} \qquad \forall \mathcal{P} \subset \Omega \tag{1.14}$$

where "$\Sigma_{\alpha=w,g}(\cdot)$" denotes the summation on index α over the two fluid phases, e_i is the internal energy volumetric density of the porous solid and $e_{i_m\alpha}$ is the internal energy for unit mass of fluid α. The first term on left side of (1.14) takes into account the internal energy variation due to solid skeleton and fluids contained in $\mathcal{P}$. The second term accounts for the internal energy variation due to the flow of fluids through the solid-skeleton boundary $\partial\mathcal{P}$. Right side of (1.14) denotes the power of external loads, whose terms $P_{e,u}$ and $P_{e,q}$ are due to porous continuum velocity field $\dot{\mathbf{u}}$ and fluid flows $\mathbf{q}_\alpha$, that is, respectively,

$$\begin{aligned} P_{e,u} &:= \int_{\mathcal{P}} \rho \mathbf{f} \cdot \dot{\mathbf{u}} \, dV + \int_{\partial\mathcal{P}} \mathbf{t} \cdot \dot{\mathbf{u}} \, dA \\ P_{e,q} &:= \sum_{\alpha=w,g} \left(\int_{\mathcal{P}} \mathbf{f} \cdot \mathbf{q}_\alpha \, dV - \int_{\partial\mathcal{P}} \frac{p_\alpha}{\rho_\alpha} \mathbf{n} \cdot \mathbf{q}_\alpha \, dA \right) \end{aligned} \tag{1.15}$$

where $\mathbf{f}$ are the mass forces in $\mathcal{P}$ and $\mathbf{t}$ are the tractions on $\partial\mathcal{P}$. In (1.15), ρ is the porous solid density and ρ_α denotes the so-called "intrinsic" fluid density observed at the microscopic scale, that is, the mass of unit current volume of fluid α. We have assumed as ideal both the fluid phases, introducing in (1.15) a consistent spherical form $\boldsymbol{\sigma}_\alpha = -p_\alpha \mathbf{1}$ for their stress tensors $\boldsymbol{\sigma}_w$ and $\boldsymbol{\sigma}_g$ in terms of the corresponding pressures p_w and p_g, respectively. We note that in this paper, compressive fluid pressures p_w and p_g are considered as positive. On the other hand, tensile normal components of stress tensors $\boldsymbol{\sigma}_w$, $\boldsymbol{\sigma}_g$ and $\boldsymbol{\sigma}$ are considered as positive, with $\boldsymbol{\sigma}$ the (total) Cauchy stress tensor defined in the porous solid.

Combination of (1.14) with $(1.15)_2$ and with the weak form of momentum equation, that is,

$$P_{e,u} = \int_{\mathcal{P}} \boldsymbol{\sigma} : \dot{\boldsymbol{\varepsilon}} \; dV \tag{1.16}$$

leads to:

$$\int_{\mathcal{P}} \dot{e}_i \; dV = \sum_{\alpha=w,g} \left[\int_{\mathcal{P}} \mathbf{f} \cdot \mathbf{q}_\alpha \; dV - \int_{\partial\mathcal{P}} h_\alpha \mathbf{q}_\alpha \cdot \mathbf{n} \; dA \right] + \int_{\mathcal{P}} \boldsymbol{\sigma} : \nabla^s \dot{\mathbf{u}} \; dV \tag{1.17}$$

where we have used the definitions $\boldsymbol{\varepsilon} := \nabla^s \mathbf{u}$ for the infinitesimal strain tensor of the porous continuum and

$$h_\alpha := e_{i_m \alpha} + \frac{p_\alpha}{\rho_\alpha} \tag{1.18}$$

for the enthalpy of fluid phase α. So, applying divergence theorem to (1.17) and considering the arbitrary choice of $\mathcal{P}$, we obtain:

$$\dot{e}_i = \boldsymbol{\sigma} : \dot{\boldsymbol{\varepsilon}} - \sum_{\alpha=w,g} \left[\nabla \mathcal{V}_{ext} \cdot \mathbf{q}_\alpha + \operatorname{div}(h_\alpha \mathbf{q}_\alpha) \right] \tag{1.19}$$

where we have assumed the existence of an external potential $\mathcal{V}_{ext}$ for the mass forces, that is, $\mathbf{f} = -\nabla \mathcal{V}_{ext}$.

1.3.2 Dissipation inequality

For every thermodynamic process, the non-negative entropy production postulated by the second law can be written for the multiphase medium as follows:

$$\int_{\mathcal{P}} \dot{\eta} \; dV + \sum_{\alpha=w,g} \int_{\partial\mathcal{P}} \eta_\alpha \, \mathbf{q}_\alpha \cdot \mathbf{n} \; dA \geq 0 \qquad \forall \mathcal{P} \subset \Omega \tag{1.20}$$

with η the entropy density of the porous medium and η_α the entropy for unit mass of fluid α. On left side of (1.20) there are the entropy variations due to solid skeleton and fluids contained in $\mathcal{P}$ (first term) as well as to the flow of fluids through $\partial\mathcal{P}$ (second term).

The following local expression of the second law in terms of density Γ of entropy production is then obtained from application of divergence and localization theorems to (1.20):

$$\Gamma := \dot{\eta} + \sum_{\alpha=w,g} \mathrm{div}(\eta_\alpha \mathbf{q}_\alpha) \geq 0 \tag{1.21}$$

Denoting by T the absolute temperature, entropies η and η_α appearing in (1.21) can be expressed in terms of Helmholtz free energy density $\psi := e_i - T\eta$ of the porous continuum and free enthalpy $\mu_\alpha := h_\alpha - T\,\eta_\alpha$ for unit mass of the fluid phase α (or Gibbs free energy). The so-obtained inequality can be combined with the local form of first law (1.19) and with fluid mass balances (1.13), thus leading to the following expression for dissipation D of the porous solid in the assumed isothermal setting ($T = T_0$):

$$D := \Gamma T_0 = \underbrace{\boldsymbol{\sigma} : \dot{\boldsymbol{\varepsilon}} + \sum_{\alpha=w,g} \mu_\alpha \dot{M}_\alpha - \dot{\psi}}_{=:D_{int}} \underbrace{- \sum_{\alpha=w,g} \nabla(\mu_\alpha + \mathcal{V}_{ext}) \cdot \mathbf{q}_\alpha}_{=:D_{cond}} \geq 0 \tag{1.22}$$

According to a standard argument [52], non-negativeness of total dissipation D implies the following dissipation inequalities in terms of D_{int} and D_{cond}:

$$D_{int} := \boldsymbol{\sigma} : \dot{\boldsymbol{\varepsilon}} + \sum_{\alpha=w,g} \mu_\alpha \dot{M}_\alpha - \dot{\psi} \geq 0 \tag{1.23}$$

$$D_{cond} := - \sum_{\alpha=w,g} \nabla(\mu_\alpha + \mathcal{V}_{ext}) \cdot \mathbf{q}_\alpha \geq 0 \tag{1.24}$$

Remark 1.1 *A possible conduction law satisfying dissipation inequality (1.24) is*

$$\mathbf{q}_\alpha = -\rho_\alpha^2 \mathbf{k}_\alpha \nabla(\mu_\alpha + \mathcal{V}_{ext}) \qquad \textit{for} \qquad \alpha = w, g \tag{1.25}$$

with positive semi-defined permeability tensors $\mathbf{k}_w$ and $\mathbf{k}_g$. In particular, a typical extension of Darcy's law to the case of multiphase flow employs "relative" permeabilities [99, 46], defined as

$$\mathbf{k}_\alpha := k_\alpha^{rel} \mathbf{k}_\alpha^{sat} \qquad \textit{for} \qquad \alpha = w, g \tag{1.26}$$

where the relative permeability coefficient k_α^{rel} models the effects of interaction between the fluid phases in terms of permeability reduction with respect to tensor $\mathbf{k}_\alpha^{sat}$ characterizing the single-phase seepage of fluid α.

1.3.3 Porous solid hyperelastic equations

In the considered macroscopic point of view, the reversible response of porous continuum is fully defined by solid-skeleton deformation and fluid mass contents, that is, in terms of Helmholtz free energy: $\psi = \hat{\psi}(\boldsymbol{\varepsilon}, M_w, M_g)$. As a consequence, the application of Coleman's method [52] in the treatment of internal dissipation inequality (1.23) leads to:

$$\boldsymbol{\sigma} = \frac{\partial \psi}{\partial \boldsymbol{\varepsilon}} \qquad \text{and} \qquad \mu_\alpha = \frac{\partial \psi}{\partial M_\alpha} \quad \text{for} \quad \alpha = w, g \tag{1.27}$$

These hyperelastic relations represent a so-called "pure stiffness" formulation [150], that is, all the dependent variables have the dimension of stresses (1.27). However, we are more interested to a a "mixed stiffness" formulation, based on the consideration of solid-skeleton displacements $\mathbf{u}$ and fluid pressures p_α as primary variables.

With this motivations, we introduce the potential $\phi = \hat{\phi}(\boldsymbol{\varepsilon}, \mu_w, \mu_g)$ obtained as the partial Legendre transform of the free energy function $\psi = \hat{\psi}(\boldsymbol{\varepsilon}, M_w, M_g)$ in the coniugate variables $\{\mu_w, M_w\}$ and $\{\mu_g, M_g\}$:

$$\begin{aligned} \hat{\phi}(\boldsymbol{\varepsilon}, \mu_w, \mu_g) &:= -\max_{M_w, M_g} \left[\sum_{\alpha=w,g} \mu_\alpha M_\alpha - \hat{\psi}(\boldsymbol{\varepsilon}, M_w, M_g) \right] = \\ &= -\sum_{\alpha=w,g} \mu_\alpha \hat{M}_\alpha(\boldsymbol{\varepsilon}, \mu_\alpha) + \hat{\psi}\left(\boldsymbol{\varepsilon}, \hat{M}_w(\boldsymbol{\varepsilon}, \mu_w), \hat{M}_g(\boldsymbol{\varepsilon}, \mu_g)\right) \end{aligned} \tag{1.28}$$

where the functions $\hat{M}_\alpha(\boldsymbol{\varepsilon}, \mu_\alpha)$ for $\alpha = w, g$ are obtained from the inversion of hyperelastic relations $(1.27)_2$. Internal dissipation inequality (1.23) can then be rewritten in terms of ϕ:

$$D_{int} = \boldsymbol{\sigma} : \dot{\boldsymbol{\varepsilon}} - \sum_{\alpha=w,g} M_\alpha \dot{\mu}_\alpha - \dot{\phi} \geq 0 \tag{1.29}$$

which provides, after application of Coleman's method [52], to the following hyperelastic laws, alternative to (1.27):

$$\boldsymbol{\sigma} = \frac{\partial \phi}{\partial \boldsymbol{\varepsilon}} \qquad \text{and} \qquad M_\alpha = -\frac{\partial \phi}{\partial \mu_\alpha} \quad \text{for} \quad \alpha = w, g \tag{1.30}$$

1.3.4 Rate form of hyperelastic relations

Rate form of porous solid hyperelastic relations (1.30) reads

$$\begin{bmatrix} \dot{\boldsymbol{\sigma}} \\ \dot{M}_w \\ \dot{M}_g \end{bmatrix} = \begin{bmatrix} \tilde{\mathbb{C}}_{sk} & -\rho_w \mathbf{b}_w & -\rho_g \mathbf{b}_g \\ \rho_w \mathbf{b}_w & \rho_w^2 C_{ww} & \rho_w \rho_g C_{wg} \\ \rho_g \mathbf{b}_g & \rho_g \rho_w C_{gw} & \rho_g^2 C_{gg} \end{bmatrix} \begin{bmatrix} \dot{\boldsymbol{\varepsilon}} \\ \dot{\mu}_w \\ \dot{\mu}_g \end{bmatrix} \tag{1.31}$$

where we employed the following definitions for two coupling tensors and three specific storage functions, respectively:

$$\mathbf{b}_\alpha := -\frac{1}{\rho_\alpha} \frac{\partial^2 \phi}{\partial \boldsymbol{\varepsilon} \partial \mu_\alpha} \quad \text{and} \quad C_{\alpha\beta} := -\frac{1}{\rho_\alpha \rho_\beta} \frac{\partial^2 \phi}{\partial \mu_\alpha \partial \mu_\beta} \qquad \text{for} \quad \alpha, \beta = w, g \tag{1.32}$$

Equation $(1.31)_1$ is written also in terms of the elastic tangent tensor:

$$\tilde{\mathbb{C}}_{sk} := \frac{\partial^2 \phi}{\partial \boldsymbol{\varepsilon}^2} \tag{1.33}$$

which relates the increments of solid-skeleton strain and (total) stress for the particular case of vanishing free-enthalpy increments in both the fluid phases. As shown by equations (1.31), coupling and storage operators defined by (1.32), can be seen as an extension to the case of three-phase porous solid of Biot's coefficient and of the inverse of Biot's modulus [18], respectively.

It can be easily shown that relations (1.31–1.33) leads to satisfaction of following symmetry conditions:

$$\tilde{\mathbb{C}}_{sk} = \tilde{\mathbb{C}}_{sk}^T \qquad \mathbf{b}_\alpha = \mathbf{b}_\alpha^T \qquad C_{\alpha\beta} = C_{\beta\alpha} \qquad \text{for} \quad \alpha, \beta = w, g \tag{1.34}$$

and Maxwell relations:

$$\left.\begin{aligned} \frac{\partial \tilde{\mathbb{C}}_{sk}}{\partial \mu_\alpha} &= -\frac{\partial}{\partial \boldsymbol{\varepsilon}}(\rho_\alpha \mathbf{b}_\alpha) \\ \frac{\partial}{\partial \mu_\beta}(\rho_\alpha \mathbf{b}_\alpha) &= \frac{\partial}{\partial \mu_\alpha}(\rho_\beta \mathbf{b}_\beta) \\ \frac{\partial}{\partial \mu_\beta}(\rho_\alpha \mathbf{b}_\alpha) &= \frac{\partial}{\partial \boldsymbol{\varepsilon}}(\rho_\alpha \rho_\beta C_{\alpha\beta}) \\ \frac{\partial}{\partial \mu_\beta}\left(\rho_\alpha^2 C_{\alpha\alpha}\right) &= \frac{\partial}{\partial \mu_\alpha}(\rho_\alpha \rho_\beta C_{\alpha\beta}) \end{aligned}\right\} \quad \text{for} \quad \alpha, \beta = w, g \tag{1.35}$$

On the other hand, for a set of constitutive equations directly formulated in rate form (1.31), symmetry conditions (1.34) and Maxwell relations (1.35) represent not only necessary but also sufficient conditions for the existence of a hyperelastic potential (1.28), as shown in Appendix D. Moreover, also sufficient conditions for stability can be obtained for a constitutive system given in the rate form (1.31). In fact, as shown in Appendix C, the Helmholtz free energy ψ is a convex function of strains $\boldsymbol{\varepsilon}$ and fluid mass contents M_α if the elastic tangent tensor $\tilde{\mathbb{C}}_{sk}$ and the matrix of storage modulus $\mathbf{C}$ are both positive defined, i.e.:

$$\mathbf{A} : \tilde{\mathbb{C}}_{sk}\, \mathbf{A} > 0 \quad \forall\, \mathbf{A} \in Sym \setminus \{\mathbf{0}\} \qquad \text{and} \qquad \mathbf{a} : \mathbf{C}\, \mathbf{a} > 0 \quad \forall\, \mathbf{a} \in \mathbb{R}^2 \setminus \{\mathbf{0}\} \tag{1.36}$$

where

$$\mathbf{C} := \begin{bmatrix} C_{ww} & C_{wg} \\ C_{gw} & C_{gg} \end{bmatrix} \tag{1.37}$$

1.4 Particular forms of hyperelastic relations

We suppose that the porous space is saturated by two immiscible barotropic fluids where the density of each fluid is fully characterized by its own pressure, that is, $\rho_\alpha = \hat{\rho}_\alpha(p_\alpha)$ for $\alpha = w, g$. In this case, we have the following expression for the free enthalpies of fluids:

$$\frac{d\mu_\alpha}{dp_\beta} = \frac{1}{\rho_\alpha}\delta_{\alpha\beta} \qquad \text{for} \quad \alpha, \beta = w, g \tag{1.38}$$

with $\delta_{\alpha\beta}$ the Kronecker delta. Furthermore, the following general expression is assumed for coupling tangent tensors $(1.32)_1$:

$$\mathbf{b}_\alpha = \zeta_\alpha \mathbf{b} \qquad \text{with} \quad \zeta_\alpha \in \mathbb{R} \qquad \text{for} \quad \alpha = w, g \tag{1.39}$$

and $\mathbf{b}$ a symmetric tensor.

As a consequence of (1.38) and (1.39), hyperelastic relations in general rate form (1.31) can be rewritten as:

$$\begin{cases} \dot{\boldsymbol{\sigma}} &= \tilde{\mathbb{C}}_{sk}\dot{\boldsymbol{\varepsilon}} - \mathbf{b} \displaystyle\sum_{\gamma=w,g} \zeta_\gamma \dot{p}_\gamma \\ \dfrac{\dot{M}_\alpha}{\rho_\alpha} &= \zeta_\alpha \mathbf{b} : \dot{\boldsymbol{\varepsilon}} + \displaystyle\sum_{\gamma=w,g} C_{\alpha\gamma}\dot{p}_\gamma \qquad \text{for} \quad \alpha = w, g \end{cases} \tag{1.40}$$

In the following sections, arguments of mixture theories are employed to obtain possible expressions for tangent coupling tensors $\mathbf{b}_\alpha$ and tangent storage modulus $C_{\alpha\beta}$ appearing in the general rate form (1.40) of porous solid hyperelastic relations (1.30).

In particular, we will separately consider in Sections 1.4.1 and 1.4.2 the tangent operators appearing in stress equation $(1.40)_1$ and in fluid content equation $(1.40)_2$, respectively. The so-obtained particular form of constitutive equations will then be investigated by means of conditions (1.34–1.35), in order to assess its compatibility with the macroscopic thermodynamical framework presented in Section 1.3.

1.4.1 Stress equation

In this work, as possible forms for tangent tensors $\tilde{\mathbb{C}}_{sk}$ and $\mathbf{b}_\alpha = \zeta_\alpha \mathbf{b}$ appearing in stress equation $(1.40)_1$, we consider the ones obtained from differentiation of the following expression of (total) stress:

$$\boldsymbol{\sigma} = \boldsymbol{\sigma}' - \mathbf{b}\, p_f \tag{1.41}$$

where

$$p_f := \sum_{\alpha=w,g} s_\alpha p_\alpha \tag{1.42}$$

is the average pressure of fluid mixture, expressed in terms of saturation degree s_α, which in turn is defined as the current volume of single fluid α per unit volume of the deformed fluid mixture. In equation (1.41), tensor $\boldsymbol{\sigma}'$ can be understood as the so-called "effective" stress, that is, the part of total stress whose rate $\dot{\boldsymbol{\sigma}}'$ is directly linked to solid-skeleton strain increment rate $\dot{\boldsymbol{\varepsilon}}$:

$$\dot{\boldsymbol{\sigma}}' = \mathbb{C}_{sk}\, \dot{\boldsymbol{\varepsilon}} \tag{1.43}$$

The fourth-order symmetric tensor $\mathbb{C}_{sk}$ characterize the so-called "drained" elastic response of the solid skeleton. Under these assumptions, equation (1.41) can be viewed as an extension to the general case of anisotropic solid skeleton and compressible solid phase of the Bishop [21] effective stress equation form obtained by Lewis and Schrefler [94], employing techniques of volume averaging.

In the developments that follow, tensor $\mathbf{b}$ is assumed as constant and, in view of (1.43), the general rate form of stress equation (1.41) is then

$$\dot{\boldsymbol{\sigma}} = \mathbb{C}_{sk}\,\dot{\boldsymbol{\varepsilon}} - \mathbf{b}\,\dot{p}_f \tag{1.44}$$

where the rate of average pore pressure (1.42) reads:

$$\dot{p}_f = \sum_{\alpha=w,g} (s_\alpha \dot{p}_\alpha + \dot{s}_\alpha p_\alpha) \tag{1.45}$$

In general, saturation degrees can be functions of both the primary variables of system (1.40), that is, solid-skeleton displacements and pore pressures. Therefore, the increment rate of s_α can be written in terms of $\dot{\boldsymbol{\varepsilon}}$, $\dot{p}_w$ and $\dot{p}_g$ as:

$$\dot{s}_\alpha = \frac{\partial s_\alpha}{\partial \boldsymbol{\varepsilon}} : \dot{\boldsymbol{\varepsilon}} + \sum_{\gamma=w,g} \frac{\partial s_\alpha}{\partial p_\gamma} \dot{p}_\gamma \qquad \text{for} \quad \alpha = w, g \tag{1.46}$$

whose substitution in expression (1.45) for the rate of average pore pressure yields:

$$\dot{p}_f = \sum_{\alpha=w,g} \left(s_\alpha \dot{p}_\alpha + p_\alpha \frac{\partial s_\alpha}{\partial \boldsymbol{\varepsilon}} : \dot{\boldsymbol{\varepsilon}} + p_\alpha \sum_{\gamma=w,g} \frac{\partial s_\alpha}{\partial p_\gamma} \dot{p}_\gamma \right) \tag{1.47}$$

Denoting by x any of the considered primary variables, it is:

$$\sum_{\alpha=w,g} \frac{\partial s_\alpha}{\partial x} = 0 \qquad \text{for} \quad x = \boldsymbol{\varepsilon}, p_w, p_g \tag{1.48}$$

which is a consequence of the geometric constraint on the summation of saturation degrees, that is,

$$\sum_{\alpha=w,g} s_\alpha = 1 \tag{1.49}$$

So, the following summations appearing in (1.47) can be simplified as follows:

$$\begin{aligned} \sum_{\alpha=w,g} p_\alpha \frac{\partial s_\alpha}{\partial x} &= (p_g - p_w)\frac{\partial s_g}{\partial x} = \\ &= p_c \frac{\partial p_c}{\partial p_\gamma} \frac{\partial s_\gamma}{\partial x} \qquad \text{for} \quad \gamma = w, g \qquad \text{and} \quad x = \boldsymbol{\varepsilon}, p_w, p_g \end{aligned} \tag{1.50}$$

where we have introduced the definition of capillary pressure

$$p_c := p_g - p_w \tag{1.51}$$

and employed relations:

$$\frac{\partial s_\alpha}{\partial x}\frac{\partial p_c}{\partial p_\alpha} = \frac{\partial s_\beta}{\partial x}\frac{\partial p_c}{\partial p_\beta} \qquad \text{for} \quad \alpha,\beta = w,g \qquad \text{and} \quad x = \boldsymbol{\varepsilon}, p_w, p_g \tag{1.52}$$

resulting from (1.48) and definition (1.51). Therefore, in view of (1.50), expression (1.47) of average pore pressure rate reads:

$$\dot{p}_f = p_c \frac{\partial p_c}{\partial p_\gamma}\frac{\partial s_\gamma}{\partial \boldsymbol{\varepsilon}} : \dot{\boldsymbol{\varepsilon}} + \sum_{\alpha=w,g} \xi_\alpha \dot{p}_\alpha \qquad \text{for} \quad \gamma = w,g \tag{1.53}$$

with

$$\xi_\alpha := s_\alpha + p_c \frac{\partial s_\alpha}{\partial p_\alpha}\frac{\partial p_c}{\partial p_\alpha} \qquad \text{for} \quad \alpha = w,g \tag{1.54}$$

Finally, introduction of (1.53) in general rate form (1.44) of stress equation (1.41) yields:

$$\dot{\boldsymbol{\sigma}} = \left[\mathbb{C}_{sk} - p_c \frac{\partial p_c}{\partial p_\gamma}\left(\mathbf{b} \otimes \frac{\partial s_\gamma}{\partial \boldsymbol{\varepsilon}}\right)\right] \dot{\boldsymbol{\varepsilon}} - \mathbf{b} \sum_{\alpha=w,g} \xi_\alpha \dot{p}_\alpha \qquad \text{for} \quad \gamma = w,g \tag{1.55}$$

and a direct comparison between this equation and hyperelastic relation $(1.40)_1$ leads to the following general forms for the considered tangent operators:

$$\tilde{\mathbb{C}}_{sk} = \mathbb{C}_{sk} - p_c \frac{\partial p_c}{\partial p_\alpha}\left(\mathbf{b} \otimes \frac{\partial s_\alpha}{\partial \boldsymbol{\varepsilon}}\right) \qquad \text{and} \qquad \zeta_\alpha = \xi_\alpha \qquad \text{for} \quad \alpha = w,g \tag{1.56}$$

with ξ_α defined by (1.54). An expression for tensor $\mathbf{b}$ is evaluated in the next Section.

Coupling tensor expression resulting from unjacketed compression test

An expression for tangent coupling tensor $\mathbf{b}$ appearing in (1.40) and (1.41) can be obtained by extending to the three-phase case the consideration of the so-called "unjacketed" test, proposed by Biot and Willis [20] to characterize the response of fully saturated porous solids. In this test, an unjacketed sample of the porous continuum is fully immersed in the same fluid mixture saturating the solid-skeleton voids, and a uniform pressure p_{uj} is applied at the boundary of such a mixture (Fig. 1.2). In the porous sample, the corresponding total stress is then:

$$\boldsymbol{\sigma} = -p_{uj}\mathbf{1} \tag{1.57}$$

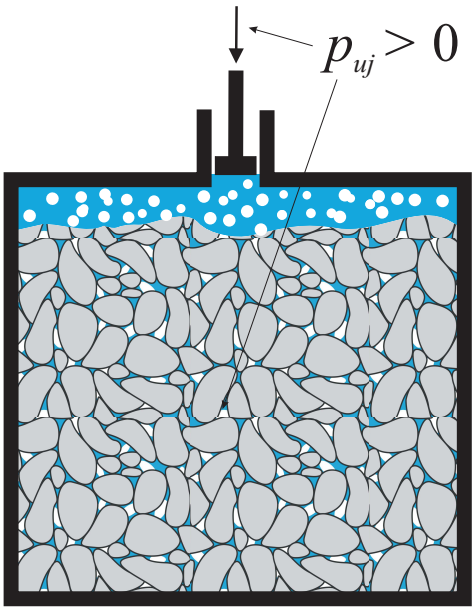

Figure 1.2: Unjacketed compression test on a three-phase sample [2]

and the "unjacketed" volumetric stiffness modulus appearing in following equations can be evaluated for solid skeleton, void space and solid phase, respectively:

$$\dot{p}_{uj} = -\kappa_{sk}^{uj}\,\dot{\varepsilon}_v \qquad \dot{p}_{uj} = -\kappa_{vd}^{uj}\,\dot{\varepsilon}_{vd} \qquad \dot{p}_{uj} = -\kappa_{s}^{uj}\,\dot{\varepsilon}_s \tag{1.58}$$

for the traces $\varepsilon_v := \boldsymbol{\varepsilon} : \mathbf{1}$, ε_{vd} and ε_s of infinitesimal strain tensors associated to deformation of solid skeleton, void space and solid phase, respectively.

As often considered in mixture theories, surface and volumetric fractions of the considered fluid phases are assumed to be coincident, thus leading to the following equilibrium relation between the compressive load p_{uj} applied to the fluid mixture and the pressures of single constituents:

$$p_{uj} = \sum_{\alpha=w,g} s_\alpha p_\alpha =: p_f \tag{1.59}$$

Stress equation (1.44) can then be easily written in terms of $\dot{p}_{uj}$ and combined with the rate form of (1.57) to obtain:

$$\mathbb{C}_{sk}\,\dot{\boldsymbol{\varepsilon}} = (\mathbf{b} - \mathbf{1})\dot{p}_{uj} \tag{1.60}$$

In this equation, the rate of applied average pore pressure p_{uj} can be expressed by means of $(1.58)_1$, thus leading to the following expression for the coupling tensor:

$$\mathbf{b} = \mathbf{1} - \frac{1}{3\kappa_{sk}^{uj}}\mathbb{C}_{sk}\mathbf{1} \tag{1.61}$$

We introduce now the porosity n, defined as the current void volume per unit volume of the deformed porous solid. As shown in Appendix A, among other implications of solid-phase mass balance, there is the following rate equation between porosity and volumetric strains of void space and solid skeleton:

$$\dot{n} = n_0(\dot{\varepsilon}_{vd} - \dot{\varepsilon}_v) \tag{1.62}$$

as well as the following relation among volumetric strains of solid skeleton, void space and solid phase:

$$\dot{\varepsilon}_v = n_0\,\dot{\varepsilon}_{vd} + (1 - n_0)\,\dot{\varepsilon}_s \tag{1.63}$$

with n_0 the initial porosity value. Equations (1.58) and (1.63) can be combined to obtain the following relation among the three aforementioned unjacketed volumetric stiffness modulus [28]:

$$\frac{1}{\kappa_{sk}^{uj}} = \frac{n_0}{\kappa_{vd}^{uj}} + \frac{1 - n_0}{\kappa_s^{uj}} \tag{1.64}$$

On the other hand, porosity rate equation (1.62) shows that for vanishing porosity increments ($\dot{n} = 0$), coincidence is obtained between the volumetric strain increments of solid skeleton and void space ($\dot{\varepsilon}_v = \dot{\varepsilon}_{vd}$). Therefore, keeping in mind relations (1.58), if we assume as negligible the porosity variation measured in an unjacketed test, the unjacketed volumetric stiffness modulus characterizing solid skeleton and void space are approximately coincident:

$$\kappa_{sk}^{uj} \simeq \kappa_{vd}^{uj} \tag{1.65}$$

and from relation (1.64) also the following approximate coincidence is obtained:

$$\kappa_{sk}^{uj} \simeq \kappa_s^{uj} \tag{1.66}$$

Another common constitutive assumption on the unjacketed response of porous continua is:

$$\kappa_s^{uj} \simeq \kappa_s \tag{1.67}$$

for the microscopic volumetric stiffness modulus κ_s of the solid phase, that is,

$$\dot{p}_s = \kappa_s \dot{\varepsilon}_s \tag{1.68}$$

for the spherical part p_s of microscopic stress acting on solid phase. The following expression for the coupling tensor (1.61) is then obtained from (1.66) and (1.67):

$$\mathbf{b} = \mathbf{1} - \frac{1}{3\kappa_s}\mathbb{C}_{sk}\mathbf{1} \tag{1.69}$$

We note how this expression is consistent with the one obtained for anisotropic porous media saturated by only a fluid phase in [41, 45, 140] and generalizing the results presented in [103, 131] for an isotropic solid skeleton, where both partial stress and unjacketed test concepts are considered together with the assumption $\kappa_{sk}^{uj} \simeq \kappa_s$. It is also to be remarked that only the total stress decomposition (1.41) is able to ensure that the expected relation (1.69) is obtained from the unjacketed test argument.

In the case of isotropic response of solid skeleton, relation (1.69) reads:

$$\mathbf{b} = b\mathbf{1} \qquad \text{where} \qquad b := 1 - \frac{\kappa_{sk}}{\kappa_s} \tag{1.70}$$

thus recovering expressions proposed by Skempton [131] for the coupling coefficient appearing in effective stress equation.

In this section we have supposed that the coupling tensor $\mathbf{b}$ is constant. Therefore, due to expression (1.69), a constant solid phase bulk modulus κ_s and a constant "drained" elastic tensor will be consistently considered in subsequent developments.

Remark 1.2 *If void space variations are assumed as negligible in unjacketed conditions, it is:*

$$\kappa_{sk}^{uj} = \frac{\kappa_s^{uj}}{1 - n_0} \tag{1.71}$$

as shown by imposing $1/\kappa_{vd}^{uj} = 0$ *in relation (1.64) among unjacketed stiffness modulus. As a consequence of (1.67) and (1.71), expression (1.61) of coupling tensor reads:*

$$\mathbf{b} = \mathbf{1} - \frac{1 - n_0}{3\kappa_s}\mathbb{C}_{sk}\mathbf{1} \tag{1.72}$$

The consideration of expression (1.72) in (1.41) can be seen as an extension to the general case of anisotropic three-phase porous continua of the effective stress definition proposed by Suklje [135] and investigated by Lade and de Boer [89].

1.4.2 Fluid content equations

The relation between reduced and intrinsic density of fluid α can be expressed as

$$\bar{\rho}_\alpha = \rho_\alpha \theta_\alpha \tag{1.73}$$

for the *volumetric* fluid content θ_α, defined as the current volume of fluid α per unit volume of the deformed configuration of the porous solid. In the finite deformation range of the solid skeleton, the following relation between mass and volumetric contents of the generic fluid is then obtained from definition (1.10):

$$M_\alpha = J \rho_\alpha \theta_\alpha \tag{1.74}$$

whose material time derivative is

$$\dot{M}_\alpha = J \rho_\alpha (\theta_\alpha \dot{e}_\alpha + \dot{\theta}_\alpha + \theta_\alpha d_v) \tag{1.75}$$

as a consequence of differential relation (1.11) for the volumetric strain of solid skeleton, and of the following rate equation between logarithmic volumetric strain e_α and density of fluid α.

$$\dot{e}_\alpha = \frac{\dot{\rho}_\alpha}{\rho_\alpha} \tag{1.76}$$

The volumetric fluid content is typically expressed in terms of saturation degree and porosity:

$$\theta_\alpha = n s_\alpha \tag{1.77}$$

Expression (1.75) of fluid mass content increment rate can then be written as:

$$\dot{M}_\alpha = J \rho_\alpha (n s_\alpha \dot{e}_\alpha + s_\alpha \dot{n} + n \dot{s}_\alpha + n s_\alpha d_v) \tag{1.78}$$

In the range of infinitesimal deformations of the solid skeleton considered herein, it is $d_v \simeq \dot{\varepsilon}_v$ and $J \simeq 1$. So expression (1.78) reads:

$$\frac{\dot{M}_\alpha}{\rho_\alpha} = n s_\alpha \dot{\varepsilon}_v + n s_\alpha \dot{e}_\alpha + \dot{n} s_\alpha + n \dot{s}_\alpha \tag{1.79}$$

Assuming also infinitesimal deformations of the solid phase, the porosity expressions

$$\dot{n} = (1 - n_0)(\dot{\varepsilon}_v - \dot{\varepsilon}_s) \tag{1.80}$$

$$n = n_0 + \varepsilon_v - \varepsilon_s \tag{1.81}$$

obtained in Appendix A can be substituted in (1.79) and approximations $1 \mp \varepsilon_v \simeq 1$ as well as $1 \mp \varepsilon_s \simeq 1$ can be used to obtain:

$$\frac{\dot{M}_\alpha}{\rho_\alpha} = s_\alpha \dot{\varepsilon}_v + n s_\alpha \dot{e}_\alpha - s_\alpha (1 - n_0)\dot{\varepsilon}_s + n \dot{s}_\alpha \qquad \text{for} \quad \alpha = w, g \tag{1.82}$$

In the developments that follow, we consider the following general rate form for the constitutive equations of both the fluid phases:

$$\dot{e}_\alpha = \frac{\dot{p}_\alpha}{\kappa_\alpha} \qquad \text{for} \quad \alpha = w, g \tag{1.83}$$

where $\kappa_\alpha = \hat{\kappa}_\alpha(p_\alpha)$ is the tangent volumetric stiffness modulus of fluid α. Combination of kinematic equation (1.76) with (1.83) leads to the following relation between densities and pressures in the considered immiscible barotropic fluids:

$$\frac{\partial \rho_\alpha}{\partial p_\beta} = \frac{\rho_\alpha}{\kappa_\alpha} \delta_{\alpha\beta} \qquad \text{for} \quad \alpha = w, g \tag{1.84}$$

An elastic potential consistent with (1.83) and able to describe the non-linear response of both the gaseous and liquid phases is for example proposed in [34].

In view of fluid constitutive equations (1.83) and of expression (1.46) for the rate of saturation degrees, fluid-content rate equations (1.82) can be rewritten in terms of primary variables (i.e. solid-skeleton strain and fluid pressures) and solid phase strain as:

$$\frac{\dot{M}_\alpha}{\rho_\alpha} = \left(s_\alpha \mathbf{1} + n \frac{\partial s_\alpha}{\partial \boldsymbol{\varepsilon}} \right) : \dot{\boldsymbol{\varepsilon}} + n \sum_{\gamma = w,g} \left(\frac{s_\alpha}{\kappa_\alpha} \delta_{\alpha\gamma} + \frac{\partial s_\alpha}{\partial p_\gamma} \right) \dot{p}_\gamma - s_\alpha (1 - n_0)\dot{\varepsilon}_s \tag{1.85}$$

Tangent operators and porosity model resulting from the partial stress concept

To fully characterize the evolution of fluid contents, constitutive equations for solid phase strain ε_s and porosity n are to be defined in terms of considered primary variables and introduced in (1.85). These goals motivates the developments presented in this section.

Following typical arguments of mixture theories the total stress can be decomposed in the so-called "partial stress" tensors characterizing the solid and the fluid phases. Assuming again surface fractions of constituents as coincident with volumetric contents, the spherical part of such a decomposition is:

$$\frac{1}{3}\boldsymbol{\sigma} : \mathbf{1} = (1-n)p_s - n\sum_{\alpha=w,g} s_\alpha p_\alpha \tag{1.86}$$

In the infinitesimal deformation range considered herein for the solid skeleton, current and reference configuration of the porous space can be considered as coincident. Equation (1.86) can then be rewritten as:

$$\frac{1}{3}\boldsymbol{\sigma} : \mathbf{1} = (1-n_0)p_s - n_0 p_f \tag{1.87}$$

where we have also employed definition (1.42) of average pore pressure p_f. Substitution of the spherical part of total stress rate (1.44) and of microscopic solid-phase equation (1.68) in rate form of partial stress decomposition (1.87) yields the required expression for the solid-phase strain rate:

$$(1-n_0)\dot{\varepsilon}_s = (\mathbf{1}-\mathbf{b}) : \dot{\boldsymbol{\varepsilon}} - \frac{1}{3\kappa_s}(\mathbf{b}-n_0\mathbf{1}) : \mathbf{1}\,\dot{p}_f \tag{1.88}$$

where expression (1.69) for the coupling tensor $\mathbf{b}$ was employed.

Substitution of (1.88) in (1.85) leads to the following expression for fluid content increment rates:

$$\frac{\dot{M}_\alpha}{\rho_\alpha} = \left(s_\alpha\mathbf{b} + n\frac{\partial s_\alpha}{\partial \boldsymbol{\varepsilon}}\right) : \dot{\boldsymbol{\varepsilon}} + n\sum_{\gamma=w,g}\left(\frac{s_\alpha}{\kappa_\alpha}\delta_{\alpha\gamma} + \frac{\partial s_\alpha}{\partial p_\gamma}\right)\dot{p}_\gamma + \frac{s_\alpha}{3\kappa_s}(\mathbf{b}-n_0\mathbf{1}) : \mathbf{1}\,\dot{p}_f \tag{1.89}$$

for $\alpha = w, g$. Fluid content rate equations in terms of $\dot{\boldsymbol{\varepsilon}}$, $\dot{p}_w$ and $\dot{p}_g$ are then obtained by substituting expression (1.53) for average pore pressure rate in (1.89). A direct comparison of such equations with hyperelastic relations $(1.40)_2$ leads to the following general form of considered tangent operators:

$$\left.\begin{aligned} \zeta_\alpha\mathbf{b} &= s_\alpha\mathbf{b} + \left[n + p_c\frac{\partial p_c}{\partial p_\alpha}\frac{s_\alpha}{3\kappa_s}(\mathbf{b}-n_0\mathbf{1}) : \mathbf{1}\right]\frac{\partial s_\alpha}{\partial \boldsymbol{\varepsilon}} \\ C_{\alpha\beta} &= n\left(\frac{s_\alpha}{\kappa_\alpha}\delta_{\alpha\beta} + \frac{\partial s_\alpha}{\partial p_\beta}\right) + \frac{s_\alpha\xi_\beta}{3\kappa_s}(\mathbf{b}-n_0\mathbf{1}) : \mathbf{1} \end{aligned}\right\} \quad \text{for} \quad \alpha,\beta = w,g \tag{1.90}$$

with coupling operators ξ_α and $\mathbf{b}$ given by (1.54) and (1.69), respectively.

We remark that two expressions are now available for tangent operators $\zeta_\alpha \mathbf{b}$, that is, $(1.56)_2$ and $(1.90)_1$. These two expressions obtained for stress equation and fluid content equation, respectively, must be coincident to ensure major symmetry of system (1.40). The implications of such a requirement will be discussed in Section 1.4.3 below.

Solid-phase strain rate equation (1.88), substituted in kinematic relation (1.80), yields also a constitutive equation for porosity, that is,

$$\dot{n} = (\mathbf{b} - n_0 \mathbf{1}) : \dot{\boldsymbol{\varepsilon}} + \frac{1}{3\kappa_s} (\mathbf{b} - n_0 \mathbf{1}) : \mathbf{1}\, \dot{p}_f \tag{1.91}$$

Rate relation (1.91) can be integrated with respect to solid-skeleton strain tensor $\boldsymbol{\varepsilon}$ and average pore pressure p_f to obtain a function $n = \hat{n}(\boldsymbol{\varepsilon};\, p_f)$. In particular, denoting by p_{f0} the initial value of average pore pressure, the initial condition $\hat{n}(\mathbf{0};\, p_{f0}) = n_0$ yields:

$$\hat{n}(\boldsymbol{\varepsilon};\, p_f) = n_0 + \mathbf{b} : \boldsymbol{\varepsilon} + \frac{1}{3\kappa_s} (\mathbf{b} - n_0 \mathbf{1}) : \mathbf{1}\, (p_f - p_{f0}) \tag{1.92}$$

where we have employed the approximation $1 - \varepsilon_v \simeq 1$, consistently with the assumed infinitesimal strains of the solid skeleton.

Developments that follow require the existence of a function expressing porosity in terms of primary variables, that is, $n(\boldsymbol{\varepsilon}; p_w; p_g) = \hat{n}(\boldsymbol{\varepsilon};\, p_f)$. For a general model $\hat{n}(\boldsymbol{\varepsilon};\, p_f)$, partial derivatives of such a function can then be calculated as:

$$\frac{\partial n}{\partial \boldsymbol{\varepsilon}} = \frac{\partial \hat{n}}{\partial \boldsymbol{\varepsilon}} + \frac{\partial \hat{n}}{\partial p_f} \frac{\partial p_f}{\partial \boldsymbol{\varepsilon}} \qquad \text{and} \qquad \frac{\partial n}{\partial p_\alpha} = \frac{\partial \hat{n}}{\partial p_f} \frac{\partial p_f}{\partial p_\alpha} \quad \text{for} \quad \alpha = w, g \tag{1.93}$$

where, in turn, the derivatives of average pore pressure obtained from rate expression (1.53), that is,

$$\frac{\partial p_f}{\partial \boldsymbol{\varepsilon}} = p_c \frac{\partial p_c}{\partial p_\alpha} \frac{\partial s_\alpha}{\partial \boldsymbol{\varepsilon}} \qquad \text{and} \qquad \frac{\partial p_f}{\partial p_\alpha} = \xi_\alpha \qquad \text{for} \quad \alpha = w, g \tag{1.94}$$

can be substituted, thus yielding:

$$\frac{\partial n}{\partial \boldsymbol{\varepsilon}} = \frac{\partial \hat{n}}{\partial \boldsymbol{\varepsilon}} + p_c \frac{\partial \hat{n}}{\partial p_f} \frac{\partial p_c}{\partial p_\alpha} \frac{\partial s_\alpha}{\partial \boldsymbol{\varepsilon}} \qquad \text{and} \qquad \frac{\partial n}{\partial p_\alpha} = \xi_\alpha \frac{\partial \hat{n}}{\partial p_f} \quad \text{for} \quad \alpha = w, g \tag{1.95}$$

For the porosity law (1.92), it is:

$$\frac{\partial \hat{n}}{\partial \boldsymbol{\varepsilon}} = \mathbf{b} \qquad \text{and} \qquad \frac{\partial \hat{n}}{\partial p_f} = \frac{1}{3\kappa_s} (\mathbf{b} - n_0 \mathbf{1}) : \mathbf{1} \tag{1.96}$$

which leads to the following particular form of derivatives (1.95):

$$\left.\begin{aligned} \frac{\partial n}{\partial \boldsymbol{\varepsilon}} &= \mathbf{b} + p_c \frac{\partial p_c}{\partial p_\alpha} \frac{\partial s_\alpha}{\partial \boldsymbol{\varepsilon}} \frac{1}{3\kappa_s} (\mathbf{b} - n_0 \mathbf{1}) : \mathbf{1} \\ \frac{\partial n}{\partial p_\alpha} &= \frac{\xi_\alpha}{3\kappa_s} (\mathbf{b} - n_0 \mathbf{1}) : \mathbf{1} \end{aligned}\right\} \quad \text{for} \quad \alpha = w, g \tag{1.97}$$

1.4.3 Application of thermodynamic restrictions

In the following, we evaluate the implications of symmetry requirements (1.34) on the poro-elastic model obtained in previous sections. In summary, such a model is given by rate equation system (1.40), where the coupling tensor $\mathbf{b}$ is expressed by (1.69), tangent operators appearing in stress equation $(1.40)_1$ and in fluid content equation $(1.40)_2$ are given by (1.56) and by (1.90), respectively. The porosity evolution is described by model (1.92).

Symmetry requirement $(1.34)_2$ is satisfied by expression (1.69) assumed for $\mathbf{b}$. The following condition on fluid retention model is obtained from (1.56) by imposing requirement $(1.34)_1$ on symmetry of tangent tensor $\tilde{\mathbb{C}}_{sk}$:

$$\frac{\partial s_\alpha}{\partial \boldsymbol{\varepsilon}} = s_{\alpha,\varepsilon}\, \mathbf{b} \qquad \text{with} \quad s_{\alpha,\varepsilon} \in \mathbb{R} \qquad \text{for} \quad \alpha = w, g \tag{1.98}$$

Major symmetry of system (1.40) requires that the expression of ζ_α obtained for stress equation, that is, (1.54, 1.56_2) must be coincident with the one obtained for fluid content equation, that is, (1.90_1). Taking also into account condition (1.98), such a symmetry requirement reads:

$$p_c \frac{\partial s_\alpha}{\partial p_\alpha} \frac{\partial p_c}{\partial p_\alpha} = \left[n + p_c \frac{\partial p_c}{\partial p_\alpha} \frac{s_\alpha}{3\kappa_s} (\mathbf{b} - n_0 \mathbf{1}) : \mathbf{1} \right] s_{\alpha,\varepsilon} \qquad \text{for} \quad \alpha = w, g \tag{1.99}$$

Furthermore, expression $(1.90)_2$ must satisfy requirement $(1.34)_3$ on symmetry of storage modulus, that is,

$$n \frac{\partial s_\alpha}{\partial p_\beta} + \frac{s_\alpha \xi_\beta}{3\kappa_s} (\mathbf{b} - n_0 \mathbf{1}) : \mathbf{1} = n \frac{\partial s_\beta}{\partial p_\alpha} + \frac{s_\beta \xi_\alpha}{3\kappa_s} (\mathbf{b} - n_0 \mathbf{1}) : \mathbf{1} \tag{1.100}$$

for $\alpha, \beta = w, g$.

We note that a very common simplifying assumption considers the saturation degrees as independent on the solid-skeleton strain. However, it is immediately apparent

that such a widely used class of retention models considering $s_{\alpha,\varepsilon} = 0$ cannot satisfy symmetry condition (1.99), with the trivial exception of a model assuming constant saturation degrees, which is of interest in the analysis of porous continua saturated by a single fluid phase.

On the contrary, as shown in Section 1.4.3 below, the aforementioned symmetry requirements as well as Maxwell conditions (1.35) are fully satisfied by a class of porosity dependent saturation models, and it will be also pointed out how the assumed dependency is consistent with experimental results and recent advances in modelling retention curves in deformable solids.

Furthermore, in the section that follows, we will show that a classical strain-independent model for fluid retention is thermodynamically consistent with a *simplified* version of the poro-elastic model presented in previous sections, implementing an approximate expression of stress equation (1.44).

Poro-elastic laws based on a common class of strain-independent retention models

In the analysis of partially-saturated porous continua, relations considering the saturation degrees as fully characterized by capillary pressure are typically employed, that is,

$$s_\alpha = \check{s}_\alpha(p_c) \qquad \text{for} \qquad \alpha, \beta = w, g \tag{1.101}$$

For the class of retention models characterized by (1.101), the partial derivatives of the saturation degrees with respect to considered primary variables are:

$$\frac{\partial s_\alpha}{\partial \boldsymbol{\varepsilon}} = \mathbf{0} \qquad \text{and} \qquad \frac{\partial s_\alpha}{\partial p_\beta} = \check{s}'_\alpha \frac{\partial p_c}{\partial p_\beta} \qquad \text{for} \qquad \alpha, \beta = w, g \tag{1.102}$$

with

$$\check{s}'_\alpha(p_c) := \frac{d\check{s}_\alpha}{dp_c} \qquad \text{for} \qquad \alpha = w, g \tag{1.103}$$

In view of (1.102), general expressions (1.56) for tangent elastic tensor and coupling operators ζ_w and ζ_g appearing in stress equation $(1.40)_1$ reduce to:

$$\tilde{\mathbb{C}}_{sk} = \mathbb{C}_{sk} \qquad \text{and} \qquad \zeta_\alpha = s_\alpha + p_c\, \check{s}'_\alpha =: \check{\xi}_\alpha \qquad \text{for} \quad \alpha = w, g \tag{1.104}$$

On the other hand, the particular form of expressions (1.90) for coupling operators and storage modulus appearing in fluid content equation $(1.40)_2$ is

$$\left.\begin{aligned} \zeta_\alpha &= s_\alpha \\ C_{\alpha\beta} &= n\left(\frac{s_\alpha}{\kappa_\alpha}\delta_{\alpha\beta} + \check{s}'_\alpha\frac{\partial p_c}{\partial p_\beta}\right) + \frac{s_\alpha\check{\xi}_\beta}{3\kappa_s}(\mathbf{b}-n_0\mathbf{1}):\mathbf{1} \end{aligned}\right\} \quad \text{for} \quad \alpha,\beta = w,g \tag{1.105}$$

with $\check{\xi}_w$ and $\check{\xi}_g$ defined by $(1.104)_2$. We observe that the so-obtained poro-elastic rate equations, frequently occurring in the literature, violate major symmetry of system (1.40), not only in terms of coupling operators, as previously shown for the whole class of strain-independent retention models by means of condition (1.99), but also in terms of storage modulus.

To recover such symmetries, a simplified version of this model can be obtained by forcing the approximation for the coupling coefficient:

$$\check{\xi}_\alpha \simeq s_\alpha \tag{1.106}$$

in tangent operators appearing in both the stress and fluid content rate equations, that is,

$$\left.\begin{aligned} \tilde{\mathbb{C}}_{sk} &= \mathbb{C}_{sk} \\ \zeta_\alpha &= s_\alpha \qquad \text{and} \qquad \mathbf{b} = \mathbf{1} - \frac{1}{3\kappa_s}\mathbb{C}_{sk}\mathbf{1} \\ C_{\alpha\beta} &= n\left(\frac{s_\alpha}{\kappa_\alpha}\delta_{\alpha\beta} + \check{s}'_\alpha\frac{\partial p_c}{\partial p_\beta}\right) + \frac{s_\alpha s_\beta}{3\kappa_s}(\mathbf{b}-n_0\mathbf{1}):\mathbf{1} \end{aligned}\right\} \quad \text{for} \quad \alpha,\beta = w,g \tag{1.107}$$

In fact, symmetry condition $(1.34)_3$ on storage modulus is verified by $(1.107)_3$ since it is

$$\check{s}'_\alpha\frac{\partial p_c}{\partial p_\beta} = \check{s}'_\beta\frac{\partial p_c}{\partial p_\alpha} \qquad \text{for} \quad \alpha,\beta = w,g \tag{1.108}$$

as a consequence of definition (1.51) of capillary pressure and of

$$\sum_{\alpha=w,g}\check{s}'_\alpha = 0 \tag{1.109}$$

resulting from (1.49).

We observe that in view of $(1.102)_1$, the consideration of approximation (1.106) in $(1.104)_2$ is equivalent to the following approximate evaluation of average pore pressure rate (1.53):

$$\dot{p}_f \simeq \dot{\check{p}}_f \qquad \text{where} \qquad \dot{\check{p}}_f := \sum_{\alpha=w,g} s_\alpha \dot{p}_\alpha \tag{1.110}$$

is an exact differential as shown by relations $(1.102)_2$ and (1.108). The introduction of relation (1.110) in stress rate equation (1.44) leads to:

$$\dot{\boldsymbol{\sigma}} = \mathbb{C}_{sk}\dot{\boldsymbol{\varepsilon}} - \mathbf{b} \sum_{\alpha=w,g} s_\alpha \dot{p}_\alpha \tag{1.111}$$

which is an extension to the case of anisotropic solid skeleton of the total stress expression proposed by Coussy [54]. We refer to the work by Schrefler and Gawin [120], among others, for an investigation of the comparison between stress equation (1.44) and its approximated form (1.111).

In Appendix B.1, we employ Maxwell relations (1.35) to assess the thermodynamic admissibility of the simplified model represented by system (1.40) with tangent operators (1.107) and porosity law (1.92) for $p_f = \check{p}_f$ obtained from integration of (1.110).

Remark 1.3 *For the class of saturation degree models (1.101), conditions (1.36) ensuring the convexity of the Helmholtz free energy are satisfied if all the following constitutive assumptions hold:*

i) the "drained" elastic tensor $\mathbb{C}_{sk}$ is positive defined;

ii) at least one phase (solid or fluid) is compressible;

iii) the liquid saturation degree is a monotonically decreasing function of capillary pressure.

Beside their significance in stability issues with the consequent theoretical and numerical implications, we remark that such constitutive assumptions are also physically meaningful.

Remark 1.4 *The results presented in this section are to be contrasted with the ones obtained by Coussy and co-workers [54, 56]. In these references, in fact, a strain-independent retention model is proved to be thermodynamically consistent with approximated forms of average pore pressure (1.110) and effective stress equation (1.111) in the case of incompressible solid and liquid phases. Furthermore, particular forms of hyperelastic tangent operators are obtained in a quite different way. In particular, symmetry and Maxwell conditions provided by the same macroscopic framework outlined in Section 1.3 are explicitly enforced in deriving particular forms of hyperelastic tangent operators. A similar approach can be also found in [97], where the direct application of admissibility conditions allows to employ a Bishop effective stress equation with pressure contributions weighted by general functions of capillary pressure. On the contrary, in this work particular forms for hyperelastic tangent operators are obtained only by means of mixture theory concepts and their thermodynamic consistency is investigated independently.*

Poro-elastic laws based on porosity-dependent retention models

In spite of frequent simplifying assumption (1.101), that is, of saturation degrees fully characterized by capillary pressure, also the influence of solid-skeleton strain should be considered in the formulation of retention models, as suggested by the experimentally observed stress-dependency of liquid retention curves [71, 101, 146] and by results obtained from mixture theories as, for example, in [4, 80, 82].

In the present section, consistently with these results indicating the strain dependence as a requirement for an effective retention model, we will show that the following class of retention laws:

$$s_\alpha = \breve{s}_\alpha(np_c) \qquad \text{for} \qquad \alpha, \beta = w, g \tag{1.112}$$

is a requirement for the thermodynamic admissibility of rate equation system (1.40), if relations (1.56) and (1.90) are employed to express tangent operators appearing in stress equation $(1.40)_1$ and in fluid content equation $(1.40)_2$, respectively.

For the class (1.112) of retention models, the partial derivative of saturation degree with respect to solid-skeleton strain can be computed recalling porosity derivatives $(1.95)_1$, that is,

$$\frac{\partial s_\alpha}{\partial \boldsymbol{\varepsilon}} = \frac{\partial s_\alpha}{\partial n}\frac{\partial n}{\partial \boldsymbol{\varepsilon}} = \breve{s}'_\alpha p_c \left(\frac{\partial \hat{n}}{\partial \boldsymbol{\varepsilon}} + p_c \frac{\partial \hat{n}}{\partial p_f}\frac{\partial p_c}{\partial p_\alpha}\frac{\partial s_\alpha}{\partial \boldsymbol{\varepsilon}} \right) \qquad \text{for} \quad \alpha = w, g \tag{1.113}$$

with

$$\breve{s}'_\alpha(np_c) := \frac{d\breve{s}_\alpha}{d(np_c)} \qquad \text{for} \qquad \alpha = w, g \tag{1.114}$$

and solving (1.113) with respect to $\partial s_\alpha / \partial \boldsymbol{\varepsilon}$:

$$\frac{\partial s_\alpha}{\partial \boldsymbol{\varepsilon}} = \frac{p_c}{\omega}\breve{s}'_\alpha \frac{\partial \hat{n}}{\partial \boldsymbol{\varepsilon}} \qquad \text{for} \quad \alpha = w, g \tag{1.115}$$

where the following assumption is introduced:

$$\omega \neq 0 \qquad \text{with} \qquad \omega := 1 - p_c^2 \frac{\partial \hat{n}}{\partial p_f}\breve{s}'_\alpha \frac{\partial p_c}{\partial p_\alpha} \qquad \text{for} \quad \alpha = w, g \tag{1.116}$$

We observe that function ω is independent on the choice of α (w or g), being

$$\breve{s}'_\alpha \frac{\partial p_c}{\partial p_\beta} = \breve{s}'_\beta \frac{\partial p_c}{\partial p_\alpha} \qquad \text{for} \quad \alpha, \beta = w, g \tag{1.117}$$

which is a consequence of definition (1.51) of capillary pressure and of

$$\sum_{\alpha = w,g} \breve{s}'_\alpha = 0 \tag{1.118}$$

resulting, in turn, from (1.49).

Similarly, according to models (1.112) and using porosity derivative $(1.95)_2$ as well as definition (1.114), the partial derivatives of saturation degrees with respect to fluid pressures reads:

$$\begin{aligned} \frac{\partial s_\alpha}{\partial p_\beta} &= \frac{\partial s_\alpha}{\partial n}\frac{\partial n}{\partial p_\beta} + \frac{\partial s_\alpha}{\partial p_c}\frac{\partial p_c}{\partial p_\beta} = \\ &= \breve{s}'_\alpha \left(p_c \frac{\partial \hat{n}}{\partial p_f}\xi_\beta + n\frac{\partial p_c}{\partial p_\beta} \right) \qquad \text{for} \quad \alpha, \beta = w, g \end{aligned} \tag{1.119}$$

In this expression, definition (1.54) of ξ_β is substituted taking into account relation (1.52), thus obtaining:

$$\frac{\partial s_\alpha}{\partial p_\beta} = \breve{s}'_\alpha \left(p_c \frac{\partial \hat{n}}{\partial p_f} s_\beta + p_c^2 \frac{\partial \hat{n}}{\partial p_f}\frac{\partial s_\alpha}{\partial p_\beta}\frac{\partial p_c}{\partial p_\alpha} + n\frac{\partial p_c}{\partial p_\beta} \right) \qquad \text{for} \quad \alpha, \beta = w, g \tag{1.120}$$

which is finally solved with respect to $\partial s_\alpha/\partial p_\beta$:

$$\frac{\partial s_\alpha}{\partial p_\beta} = \frac{\breve{s}'_\alpha}{\omega}\left(p_c \frac{\partial \hat{n}}{\partial p_f} s_\beta + n \frac{\partial p_c}{\partial p_\beta}\right) \qquad \text{for} \quad \alpha, \beta = w, g \tag{1.121}$$

with function ω previously defined by (1.116). Therefore, keeping in mind (1.121) and using the following consequence of definition (1.51) of capillary pressure:

$$\frac{\partial p_c}{\partial p_\alpha}\frac{\partial p_c}{\partial p_\beta} = 2\,\delta_{\alpha\beta} - 1 \tag{1.122}$$

we obtain a particular form of expression (1.54) for ξ_α:

$$\xi_\alpha = s_\alpha\left(1 + \frac{p_c^2}{\omega}\frac{\partial \hat{n}}{\partial p_f}\breve{s}'_\alpha \frac{\partial p_c}{\partial p_\alpha}\right) + n p_c \frac{\breve{s}'_\alpha}{\omega} =: \breve{\xi}_\alpha \qquad \text{for} \quad \alpha = w, g \tag{1.123}$$

From definition (1.116) of function ω, the following relation can be easily obtained for the term in parentheses appearing in (1.123):

$$1 + \frac{p_c^2}{\omega}\frac{\partial \hat{n}}{\partial p_f}\breve{s}'_\alpha \frac{\partial p_c}{\partial p_\alpha} = \frac{1}{\omega} \qquad \text{for} \quad \alpha = w, g \tag{1.124}$$

that, introduced in (1.123) leads to:

$$\breve{\xi}_\alpha = \frac{\breve{\xi}^*_\alpha}{\omega} \qquad \text{with} \quad \breve{\xi}^*_\alpha := s_\alpha + n p_c \breve{s}'_\alpha \qquad \text{for} \quad \alpha = w, g \tag{1.125}$$

In view of (1.125), partial derivative (1.119) can be written in the following form, equivalent to (1.121):

$$\frac{\partial s_\alpha}{\partial p_\beta} = \breve{s}'_\alpha \varsigma_\beta \qquad \text{for} \quad \alpha, \beta = w, g \tag{1.126}$$

with:

$$\varsigma_\beta := \frac{p_c}{\omega}\frac{\partial \hat{n}}{\partial p_f}\breve{\xi}^*_\beta + n\frac{\partial p_c}{\partial p_\beta} \qquad \text{for} \quad \beta = w, g \tag{1.127}$$

Now it can be easily verified that class (1.112) of porosity-dependent retention models is able to satisfy the symmetry conditions (1.98–1.100) formulated at the beginning of Section 1.4.3. In particular, condition (1.98) on symmetry of tangent tensor $\tilde{\mathbb{C}}_{sk}$ is satisfied as a consequence of partial derivative (1.115) and assumed porosity model (1.92), yielding $(1.96)_1$ and expression

$$s_{\alpha,\varepsilon} = \frac{p_c}{\omega}\breve{s}'_\alpha \qquad \text{for} \quad \alpha = w, g \tag{1.128}$$

for the scalar part of $\partial s_\alpha / \partial \boldsymbol{\varepsilon}$.

Due to partial derivatives (1.121,1.128) and to relation (1.122), condition (1.99) imposing the major symmetry in terms of ζ_α reduces to $(1.96)_2$, which, in turn, is satisfied as a consequence of the assumed porosity law (1.92).

Finally, satisfaction of condition (1.100) on symmetry of storage modulus can be proven using again partial derivatives $(1.96)_2$ and (1.121) as well as relations (1.117–1.118,1.125).

In summary, all symmetry requirements on rate equation system (1.40) are ensured by the following tangent operators:

$$\left.\begin{array}{rcl} \tilde{\mathbb{C}}_{sk} & = & \mathbb{C}_{sk} - \dfrac{p_c^2}{\omega} \breve{s}'_\alpha \dfrac{\partial p_c}{\partial p_\alpha}\, \mathbf{b} \otimes \mathbf{b} \\ \zeta_\alpha & = & \dfrac{\breve{\xi}^*_\alpha}{\omega} \qquad \text{and} \qquad \mathbf{b} = \mathbf{1} - \dfrac{1}{3\kappa_s}\mathbb{C}_{sk}\mathbf{1} \\ C_{\alpha\beta} & = & n\left(\dfrac{s_\alpha}{\kappa_\alpha}\delta_{\alpha\beta} + n\breve{s}'_\alpha \dfrac{\partial p_c}{\partial p_\beta}\right) + \dfrac{\breve{\xi}^*_\alpha \breve{\xi}^*_\beta}{\omega}(\mathbf{b} - n_0\mathbf{1}) : \dfrac{\mathbf{1}}{3\kappa_s} \end{array}\right\} \quad \text{for} \quad \alpha, \beta = w, g \tag{1.129}$$

These operators have been obtained from the introduction in (1.56,1.90) of partial derivatives (1.115,1.126–1.127) and (1.96), which, in turn, are consequences of assumed retention and porosity models, respectively. In expressions (1.129), functions n, ω and $\breve{\xi}^*_\alpha$ are given by (1.92), (1.116) and (1.125), respectively.

In Appendix B.2, the full thermodynamic admissibility of poro-elastic model presented in this Section is assessed by means of Maxwell relations (1.35).

Remark 1.5 *Among the different features of the hyperelastic tangent operator set presented in this section, we remark that the functional dependency of the strain-dependent retention model (1.112) is constrained by the admissibility condition (1.116). We also remark that this constraint is satisfied by an arbitrary porosity-dependent model of the type (1.112) if an incompressible solid phase is assumed, in view of equation (1.97) for the partial derivative of the porosity with respect to the average fluid pressure.*

Remark 1.6 *For strain-dependent retention models (1.112), the implications of conditions (1.36) ensuring convexity of Helmholtz free energy are commented in the following.*

For the sake of simplicity, we will assume that the solid phase is incompressible. With reference to condition (1.36)$_1$, we note that a positive defined $\mathbb{C}_{sk}$ does not necessarily lead to a positive defined $\tilde{\mathbb{C}}_{sk}$. For example, in the isotropic case, the condition is fulfilled if

$$\underbrace{E_{sk}\frac{1-\nu_{sk}}{(1+\nu_{sk})(1-2\nu_{sk})}}_{=:E_{ed,sk}} + p_c^2 \breve{s}'_w > 0 \tag{1.130}$$

where E_{sk}, ν_{sk} and $E_{ed,sk}$ are the Young modulus, the Poisson coefficient and the oedometric modulus of the solid skeleton, respectively. Condition (1.36)$_2$ is instead satisfied, if we assume at least one fluid phase as compressible and the liquid saturation degree as a monotonic decreasing function of quantity np_c. As for strain-independent retention models, the latter constitutive assumption is physically meaningful. In fact, there is experimental evidence that, for constant capillary pressures, the liquid saturation degree decreases for increasing porosity [71, 146].

Unjacketed storage modulus

In Section 1.4.2, we employed the partial stress concept to evaluate possible expressions for tangent operators appearing in fluid content equations. In the following, such tangent operators are obtained following an alternative procedure, based on the consideration of the unjacketed conditions described in Section 1.4.1.

Relation (1.63) among volumetric strain rates can be substituted in (1.85), thus leading to the following expression for fluid content rate in terms of void-space strain rate $\dot{\varepsilon}_{vd}$:

$$\frac{\dot{M}_\alpha}{\rho_\alpha} = n\frac{\partial s_\alpha}{\partial \boldsymbol{\varepsilon}} : \dot{\boldsymbol{\varepsilon}} + n\sum_{\gamma=w,g}\left(\frac{s_\alpha}{\kappa_\alpha}\delta_{\alpha\gamma} + \frac{\partial s_\alpha}{\partial p_\gamma}\right)\dot{p}_\gamma + n_0 s_\alpha \dot{\varepsilon}_{vd} \tag{1.131}$$

A direct comparison between equation (1.131) and general form (1.40)$_2$ of fluid content rate hyperelastic relation yields:

$$\left(\zeta_\alpha \mathbf{b} - n\frac{\partial s_\alpha}{\partial \boldsymbol{\varepsilon}}\right) : \dot{\boldsymbol{\varepsilon}} + \sum_{\gamma=w,g}\left[C_{\alpha\gamma} - n\left(\frac{s_\alpha\delta_{\alpha\gamma}}{\kappa_\alpha} + \frac{\partial s_\alpha}{\partial p_\gamma}\right)\right]\dot{p}_\gamma - n_0 s_\alpha \dot{\varepsilon}_{vd} = 0 \tag{1.132}$$

for $\alpha = w, g$. The terms of this equation multiplying $\dot{\boldsymbol{\varepsilon}}$ and $\dot{\varepsilon}_{vd}$ can be both rewritten for the particular case of unjacketed compression in terms of $\dot{p}_f = \dot{p}_{uj}$, combining (1.60)

and (1.61) to obtain the solid-skeleton strain rate and employing $(1.58)_2$ to express void-space strain rate in terms of the unjacketed modulus κ_{vd}^{uj}, that is,

$$\left(\zeta_\alpha \mathbf{b} - n\frac{\partial s_\alpha}{\partial \boldsymbol{\varepsilon}}\right) : \dot{\boldsymbol{\varepsilon}} - n_0 s_\alpha \dot{\varepsilon}_{vd} = \left[\left(-\zeta_\alpha \mathbf{b} + n\frac{\partial s_\alpha}{\partial \boldsymbol{\varepsilon}}\right) : \frac{\mathbf{1}}{3\kappa_{sk}^{uj}} + \frac{n_0 s_\alpha}{\kappa_{vd}^{uj}}\right] \dot{p}_{uj} \tag{1.133}$$

Furthermore, elimination of $\dot{\boldsymbol{\varepsilon}}$ in relation (1.53) by means of (1.60– 1.61) yields:

$$\dot{p}_{uj} \underbrace{\left(1 + \frac{p_c}{3\kappa_{sk}^{uj}} \frac{\partial p_c}{\partial p_\gamma} \frac{\partial s_\gamma}{\partial \boldsymbol{\varepsilon}} : \mathbf{1}\right)}_{=: \eta} = \sum_{\alpha=w,g} \xi_\alpha \dot{p}_\alpha \qquad \text{for} \quad \gamma = w, g \tag{1.134}$$

Assuming the term in parentheses $\eta \neq 0$, the expression for $\dot{p}_{uj}$ obtained from (1.134) is substituted in (1.133), which, in turn, is combined with (1.132), leading to:

$$\sum_{\gamma=w,g} \left\{ C_{\alpha\gamma}^{uj} - n\frac{s_\alpha \delta_{\alpha\gamma}}{\kappa_\alpha} - n\frac{\partial s_\alpha}{\partial p_\gamma} - \left[\left(\xi_\alpha \mathbf{b} - n\frac{\partial s_\alpha}{\partial \boldsymbol{\varepsilon}}\right) : \frac{\mathbf{1}}{3\kappa_{sk}^{uj}} - \frac{n_0 s_\alpha}{\kappa_{vd}^{uj}}\right] \frac{\xi_\gamma}{\eta} \right\} \dot{p}_\gamma = 0 \tag{1.135}$$

where expression $\zeta_\alpha = \xi_\alpha$, with ξ_α defined by (1.54), was used for the coupling operators. In view of the arbitrariness of $\dot{p}_w$ and $\dot{p}_g$ appearing in equation (1.135), the following relations are obtained for tangent storage modulus in unjacketed conditions:

$$C_{\alpha\beta}^{uj} = n\left(\frac{s_\alpha}{\kappa_\alpha}\delta_{\alpha\beta} + \frac{\partial s_\alpha}{\partial p_\beta}\right) + \left[\left(\xi_\alpha \mathbf{b} - n\frac{\partial s_\alpha}{\partial \boldsymbol{\varepsilon}}\right) : \frac{\mathbf{1}}{3\kappa_{sk}^{uj}} - \frac{n_0 s_\alpha}{\kappa_{vd}^{uj}}\right] \frac{\xi_\beta}{\eta} \tag{1.136}$$

for $\alpha, \beta = w, g$.

If the saturation degree is assumed to be fully characterized by the capillary pressure, i.e. (1.101), it is $\eta = 1$, and as a consequence of $(1.102, 1.104_2)$, expression (1.136) of unjacketed storage modulus reads:

$$C_{\alpha\beta}^{uj} = n\left(\frac{s_\alpha}{\kappa_\alpha}\delta_{\alpha\beta} + \check{s}'_\alpha \frac{\partial p_c}{\partial p_\beta}\right) + \check{\xi}_\alpha \check{\xi}_\beta \frac{1}{3\kappa_{sk}^{uj}} \mathbf{b} : \mathbf{1} - s_\alpha \check{\xi}_\beta \frac{n_0}{\kappa_{vd}^{uj}} \tag{1.137}$$

for $\alpha, \beta = w, g$.

Therefore, based on assumed strain-independent retention models (1.101), a possi-

ble set of hyperelastic tangent operators:

$$\left.\begin{array}{rcl} \tilde{\mathbb{C}}_{sk} &=& \mathbb{C}_{sk} \\ \zeta_\alpha &=& s_\alpha \qquad \text{and} \qquad \mathbf{b} = \mathbf{1} - \dfrac{1}{3\kappa_{sk}^{uj}}\mathbb{C}_{sk}\mathbf{1} \\ C_{\alpha\beta} &=& n\left(\dfrac{s_\alpha}{\kappa_\alpha}\delta_{\alpha\beta} + \check{s}'_\alpha\dfrac{\partial p_c}{\partial p_\beta}\right) + s_\alpha s_\beta\left(\dfrac{1}{3\kappa_{sk}^{uj}}\mathbf{b}:\mathbf{1} - \dfrac{n_0}{\kappa_{vd}^{uj}}\right) \end{array}\right\} \quad \text{for} \quad \alpha,\beta = w,g \tag{1.138}$$

is obtained by introducing approximation (1.106) for the coupling coefficient (i.e. $\check{\xi}_\alpha \simeq s_\alpha$) in (1.137), thus recovering major symmetry of system (1.40) in terms of storage modulus. Following the same arguments used in Appendix B.1, the full thermodynamic admissibility of (1.138) can be shown by means of Maxwell conditions (1.35), indicating that expressions

$$\frac{\partial \hat{n}}{\partial \boldsymbol{\varepsilon}} = \mathbf{b} \qquad \text{and} \qquad \frac{\partial \hat{n}}{\partial p_f} = \frac{1}{3\kappa_{sk}^{uj}}\mathbf{b}:\mathbf{1} - \frac{n_0}{\kappa_{vd}^{uj}} \tag{1.139}$$

are a requirement for the partial derivatives of the adopted porosity model $\hat{n}(\boldsymbol{\varepsilon}, p_f)$.

As expected, hyperelastic operators (1.107) and porosity derivatives (1.96) previously considered in Section 1.4.3 are re-obtained from (1.138) and (1.139), respectively, by introducing assumptions (1.65–1.67) on unjacketed compression modulus (i.e. $\kappa_{sk}^{uj} \simeq \kappa_{vd}^{uj} \simeq \kappa_s$).

Another particular form of (1.138–1.139) is obtained by setting $1/\kappa_{vd}^{uj} = 0$ and $\kappa_s^{uj} = \kappa_s$, that is, a hyperelastic model based on Suklje form (1.72) of coupling tensor $\mathbf{b}$ with $\kappa_{sk}^{uj} = \kappa_s/(1-n_0)$ (see Remark 1.2).

Remark 1.7 *Setting* $1/\kappa_{vd}^{uj} \simeq 0$ *directly in expression (1.137) ensure major symmetry of system (1.40) in terms of storage modulus. However, thermodynamic admissibility of the corresponding poro-elastic model still require approximation (1.106) for the coupling coefficient, as it can be easily shown by imposing Maxwell condition* $(1.35)_3$.

1.5 Infinitesimal deformations of fluids

In this Section, in addition to solid phase and solid skeleton, we also assume both the fluid phases as subjected to infinitesimal deformations. In such a case, logarithmic

volumetric strain and current density of generic fluid phase α can be approximated by trace ε_α of infinitesimal strain tensor and by initial value $\rho_{\alpha 0}$ of density, respectively, that is,

$$e_\alpha \simeq \varepsilon_\alpha \qquad \text{and} \qquad \rho_\alpha \simeq \rho_{\alpha 0} \qquad \text{for} \quad \alpha = w, g \tag{1.140}$$

The fluids are assumed again to be barotropic and, in view of (1.38), definitions (1.32) for coupling and storage operators can be rewritten as:

$$\mathbf{b}_\alpha := -\frac{\partial^2 \phi}{\partial \boldsymbol{\varepsilon} \partial p_\alpha} \quad \text{and} \quad C_{\alpha\beta} := -\frac{\partial^2 \phi}{\partial p_\alpha \partial p_\beta} \qquad \text{for} \quad \alpha, \beta = w, g \tag{1.141}$$

and, as a consequence of (1.140), linearized form of (1.38–1.83,1.84) reads:

$$\frac{d\mu_\alpha}{dp_\beta} = \frac{1}{\rho_{\alpha 0}} \delta_{\alpha\beta} \qquad \dot{\varepsilon}_\alpha = \frac{\dot{p}_\alpha}{\kappa_\alpha} \qquad \frac{\partial \rho_\alpha}{\partial p_\beta} = \frac{\rho_{\alpha 0}}{\kappa_\alpha} \delta_{\alpha\beta} \qquad \text{for} \quad \alpha, \beta = w, g \tag{1.142}$$

Therefore, by taking into account also assumption (1.39) on coupling tensor expression, hyperelastic relations in rate form (1.40) reads:

$$\left\{ \begin{array}{rcll} \dot{\boldsymbol{\sigma}} & = & \tilde{\mathbb{C}}_{sk} \dot{\boldsymbol{\varepsilon}} - \mathbf{b} \displaystyle\sum_{\gamma = w,g} \zeta_\gamma \dot{p}_\gamma & \\ \dfrac{\dot{M}_\alpha}{\rho_{\alpha 0}} & = & \zeta_\alpha \mathbf{b} : \dot{\boldsymbol{\varepsilon}} + \displaystyle\sum_{\gamma = w,g} C_{\alpha\gamma} \dot{p}_\gamma & \text{for} \quad \alpha = w, g \end{array} \right. \tag{1.143}$$

Relations (1.33,1.141,1.143) leads to satisfaction of symmetry conditions (1.34) as well as of the following form of Maxwell relations:

$$\left. \begin{array}{rcl} \dfrac{\partial \tilde{\mathbb{C}}_{sk}}{\partial p_\alpha} & = & -\dfrac{\partial \zeta_\alpha}{\partial \boldsymbol{\varepsilon}} \otimes \mathbf{b} \\ \dfrac{\partial \zeta_\alpha}{\partial p_\beta} & = & \dfrac{\partial \zeta_\beta}{\partial p_\alpha} \\ \dfrac{\partial \zeta_\alpha}{\partial p_\beta} \mathbf{b} & = & \dfrac{\partial C_{\alpha\beta}}{\partial \boldsymbol{\varepsilon}} \\ \dfrac{\partial C_{\alpha\alpha}}{\partial p_\beta} & = & \dfrac{\partial C_{\alpha\beta}}{\partial p_\alpha} \end{array} \right\} \quad \text{for} \quad \alpha, \beta = w, g \tag{1.144}$$

As possible forms for tangent operators $\tilde{\mathbb{C}}_{sk}$ and ζ_α appearing in equation $(1.143)_1$, we consider again relations (1.54,1.56) obtained in Section 1.4.1 from differentiation of Lewis-Schrefler decomposition (1.41) of total stress. Similarly, expression (1.69) for coupling tensor $\mathbf{b}$ is taken into account.

As a consequence of the now assumed infinitesimal deformations of fluid phases, the expression obtained in Section 1.4.2 for tangent operators appearing in fluid content equation are slightly simplified, as briefly shown in the following. We consider a macroscopic strain measure for the fluid phases, defined as:

$$\bar{\varepsilon}_\alpha := \theta_\alpha \varepsilon_\alpha = n s_\alpha \varepsilon_\alpha \tag{1.145}$$

whose linearized form in terms of initial value $\theta_{\alpha 0}$ of volumetric fluid content, that is,

$$\bar{\varepsilon}_\alpha = \theta_{\alpha 0} \varepsilon_\alpha \tag{1.146}$$

can be effectively employed in the assumed infinitesimal deformation range. Therefore, in view of (1.140) and (1.145–1.146), expression (1.82) of fluid content rate reads:

$$\frac{\dot{M}_\alpha}{\rho_{\alpha 0}} = s_\alpha \dot{\varepsilon}_v + \theta_{\alpha 0} \dot{\varepsilon}_\alpha - s_\alpha (1 - n_0) \dot{\varepsilon}_s + n \dot{s}_\alpha \tag{1.147}$$

By means of the same arguments employed to obtain (1.90) from (1.82), using equations (1.46,1.53,1.88,1.142_2), expression $(1.90)_1$ is recovered again for the coupling tensor and expression $(1.90)_2$ of the storage modulus now reads:

$$C_{\alpha\beta} = \frac{\theta_{\alpha 0}}{\kappa_\alpha} \delta_{\alpha\beta} + n \frac{\partial s_\alpha}{\partial p_\beta} + \frac{s_\alpha \xi_\beta}{3\kappa_s} (\mathbf{b} - n_0 \mathbf{1}) : \mathbf{1} \quad \text{for} \quad \alpha, \beta = w, g \tag{1.148}$$

with coupling operators ξ_α and $\mathbf{b}$ given by (1.54) and (1.69), respectively.

As an example, we can consider strain-independent retention models (1.101) associated to approximation $\check{\xi}_\alpha \simeq s_\alpha$ ensuring satisfaction of symmetry requirements (see Section 1.4.3). With these assumptions, expression (1.148) of storage modulus reduce to:

$$C_{\alpha\beta} = \underbrace{\frac{\theta_{\alpha 0}}{\kappa_\alpha} \delta_{\alpha\beta} + \frac{s_\alpha s_\beta}{3\kappa_s} (\mathbf{b} - n_0 \mathbf{1}) : \mathbf{1}}_{=: C^{cp}_{\alpha\beta}} + \underbrace{n \check{s}'_\alpha \frac{\partial p_c}{\partial p_\beta}}_{=: C^{sd}_{\alpha\beta}} \quad \text{for} \quad \alpha, \beta = w, g \tag{1.149}$$

where we have denoted by $C^{cp}_{\alpha\beta}$ and by $C^{sd}_{\alpha\beta}$ the components of storage modulus due to compressibility of the three phases and to changes in saturation degrees, respectively.

As expected, Maxwell conditions (1.144) are satisfied by tangent operator set consisting of $(1.107)_{1-2}$ and (1.149), as it can be easily shown by means of the same arguments employed in Appendix B.1, that is, by using relations (1.49,1.97,1.102,1.106,1.108).

Finally, it can be observed that due to infinitesimal deformations of fluid phases, expression $(1.138)_3$ of unjacketed storage modulus reads:

$$C_{\alpha\beta} = \frac{\theta_{\alpha 0}}{\kappa_\alpha}\delta_{\alpha\beta} + n\check{s}'_\alpha \frac{\partial p_c}{\partial p_\beta} + s_\alpha s_\beta \left(\frac{1}{3\kappa_{sk}^{uj}} \mathbf{b} : \mathbf{1} - \frac{n_0}{\kappa_{vd}^{uj}} \right) \tag{1.150}$$

Remark 1.8 *Assuming the porous solid as fully saturated by liquid phase (i.e. $s_w = 1$), a unique constant storage modulus is obtained from (1.149), that is,*

$$C_w^{sat} = \frac{n_0}{\kappa_w} + \frac{1}{3\kappa_s}(\mathbf{b} - n_0\mathbf{1}) : \mathbf{1} \tag{1.151}$$

which is an extension to the anisotropic case of expression found by Rice and Cleary [114] for the inverse of Biot modulus.

Remark 1.9 *The thermodynamic framework presented in Sections 1.3–1.4 leads to an expression for total mechanical power which includes the one proposed by Houlsby [80] as a particular case. As shown in the following, such a particularization is obtained assuming incompressibility of solid and liquid phases as well as infinitesimal strains of gas phase. Assuming a gravitational field for the volume forces and keeping in mind linearized expression $(1.142)_1$, dissipation inequality (1.22) can be rewritten as:*

$$D = \boldsymbol{\sigma} : \dot{\boldsymbol{\varepsilon}} + \sum_{\alpha=w,g} p_\alpha \frac{\dot{M}_\alpha}{\rho_{\alpha 0}} - \dot{\psi} - \sum_{\alpha=w,g} (\nabla p_\alpha - \rho_{\alpha 0}\mathbf{g}) \cdot \mathbf{w}_\alpha \geq 0 \tag{1.152}$$

with:

$$\mathbf{w}_\alpha := n s_\alpha (\mathbf{v}_\alpha - \mathbf{v}) \tag{1.153}$$

To obtain (1.152) we have also used definition (1.8) of fluid flow and expressions (1.73) and (1.77) for reduced densities and volumetric contents of fluids, respectively. In view of linearized expressions $(1.140_2, 1.142_2, 1.146)$, the substitution in (1.152) of general form (1.89) for the fluid mass content rate leads to:

$$\begin{aligned} D \;=\; & (\boldsymbol{\sigma} + \mathbf{b}p_f) : \dot{\boldsymbol{\varepsilon}} - n p_c \dot{s}_w + \sum_{\alpha=w,g} p_\alpha \dot{\tilde{\varepsilon}}_\alpha + p_f \frac{\dot{p}_f}{3\kappa_s}(\mathbf{b} - n_0\mathbf{1}) : \mathbf{1} - \\ & - \dot{\psi} - \sum_{\alpha=w,g} (\nabla p_\alpha - \rho_{\alpha 0}\mathbf{g}) \cdot \mathbf{w}_\alpha \geq 0 \end{aligned} \tag{1.154}$$

where we have also used definition (1.42) of average pore pressure, constraint (1.49) on saturation degrees and definition (1.51) of capillary pressure. If solid and liquid phases are assumed as incompressible, in view of (1.69), dissipation inequality (1.154) reduces to:

$$D = (\boldsymbol{\sigma} + p_f \mathbf{1}) : \dot{\boldsymbol{\varepsilon}} - n p_c \dot{s}_w + p_g \dot{\tilde{\varepsilon}}_g - \dot{\psi} - \sum_{\alpha=w,g} (\nabla p_\alpha - \rho_{\alpha 0} \mathbf{g}) \cdot \mathbf{w}_\alpha \geq 0 \tag{1.155}$$

In the isothermal case, the volumetric density p_e of the mechanical power of the porous solid equals the sum between dissipation and free energy rate, that is,

$$p_e = (\boldsymbol{\sigma} + p_f \mathbf{1}) : \dot{\boldsymbol{\varepsilon}} - n p_c \dot{s}_w + p_g \dot{\tilde{\varepsilon}}_g - \sum_{\alpha=w,g} (\nabla p_\alpha - \rho_{\alpha 0} \mathbf{g}) \cdot \mathbf{w}_\alpha \geq 0 \tag{1.156}$$

which is coincident with the work rate expression obtained by Houlsby [80].

2

Finite element formulation and numerical simulations

2.1 Introduction

In this chapter we present the finite element approximation for the differential problem resulting from governing equations presented in Chapter 1. In particular, in Section 2.2 we introduce the weak forms for linear momentum balance of the multiphase continuum and for the mass conservation of fluids. These equations are then rewritten in Section 2.3 in a discrete residual form after nodal interpolation of the assumed primary variables: solid skeleton displacements $\mathbf{u}$ and pore pressures p_α. The discretization in the time domain is obtained by the Backward-Euler implicit scheme. The resulting highly non-linear solving system is solved by a standard Newton-Raphson iterative procedure and a particular attention is payed on the different sources of non-linearity as well as on the linearization process. In Section 2.3.1, a simplified version of the constitutive model presented in Chapter 1 is considered to obtain an explicit form of linearization operators. We also remark the differences between the operators obtained by linearization of the continuum poro-elastic model and of time-integrated fluid mass balances, respectively. Also a mass-conservative scheme is considered for the time integration of the fluid mass balance. The presented finite element formulation has been

implemented in the general code FEAP [138]. Numerical examples are presented in Section 2.4 to validate the poro-elastic model presented in Chapter 1 and to assess the performance of the numerical formulation. In particular, a benchmark problem involving the desaturation of a sand column is simulated. As a well-known severe test, we consider the propagation of saturation front in an initially dry solid. Finally, the formulation is applied to a problem of interest for dam engineering.

The main results reported in the present chapter are also presented by Callari and Abati [32].

2.2 Governing equations

In this section we briefly summarize equations governing the problem of a porous solid where both the liquid and gaseous phases fill the porous space. The linear momentum balance of the whole porous solid and equations of fluid mass conservation for the fluid phases are written in weak form for quasi-static problems and in the infinitesimal deformation range. Hyperelastic rate equations presented in Chapter 1 are then employed to formulate the problem in terms of the considered primary variables.

In the infinitesimal deformation range, current and reference configurations of the multiphase porous solid are coincident with the domain $\Omega \subset \mathbb{R}^{n_{\rm dim}}$, where $n_{\rm dim} = 1, 2$ or 3 is the spatial dimension of the problem. The weak form of the quasi-static equilibrium of the porous solid can be expressed in terms of the total stress tensor $\boldsymbol{\sigma}$ by the principle of virtual work as

$$\int_\Omega \boldsymbol{\sigma} : \nabla^s \boldsymbol{\eta} \, d\Omega = \int_\Omega \mathbf{f} \cdot \boldsymbol{\eta} \, d\Omega + \int_{\partial_t \Omega} \bar{\mathbf{t}} \cdot \boldsymbol{\eta} \, dA \tag{2.1}$$

with $\mathbf{f}$ and $\bar{\mathbf{t}}$ being imposed volumetric body forces and tractions acting on the boundary portion $\partial_t \Omega \subset \partial\Omega$, respectively, and being $\nabla^s(\cdot)$ the symmetric part of the gradient operator $\nabla(\cdot)$. Equation (2.1) must hold for all admissible variations $\boldsymbol{\eta} \in \mathcal{V}_u$, where

$$\mathcal{V}_u = \{\boldsymbol{\eta} : \Omega \to \mathbb{R}^{n_{\rm dim}} \ : \boldsymbol{\eta} = \mathbf{0} \quad \text{on} \quad \partial_u \Omega\} \tag{2.2}$$

for the part of the boundary $\partial_u \Omega \subset \partial\Omega$ with imposed displacements $\mathbf{u} = \bar{\mathbf{u}}$.

If no volumetric fluid sources are present in Ω, the mass content M_α of the fluid α, with $\alpha = w, g$, can be obtained in terms of the relative mass flow $\mathbf{q}_\alpha$ by the following weak form of the fluid mass balance:

$$\int_\Omega \dot{M}_\alpha w_\alpha \, d\Omega = \int_\Omega \mathbf{q}_\alpha \cdot \nabla w_\alpha \, d\Omega - \int_{\partial_{q_\alpha}\Omega} \bar{q}_{\alpha n} w_\alpha \, dA \tag{2.3}$$

for all admissible variations $w \in \mathcal{V}_p$ of the pore pressure field, with

$$\mathcal{V}_p = \{w : \Omega \to \mathbb{R} \ : w = 0 \quad \text{on} \quad \partial_p\Omega\} \tag{2.4}$$

where $\partial_p\Omega \subset \partial\Omega$ is the part of the boundary with an imposed pore pressure $p_\alpha = \bar{p}_\alpha$ and $\partial_q\Omega \subset \partial\Omega$ is the part of the boundary with imposed normal component of the fluid flow $\mathbf{q}_\alpha \cdot \mathbf{n} =: q_{\alpha n} = \bar{q}_{wn}$, for the outward unit normal $\mathbf{n}$ to the domain boundary.

2.3 Finite element formulation

In the following, finite element methods for the solution of multiphase continuum governing equations presented in the previous sections are developed. Isoparametric interpolations are employed to approximate displacement $\mathbf{u}$ and pore pressures p_α at a point $\mathbf{x}$ of a generic finite element Ω_e, that is:

$$\mathbf{u}_e(\mathbf{x}) = \mathbf{N}_e(\mathbf{x})\mathbf{d}_e \qquad \text{and} \qquad p_{\alpha_e}(\mathbf{x}) = \mathbf{N}^p_e(\mathbf{x})\mathbf{p}_{\alpha_e} \quad \text{for} \quad \alpha = w, g \tag{2.5}$$

where $\mathbf{N}_e(\mathbf{x})$ and $\mathbf{N}^p_e(\mathbf{x})$ are shape functions used to interpolate nodal displacements $\mathbf{d}_e$ and nodal pore pressures $\mathbf{p}_{\alpha_e}$, respectively. Approximations of strain and pore pressure gradients are based on strain operator $\bar{\mathbf{B}}_e$ of a mixed B-bar type formulation [81] and on a standard gradient operator $\mathbf{B}^p_e := \nabla\mathbf{N}^p_e$, respectively, that is:

$$\boldsymbol{\varepsilon}_e = \bar{\mathbf{B}}_e\mathbf{d}_e \qquad \text{and} \qquad \nabla p_{\alpha_e} = \mathbf{B}^p_e\mathbf{p}_{\alpha_e} \quad \text{for} \quad \alpha = w, g \tag{2.6}$$

An ordinary differential system is obtained by using interpolations (2.5–2.6) in the finite-element discretization of weak forms of linear momentum (2.1) and fluid mass balances (2.3). This system is written in residual algebraic form for the generic time step $[t_n, t_{n+1}]$, with the linear momentum balance equation calculated at time t_{n+1}

and rate equations of fluid-mass balances approximated by a backward-Euler scheme. Denoting by $\Delta t = t_{n+1} - t_n$ the time increment and omitting index $n+1$ to simplify the notation, the coupled residual system reads:

$$\left\{ \begin{array}{rcl} \mathbf{r}_m &=& \mathbf{f}^{ext} - \mathop{\mathbf{A}}_{e=1}^{n_{\rm el}} \int_{\Omega_e} \bar{\mathbf{B}}_e^T \boldsymbol{\sigma} \, d\Omega = \mathbf{0} \\ \mathbf{r}_\alpha &=& \mathbf{f}_\alpha^{ext} - \mathop{\mathbf{A}}_{e=1}^{n_{\rm el}} \left[\int_{\Omega_e} \mathbf{N}_e^{pT} \frac{M_\alpha - M_{\alpha,n}}{\Delta t} \, d\Omega - \int_{\Omega_e} \mathbf{B}_e^{pT} \mathbf{q}_\alpha \, d\Omega \right] = \mathbf{0} \end{array} \right. \tag{2.7}$$

with $\mathbf{f}^{ext}$ and $\mathbf{f}_\alpha^{ext}$ the vectors of imposed external forces and flows, respectively, and $\alpha = w, g$. In system (2.7), symbol $\mathbf{A}$ denotes the assembly of contributions of all the $n_{\rm el}$ finite elements. This non-linear algebraic system can be solved by a Newton-Raphson iterative procedure, where the increments $\Delta(\cdot) = (\cdot)_{n+1}^{(k+1)} - (\cdot)_{n+1}^{(k)}$ of unknown nodal variables at t_{n+1}, are evaluated at iteration $(k+1)$ by means of the following linearized form of system (2.7):

$$\mathbf{r}_\alpha^{(k)} = - \left(\frac{\partial \mathbf{r}_\alpha}{\partial \mathbf{d}} \right)^{(k)} \Delta \mathbf{d} - \sum_{\gamma=w,g} \left(\frac{\partial \mathbf{r}_\alpha}{\partial \mathbf{p}_\gamma} \right)^{(k)} \Delta \mathbf{p}_\gamma \qquad \text{for} \quad \alpha = m, w, g \tag{2.8}$$

In the following, the linearized kinematics described in Section 1.5 is considered for both the fluid phases. Extensions accounting for finite deformations of fluids can be easily devised. So, in view of assumed barotropy of fluid phases $(1.142)_1$, the following finite element approximation of extended Darcy law (1.25) is obtained by introducing interpolation $(2.6)_2$:

$$\mathbf{q}_\alpha = -\rho_{\alpha 0} \mathbf{k}_\alpha \left(\mathbf{B}_e^p \mathbf{p}_{\alpha_e} - \rho_{\alpha 0} \mathbf{g} \right) \qquad \text{for} \qquad \alpha = w, g \tag{2.9}$$

where the gravity acceleration $\mathbf{g}$ was considered as external mass loading, that is: $\mathbf{f} = -\nabla \mathcal{V}_{ext} = \mathbf{g}$.

By applying the chain rule to differentiation of residuals (2.7), using relations (2.5–2.6), it can be shown that linearized system (2.8) reads:

$$\left\{ \begin{array}{rcl} \mathbf{r}_m^{(k)} &=& \mathbf{K}^{(k)} \Delta \mathbf{d} - \sum_{\gamma=w,g} \mathbf{Q}_{m\gamma}^{(k)} \Delta \mathbf{p}_\gamma \\ \mathbf{r}_\alpha^{(k)} &=& \left(\frac{\mathbf{Q}_{\alpha m}}{\Delta t} - \mathbf{G}_\alpha \right)^{(k)} \Delta \mathbf{d} + \sum_{\gamma=w,g} \left(\frac{\mathbf{S}_{\alpha\gamma}}{\Delta t} - \mathbf{G}_{\alpha\gamma} + \mathbf{H}_\alpha \delta_{\alpha\gamma} \right)^{(k)} \Delta \mathbf{p}_\gamma \end{array} \right. \tag{2.10}$$

for $\alpha = w, g$. System (2.10) is written in terms of global matrices of stiffness $\mathbf{K}$, storage $\mathbf{S}_{\alpha\beta}$, fluid-mechanical coupling $\mathbf{Q}_{m\alpha}, \mathbf{Q}_{\alpha m}$ and permeability $\mathbf{H}_\alpha$, defined as:

$$\mathbf{K} = \mathop{\mathbf{A}}_{e=1}^{n_{\text{el}}} \int_{\Omega_e} \bar{\mathbf{B}}_e^T \frac{\partial \boldsymbol{\sigma}}{\partial \boldsymbol{\varepsilon}} \bar{\mathbf{B}}_e \, d\Omega \tag{2.11}$$

$$\mathbf{S}_{\alpha\beta} = \mathop{\mathbf{A}}_{e=1}^{n_{\text{el}}} \int_{\Omega_e} \mathbf{N}_e^{pT} \frac{\partial M_\alpha}{\partial p_\beta} \mathbf{N}_e^p \, d\Omega \qquad \text{for} \quad \alpha, \beta = w, g \tag{2.12}$$

$$\left.\begin{aligned} \mathbf{Q}_{m\alpha} &= \mathop{\mathbf{A}}_{e=1}^{n_{\text{el}}} \int_{\Omega_e} \bar{\mathbf{B}}_e^T \frac{\partial \boldsymbol{\sigma}}{\partial p_\alpha} \mathbf{N}_e^p \, d\Omega \\ \mathbf{Q}_{\alpha m} &= \mathop{\mathbf{A}}_{e=1}^{n_{\text{el}}} \int_{\Omega_e} \mathbf{N}_e^{pT} \frac{\partial M_\alpha}{\partial \boldsymbol{\varepsilon}} \bar{\mathbf{B}}_e \, d\Omega \end{aligned}\right\} \qquad \text{for} \quad \alpha = w, g \tag{2.13}$$

$$\mathbf{H}_\alpha = \mathop{\mathbf{A}}_{e=1}^{n_{\text{el}}} \int_{\Omega_e} \rho_{\alpha 0} \mathbf{B}_e^{pT} \mathbf{k}_\alpha \mathbf{B}_e^p \, d\Omega \qquad \text{for} \quad \alpha = w, g \tag{2.14}$$

Remaining operators appearing in (2.10) are obtained from permeability linearization with respect to strains and fluid pressures, respectively:

$$\mathbf{G}_\alpha = \mathop{\mathbf{A}}_{e=1}^{n_{\text{el}}} \int_{\Omega_e} \mathbf{B}^{pT} \left(\frac{\partial \mathbf{k}_\alpha}{\partial \boldsymbol{\varepsilon}} \cdot \mathbf{q}_\alpha^{uni} \right) \bar{\mathbf{B}}_e \, d\Omega \qquad \mathbf{G}_{\alpha\beta} = \mathop{\mathbf{A}}_{e=1}^{n_{\text{el}}} \int_{\Omega_e} \mathbf{B}_e^{pT} \frac{\partial \mathbf{k}_\alpha}{\partial p_\beta} \mathbf{q}_\alpha^{uni} \mathbf{N}_e^p \, d\Omega \tag{2.15}$$

with

$$\mathbf{q}_\alpha^{uni} := -\rho_{\alpha 0} (\mathbf{B}_e^p \mathbf{p}_{\alpha_e} - \rho_{\alpha 0} \mathbf{g}) \tag{2.16}$$

in the linearization operator $(2.15)_1$ we have employed the following convention:

$$\left(\frac{\partial \mathbf{k}_\alpha}{\partial \boldsymbol{\varepsilon}} \cdot \mathbf{q}_\alpha^{uni} \right)_{ik} = \left(\frac{\partial \mathbf{k}_\alpha}{\partial \boldsymbol{\varepsilon}} \right)_{ijk} \mathbf{q}_{\alpha_j}^{uni} = \mathbf{k}_{\alpha_{ij,k}} \mathbf{q}_{\alpha_j}^{uni} \tag{2.17}$$

for $i, j = 1 \ldots n_{dim}$ and $k = 1 \ldots a$, being a the number of strain components of the problem, and where repeated indexes are summated.

Remark 2.1 *In general, relative permeability tensors $\mathbf{k}_\alpha$ can be functions of all the considered primary variables, that is, pore pressures and solid-skeleton displacements. In particular, a quite general constitutive assumption considers the single-phase permeability tensors $\mathbf{k}_\alpha^{sat}$ and the relative permeability coefficients k_α^{rel} as dependent on strain [132] and corresponding saturation degree [46, 99], respectively, that is:*

$$\mathbf{k}_\alpha = k_\alpha^{rel}(s_\alpha) \mathbf{k}_\alpha^{sat}(\boldsymbol{\varepsilon}) \qquad \textit{for} \qquad \alpha = w, g \tag{2.18}$$

In such a case, the eventual dependance of k_α^{rel} *on* $\boldsymbol{\varepsilon}$*,* p_w *and* p_g *is regulated by the assumed fluid retention model, and the derivatives appearing in (2.15) reads:*

$$\left.\begin{aligned} \frac{\partial \mathbf{k}_\alpha}{\partial \boldsymbol{\varepsilon}} &= \frac{dk_\alpha^{rel}}{ds_\alpha}\Theta_\alpha + k_\alpha^{rel}\frac{\partial \mathbf{k}_\alpha^{sat}}{\partial \boldsymbol{\varepsilon}} \\ \frac{\partial \mathbf{k}_\alpha}{\partial p_\beta} &= \frac{dk_\alpha^{rel}}{ds_\alpha}\frac{\partial s_\alpha}{\partial p_\beta}\mathbf{k}_\alpha^{sat} \end{aligned}\right\} \quad for \quad \alpha,\beta = w,g \tag{2.19}$$

where the following notation has been used:

$$\Theta_{\alpha_{ijk}} := \mathbf{k}_{\alpha_{ij}}^{sat}\left(\frac{\partial s_\alpha}{\partial \boldsymbol{\varepsilon}}\right)_k \tag{2.20}$$

for $i,j = 1\ldots n_{dim}$ *and* $k = 1\ldots a$*, with* a *the number of strain components of the problem. For example, if classic strain-independent models* $s_\alpha = \check{s}_\alpha(p_c)$ *are employed, derivatives (2.19) reduce to:*

$$\left.\begin{aligned} \frac{\partial \mathbf{k}_\alpha}{\partial \boldsymbol{\varepsilon}} &= k_\alpha^{rel}\frac{\partial \mathbf{k}_\alpha^{sat}}{\partial \boldsymbol{\varepsilon}} \\ \frac{\partial \mathbf{k}_\alpha}{\partial p_\beta} &= \frac{dk_\alpha^{rel}}{ds_\alpha}\check{s}'_\alpha\frac{\partial p_c}{\partial p_\beta}\mathbf{k}_\alpha^{sat} \end{aligned}\right\} \quad for \quad \alpha,\beta = w,g \tag{2.21}$$

as it can be easily shown by means of (1.102).

2.3.1 Time-integration consistent tangents

Stress-term tangent operators appearing in matrices (2.11) and $(2.13)_1$ of finite element system (2.10) can be obtained as follows by linearization of the continuum poro-elastic model:

$$\frac{\partial \boldsymbol{\sigma}}{\partial \boldsymbol{\varepsilon}} = \tilde{\mathbb{C}}_{sk} \qquad \frac{\partial \boldsymbol{\sigma}}{\partial p_\alpha} = -\zeta_\alpha \mathbf{b} \qquad \text{for} \quad \alpha = w,g \tag{2.22}$$

that is, from rate form $(1.143)_1$ of hyperelastic relation for stress. On the other hand, the fluid-term tangents appearing in matrices (2.12) and $(2.13)_2$ have to be consistent with the time-integration scheme used to numerically solve the fluid-mass balance equation. Therefore, the computation of such operators requires linearization of the backward-Euler scheme employed for time discretization of fluid-content rate equation $(1.143)_2$.

As an example, we consider such a time integration for the simplified hyperelastic laws based on strain-independent retention models (1.101):

$$\frac{M_\alpha}{\rho_{\alpha 0}} = \frac{M_{\alpha,n}}{\rho_{\alpha 0}} + s_\alpha \mathbf{b} : (\boldsymbol{\varepsilon} - \boldsymbol{\varepsilon}_n) + \sum_{\gamma=w,g} C_{\alpha\gamma}(p_\gamma - p_{\gamma,n}) \qquad \text{for} \quad \alpha = w, g \tag{2.23}$$

where the storage modulus is given by expression (1.149). In view of scheme (2.23), the consideration of derivatives of the porosity model (1.92) with respect to the primary variables and (1.103) for the retention law, leads to the following consistent expressions for tangents appearing in matrices (2.12) and $(2.13)_2$, respectively:

$$\left\{ \begin{array}{rcl} \dfrac{\partial M_\alpha}{\partial \boldsymbol{\varepsilon}} & = & \rho_{\alpha 0} \left[s_\alpha + \check{s}'_\alpha (p_c - p_{c,n}) \right] \mathbf{b}^T \\ \dfrac{\partial M_\alpha}{\partial p_\beta} & = & \rho_{\alpha 0} \check{s}'_\alpha \dfrac{\partial p_c}{\partial p_\beta} \mathbf{b} : (\boldsymbol{\varepsilon} - \boldsymbol{\varepsilon}_n) + \left(\dfrac{\partial M_\alpha}{\partial p_\beta} \right)_C \end{array} \right. \tag{2.24}$$

where the tangent component defined as

$$\left(\frac{\partial M_\alpha}{\partial p_\beta} \right)_C := \rho_{\alpha 0} \left[C_{\alpha\beta} + \sum_{\gamma=w,g} \frac{\partial C_{\alpha\gamma}}{\partial p_\beta} (p_\gamma - p_{\gamma,n}) \right] \tag{2.25}$$

is given in terms of the following derivative of storage modulus (1.149):

$$\frac{\partial C_{\alpha\gamma}}{\partial p_\beta} = \frac{\partial C^{cp}_{\alpha\gamma}}{\partial p_\beta} + \frac{\partial C^{sd}_{\alpha\gamma}}{\partial p_\beta} \tag{2.26}$$

$$\text{with} \quad \left\{ \begin{array}{rcl} \dfrac{\partial C^{cp}_{\alpha\gamma}}{\partial p_\beta} & = & (\mathbf{b} - n_0 \mathbf{1}) : \dfrac{\mathbf{1}}{3\kappa_s} (\check{s}'_\alpha s_\gamma + s_\alpha \check{s}'_\gamma) \dfrac{\partial p_c}{\partial p_\beta} \\ \dfrac{\partial C^{sd}_{\alpha\gamma}}{\partial p_\beta} & = & (\mathbf{b} - n_0 \mathbf{1}) : \dfrac{\mathbf{1}}{3\kappa_s} \check{s}'_\alpha s_\beta \dfrac{\partial p_c}{\partial p_\gamma} + n \check{s}''_\alpha \dfrac{\partial p_c}{\partial p_\beta} \dfrac{\partial p_c}{\partial p_\gamma} \end{array} \right. \tag{2.27}$$

and $\alpha, \beta = w, g$. To obtain (2.24–2.27) we also used definitions (1.51,1.103,B.8) and assumption (1.106).

Consistent tangent operators (2.24–2.27) can be seen as an extension to the mechanically coupled case of the results presented for example in [93] for the numerical treatment of fluid flow in variably saturated rigid porous media. As expected, the difference between the consistent and the following "continuum" tangents

$$\frac{\partial M_\alpha}{\partial \boldsymbol{\varepsilon}} = \rho_{\alpha 0} s_\alpha \mathbf{b}^T \qquad \frac{\partial M_\alpha}{\partial p_\beta} = \rho_{\alpha 0} C_{\alpha\beta} \qquad \text{for} \quad \alpha, \beta = w, g \tag{2.28}$$

obtained from rate form $(1.143)_2$ of fluid-content hyperelastic relation, vanishes as time step increment Δt approaches zero.

Furthermore, consistent (2.24–2.27) and continuum (2.28) tangent operators are coincident for assumed constant saturation degrees, as it is the case of porous continua saturated by a single phase. On the other hand, differences between the two tangent operator sets are normally significant in the case of large variations of saturation degrees, typically involving large absolute values of $\check{s}'_\alpha$.

2.3.2 Mass conservative scheme

For numerical time integration of saturation degree rate by means of a backward Euler scheme, expression $\dot{s}_\alpha$ is to be preferred to $\check{s}'_\alpha \dot{p}_c$ considered in (2.23). In fact, time discretization of latter expression can lead to unacceptable errors in fluid mass balance, especially in the case of strongly non-linear response, typically characterizing infiltration problems.

Therefore, following the same arguments presented in [43] for the uncoupled case, we consider also the time integration of a mixed form of fluid-content rate equation, obtained by substituting the following relation in $(1.143)_2$:

$$\sum_{\gamma=w,g} C_{\alpha\gamma}\dot{p}_\gamma = \sum_{\gamma=w,g} C^{cp}_{\alpha\gamma}\dot{p}_\gamma + n\dot{s}_\alpha \qquad \text{for} \quad \alpha = w, g \tag{2.29}$$

where we have used the notation introduced in (1.149) for the component $C^{cp}_{\alpha\gamma}$ of storage modulus. Therefore, backward-Euler time discretization of (2.29), that is,

$$\sum_{\gamma=w,g} C_{\alpha\gamma}\,(p_\gamma - p_{\gamma,n}) = \sum_{\gamma=w,g} C^{cp}_{\alpha\gamma}\,(p_\gamma - p_{\gamma,n}) + n(s_\alpha - s_{\alpha,n}) \qquad \text{for} \quad \alpha = w, g \tag{2.30}$$

is substituted in (2.23) and the so-obtained integration scheme with improved mass conservation properties can be considered to calculate the fluid-content term of residual $(2.7)_2$.

The consistent linearization of such a time-discretized equation employs the same arguments used to obtain (2.24–2.27) and leads to the following consistent expressions

for tangents appearing in matrices $(2.13)_2$ and (2.12), respectively:

$$\begin{cases} \dfrac{\partial M_\alpha}{\partial \boldsymbol{\varepsilon}} &= \rho_{\alpha 0}(2s_\alpha - s_{\alpha,n})\,\mathbf{b}^T \\ \dfrac{\partial M_\alpha}{\partial p_\beta} &= \rho_{\alpha 0}\check{s}'_\alpha \dfrac{\partial p_c}{\partial p_\beta}\mathbf{b}^T(\boldsymbol{\varepsilon}-\boldsymbol{\varepsilon}_n) + \left(\dfrac{\partial M_\alpha}{\partial p_\beta}\right)_{C^{cp}} + \left(\dfrac{\partial M_\alpha}{\partial p_\beta}\right)_{\theta} \end{cases} \tag{2.31}$$

where

$$\left(\frac{\partial M_\alpha}{\partial p_\beta}\right)_{\theta} := \rho_{\alpha 0}\left[n\check{s}'_\alpha \frac{\partial p_c}{\partial p_\beta} + (\mathbf{b} - n_0\mathbf{1}) : \frac{\mathbf{1}}{3\kappa_s}(s_\alpha - s_{\alpha,n})s_\beta\right] \tag{2.32}$$

and $(\partial M_\alpha/\partial p_\beta)_{C^{cp}}$ is obtained by setting $C = C^{cp}$ in (2.25) and by $(2.27)_1$.

Remark 2.2 *In numerical simulations presented in Section 2.4 below, we investigate also the ability of lumped forms of storage matrix (2.12) in avoiding oscillatory solutions. We recall that improvements in solution quality resulting from the use of diagonalized mass operators are often observed in the analysis of uncoupled infiltration problems, for example in [43, 93] among many others. In fact, it is well known how finite-element approximations of parabolic problems employing a finite-difference discretization, e.g the backward Euler scheme, of the time domain violate the discrete form of the maximum principle [67, 110]. In this case, oscillatory solutions are attained if the time step employed in calculations is smaller than a minimum value. This limit value depends on the out-of-diagonal components of the storage matrix. Therefore, the use of a lumped storage matrix is particularly suitable in those frequent situations where very small time steps are necessary to solve highly non-linear problems [58, 93].*

Remark 2.3 *In numerical simulations presented in Section 2.4, a general backward-Euler scheme, that is,*

$$\check{p}_f = \check{p}_{f,n} + \sum_{\gamma=w,g} s_\gamma(p_\gamma - p_{\gamma,n}) \tag{2.33}$$

was preferred to analytical time integration of the pore-pressure term (1.110) appearing in stress-rate equation $(1.143)_1$. From linearization of (2.33) and consideration of relations (1.50,1.102,1.122), we obtained the operator:

$$\frac{\partial \boldsymbol{\sigma}}{\partial p_\alpha} = -\mathbf{b}\frac{\partial \check{p}_f}{\partial p_\alpha} = -\mathbf{b}[s_\alpha + \check{s}'_\alpha(p_c - p_{c,n})] \tag{2.34}$$

which was implemented in matrix (2.13)$_1$, as an alternative to the "continuum" tangent (2.22)$_2$. Moreover, considering expression (2.33) in the porosity model (1.92), the tangent coefficient expression (2.27)$_2$ has to be modified into

$$\frac{\partial C^{sd}_{\alpha\gamma}}{\partial p_\beta} = n\check{s}''_\alpha \frac{\partial p_c}{\partial p_\beta}\frac{\partial p_c}{\partial p_\gamma} + (\mathbf{b} - n_0\mathbf{1}) : \frac{\mathbf{1}}{3\kappa_s}\check{s}'_\alpha \frac{\partial p_c}{\partial p_\gamma}[s_\beta + \check{s}'_\beta(p_c - p_{c,n})] \tag{2.35}$$

For a similar reason, if we consider a mass conservative approach for the fluid mass content rate, instead of tangent coefficient (2.32) we have

$$\left(\frac{\partial M_\alpha}{\partial p_\beta}\right)_\theta := \rho_{\alpha 0}\left\{n\check{s}'_\alpha \frac{\partial p_c}{\partial p_\beta} + (\mathbf{b} - n_0\mathbf{1}) : \frac{\mathbf{1}}{3\kappa_s}(s_\alpha - s_{\alpha,n})[s_\beta + \check{s}'_\beta(p_c - p_{c,n})]\right\} \tag{2.36}$$

2.4 Representative numerical simulations

In the following, to assess the accuracy of the hyperelastic model and the performance of the finite element method proposed in previous sections we present the results of representative numerical tests. Firstly, we consider the bi-dimensional simulation of two well-known one-dimensional problems: the desaturation of a sand column and the infiltration of an almost initially dry porous layer. The obtained numerical results are compared with experimental data presented in [96] for the former test and with the semi-analytical solution of the infiltration problem proposed in [106].

Finally, the presented formulation is applied in a problem of interest for dam engineering, that is, the analysis of the effects of rapid drawdown on a reservoir bank.

In the following, a strain-independent model for the saturation degree is considered. Extensions of this numerical formulation to the more general case considered in Section 1.4.3 can be devised. However, practical applications of such an extension would require the availability of models (1.112) validated by experimental data.

We assume an isotropic response of the solid skeleton, characterized by Young modulus E_{sk}, Poisson coefficient ν_{sk} and relation (1.70) for the coupling tensor $\mathbf{b}$. Similarly, we consider an isotropic permeability, that is, the following form for (2.18)

$$\mathbf{k}_\alpha = k^{rel}_\alpha(s_\alpha)k^{sat}_\alpha\mathbf{1} \qquad \text{for} \qquad \alpha = w, g \tag{2.37}$$

where a constant value is assumed for the scalar single-phase permeability k^{sat}_α.

In all the test, the water density value $\rho_{w0} = 1000\ kg/m^3$ is assumed. We refer to [38] for the numerical treatment and application of strain-dependent models typically employed for single-phase permeability $\mathbf{k}_\alpha^{sat}$ of rock masses.

In the presented simulations, a constant atmospheric value is assumed for the gas pressure, that is, $p_g = 0$. This simplifying assumption is reasonable in many situation of interest in geomechanics. On the other hand, also the mass balance equation of the gaseous phase has to be taken into account if accurate capillary pressure distributions above the water table are required, for example in those cases where capillary pressures affect the irreversible response [22, 117]. The simplifying assumption of a constant gas pressure overcomes problems encountered in numerical simulation of the transition from full to partial saturation conditions. We refer for example to [95, 122, 149] among the many others investigating this issue.

In all these three examples plane conditions are assumed for strain and flow fields. The finite element method developed in previous sections is implemented over the mixed triangle with linear interpolation of the displacement and constant interpolation of volumetric strain and stress, that is, the so called P1/P0 three noded triangle [81]. Linear interpolations are also used for the pore pressure field and a three point Gauss quadrature rule is employed in evaluating tangent and residual terms.

The presented finite element method has been implemented in general code FEAP [138]. To assess the convergence of Newton-Raphson procedure, we set $tol = 1 \cdot 10^{-16}$ for the tolerance in the following energy criterion:

$$E^{(k+1)} := \Delta\mathbf{d}^T\mathbf{r}_m^{(k+1)} + \sum_{\gamma=w,g} \Delta\mathbf{p}_\gamma^T\mathbf{r}_\gamma^{(k+1)} < tol\, E^{(1)} \tag{2.38}$$

2.4.1 Desaturation of a sand column

In this section we consider the numerical simulation of a well known drainage test [96] considered by various researchers [66, 90, 95] to validate their numerical formulations. In the original experimental test, a fully saturated 1.00 m high vertical sand column contained in rigid and impervious lateral walls was initially characterized by uniform descending flow and zero water pressures throughout the column due to a water supply

from the top of the sample and a free drainage at the base. After instantaneous interruption of inflow at the top of the column, water outflow at column base and water pressures at different elevations were measured.

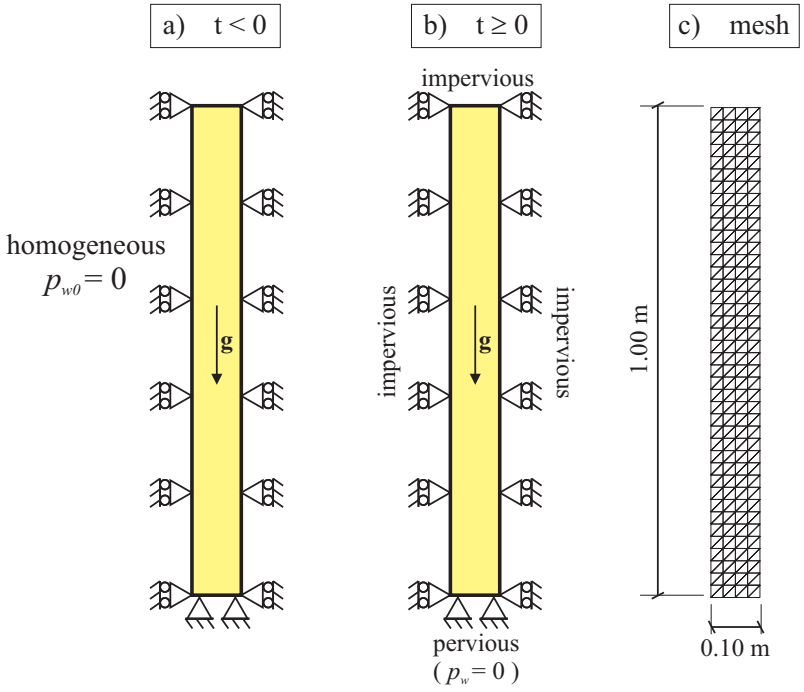

Figure 2.1: Simulation of Liakopoulos test. Configuration of the problem with assumed boundary conditions (a,b) and finite element discretization (c)

Consistently with the experimental test, we consider the boundary conditions on displacements and pore water pressures illustrated in Figure 2.1a,b. In particular, to reproduce the initial experimental conditions, we impose a homogeneous field $p_{w0} = 0$ for $t < 0$ (Fig. 2.1a). In the considered coupled setting, displacements are induced by the gravity action and the assigned initial water pressure distribution. Initial displacement are then set to zero and the calculated effective stress state is assumed as the initial one. The zero water pressure constraint imposed to the whole domain is removed at $t = 0$, with the exception of the column base which is assumed to be pervious (Fig. 2.1b).

The column is discretized with $2 \times 4 \times 40$ triangular finite elements (Fig. 2.1c). For the "Del Monte" sand used in the test, we employ the hydraulic properties listed

in Table 2.1 and the following relations proposed in [96] to model water retention and relative permeability, respectively:

$$\begin{cases} \check{s}_w(p_c) &= 1 - 1.9722 \cdot 10^{-11} p_c^{2.4279} \\ k_w^{rel}(s_w) &= 1 - 2.207(1 - s_w)^{1.0121} \end{cases} \tag{2.39}$$

for $s_w > 0.91$ and $p_c \geq 0$. The mechanical parameters listed in the same table are the ones suggested in [122].

Table 2.1: Material parameters considered in the simulation of Liakopoulos test

porous solid density	ρ	1700	kg/m^3
drained Young modulus	E_{sk}	1300	kPa
drained Poisson coefficient	ν_{sk}	0.4	
Biot coefficient	b	1.0	
solid phase volumetric stiffness	κ_s	$1.0 \cdot 10^9$	kPa
water stiffness modulus	κ_w	$2.0 \cdot 10^6$	kPa
single-phase permeability	k_w^{sat}	$4.5 \cdot 10^{-7}$	$m^2/(kPa \cdot s)$
initial porosity	n_0	0.2975	

As shown in Figure 2.2, in spite of the simplifying assumption of a constant zero value of gas pressure, the obtained numerical results are in good agreement with available experimental data, both in terms of water flow at the column base (Fig. 2.2a) and pore water pressure distribution along the sample (Fig. 2.2b).

Settlements induced by the desaturation process are reported in terms of time evolution at column top (Fig. 2.3a) and of distributions along the sample calculated at different time instants (Fig. 2.3b). The comparison reported in Figure 2.3a shows that a completely different displacement evolution is obtained under the unrealistic assumption of a fully water-saturated column.

Numerical simulations have been repeated by employing both the "continuum" (2.22_2,2.28) and the time-integration consistent (2.24–2.27,2.34) expressions of tangent

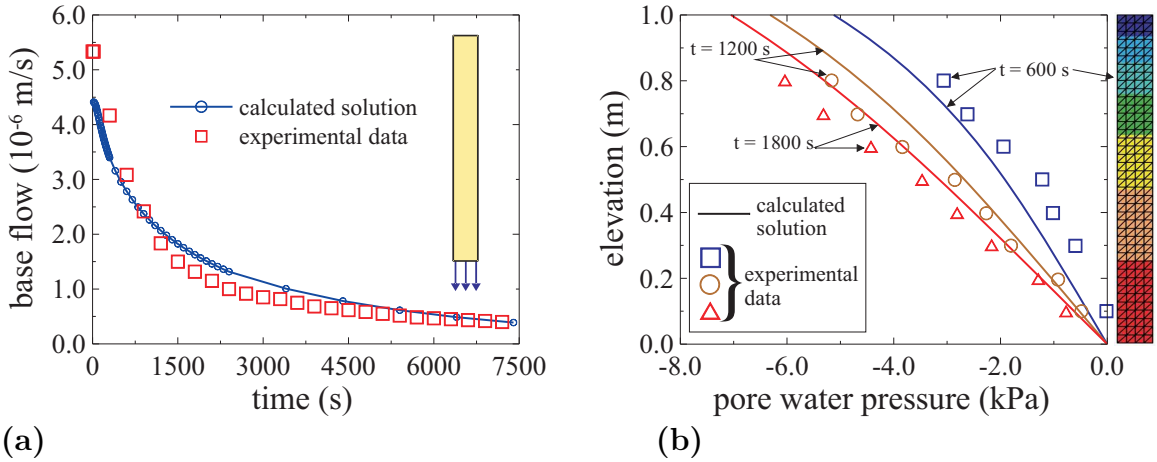

Figure 2.2: Simulation of Liakopoulos test. Comparison between measured data [96] and numerical results: a) volumetric water flow at the column base; b) pore water pressures along the column

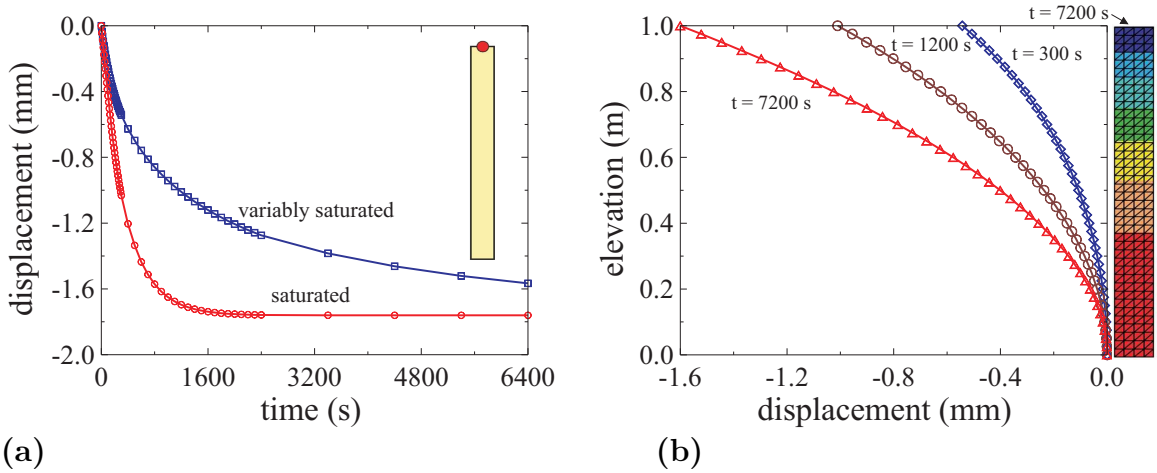

Figure 2.3: Simulation of Liakopoulos test: a) settlement evolutions calculated at column top for variably saturated and fully saturated conditions; b) settlement distributions along the column (variably saturated case)

operators. With respect to the former tangents, the consistent operators led to significant improvements in the convergence rate of adopted Newton-Raphson procedure, namely a reduction of about 33% in terms of total iteration number. As expected, we observed that such a difference between the convergence rate obtained with the two tangent sets decreases with time step size. For example, reducing by 10 the size of time steps, a 19% difference was observed in terms of total iteration number.

2.4.2 Water-pressure driven infiltration problem

For the fluid-flow part of the numerical formulation, we consider a typical benchmark test, namely the problem of water infiltration in an initially almost dry porous column. For such a test, a semi-analytical solution has been obtained by Philip [106] assuming as rigid the solid skeleton as well as the solid and the liquid phases. Due to the strongly non-linear character of the problem, this semi-analytical solution has been considered by several authors to validate their one-dimensional finite element implementations of the Richard equation, as in [43, 93]. The same uncoupled setting is then considered in our numerical simulations. So, storage modulus (1.149) reduces to component C^{sd} with constant porosity.

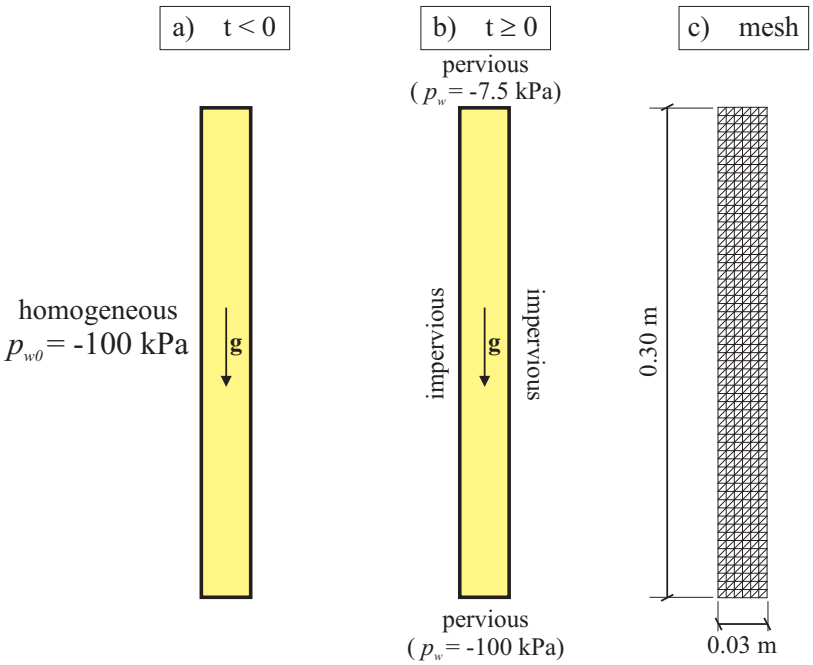

Figure 2.4: Infiltration problem. Configuration of the problem with assumed initial setting (a), boundary conditions (b) and finite element discretization (c)

To model water retention and relative permeability we employ the relations presented by van Genuchten [147] in terms of the so-called "effective saturation degree" S_w, defined as:

$$S_w := \frac{s_w - s_w^{res}}{1 - s_w^{res}} \tag{2.40}$$

that is, for $p_c \geq 0$,

$$\begin{cases} \check{s}_w(p_c) = s_w^{res} + \check{S}_w(p_c)(1 - s_w^{res}) & \text{with} \quad \check{S}_w(p_c) = \left[\dfrac{1}{1 + (a_{vg}\, p_c)^{n_{vg}}}\right]^{m_{vg}} \\ k_w^{rel}(s_w) = S_w^{1/2}\left[1 - \left(1 - S_w^{1/m_{vg}}\right)^{m_{vg}}\right]^2 & \text{with} \quad m_{vg} = 1 - 1/n_{vg} \end{cases} \tag{2.41}$$

The employed values of residual saturation degree s_w^{res} and of material constants a_{vg}, n_{vg}, as well as of other material parameters, are coincident with the ones assumed in [93] and are reported in Table 2.2.

Table 2.2: Material parameters employed to simulate the water infiltration problem

single-phase permeability	k_w^{sat}	$0.922 \cdot 10^{-5}$	$m^2/(kPa \cdot s)$
van Genuchten parameter	a_{vg}	0.335	kPa^{-1}
van Genuchten parameter	n_{vg}	2.01	
residual saturation degree	s_w^{res}	0.277	
porosity	n_0	0.368	

The geometry of problem domain and its discretization in $2 \times 6 \times 60$ triangular finite elements is shown in Figure 2.4c. As the initial condition, the homogeneous water pressure field $p_{w0} = -100\ kPa$ is imposed in the sample for $t < 0$ (Fig. 2.4a), thus obtaining from $(2.41)_1$ a initial saturation degree $s_{w0} = 0.298$ close to the residual one.

At $t = 0$, after removal of the imposed field p_{w0}, the constant water pressures $\bar{p}_{w_t} = -7.5\ kPa$ and $\bar{p}_{w_b} = -100\ kPa$ are imposed at the top and at the base of the column, respectively (Fig. 2.4b).

After first part of simulation, where 1000 time steps with $\Delta t = 1\ s$ are used, the step size is increased to $\Delta t = 10\ s$. The time step sizes considered in this work are comparable with the ones assumed by other researchers [43, 93].

The use of a lumped storage matrix avoids oscillations in computed solutions, as shown in Figure 2.5a in terms of propagation of water pressure front. In the same figure,

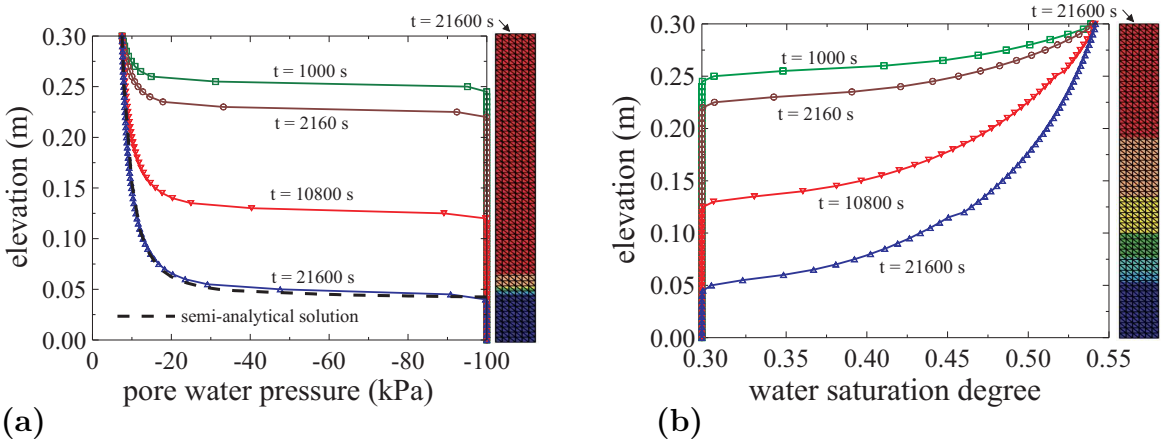

Figure 2.5: Infiltration problem: a) calculated pore water pressure distributions at different time instants and semi-analytical solution by Philip [106] at $t = 21600\ s$; b) calculated profiles of water saturation degree

we observe that numerical results are in very good agreement with the semi-analytical solution by Philip [106]. The simulated saturation process is apparent in Figure 2.5b, illustrating the distributions of water saturation degree calculated at different time instants. Calculations have been repeated by using the time discretizations of both the pore-pressure $(1.143)_2$ and the mixed (2.30) forms of fluid-mass balance. For given mesh refinement and time step size, the solutions obtained with the mass-conservative approach are significantly more accurate than the ones calculated with the former scheme. This result is shown in terms of water pressure distributions (Fig. 2.6), by comparing the semi-analytical solution with numerical results obtained for different meshes ($2\times6\times60$ and $2\times2\times20$ elements) and time discretizations (the aforementioned time stepping and a 10 times larger one).

2.4.3 Effects of rapid drawdown on a reservoir bank

In this section, the finite element method presented in Section 2.3 is applied in the analysis of a dam engineering problem, namely the evaluation of the coupled hydro-mechanical response of a 120 m high bank to rapid drawdown of reservoir water level.

Plane conditions are assumed for strain and flow. As shown in Figure 2.7, the

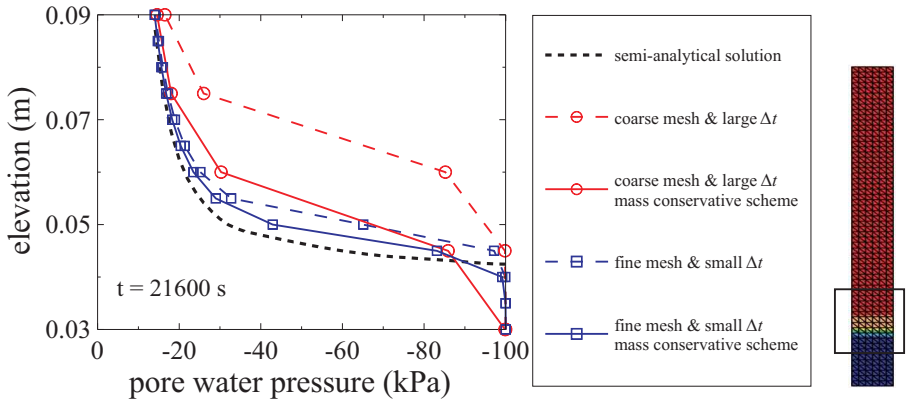

Figure 2.6: Infiltration problem. Detail of water pressure distributions near the pressure front at $t = 21600\ s$. Results obtained by means of the pore-pressure and the mixed mass-conservative schemes for different discretizations in time and space

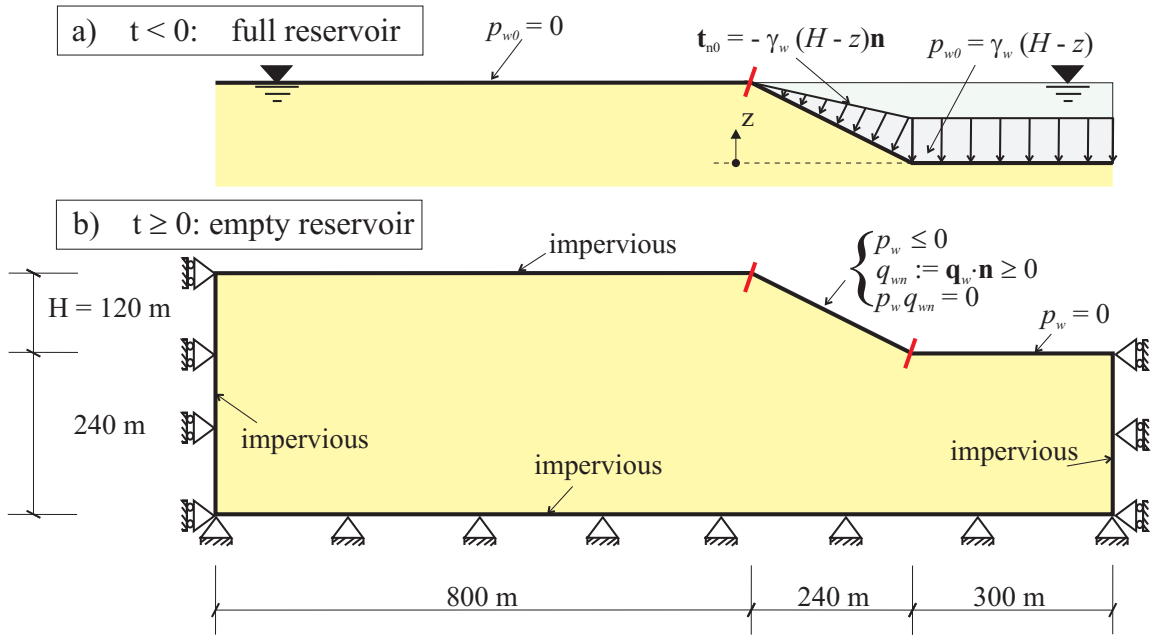

Figure 2.7: Bank response to rapid reservoir drawdown. Configuration of the problem with assumed boundary conditions. To simulate drawdown effects, pore-pressures and fluid-flow conditions on top boundaries (horizontal and sloping bank surface, reservoir bottom) are changed from configuration (a) to (b)

reservoir is full in the reference configuration, with water level coincident with bank top surface. In this initial configuration, displacements are set to zero after the attainment of the steady states of stress and pore pressure equilibrating gravity and illustrated initial boundary conditions $\bar{p}_{w0}$ and $\bar{\mathbf{t}}_0$. To simulate a rapid reservoir drawdown, at $t =$

Table 2.3: Material parameters considered in the analysis of rapid drawdown effects on a reservoir bank

porous solid density	ρ	2600	kg/m^3
drained Young modulus	E_{sk}	$4.7 \cdot 10^6$	kPa
drained Poisson coefficient	ν_{sk}	0.15	
Biot coefficient	b	0.93	
solid phase volumetric stiffness	κ_s	$1.0 \cdot 10^9$	kPa
water stiffness modulus	κ_w	$2.0 \cdot 10^6$	kPa
single-phase permeability	k_w^{sat}	$7 \cdot 10^{-8}$	$m^2/(kPa \cdot s)$
van Genuchten parameter	a_{vg}	0.1	kPa^{-1}
van Genuchten parameter	n_{vg}	2.2	
residual saturation degree	s_w^{res}	0.01	
initial porosity	n_0	0.02	

0 we instantaneously change the boundary conditions as shown in Figure 2.7, including zero boundary tractions, impervious bank top surface and pervious reservoir bottom. For the bank sloping boundary, intersected by the phreatic surface (i.e. the locus of $p_w = 0$ points) after reservoir drawdown, unilateral constraints are imposed on flow in order to simulate the two different boundary conditions, impervious and pervious, to be assigned above and below the phreatic surface, respectively. We refer to Chapter 3 for full detail on the theoretical formulation and finite element implementation of such unilateral boundary conditions.

The adopted material parameters, reported in Table 2.3, are representative of a "fair quality" fractured rock mass. We note that the employed values of hydraulic parameters and model $(2.41)_1$ assumed for water retention can lead to very narrow capillary fringes compared with the characteristic dimension of the problem, that is, to the calculation of low values of saturation degree immediately above the phreatic surface. In other words, above the phreatic surface, localized gradients are to be expected in the saturation degree distribution and, in view of assumed model $(2.41)_2$,

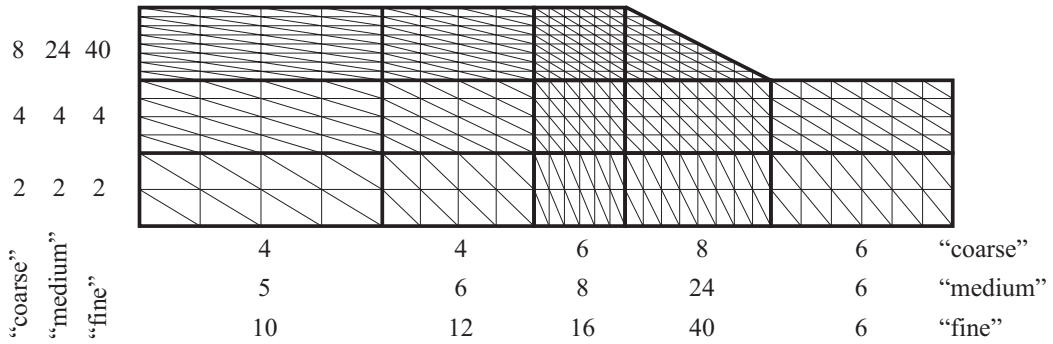

Figure 2.8: Bank response to rapid reservoir drawdown. Number of vertical and horizontal divisions defining the three finite element meshes used in simulations

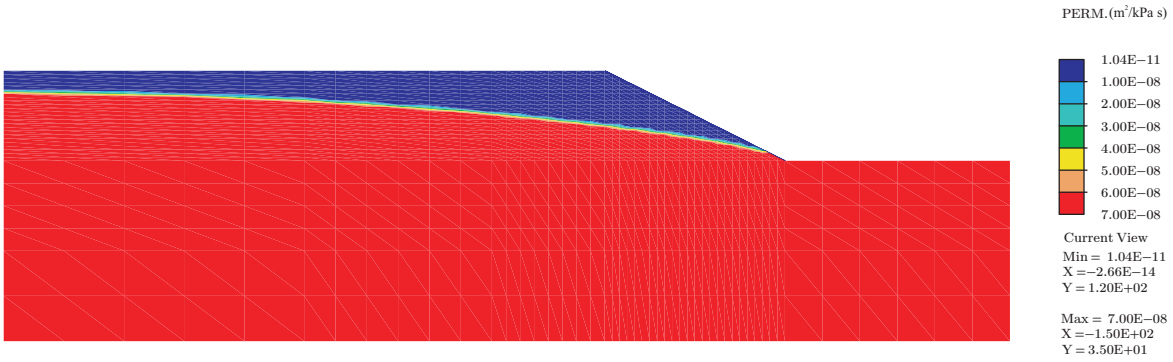

(a)

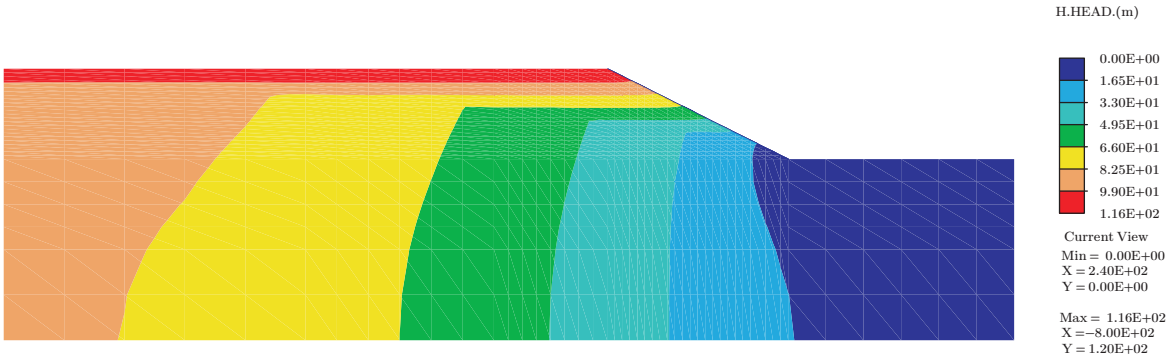

(b)

Figure 2.9: Bank response to rapid reservoir drawdown. Distributions of water permeability (a) and piezometric head (b) calculated at $t = 200$ days with the medium mesh

especially in the relative permeability field. The eventual presence of such non-smooth solutions makes the considered problem setting a severe test for the proposed finite element formulation.

To investigate this issue, computations have been repeated for three different spatial discretizations, illustrated in Figure 2.8 and named in the following as "coarse", "medium" and "fine" mesh, respectively.

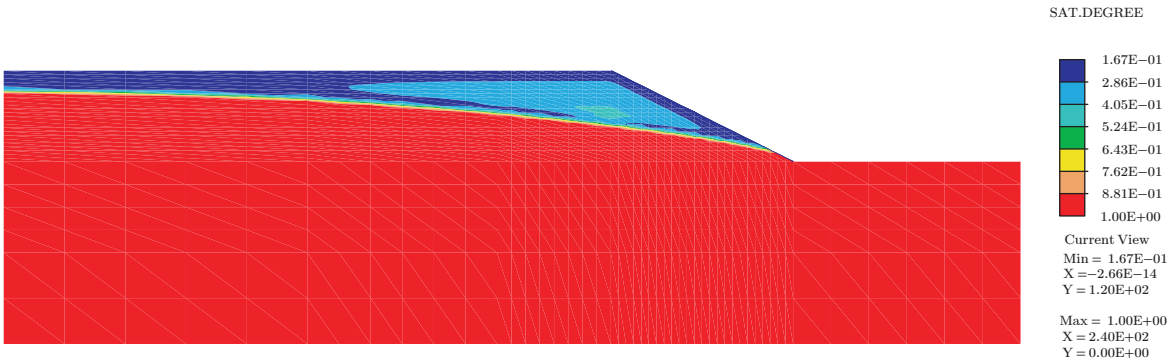

(a)

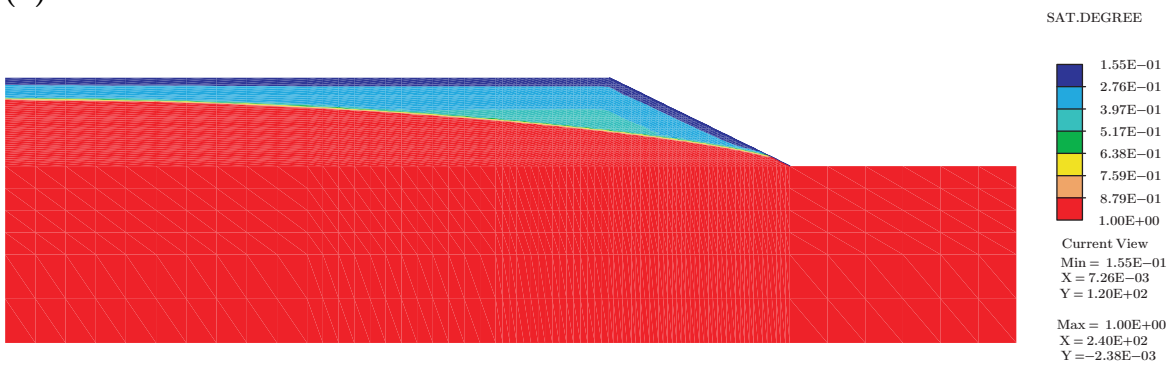

(b)

Figure 2.10: Bank response to rapid reservoir drawdown. Distributions of water saturation degree calculated at $t = 200$ days with the medium (a) and the fine mesh (b)

As expected, a localized gradient of water permeability is calculated at the phreatic surface (Fig. 2.9a) and the corresponding water-flow field is practically discontinuous across this surface, as shown by the contour plot of piezometric head (Fig. 2.9b). From the different patterns of this piezometric head field calculated above and below the phreatic surface, it can be inferred a vertically descendent flow and a seepage oriented towards the reservoir, respectively.

In spite of some slight oscillations in the neighborhood of the phreatic surface, saturation degree distributions (Fig. 2.10) and the positive part of capillary pressure fields (Figs. 2.11,2.12a) calculated with the medium discretization are practically coincident

with fine mesh results.

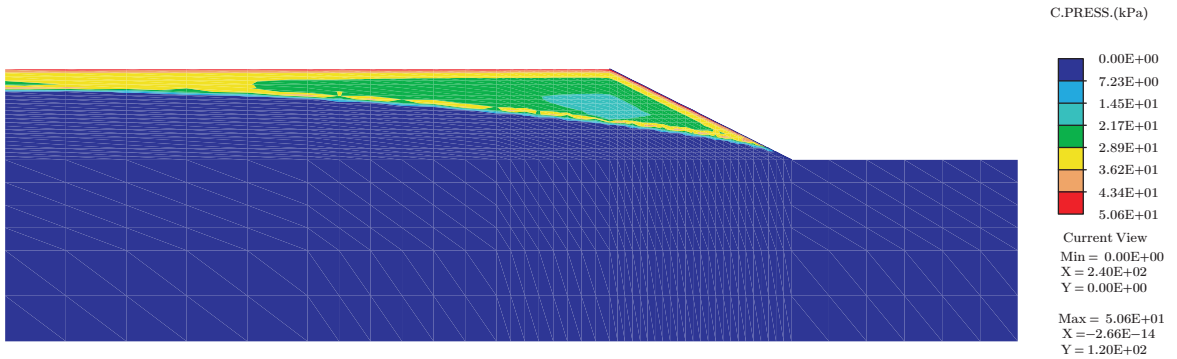

(a)

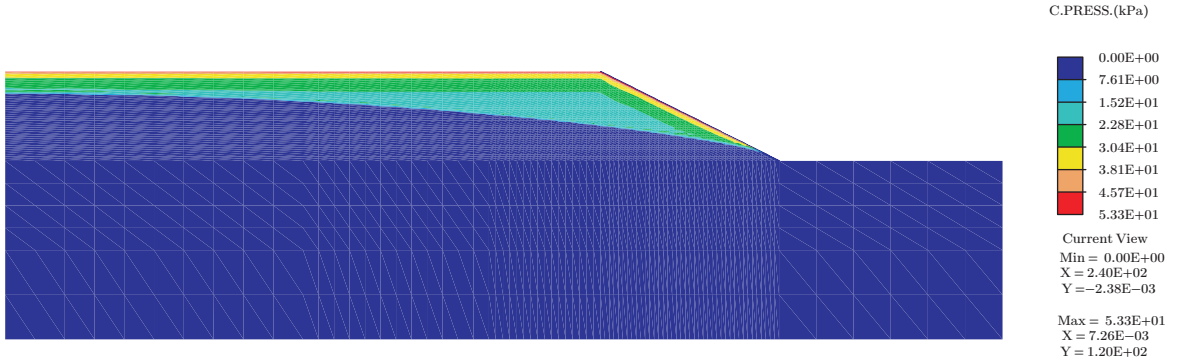

(b)

Figure 2.11: Bank response to rapid reservoir drawdown. Distributions of positive part of capillary pressure $\langle p_c \rangle$ calculated at $t = 200$ days with the medium (a) and the fine mesh (b)

On the other hand, the coarse discretization show difficulties in capturing the capillary pressure distribution (Fig. 2.12a). However, as shown in Figure 2.12b, no significant difference is apparent between the displacement fields calculated with the three different meshes. To explain this latter result, it can be observed that the differences between capillary pressure profiles above the phreatic surface (Fig. 2.12a) are negligible with respect to water pressure changes calculated in the whole domain. Furthermore, in view of the employed effective stress equation, the coupled effects of capillary pressure are significantly reduced by the low values of saturation degree calculated immediately above the phreatic surface (Fig. 2.10). Effects of inaccurate computation of capillary pressure on displacements can be significant if capillary-pressure dependent elasto-plastic model are considered, as in [124, 125, 126].

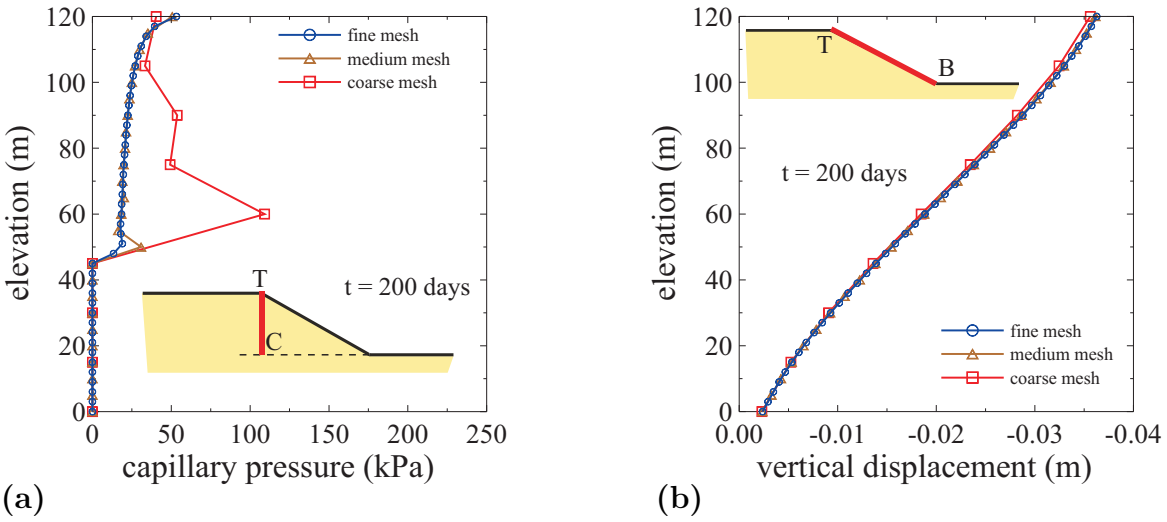

Figure 2.12: Bank response to rapid reservoir drawdown. Results calculated at $t = 200$ days with the three considered meshes in terms of: a) positive part of the capillary pressures $\langle p_c \rangle$ along vertical CT; b) settlements along sloping surface BT

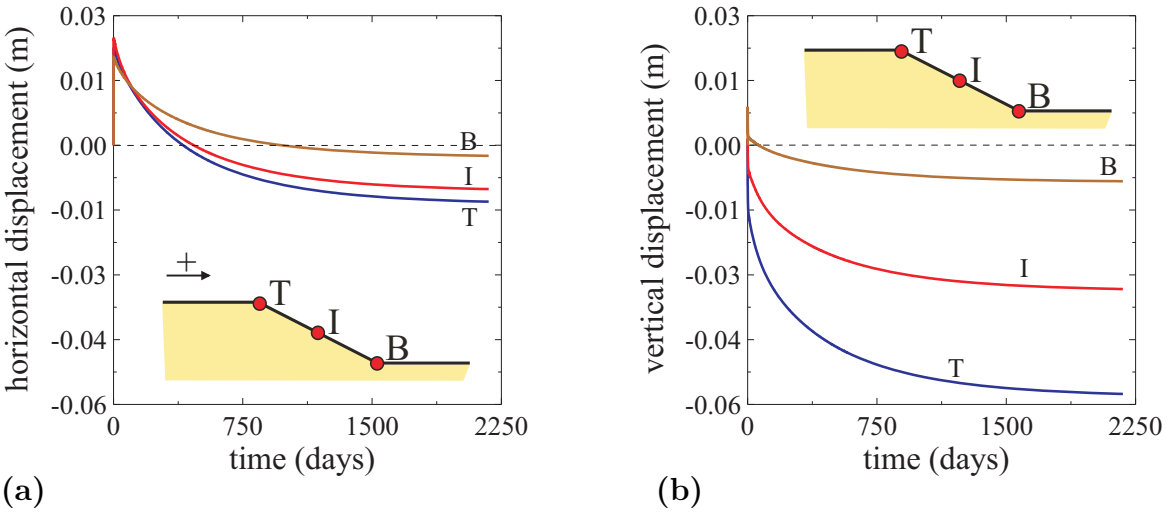

Figure 2.13: Bank response to rapid reservoir drawdown. Time evolution of horizontal (a) and vertical (b) displacements at points B, I, T on the bank sloping surface obtained with the medium mesh

In the initial response to instantaneous drawdown, horizontal displacements of the sloping bank surface are oriented towards the reservoir (Fig. 2.13a) and some heaving of the bottom of the lake is observed (~ 0.5 cm at point B in Fig. 2.13b). Such effects of the undrained removal of water surface loads ($\mathbf{t}_{n0}$ in Fig. 2.7) are then immediately followed by opposite displacement increments (Fig. 2.13) due to progressive decrease

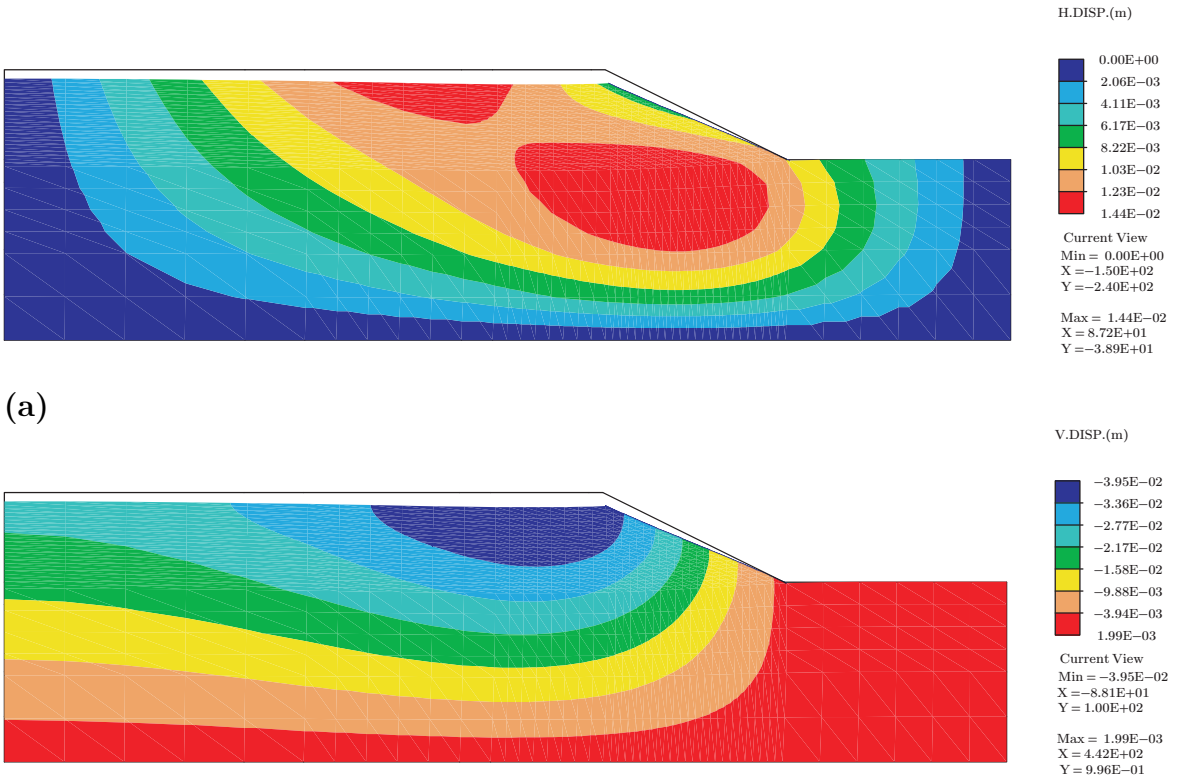

Figure 2.14: Bank response to rapid reservoir drawdown. Distributions of horizontal (a) and vertical (b) displacements reported on deformed mesh with outline of the undeformed mesh (displacement amplification factor = 500). Results calculated at $t = 200$ days with the medium mesh

of pore water pressures and to seepage driving forces under the phreatic surface. The displacement field calculated after 200 days is illustrated in Figure 2.14.

3

Unilateral boundary conditions for unsaturated flow

3.1 Introduction

In porous solid mechanics there is often the need to deal with unconfined seepage problems as, for instance, in stability analyses of dam abutments and reservoir banks during reservoir operations as well as of slopes during rainfall events or of underground openings below a water table. The problem of modelling fluid flow through porous media can then be studied as a free boundary one or introducing the hypothesis of partial saturation.

In the first approach the fluid flow domain is the portion Ω_{sat} saturated by the liquid phase below the free surface Γ (Fig. 3.1) and the portion above it is assumed to be completely dry. The position of the free surface is *a priori* unknown and, in transient problems, evolves with time. Moreover, this surface is a portion of the domain boundary, i.e. $\Gamma \subset \partial\Omega_{sat}$, thus leading to a free boundary problem.

A rigorous mathematical treatment of a particular case, the well-known "dam problem", began with the fundamental work of Baiocchi [15], where steady conditions were considered. In particular, a function defined in the whole domain Ω was introduced to reduce the free boundary problem in a variational inequality. This approach was also

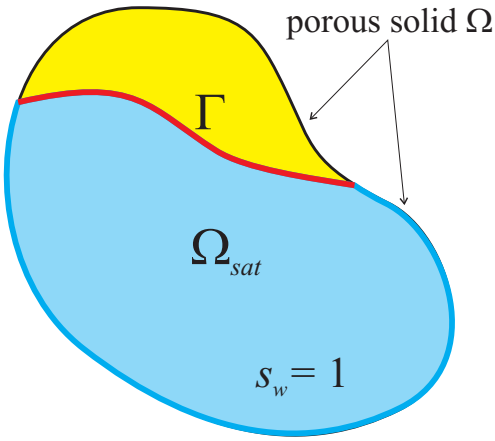

Figure 3.1: Fluid flow in porous solids: free-boundary approach [30]

applied for a similar problem involving unsteady conditions in [142]. In this framework, boundary conditions prescribed on the free surface are not included explicitly in the formulation: once the problem is solved, such a surface can be located according to some conditions. In later works, Baiocchi and co-workers obtained numerical solutions by means of finite difference and finite element methods. A comprehensive review of these works can be found in [26], together with several application problems solved by means of successive over-relaxation methods. The Baiocchi method is not the unique way to solve unconfined fluid flow problems by variational inequalities and it can be used only for dam problems with regular geometry. A possible way to overcome this shortcoming is the "extended pressure" approach introduced by Brezis et al. [25], where negative pore pressures are considered in the dry domain and the permeability tensor is multiplied by the Heaviside step function, thus leading to a null flow in the dry domain. Existence and uniqueness of the solution have been demonstrated considering a penalized problem, where the Heaviside step function has been replaced by a penalized regularization, thus reducing the original variational inequality in a penalized variational equality. The solution of such a penalized problem converges to the variational inequality one as the penalty parameter tends to zero. Therefore, a finite element approximation of the penalized problem has been considered. With respect to the numerical formulations of the Baiocchi approach, such method leads to a better approximation of the free surface and this is the reason of its widespread use, e.g. in

[24, 88]. A further application can be also found in [155], where the regularization of the Heaviside step function is introduced only to avoid numerical instabilities and the variational inequality structure is kept in the numerical solution too.

The previously described approaches reduce a free boundary problem with unknown and/or variable domain in a fixed domain problem, at least in their numerical implementations. In the "residual flow" procedure proposed in [63] for the steady problem and extended to unsteady problems in [16, 64] the fluid flow domain is only the saturated part below the free surface also in the finite element scheme; the free surface is allowed to pass through the element and is determined iteratively.

Other methods allowing to deal only with the saturated variable domain are those involving adaptive finite element techniques, as reported, for example, in [47], or other numerical techniques allowing mesh manipulations, as in [48, 68].

As it can be noted, several numerical approaches to free boundary seepage problems try to overcome the issue of dealing with a variable domain. This task can be naturally circumvented by the second approach to unconfined fluid flow problems. In fact, if partially saturated conditions are introduced in the theoretical model [55, 95], a fluid flow can be defined in the whole porous solid $\Omega = \overline{\Omega_{sat} \cup \Omega_{uns}}$. As shown in Figure 3.2, the free surface is not a part of the domain boundary, i.e. $\Gamma \not\subset \partial\Omega$, except for the intersection points $P_1, P_2 \in \partial\Omega$. On the contrary, it can be defined as the locus where the liquid pore pressure p_w takes a prescribed value $\hat{p}_w$, e.g. the atmospheric one:

$$\Gamma := \{x \in \Omega : p_w = \hat{p}_w\} \tag{3.1}$$

The problem of the evaluation of p_w in the whole domain Ω can thus be solved without knowing the position of Γ, which can be obtained *a posteriori* in view of definition (3.1).

Several reasons can make this second approach more appealing than the first one. For example, in porous solids the transition zone from a saturated region to an almost dry one is often more a fringe than a line, with a thickness depending on granulometric characteristics [127]. The simplification introduced by a free boundary approach is reasonable, for example, if the fringe thickness is negligible with respect to the

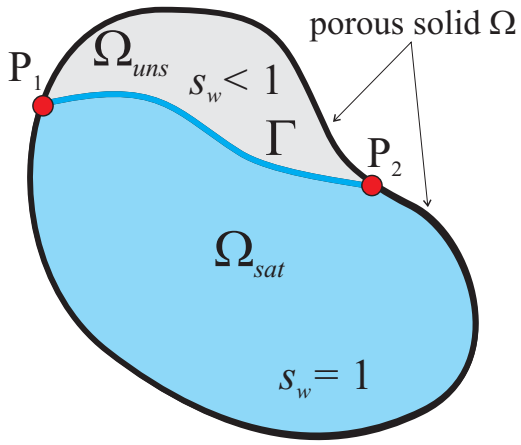

Figure 3.2: Fluid flow in porous solids: "partial saturation" approach [30]

characteristic size of the problem. If it is not the case, partially saturation effects cannot be neglected and the pore pressure field is to be evaluated also in the partially saturated region. Moreover, partial saturation approaches are normally simpler to implement than free boundary problems, as numerical solutions of unconfined fluid flow are needed. In fact, only the position of intersection points P_1 and P_2 is a problem unknown. However, suitable boundary conditions able to deal with the *a priori* unknown position of these intersection points have to be considered. In this chapter, the main purpose is to provide a numerical approach to these boundary conditions in the framework of finite element methods with unilateral constraints. An outline is as follows. In Section 3.2, it is shown that conditions characterizing portions of the boundary in contact with atmosphere and intercepted by the free surface may change between imposed-pressure and imposed-flow types during problem evolution. These boundary conditions are then considered in the more general framework of unilateral constraints in Section 3.3. Therefore, after establishing in Section 3.4 a formal analogy with frictionless contact mechanics, two regularization techniques typically employed in contact problems, the penalty and the augmented Lagrangian methods described in Section 3.5, are also applied to the hydraulic case. As described in Section 3.6, the regularized problem is then numerically solved by the finite element method for the fluid flow problem as well as for the analogous mechanical one. In Section 3.7, we in-

vestigate numerical performance of penalty and augmented Lagrangian regularization techniques employed herein by means of simple one-dimensional numerical examples. In these examples, both the numerical and formal analogies between seepage problems with unilateral constraints and frictionless contact problems are pointed out. Hence, two-dimensional strongly non-linear transient problems of interest in environmental and civil engineering are analyzed, as the propagation of a saturation front in a porous sample and the partial saturation of a concrete gravity dam.

The main results reported in the present chapter are also presented by Abati and Callari [3].

3.2 Interface between porous solid and atmosphere

During the solution process of unsaturated seepage problems, we have to know the position of points where the boundary in contact with atmosphere is intercepted by the geometric locus of zero pore pressure. In fact, different responses are typically observed on the two boundary portions located above and below these intersection points (Fig. 3.3). If we consider, for example, the evolution of reservoir bank surfaces during a rapid drawdown depicted (Fig. 3.3), we note that interstitial pressures are lower than the atmospheric value in the upper part and an outflow is observed in the remaining portion, which is the so-called "seepage surface". The free surface is not a priori known and it evolves with time in presence of unsteady fluid flow. Hence, in the analysis of these interfaces between porous solid and atmosphere, the boundary condition to be applied may change between the two types, "imposed pressure" and "imposed flow", during problem evolution. The potentially intercepted boundary portion is denoted as the "potential seepage surface" and can be expressed by the following inequalities:

$$p_w \leq 0 \qquad q_{wn} \geq 0 \qquad p_w q_{wn} = 0 \tag{3.2}$$

with q_{wn} the normal component of fluid flow.

A more general situation takes place, for example, in stability analyses of slopes during rainfall events [143] where, due to the rainfall inflow, the free surface raises

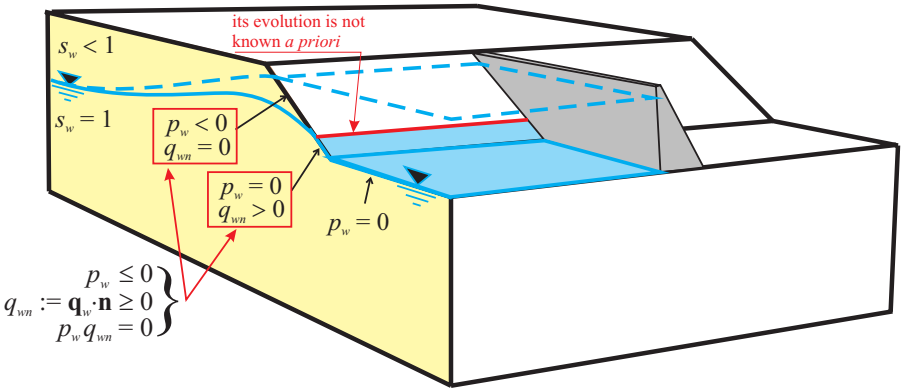

Figure 3.3: Potential seepage surface: reservoir bank after a rapid drawdown [29]

up (Fig. 3.4). The entire rainfall $\bar{q}_{wn}$ infiltrates through the slope surface if the pore pressure is lower than the atmospheric value: the boundary condition above the free surface is then an "imposed flow" one. The pore pressure can not exceed the atmospheric value, if no water ponding is allowed on the slope surface. Hence, with the attainment of atmospheric pressure, an "imposed pressure" boundary condition holds and part of the rainfall flow is returned to the environment in the portion below the free surface. This situation can be further generalized if a water ponding is allowed, thus leading to a maximum pressure $p_{w,max}$ value greater than the atmospheric one. This kind of constraint, typically indicated as the "rainfall boundary condition", can be expressed as

$$p_w \le p_{w,max} \qquad q_{wn} \ge \bar{q}_{wn} \qquad (p_w - p_{w,max})(q_{wn} - \bar{q}_{wn}) = 0 \tag{3.3}$$

Boundary conditions (3.2) and (3.3) have been implemented by means of different methods. In many variational approaches to free boundary problems, the application of the successive over-relaxation method allows to deal directly with these kind of boundary conditions. For the residual flow procedure, Desai and Li [65] proposed to model the potential seepage surface with a layer of very thin elements with a very high permeability. In partial saturation fluid flow problems, the so-called "variable" boundary conditions [83] are often employed, that is the switching between the two boundary

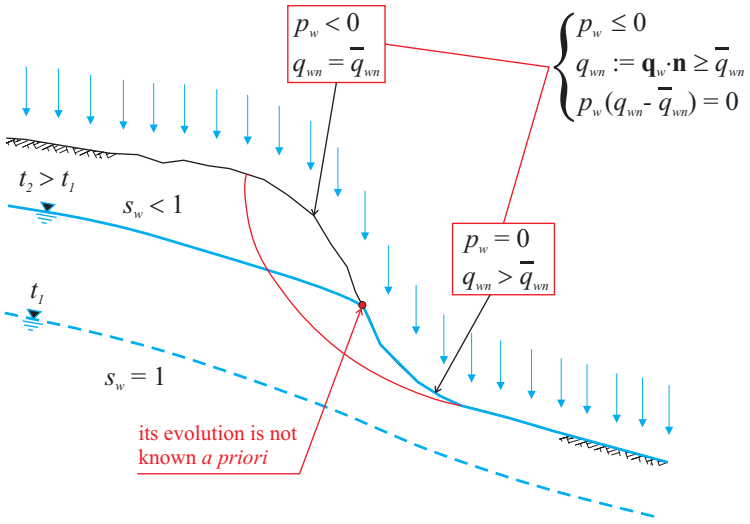

Figure 3.4: Rainfall boundary condition: stability of a slope during a rainfall event

types, imposed flow and imposed pressure, depending on the problem evolution.

In a more effective way, these boundary conditions can be considered in the more general framework of unilateral constraints, in particular for those frequent situations where large boundary regions are almost instantaneously subjected to a switch of condition type. Therefore, the explicit consideration of a Signorini type boundary condition (3.2) for the potential seepage surface recently allowed Zheng et al. [155] to keep the variational inequality structure, despite of the regularization of the Heaviside step function and thus leading to improved solutions. In the partial saturation approach, we have considered the more general rainfall boundary condition [40], where the main ideas concerning the aforementioned hydro-mechanical analogy have been introduced.

3.3 Seepage problem with unilateral constraints

In this section we consider a formulation of fluid flow through partially saturated porous continua, including unilateral boundary conditions presented in Section 3.2. We also show in detail the formal analogy with the frictionless Signorini contact problem.

For simplicity, we consider the case in which the porous space is partially saturated

by a single fluid phase. Such a formulation can be easily extended to the case of a two-phase fluid mixture, liquid plus gas, saturating the solid skeleton voids.

3.3.1 Poro-elastic model

The porous solid volume is identified by a region $\Omega \subset \mathbb{R}^{n_{\text{dim}}}$ being $n_{\text{dim}} = 1, 2$ or 3 the spatial dimension of the problem. Denoting by "$\dot{(\cdot)}$" and "$\text{div}(\cdot)$" the time derivative and the standard divergence operator, the fluid mass balance can be written in strong form as

$$\dot{M}_w = -\text{div}\, \mathbf{q}_w \qquad \text{in} \quad \Omega \tag{3.4}$$

where M_w is the fluid mass content, defined as the fluid mass per unit volume of the porous solid, and $\mathbf{q}_w$ is the fluid-mass velocity relative to solid skeleton.

Constitutive equations are employed to obtain both the fluid mass velocity $\mathbf{q}_w$ and the fluid mass content rate $\dot{M}_w$ from the interstitial fluid pressure field p_w. Namely, a generalized Darcy fluid flow law is used to describe unsaturated seepage through the porous solid in terms of the gradient "$\nabla(\cdot)$" of pore pressures:

$$\mathbf{q}_w = -\rho_{w0} k_w^{rel} \mathbf{k}_w^{sat} \left(\nabla p_w - \rho_{w0} \mathbf{g}\right) \tag{3.5}$$

where ρ_{w0} is the fluid mass density and $\mathbf{k}_w^{sat}$ is the permeability tensor characterizing the saturated porous solid. The so-called "relative" permeability coefficient k_w^{rel} is typically assumed as dependent on the saturation degree s_w, which in turn is defined as the current fluid volume per unit volume of porous space.

Following another common simplifying assumption, the saturation degree is considered as a function of the capillary pressure, which in turn is defined as $p_c := -p_w$ in the single-fluid setting.

For a deformable isotropic solid skeleton, the fluid mass content rate can be related to rates of pore pressures and strains:

$$\dot{M}_w = \rho_{w0} s_w b \dot{\varepsilon}_v + \rho_{w0} C_w \dot{p}_w \tag{3.6}$$

where $\varepsilon_v := \boldsymbol{\varepsilon} : \mathbf{1}$ is the volumetric part of solid skeleton infinitesimal strain tensor $\boldsymbol{\varepsilon}$ and $\mathbf{1}$ is the second-order identity tensor. The tangent storage modulus C_w appearing

in (3.6) can be expressed in terms of the current porosity n, defined as the void volume for unit volume of porous solid, and of the derivative s'_w of saturation degree with respect to capillary pressure p_c:

$$C_w = s_w^2 \frac{b-n}{\kappa_s} + \frac{n s_{w0}}{\kappa_w} - n s'_w \tag{3.7}$$

where s_{w0} is the initial saturation degree and κ_s, κ_w are the volumetric stiffness modulus of solid and fluid phases, respectively. Equation (3.6) is coupled to the following constitutive relation for (total) stress $\boldsymbol{\sigma}$ (see Chapter 1):

$$\dot{\boldsymbol{\sigma}} = \mathbb{C}_{sk}\dot{\boldsymbol{\varepsilon}} - s_w b \dot{p}_w \mathbf{1} \tag{3.8}$$

for the drained elastic tensor $\mathbb{C}_{sk}$. The Biot coupling coefficient appearing in (3.6-3.8) reads

$$b = 1 - \frac{\kappa_{sk}}{\kappa_s} \tag{3.9}$$

with κ_{sk} the volumetric stiffness modulus of solid skeleton. We refer to Chapter 1 and references therein for an extension of such a model to the case of two fluid phases saturating the porous space. Furthermore, a non isotropic solid skeleton and saturation degrees depending also on strains are considered in Chapter 1.

In some applications, an acceptable approximation of the pore pressure field can be evaluated by means of an uncoupled approach, assuming a vanishing total stress rate in volumetric part of constitutive equation (3.8). With this assumption, the volumetric strain rate of solid skeleton can be expressed just in terms of the pore pressure rate:

$$\dot{\varepsilon}_v = \frac{s_w b}{\kappa_{sk}} \dot{p}_w \tag{3.10}$$

which, in turn, is substituted in (3.6), leading to

$$\dot{M}_w = \rho_{w0} \underbrace{\left(C_w + \frac{s_w^2 b^2}{\kappa_{sk}} \right)}_{=: C^*_{w,k}} \dot{p}_w \tag{3.11}$$

If oedometric conditions are assumed, expressions formally identical to (3.10) and (3.11) are obtained for volumetric strain and fluid-mass content rates, that is, respectively:

$$\dot{\varepsilon}_v = \frac{s_w b}{E_{ed,sk}} \dot{p}_w \qquad\qquad \dot{M}_w = \rho_{w0} \underbrace{\left(C_w + \frac{s_w^2 b^2}{E_{ed,sk}} \right)}_{=: C^*_{w,ed}} \dot{p}_w \tag{3.12}$$

with $E_{ed,sk}$ the oedometric modulus of the solid skeleton. If fully saturated conditions and a rigid solid phase are assumed, that is $s_w = 1$ and $1/\kappa_s = 0$, fluid-mass content rate expression $(3.12)_2$ reduces to the well-known relation proposed in [84].

We recall that (3.11) and $(3.12)_2$ provide exact evaluation of fluid mass content rate in some particular coupled cases, including the classical Terzaghi's one-dimensional consolidation, and more generally represented by that oedometric problems where only changes in hydraulic boundary conditions are applied. In these problems, in fact, pore pressures can be calculated by means of (3.4-3.5) and the solid skeleton strain is obtained from combination with equations (3.12). For simplicity, only the fluid problem is considered in the rest of this chapter. In fact, boundary conditions presented in Section 3.2 affect only the fluid flow. Therefore, the equations governing the problem evolution are the fluid mass balance (3.4), the generalized Darcy law (3.5) and the constitutive equation $(3.12)_2$ for the fluid mass content rate in the Jacob form. Application examples of unilateral boundary conditions on fluid flow to fully coupled problems are presented in Chapters 2 and 4.

3.3.2 Unilateral boundary conditions

Standard conditions on fluid pressure or flow are prescribed at disjoint portions $\partial_p\Omega$ and $\partial_q\Omega$ of the porous solid boundary $\partial\Omega$, that is, respectively:

$$\begin{aligned} p_w &= \hat{p}_w \qquad \text{on} \qquad \partial_p\Omega \\ q_{wn} &= \hat{q}_{wn} \qquad \text{on} \qquad \partial_q\Omega \end{aligned} \tag{3.13}$$

for the flow normal component $q_{wn} := \mathbf{q}_w \cdot \mathbf{n}$ with $\mathbf{n}$ the outward unit normal to the domain boundary $\partial\Omega$. In addition, we consider also a boundary portion $\partial_c\Omega$, such that:

$$\begin{aligned} &\partial\Omega = \overline{\partial_p\Omega \cup \partial_q\Omega \cup \partial_c\Omega} \\ &\partial_p\Omega \cap \partial_q\Omega = \partial_q\Omega \cap \partial_c\Omega = \partial_c\Omega \cap \partial_p\Omega = \emptyset \end{aligned} \tag{3.14}$$

where a normal inflow $\bar{q}_{wn}$ is prescribed if the pore pressure is less than a maximum prescribed value $p_{w,max}$. On the contrary, an outflow is returned to the environment

as the pore pressure attains the limit value $p_{w,max}$. These requirements on $\partial_c\Omega$ can be effectively expressed by means of the following complementarity conditions

$$\left.\begin{array}{rcl} g & := & \rho_{w0}\,(p_w - p_{w,max}) \leq 0 \\ \lambda & := & q_{wn} - \bar{q}_{wn} \geq 0 \\ \lambda g & = & 0 \end{array}\right\} \quad \text{on} \quad \partial_c\Omega \tag{3.15}$$

in terms of the pore pressure "gap" g and of the runoff flow λ. We remark that a potential seepage surface can be effectively modelled by setting $p_{w,max} = 0$ and $\bar{q}_{wn} = 0$ in unilateral boundary conditions (3.15), as schematically illustrated in Figure 3.5.

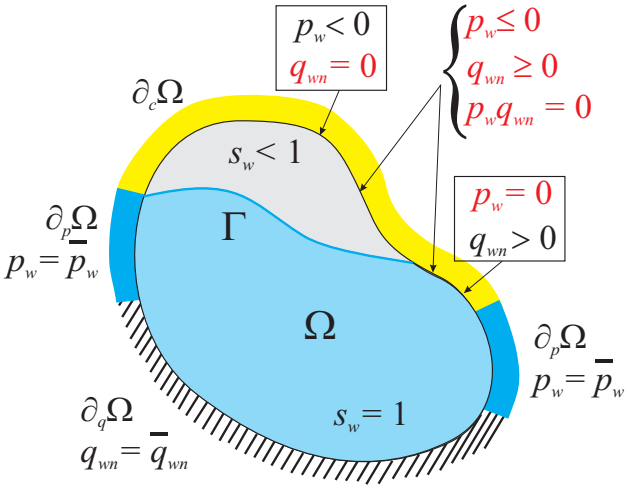

Figure 3.5: Bilateral and unilateral boundary conditions in the hydraulic seepage problem

The weak form of fluid mass balance (3.4) takes the form

$$\int_\Omega \dot{M}_w \delta p_w \, d\Omega = \int_\Omega \mathbf{q}_w \cdot \nabla \delta p_w \, d\Omega - \int_{\partial\Omega} q_{wn} \delta p_w \, dA \tag{3.16}$$

for all admissible variations $\delta p_w \in \mathcal{V}_p$, with

$$\mathcal{V}_p := \{\delta p_w : \Omega \to \mathbb{R} : \delta p_w = 0 \quad \text{on} \quad \partial_p\Omega\} \tag{3.17}$$

As a consequence of standard boundary conditions (3.13) and gap definition $(3.15)_1$, the weak balance (3.16) can be rewritten as

$$\int_\Omega \dot{M}_w \delta p_w \, d\Omega = \int_\Omega \mathbf{q}_w \cdot \nabla \delta p_w \, d\Omega - \int_{\partial_q\Omega} \hat{q}_{wn} \delta p_w \, dA - \int_{\partial_c\Omega} \frac{q_{wn}}{\rho_{w0}} \delta g \, dA \tag{3.18}$$

for all $\delta p_w \in \mathcal{V}_p$ and where δg, due to the gap definition $(3.15)_1$, takes the form

$$\delta g = \rho_{w0} \delta p_w \tag{3.19}$$

After substitution of runoff flow definition $(3.15)_2$, the preceding weak balance reads:

$$\begin{aligned} \int_\Omega \dot{M}_w \delta p_w \, d\Omega \;\; = \;\; & \int_\Omega \mathbf{q}_w \cdot \nabla \delta p_w \, d\Omega - \int_{\partial_q \Omega} \hat{q}_{wn} \delta p_w \, dA - \\ & - \int_{\partial_c \Omega} \frac{\bar{q}_{wn}}{\rho_{w0}} \delta g \, dA - \int_{\partial_c \Omega} \frac{\lambda}{\rho_{w0}} \delta g \, dA \end{aligned} \tag{3.20}$$

for all $\delta p_w \in \mathcal{V}_p$.

3.4 A formally identical mechanical problem: the Signorini contact

In this section, we consider the problem of frictionless contact of an elastic body against a rigid obstacle. In particular, it will be noted how complementarity conditions describing contacts are formally identical to (3.15). In the contact problem, the field equation is represented by the quasi-static linear momentum balance:

$$\operatorname{div} \boldsymbol{\sigma} + \mathbf{f} = \mathbf{0} \tag{3.21}$$

where $\boldsymbol{\sigma}$ is the Cauchy stress tensor (positive for the tensile case) and $\mathbf{f}$ is the volume force vector. Standard conditions on displacements $\mathbf{u}$ or normal stresses are prescribed at disjoint portions $\partial_u \Omega$ and $\partial_t \Omega$ of the solid boundary $\partial \Omega$, that is, respectively:

$$\begin{aligned} \mathbf{u} &= \hat{\mathbf{u}} \qquad \text{on} \qquad \partial_u \Omega \\ \boldsymbol{\sigma} \mathbf{n} &= \hat{\mathbf{t}} \qquad \text{on} \qquad \partial_t \Omega \end{aligned} \tag{3.22}$$

A non-linear hyperelastic model can be assumed:

$$\dot{\boldsymbol{\sigma}} = \frac{\partial^2 \psi}{\partial \boldsymbol{\varepsilon}^2} \, \dot{\boldsymbol{\varepsilon}} = \mathbb{C} \, \dot{\boldsymbol{\varepsilon}} \tag{3.23}$$

for the Helmholtz free energy ψ, the elastic tangent tensor $\mathbb{C}$ and the infinitesimal deformation tensor $\boldsymbol{\varepsilon} = \nabla^s \mathbf{u}$.

For the frictionless contact against a rigid obstacle, we consider a boundary portion $\partial_c\Omega$, such that:

$$\begin{aligned} &\partial\Omega = \overline{\partial_u\Omega \cup \partial_t\Omega \cup \partial_c\Omega} \\ &\partial_u\Omega \cap \partial_t\Omega = \partial_t\Omega \cap \partial_c\Omega = \partial_c\Omega \cap \partial_u\Omega = \emptyset \end{aligned} \tag{3.24}$$

On this portion, the gap can be defined [92, 151] as the (negative) distance between a point on the potential contact surface $\partial_c\Omega$ and the closest point on the rigid body (Fig. 3.6). The compression on $\partial_c\Omega$, given by

$$t_n := -\boldsymbol{\sigma}\mathbf{n} \cdot \mathbf{n} \tag{3.25}$$

is equal to the prescribed value $\bar{t}_n$ as far as the point in not in contact with the rigid obstacle and then the gap is negative. On the other hand, as contact is attained, the gap is zero and the compression t_n raises up due to the obstacle reaction. These requirements on $\partial_c\Omega$ can be effectively expressed by means of the following complementarity conditions

$$\left.\begin{array}{rcl} g & := & g_0 + \mathbf{u}\cdot\mathbf{n} \leq 0 \\ \lambda & := & t_n + \bar{t}_n \geq 0 \\ \lambda g & = & 0 \end{array}\right\} \quad \text{on} \quad \partial_c\Omega \tag{3.26}$$

where the particular form of the current value of the gap g in terms of displacement field $\mathbf{u}$, initial value g_0 and outward normal $\mathbf{n}$ to surface $\partial_c\Omega$ has been obtained in the infinitesimal deformation range [86]. We note that the positive sign in the definition of the compression surplus λ is due to the opposite conventions used to define t_n and $\hat{t}_n$ ($\bar{t}_n$), that is, (3.25) and $(3.22)_2$, respectively.

It can be noted how unilateral boundary conditions characterizing the frictionless contact against a rigid obstacle are formally identical to the ones introduced in the hydraulic problem, described by complementarity conditions (3.15).

The weak form of the linear momentum balance taking into account unilateral constraints in frictionless contacts reads

$$\begin{aligned} \int_\Omega \boldsymbol{\sigma} : \nabla^s(\delta\mathbf{u})\, d\Omega \;=\; & \int_\Omega \mathbf{f}\cdot\delta\mathbf{u}\, d\Omega + \int_{\partial_t\Omega} \hat{\mathbf{t}}\cdot\delta\mathbf{u}\, dA + \\ & + \int_{\partial_c\Omega} \bar{t}_n\delta g\, dA - \int_{\partial_c\Omega} \lambda\delta g\, dA \end{aligned} \tag{3.27}$$

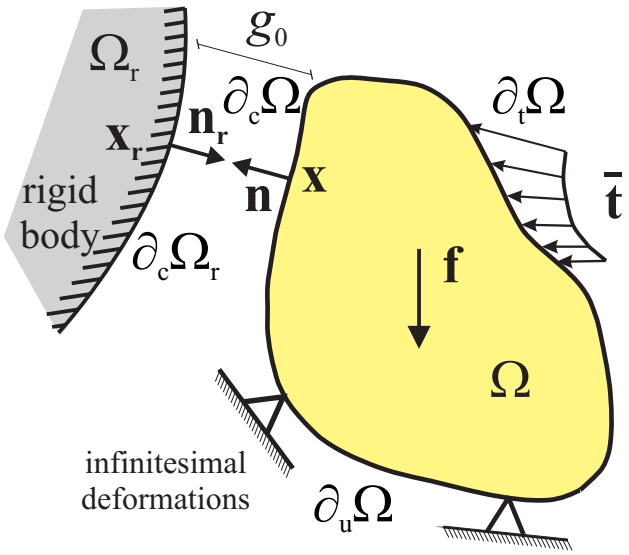

Figure 3.6: Bilateral and unilateral boundary conditions in the mechanical Signorini problem

for all admissible variations in the displacement field $\delta\mathbf{u} \in \mathcal{V}_u$ where

$$\mathcal{V}_u = \{\delta\mathbf{u} : \Omega \to \mathbb{R}^{n_{\text{dim}}} : \delta\mathbf{u} = \mathbf{0} \quad \text{on} \quad \partial_u\Omega\} \tag{3.28}$$

and with

$$\delta g = \delta\mathbf{u} \cdot \mathbf{n} \tag{3.29}$$

Remark 3.1 *It can be argued that, to obtain a mechanical problem formally identical to the hydraulic one presented in Section 3.3, time should appear explicitly in the linear momentum balance (3.21), thus leading to a parabolic problem. This result could be easily obtained by replacing the hyperelastic model (3.23) with a visco-elastic one. However, the formal analogy of interest in this work concerns the unilateral boundary conditions, not the model. Furthermore, the previously described hydraulic parabolic problem reduces to an elliptic one formally identical to its mechanical counterpart if we assume as incompressible the solid skeleton and both the solid and fluid phases.*

3.5 Numerical regularization techniques

Several numerical techniques can be employed to treat unilateral constraints expressed by complementarity conditions (3.15) and (3.26) for hydraulic and mechanical prob-

lems, respectively. In a finite element formulation, the solution on each node subjected to a unilateral constraint can be obtained iteratively, by means of a switch between imposed pressure (displacement) and flow (traction) type boundary conditions. This algorithm performs well with linear problems but for non-linear problems it may not be stable, failing to converge, especially when the number of nodes simultaneously subjected to this numerical switch becomes very high [111]. However, for seepage problems through unsaturated porous continua, this approach is commonly used and implemented in the so-called "variable boundary conditions" [83].

As an alternative, we consider two techniques typically employed in contact mechanics: the penalty and the augmented Lagrangian methods [92, 151]. Furthermore, in the following sections, we present a physical interpretation of the application of these two techniques for the hydraulic problem considered herein, comparing it with the well-known interpretation of the same techniques in the contact problem.

3.5.1 Penalty method

The penalty method is the simplest way to regularize complementarity conditions: constraints $(3.15)_2$ and $(3.26)_2$ are both satisfied by imposing

$$\lambda = \kappa\langle g\rangle \tag{3.30}$$

where κ is a positive coefficient and "$\langle\cdot\rangle$" is the classical Macaulay operator returning the positive part of $(\cdot)$. In view of (3.30), we can observe that conditions $(3.15)_1$ and $(3.15)_3$ for the hydraulic problem and $(3.26)_1$ and $(3.26)_3$ for the mechanical problem are not in general satisfied. It can also be shown that the constraint violation decreases as the penalty coefficient increases. Complementarity conditions are hence fulfilled only in the limit for $\kappa \to \infty$ (Fig. 3.7). However, only a finite value of κ can be set in a numerical solution and it is well known that a high value of the penalty coefficient can lead to numerical problems as ill-conditioning and reaction inaccuracy. However, this method is widely used, especially for those problems where accuracy is not a primary concern. We refer to [86] for numerical application of this technique in the mechanical framework.

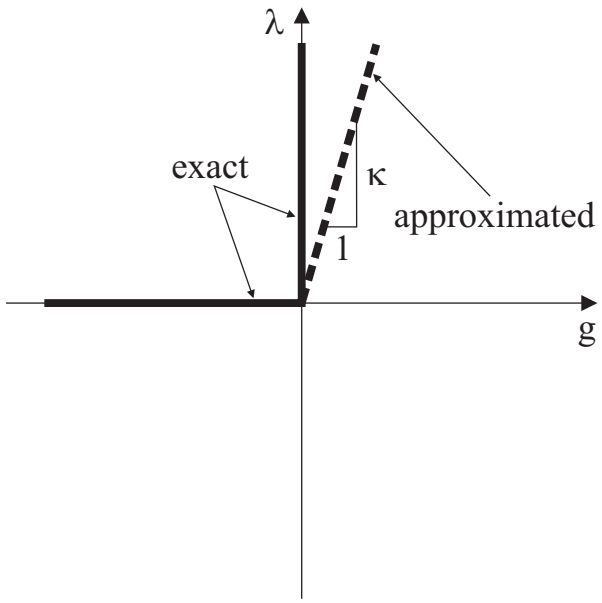

Figure 3.7: Schematic representation of complementarity condition and of its penalty regularization

We recall the physical interpretation of this method for the contact problem: the rigid obstacle is substituted with a very stiff non-linear spring that, as contact is attained, allows a small penetration. For the hydraulic problem, equation (3.30) can be viewed as a (non-linear) Darcy law governing the flow through a zero-thickness interface with a "surface" permeability κ. Increasing the permeability of this surface reduces the values of pore pressures exceeding the maximum prescribed value

3.5.2 Augmented Lagrangian method

The augmented Lagrangian method was firstly introduced to solve general constrained optimization problems by Hestenes [78] and Powell [108]. It was successively applied to frictionless contact in [152]. This method can be viewed as a compromise between Lagrange multipliers and penalization of constraint violations. A very simple numerical implementation of the augmented Lagrangian method is the Uzawa algorithm [13], where the problem solution is achieved iteratively: being m the Uzawa iteration counter, hydraulic and mechanical problems are solved taking $\lambda^{(m)}$ fixed in (3.20) and

(3.27), respectively. The multiplier value is then locally updated setting

$$\lambda^{(m+1)} = \langle \lambda^{(m)} + \kappa g^{(m)} \rangle \tag{3.31}$$

This procedure continues until achievement of convergence, established in terms of λ or g [92].

As in the penalty method, complementarity conditions (3.15) and (3.26) are fulfilled in the limit, but for $m \to \infty$, not for $\kappa \to \infty$. In this way, a finite value of κ does not compromise constraint violation, thus circumventing the penalty method shortcomings. The number of Uzawa iterations decreases for increasing κ. However, improvements with respect to the penalty method become less remarkable for increasing κ.

For the mechanical problem, the physical interpretation of the Uzawa procedure is quite simple. In the first step, the problem is solved as in the penalty method, thus obtaining a penetration $g^{(1)}$. By imposing $\lambda^{(1)} = 0$, penalty method provides a first estimate of the multiplier, that can be iteratively refined by the update (3.31). The Uzawa update (3.31) can be viewed as the application of a force $\lambda^{(2)} = \langle \kappa g^{(1)} \rangle$ to the spring; this force reduces the penetration in the rigid obstacle to $g^{(2)} < g^{(1)}$. A new force $\lambda^{(3)} = \langle \lambda^{(2)} + \kappa g^{(2)} \rangle$ is then applied to the spring, further reducing the penetration, and the procedure continues until convergence is reached. In the hydraulic problem, every single Uzawa update can be viewed as the extraction of an outflow through the boundary portion $\partial_c \Omega$ that iteratively reduces the excess pore pressure stored in a boundary surface of permeability κ.

3.6 Finite element formulation

In this section finite element methods for the hydraulic and the mechanical problems described in Sections 3.3 and 3.4, respectively, are developed. The attention is focused on nodal terms taking into account unilateral constraints by means of penalty and augmented Lagrangian methods.

3.6.1 Seepage problem

Isoparametric interpolations are employed to approximate pore pressures p_w at a point $\mathbf{x}$ of a generic finite element Ω_e, that is:

$$p_{w_e}(\mathbf{x}) = \mathbf{N}_e(\mathbf{x})\mathbf{p}_e \tag{3.32}$$

where $\mathbf{N}_e(\mathbf{x})$ is the shape function matrix used to interpolate nodal pore pressures $\mathbf{p}_{w_e}$. Approximation of pore pressure gradient is based on a standard gradient operator $\mathbf{B}_e := \nabla\mathbf{N}_e$, that is:

$$\nabla p_{w_e} = \mathbf{B}_e\mathbf{p}_e \tag{3.33}$$

An ordinary differential system is obtained by using interpolations (3.32) and (3.33) in the finite-element discretization of fluid mass balance (3.20). This system is written in residual algebraic form for the generic time step $[t_n, t_{n+1}]$, with the rate equation of fluid-mass balance approximated by a backward-Euler scheme. Denoting by $\Delta t = t_{n+1} - t_n$ the time increment and omitting index $n+1$ to simplify the notation, the residual system reads:

$$\mathbf{r}_w = \mathbf{f}_w^{ext} + \mathbf{f}_{w,c} - \mathop{\mathbf{A}}_{e=1}^{n_{\text{el}}} \left[\int_{\Omega_e} \mathbf{N}_e^T \frac{M_w - M_{w,n}}{\Delta t}\, d\Omega - \int_{\Omega_e} \mathbf{B}_e^T \mathbf{q}_w\, d\Omega \right] = \mathbf{0} \tag{3.34}$$

where

$$\mathbf{f}_w^{ext} = \mathbf{s}_w - \mathop{\mathbf{A}}_{e=1}^{n_{\text{el}}} \left[\int_{\partial\Omega_e \cap \partial_q\Omega} \mathbf{N}_e^T \hat{q}_{wn}\, dA + \int_{\partial\Omega_e \cap \partial_c\Omega} \mathbf{N}_e^T \bar{q}_{wn}\, dA \right] \tag{3.35}$$

is the external hydraulic load vector, with $\mathbf{s}_w$ the concentrated source vector, and

$$\mathbf{f}_{w,c} = -\mathop{\mathbf{A}}_{e=1}^{n_{\text{el}}} \int_{\partial_c\Omega_e} \mathbf{N}_e^T \lambda\, dA \tag{3.36}$$

is the runoff outflow vector on $\partial_c\Omega_e := \partial\Omega_e \cap \partial_c\Omega$, that is, the portion of the element boundary subjected to the unilateral constraint.

The algebraic system (3.34) is strongly non-linear, due not only to the unilateral constraint term (3.36), but also to the generalized Darcy law (3.5) and storage modulus (3.7). Therefore, a Newton-Raphson iterative procedure can be used, where the increments $\Delta(\cdot) = (\cdot)_{n+1}^{(k+1)} - (\cdot)_{n+1}^{(k)}$ of unknown nodal variables at t_{n+1}, are evaluated

at iteration $(k+1)$ by means of the following linearized form of the solving system:

$$\mathbf{r}_w^{(k)} = -\left(\frac{\partial \mathbf{r}_w}{\partial \mathbf{p}}\right)^{(k)} \Delta \mathbf{p} \tag{3.37}$$

By means of the approximated form of the generalized Darcy law

$$\mathbf{q}_w = -\rho_{w0} k_w^{rel} \mathbf{k}_w^{sat} \left(\mathbf{B}_e \mathbf{p}_e - \rho_{w0} \mathbf{g}\right) \tag{3.38}$$

and the interpolations (3.32) and (3.33), the application of the chain rule to the residual equation (3.34) allows us to rewrite the linearized solving system (3.37) as

$$\mathbf{r}_w^{(k)} = \left(\frac{\mathbf{S}}{\Delta t} - \mathbf{G} + \tilde{\mathbf{H}}\right)^{(k)} \Delta \mathbf{p} \tag{3.39}$$

where $\mathbf{S}$, the global storage matrix, is defined as

$$\mathbf{S} = \mathop{\mathbf{A}}_{e=1}^{n_{\text{el}}} \int_{\Omega_e} \mathbf{N}_e^T \frac{\partial M_w}{\partial p_w} \mathbf{N}_e \, d\Omega \tag{3.40}$$

operator $\mathbf{G}$, resulting from the linearization of relative permeability coefficient k_w^{rel} with respect to pore pressure p_w, takes the form

$$\mathbf{G} = \mathop{\mathbf{A}}_{e=1}^{n_{\text{el}}} \int_{\Omega_e} \mathbf{B}_e^T \frac{\partial k_w^{rel}}{\partial p_w} \mathbf{k}_w^{sat} \mathbf{q}_w^{uni} \mathbf{N}_e \, d\Omega \tag{3.41}$$

with

$$\mathbf{q}_w^{uni} := -\rho_{w0} (\mathbf{B}_e \mathbf{p}_e - \rho_{w0} \mathbf{g}) \tag{3.42}$$

and operator $\tilde{\mathbf{H}}$ is given by

$$\tilde{\mathbf{H}} = \mathbf{H} + \mathbf{P}_w \tag{3.43}$$

where $\mathbf{H}$ is the standard global permeability matrix, that is,

$$\mathbf{H} = \mathop{\mathbf{A}}_{e=1}^{n_{\text{el}}} \int_{\Omega_e} \rho_{w0} \mathbf{B}_e^T k_w^{rel} \mathbf{k}_w^{sat} \mathbf{B}_e \, d\Omega \tag{3.44}$$

and $\mathbf{P}_w$ is a further operator due to linearization of the non-linear unilateral term (3.36):

$$\mathbf{P}_w = \mathop{\mathbf{A}}_{e=1}^{n_{\text{el}}} \int_{\partial_c \Omega_e} \mathbf{N}_e^T \frac{\partial \lambda}{\partial p_w} \mathbf{N}_e \, d\Omega \tag{3.45}$$

Remark 3.2 *Fluid mass content derivative with respect to pore pressure in the global storage matrix (3.40) must be consistent with the time-integrated form of (3.11) or (3.12)$_2$ used in the residual (3.34). In order to avoid oscillatory solutions, a lumped storage matrix should be used, in particular for very small time increments. Moreover, in the time-integrated form of (3.11) or (3.12)$_2$, expression $\dot{s}_w$ should be preferred to $s'_w\dot{p}_c$, thus limiting mass balance errors. For details about these considerations, see Chapter 2 and references cited therein.*

In the developments that follow, the attention is focused on the linearization of the extra term due to the unilateral constraint, thus providing an explicit form for the operator $\mathbf{P}_w$, depending on which one of the regularization techniques described in Section 3.5 is employed.

Penalty method linearization

By means of substitution of runoff flow expression (3.30), vector (3.36) reads

$$\mathbf{f}_{w,c} = -\kappa \mathop{\mathbf{A}}_{e=1}^{n_{\text{el}}} \int_{\partial_c\Omega_e} \mathbf{N}_e^T \langle g \rangle \, dA \tag{3.46}$$

The derivative of runoff flow (3.30) with respect to the pore pressure can be easily obtained from gap definition (3.15)$_1$:

$$\frac{\partial \lambda}{\partial p_w} = \frac{\partial \lambda}{\partial g}\frac{\partial g}{\partial p_w} = \kappa \rho_{w0} H(g) \tag{3.47}$$

where "$H(\cdot)$" is the Heaviside function, returning 1 when $(\cdot)$ is positive, 0 otherwise. This expression allows us to rewrite explicitly the linearization operator (3.45) as

$$\mathbf{P}_w = \kappa \mathop{\mathbf{A}}_{e=1}^{n_{\text{el}}} \int_{\partial_c\Omega_e} \rho_{w0} H(g) \mathbf{N}_e^T \mathbf{N}_e \, d\Omega \tag{3.48}$$

Augmented Lagrangian method linearization

Two nested iterative schemes are needed when the augmented Lagrangian method is implemented. In fact, as pointed out in Section 3.5.2, the non-linear problem is solved by means of the Newton-Raphson iterative procedure taking the runoff flow $\lambda^{(m)}$ fixed.

The update (3.31) is performed and, with the new value $\lambda^{(m+1)}$, the non-linear problem is solved again.

Now, taking the Uzawa iteration counter m as fixed and omitting the Newton-Raphson iteration counter k, the runoff flow vector (3.36), in view of (3.31), takes the form

$$\mathbf{f}_{w,c}^{(m)} = -\mathop{\mathbf{A}}_{e=1}^{n_{\text{el}}} \int_{\partial_c\Omega_e} \mathbf{N}_e^T \langle \lambda^{(m)} + \kappa g^{(m)} \rangle \, dA \tag{3.49}$$

By means of the gap definition $(3.15)_1$, the derivative of the runoff flow $\lambda^{(m+1)}$ with respect to the pore pressure $p_w^{(m)}$ takes the form

$$\frac{\partial \lambda^{(m+1)}}{\partial p_w^{(m)}} = \kappa \rho_{w0} H(\lambda^{(m)} + \kappa g^{(m)}) \tag{3.50}$$

that, substituted in the linearization operator (3.45), leads to

$$\mathbf{P}_w^{(m)} = \kappa \mathop{\mathbf{A}}_{e=1}^{n_{\text{el}}} \int_{\partial_c\Omega_e} \rho_{w0} H(\lambda^{(m)} + \kappa g^{(m)}) \mathbf{N}_e^T \mathbf{N}_e \, d\Omega \tag{3.51}$$

3.6.2 Contact problem

In the mechanical counterpart of the seepage problem considered in previous section, the same isoparametric interpolation is employed to approximate displacement $\mathbf{u}$, i.e.:

$$\mathbf{u}_e(\mathbf{x}) = \mathbf{N}_e(\mathbf{x}) \mathbf{d}_e \tag{3.52}$$

and the strain approximation is achieved by means of a mixed B-bar [81] operator:

$$\boldsymbol{\varepsilon}_e = \bar{\mathbf{B}}_e \mathbf{d}_e \tag{3.53}$$

Substitution of interpolations (3.52) and (3.53) in the linear momentum balance (3.27) leads to the following residual algebraic system:

$$\mathbf{r}_m = \mathbf{f}_m^{ext} + \mathbf{f}_{m,c} - \mathop{\mathbf{A}}_{e=1}^{n_{\text{el}}} \int_{\Omega_e} \bar{\mathbf{B}}_e^T \boldsymbol{\sigma} \, d\Omega = \mathbf{0} \tag{3.54}$$

where

$$\mathbf{f}_m^{ext} = \mathbf{s}_m + \mathop{\mathbf{A}}_{e=1}^{n_{\text{el}}} \left[\int_{\Omega_e} \mathbf{N}_e^T \mathbf{f} \, d\Omega + \int_{\partial\Omega_e \cap \partial_t\Omega} \mathbf{N}_e^T \hat{\mathbf{t}} \, dA + \int_{\partial_c\Omega_e} \mathbf{N}_e^T \bar{t}_n \mathbf{n}_e \, dA \right] \tag{3.55}$$

is the external mechanical load vector, with $\mathbf{s}_m$ the vector of nodal loads, and

$$\mathbf{f}_{m,c} = -\mathop{\mathbf{A}}_{e=1}^{n_{\text{el}}} \int_{\partial_c\Omega_e} \mathbf{N}_e^T \lambda \mathbf{n}_e \, dA \tag{3.56}$$

is the compression surplus vector.

Remark 3.3 *It can be easily shown how the hydraulic problem is quite simpler then its mechanical counterpart: in fact, comparing gap definitions (3.15)$_1$ and (3.26)$_2$ and concentrated terms (3.36) and (3.56), we may note that only scalar quantities are involved in the hydraulic problem. On the contrary, in the contact problem, an important role is played by the numerical treatment of geometrical arguments.*

A Newton-Raphson procedure may be used to solve the algebraic system (3.54), where non-linearities are due to the contact term (3.56) and to the non-linear elastic model (3.23), leading to

$$\mathbf{r}_m^{(k)} = -\left(\frac{\partial \mathbf{r}_m}{\partial \mathbf{d}}\right)^{(k)} \Delta\mathbf{d} \tag{3.57}$$

The discretized form of the non-linear elastic relation (3.23) can be obtained by means of substitution of strain approximation (3.53), thus leading to

$$\dot{\boldsymbol{\sigma}} = \mathbb{C}\bar{\mathbf{B}}_e\dot{\mathbf{d}}_e = \frac{\partial \boldsymbol{\sigma}}{\partial \mathbf{d}_e}\dot{\mathbf{d}}_e \tag{3.58}$$

that, substituted in the residual (3.54), allows to rewrite the linearized system (3.57) as

$$\mathbf{r}_m^{(k)} = \tilde{\mathbf{K}}^{(k)}\Delta\mathbf{d} \tag{3.59}$$

with

$$\tilde{\mathbf{K}} = \mathbf{K} + \mathbf{P}_m \tag{3.60}$$

where

$$\mathbf{K} = \mathop{\mathbf{A}}_{e=1}^{n_{\text{el}}} \int_{\Omega_e} \bar{\mathbf{B}}_e^T \mathbb{C}\bar{\mathbf{B}}_e \, d\Omega \tag{3.61}$$

is the standard tangent stiffness global matrix, and

$$\mathbf{P}_m = \mathop{\mathbf{A}}_{e=1}^{n_{\text{el}}} \int_{\partial_c\Omega_e} \mathbf{N}_e^T \frac{\partial}{\partial \mathbf{u}}(\lambda \mathbf{n}_e)\mathbf{N}_e \, d\Omega \tag{3.62}$$

is a linearization operator due to the unilateral term (3.56). In the linearization operator (3.62), $\mathbf{n}_e$ is the vector normal to $\partial_c\Omega$.

Penalty method linearization

Substitution of the compression surplus (3.30) in vector (3.56) leads to

$$\mathbf{f}_{m,c} = -\kappa \mathop{\mathbf{A}}_{e=1}^{n_{\text{el}}} \int_{\partial_c \Omega_e} \mathbf{N}_e^T \langle g \rangle \mathbf{n}_e \, dA \tag{3.63}$$

by means of the gap definition $(3.26)_1$ the derivative of the compression surplus $\lambda \mathbf{n}_e$ with respect to the displacement $\mathbf{u}$ reads

$$\frac{\partial}{\partial \mathbf{u}}(\lambda \mathbf{n}_e) = \frac{\partial}{\partial g}(\lambda \mathbf{n}_e)\frac{\partial g}{\partial \mathbf{u}} = \kappa H(g)(\mathbf{n}_e \otimes \mathbf{n}_e) \tag{3.64}$$

thus leading to the following explicit expression for the linearization operator (3.62):

$$\mathbf{P}_m = \kappa \mathop{\mathbf{A}}_{e=1}^{n_{\text{el}}} \int_{\partial_c \Omega_e} H(g) \mathbf{N}_e^T (\mathbf{n}_e \otimes \mathbf{n}_e) \mathbf{N}_e \, d\Omega \tag{3.65}$$

Augmented Lagrangian method linearization

Substitution of the compression surplus (3.31) in vector (3.56) leads to

$$\mathbf{f}_{m,c}^{(m)} = -\mathop{\mathbf{A}}_{e=1}^{n_{\text{el}}} \int_{\partial_c \Omega_e} \mathbf{N}_e^T \langle \lambda^{(m)} + \kappa g^{(m)} \rangle \mathbf{n}_e \, dA \tag{3.66}$$

by means of the gap definition $(3.26)_1$, the derivative of the compression surplus $\lambda^{(m+1)} \mathbf{n}_e$ with respect to the displacement $\mathbf{u}^{(m)}$, reads

$$\frac{\partial}{\partial \mathbf{u}^{(m)}}(\lambda^{(m+1)} \mathbf{n}_e) = \kappa H(\lambda^{(m)} + \kappa g^{(m)})(\mathbf{n}_e \otimes \mathbf{n}_e) \tag{3.67}$$

that, substituted in linearization operator (3.62), gives

$$\mathbf{P}_m^{(m)} = \kappa \mathop{\mathbf{A}}_{e=1}^{n_{\text{el}}} \int_{\partial_c \Omega_e} H(\lambda^{(m)} + \kappa g^{(m)}) \mathbf{N}_e^T (\mathbf{n}_e \otimes \mathbf{n}_e) \mathbf{N}_e \, d\Omega \tag{3.68}$$

3.7 Representative numerical simulations

In this section, numerical examples performed by means of the finite element formulation presented in Section 3.6 are considered. Firstly, two simple one-dimensional problems are analyzed. The main goal is to assess the analogy between hydraulic and

mechanical problems in terms of penalty and augmented Lagrangian algorithm performance. Linear interpolation on one-dimensional elements is considered both for the pore-pressures and the displacements, with one Gauss quadrature point.

The problem of infiltration into a partially saturated porous layer is then considered, as an example of application of unilateral boundary condition to model the so-called "rainfall boundary condition". Finally, partial saturation of a concrete gravity dam during reservoir operations is analyzed, focusing the attention on the drainage system in the dam body, modelled by means of proposed unilateral boundary constraints. In both problems, we employ bi-dimensional three-node triangles with linear interpolation of pore-pressure and three Gauss quadrature points. These last two numerical tests are performed by means of the penalty method implementation of unilateral boundary conditions in a two-node linear element, which is then connected to boundary $\partial\Omega_c$ of the porous solid. In these elements, a two-node Newton-Cotes/Lobatto quadrature rule is considered in order to avoid an oscillatory pressure profile on the interface. The same quadrature rule is typically employed for interface elements in mechanical problems [74, 118].

3.7.1 One-dimensional mechanical and hydraulic examples

In this section, two formally equivalent one-dimensional problems are considered: the contact of a linear elastic truss against a rigid obstacle and the infiltration into a saturated soil column. The main goal is to compare the numerical performances of penalty and augmented Lagrangian methods observed in the numerical simulation of both the problems.

The analytical solution of these problems is employed here to estimate accuracy in the reaction calculated by numerical methods. In the contact problem illustrated in Figure 3.8a we consider a steel truss with $L = 2\,m$, clamped at one end and loaded by a concentrated force $F = 2 \cdot 10^3\,kN$. Initially, the loaded end is distant $|g_0| = 10^{-3}\,m$ from a rigid obstacle. We assume $E = 2 \cdot 10^8\,kPa$ for the Young modulus and $A = 1.3 \cdot 10^{-2}\,m^2$ for the a cross area. With this setting, the applied load is greater than

the maximum traction allowed by the initial gap g_0 and effectively loading the truss, that is,

$$N = -|g_0|\frac{EA}{L} \tag{3.69}$$

We note that N is negative, consistently with definition (3.25) of normal stresses on the contact surface. The compression surplus due to rigid obstacle reaction is

$$R_v = N + F \tag{3.70}$$

which can be compared with its general expression $(3.26)_2$.

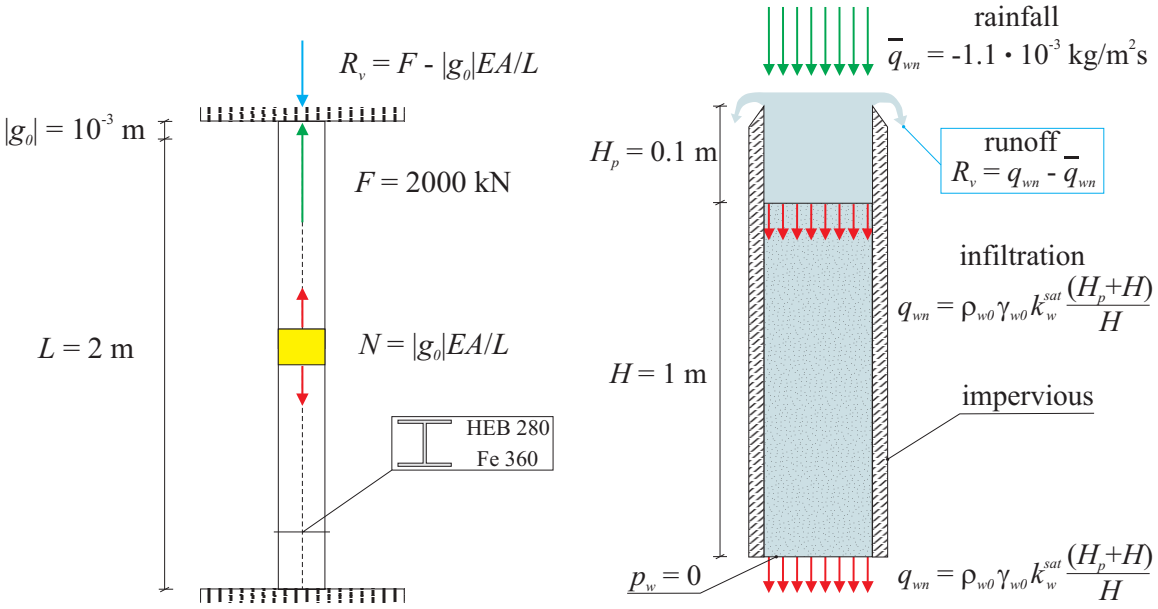

Figure 3.8: One-dimensional linear problems: frictionless contact of an elastic truss against a rigid obstacle (a) and infiltration into a saturated soil column (b)

A formally equivalent hydraulic problem is shown in Figure 3.8b. A porous column $H = 1\,m$ high is contained in a cylinder of height $H + H_p = 1.1\,m$, with impervious lateral surface and draining base. The water inflow $\bar{q}_{wn} = -1.1 \times 10^{-3}\,kg/(m^2 s)$ is prescribed at the top surface. Solid skeleton, solid and liquid phases are assumed to be incompressible. Therefore, in the hydraulic equation, time contributions vanish, thus leading to an elliptic problem. Moreover, if the full saturation hypothesis holds, the permeability tensor does not depend on the pore pressure. The solving system (3.39) takes then a form similar to the mechanical one (3.59), as storage and fluid linearization

operators disappear. The only non linear term is due to the unilateral constraint. As in the contact problem, the applied load is greater than the maximum allowed one. In fact, the water ponding on the top surface of the soil column is limited by the cylinder height, with a maximum pressure value $p_{w,max} = \gamma_{w0} H_p$, where γ_{w0} is unit weight of water. Therefore, the water inflow into the soil column cannot exceed the limit value

$$q_{wn} = -\rho_{w0}\gamma_{w0} k_w^{sat} \frac{H + H_p}{H} \tag{3.71}$$

If the permeability of the soil is $k_w^{sat} = 10^{-7}\, m^2/(kPa\, s)$, the absolute vale of this limit flow is lower than $|\bar{q}_{wn}|$. Hence, in order to keep $p_w = p_{w,max}$ on the top surface, a runoff outflow

$$R_v = q_{wn} - \bar{q}_{wn} \tag{3.72}$$

is returned to the external environment through the same surface.

Analytical solutions (3.69–3.72) are now employed to investigate the accuracy of numerical solutions. Denoting by λ the unilateral reaction computed by means of relations (3.30) and (3.31) adopted in penalty and augmented Lagrangian method, respectively, the error measure

$$\text{reac.err.} := \frac{|\lambda - R_v|}{R_v} \tag{3.73}$$

can be introduced. The performance of numerical methods considered herein may be assessed not only in terms of reaction accuracy, but also considering relevant quantities:

- the minimum tolerance in solution error which is admissible for the Newton-Raphson algorithm;
- the ratio between the constraint violation to the initial gap value (in the hydraulic problem we may set $g_0 = \rho_{w0} p_{w,max}$);
- the condition number

$$N_c := \|\mathbf{A}\|_p \|\mathbf{A}^{-1}\|_p \tag{3.74}$$

where "$\|\cdot\|_p$" is the norm induced by the vectorial p-norm and $\mathbf{A}$ is equal to tangent stiffness $\tilde{\mathbf{K}}$ and to permeability $\tilde{\mathbf{H}}$, for the mechanical and the hydraulic problems, respectively. In order to reduce the computational effort, the $p = 1$ norm, defined as

$$\|\mathbf{A}\|_1 = \max_{1\leq j\leq n} \sum_{i=1}^{n} |a_{ij}| \tag{3.75}$$

can be employed to estimate the condition number. All the aforementioned quantities are mutually linked. For example, it is well known how the accuracy of the solution of a linear system obtained by means of direct or iterative solvers is strongly affected by the condition number [109]. In the following, it will be shown how such interaction appears also in numerical results.

Numerical solutions are obtained by means of a uniform discretization of 100 one-dimensional linear element. Firstly, solutions obtained by means of the augmented Lagrangian algorithm are presented. In Figure 3.9 the convergence path of the Uzawa algorithm is shown; numerical results refer to two different values of the ratio of penalty coefficient κ to a characteristic stiffness, or permeability, that can be defined as

$$\kappa^* := \frac{EA}{h_e} \tag{3.76}$$

for the mechanical problem and

$$\kappa^* := \rho_{w0} \frac{k_w^{sat}}{h_e} \tag{3.77}$$

for the hydraulic problem, where h_e is the finite element size. As it can be expected, in the Uzawa algorithm the penalty coefficient plays the role of a convergence acceleration factor for the hydraulic problem (Fig. 3.9b) as well as for the mechanical one (Fig. 3.9a).

For strongly non-linear transient problems as, for example, the infiltration in partially saturated porous continua, the use of the augmented Lagrangian method could results in an unacceptable computational effort. For this reason, the numerical results of the penalty method are considered and compared with the ones obtained by Uzawa algorithm. In Figure 3.10 some quantities related to solution accuracy are plotted as functions of the penalty coefficient. In view of relation (3.30), the constraint violation

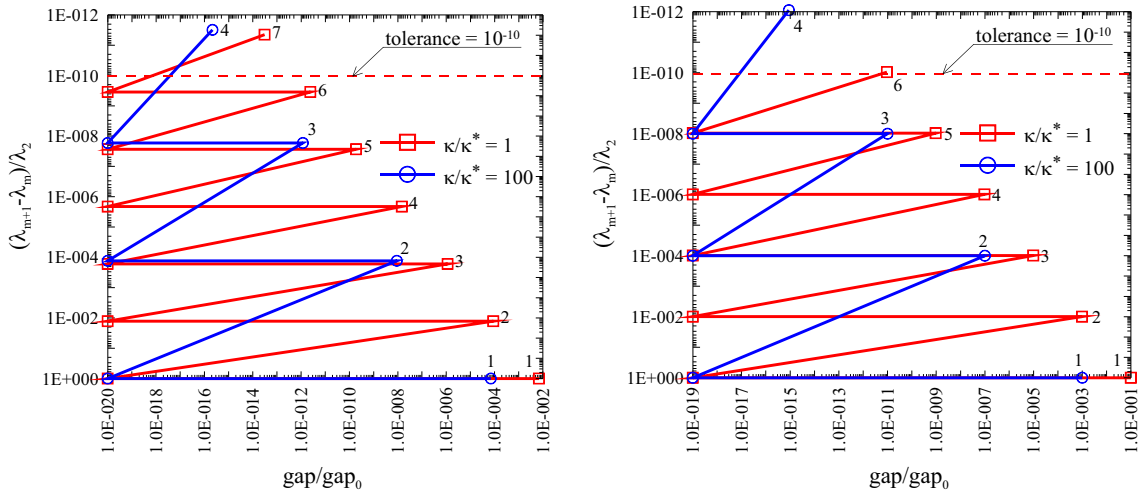

Figure 3.9: One-dimensional linear problems: Uzawa algorithm convergence path for mechanical (a) and hydraulic (b) problems

decays as the penalty coefficient increases. This is not the case of the reaction error: in fact, the condition number N_c increases when high penalty coefficients are employed, thus leading to the well known ill-conditioning issues, as, for example, an increasing minimum admissible tolerance for the Newton-Raphson algorithm. Therefore, it can be shown for the mechanical problem in Figure 3.10a, as well as for the hydraulic one in Figure 3.10b, how the reaction error decreases when the penalty coefficients increase up to an "optimal" value. Below such a value, the positive effect of an increasing accuracy in the final gap prevails on ill-conditioning issues. Above such an optimal value of the penalty coefficient, the reaction error increases, as a consequence of the precision loss due to ill-conditioning effects. The optimal penalty value can be taken approximatively equal to $10^6 \div 10^7\, \kappa^*$ for both the problems, which is consistent with penalty coefficient values recommended for penalty methods by Taylor [138] and satisfies the condition

$$\kappa \leq \frac{\kappa_{min}}{\sqrt{n_u e_r}} \tag{3.78}$$

obtained in [102] by means of an error analysis taking into account roundoff and penalty induced errors, where κ_{min} is the smallest term of the stiffness matrix, n_u is the number of unknowns (here it is $n_u = 100$) and e_r is the roundoff error ($e_r \simeq 10^{-17}$ for a double precision machine).

Finally, reaction errors obtained with penalty and augmented Lagrangian approach

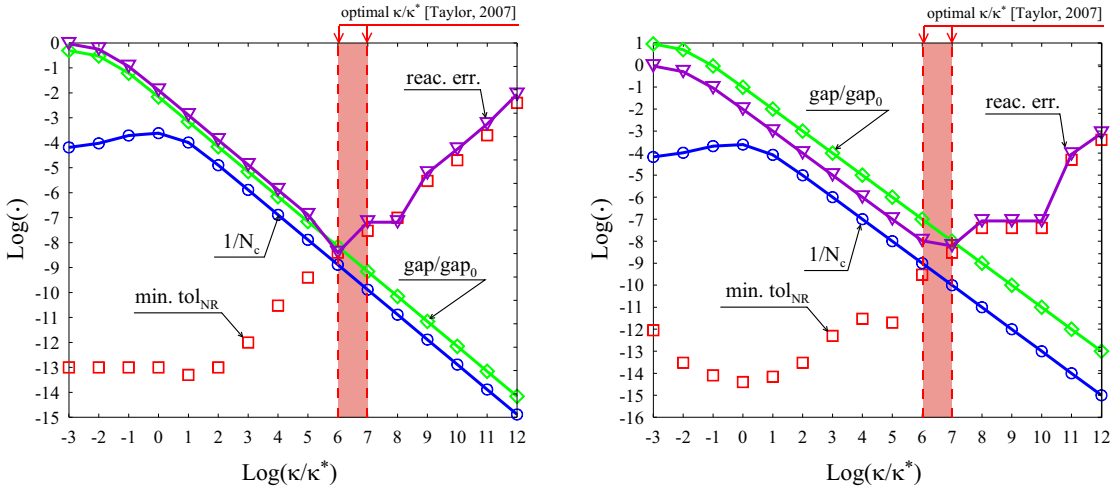

Figure 3.10: One-dimensional linear problems: penalty method performance for mechanical (a) and hydraulic (b) problems

are compared in Figure 3.11. If augmented Lagrangian does not converge at the second Uzawa iteration, the obtained reaction error is obviously smaller with respect to the penalty one. Also in the augmented Lagrangian method, the reaction error increases with the penalty coefficient. On the other hand, the Uzawa iteration number rapidly increases for very small penalty coefficients. A good compromise between reaction accuracy and convergence rate is $\kappa = 10^1 \div 10^3\,\kappa^*$, as indicated in [138] for many problems.

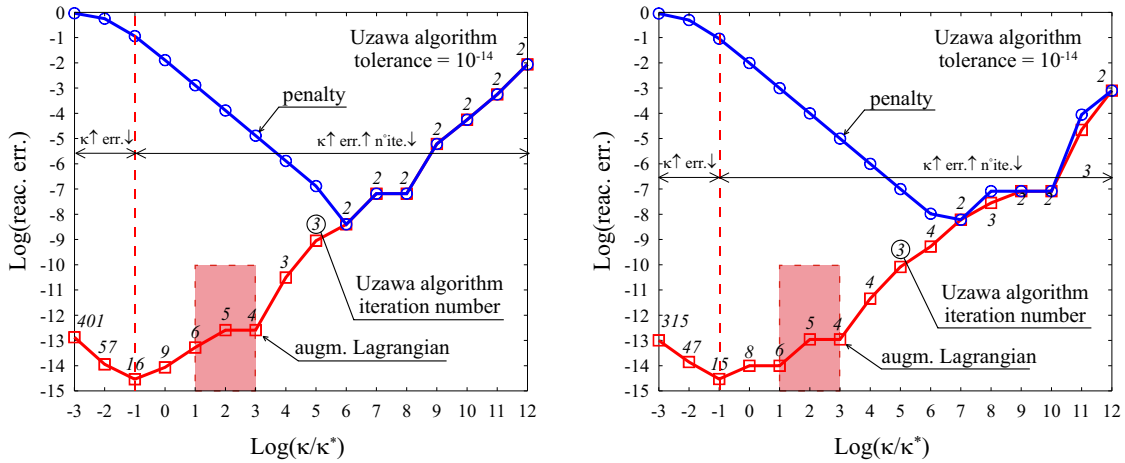

Figure 3.11: One-dimensional linear problems: augmented Lagrangian vs. penalty performance in terms of reaction accuracy for mechanical (a) and hydraulic (b) problems

However, in hydraulic problems, requirements on runoff flow accuracy and on the pressure constraint fulfillment are typically less severe than in contact problems. It can be reasonable to accept a constraint violation and a reaction accuracy of $10^{-2} \div 10^{-3}$. Therefore, the penalty method is suitable for solution of the highly non-linear transient problems involving partial saturation.

3.7.2 Infiltration through a partially saturated layer

In this section, the application of unilateral boundary conditions to a strongly non-linear transient problem is considered. An initially nearly dry $10\,m$ deep soil layer is subjected to a rainfall event. Hence, an infiltration process takes place, leading to the propagation of a wetting front in the porous solid.

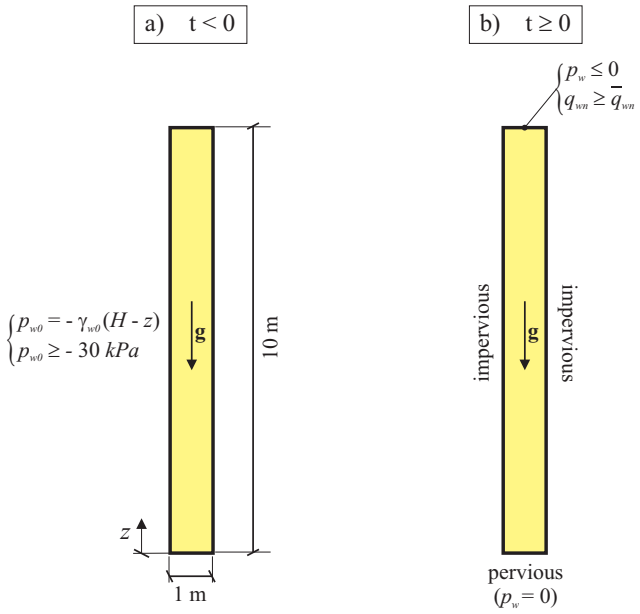

Figure 3.12: Infiltration into a partially saturated soil: initial setting (a) and (b) boundary conditions

Initial and boundary conditions of the problem are shown in Figure 3.12a,b, respectively. Assuming that the water table is placed on the layer base, hydrostatic initial conditions could be imposed to the problem. Anyway, in order to avoid unrealistic capillary pressure values, a cutoff on the initial pressure is imposed, such that $p_{w0} \geq -30\,kPa$. In the following, we will provide motivations for the consideration of

a cut-off on the initial distribution of pore pressures and for the particular assumed value. Lateral surfaces are impervious, thus leading to a one-dimensional problem that is simulated here with a plane analysis. A null value of the pore pressure is prescribed on the base, thus modelling a water table position not affected by the infiltration process. The interface between porous solid and atmosphere on the top surface is modelled

Table 3.1: Infiltration into a partially saturated soil: material parameters

solid skeleton Young modulus	E_{sk}	5000	kPa
solid skeleton Poisson coefficient	ν_{sk}	0.3	
Biot coefficient	b	1.0	
solid phase bulk stiffness	κ_s	10^9	kPa
water bulk stiffness	κ_w	2×10^6	kPa
porosity	n	0.38	
water-saturated permeability	k_w^{sat}	6×10^{-6}	$m^2/(kPa\,s)$
van Genuchten parameter	a_{vg}	0.1	kPa^{-1}
van Genuchten parameter	n_{vg}	5.6	
residual saturation degree	s_w^{res}	0.4	

by means of unilateral boundary conditions, where the prescribed rainfall is $\bar{q}_{wn}$ and no water ponding is allowed, that is, $p_{w,max} = 0$. Before the pressure reaches such a maximum value, the infiltration is a "flow-driven" process. After a null pressure value is attained at the top of the layer, a positive runoff is returned to the environment to keep such a pressure condition, thus representing a "pressure-driven" process.

Saturation degree and relative permeability functions are assumed to follow the van Genuchten model [147]:

$$\begin{cases} S_w(p_c) = \left[\dfrac{1}{1+(a_{vg}\,p_c)^{n_{vg}}}\right]^{m_{vg}} & \text{with} \quad S_w := \dfrac{s_w - s_w^{res}}{1 - s_w^{res}} \\ k_w^{rel}(s_w) = S_w^{1/2}\left[1-\left(1-S_w^{1/m_{vg}}\right)^{m_{vg}}\right]^2 & \text{with} \quad m_{vg} = 1 - 1/n_{vg} \end{cases} \tag{3.79}$$

for $p_c \geq 0$ and the residual saturation degree s_w^{res}. Mechanical and hydraulic properties of the sandy loam considered herein are reported in Table 3.1.

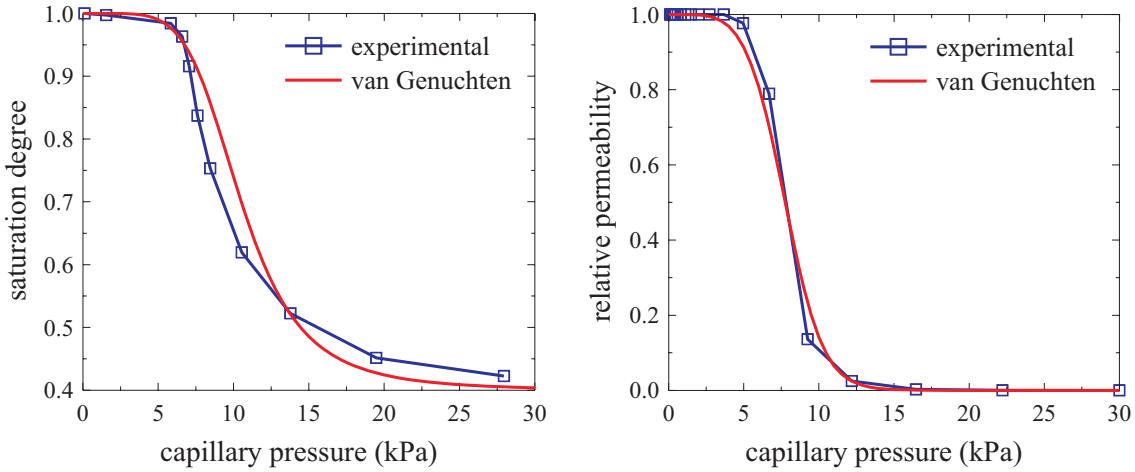

Figure 3.13: Infiltration into a partially saturated soil: saturation degree (a) and relative permeability coefficient (b)

As shown in Figure 3.13, the assumed values for van Genuchten parameters a_{vg} and n_{vg} are obtained by interpretation of experimental data reported by Topp [141] for this soil.

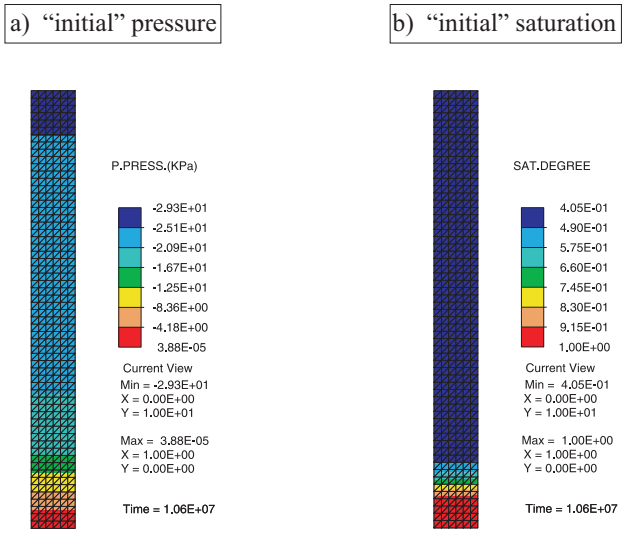

Figure 3.14: Infiltration into a partially saturated soil: pore pressure (a) and saturation degree (b) distributions after a desaturation analysis

With the assumed hydro-mechanical properties, the pressure cutoff on the initial conditions can then be easily motivated. In fact, from the simulation of a desaturation process of such a soil layer, the assumed initial pore pressure distribution corresponds

approximatively to a 4 months desaturation period (Fig. 3.14a). A further reduction in pore pressure distribution needs a very long desaturation period, because above the water table the saturation degree is almost equal to the residual value (Fig. 3.14b).

With these settings, the infiltration process is analyzed for several values of rainfall $\bar{q}_{wn}$. Unilateral boundary conditions on the top surface are numerically treated by the penalty technique, with a coefficient $\kappa = 10^5\, m/(kPa\, s)$. The runoff flow is calculated

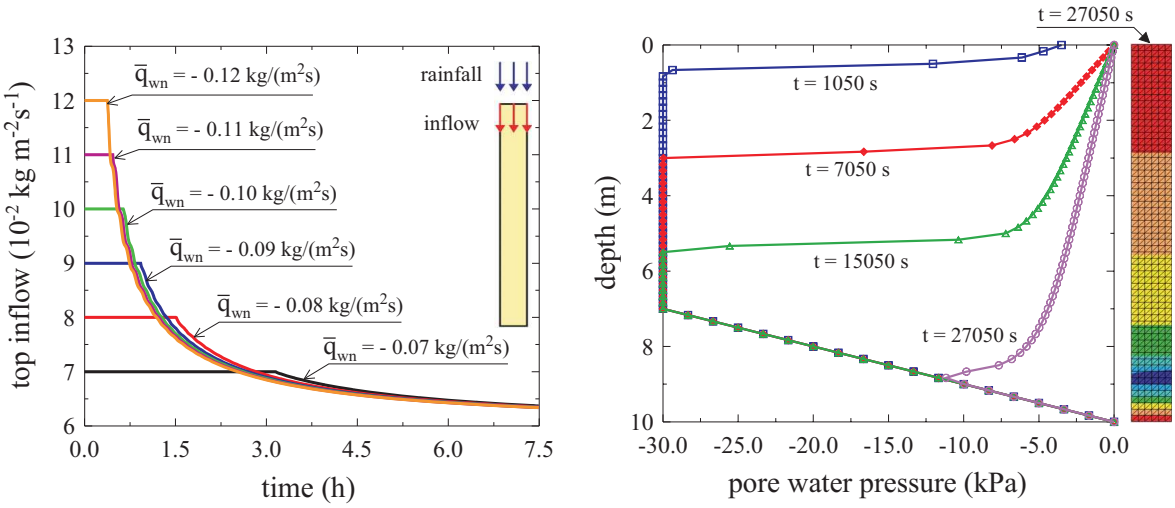

Figure 3.15: Infiltration into a partially saturated soil: water inflow through the top surface (a) and pore pressure distribution (b) obtained for $\bar{q}_{wn} = -0.10\, kg/(m^2 s)$

by means of approximation (3.30) and is plotted in Figure 3.15a. It can be noted how the whole rainfall $\bar{q}_{wn}$ infiltrates in the porous solid until the top pressure is lower than the maximum (null) value. As this maximum value is attained, a positive runoff reduces the infiltration amount. All curves lay approximatively on a hyperbole shaped branch: time required by the pore pressure to attain the limit value deceases for increasing rainfall events. Moreover, increasing rainfall events lead to increasing pore pressure gradients near the top surface and to more rapid infiltration reductions as the limit pore pressure value is attained. As a limit case, a prescribed null pore pressure value on the top surface at $t = 0$ result in a divergent infiltration reduction. In Figure 3.15a it can also be shown how there is an asymptotic infiltration value. In fact, as the wetting front moves in the porous solid (Fig. 3.15b), the pore pressure distribution in the layer becomes closer to the steady-state uniformly null distribution, with the corresponding

infiltration $q_{wn} = \rho_{w0}\gamma_{w0}k_w^{sat}$. Finally, the evolution of pore pressure distributions is shown in Figure 3.15b.

3.7.3 Partial saturation of a concrete gravity dam

In this section an example of application of hydraulic unilateral boundary conditions to dam engineering is considered. In the body and in foundation of concrete gravity dams a system of drainage holes is often placed near the upstream face in order to relief uplift pressures at the dam base. Here this drainage system is modelled as a unilateral constraint in an uncoupled analysis of seepage through the dam body. Material properties of concrete are summarized in Table 3.2. A relatively high value

Table 3.2: Partial saturation of a concrete gravity dam: material parameters

solid skeleton Young modulus	E_{sk}	2.5×10^7	kPa
solid skeleton Poisson coefficient	ν_{sk}	0.2	
Biot coefficient	b	0.5	
solid phase bulk stiffness	κ_s	2.8×10^7	kPa
water bulk stiffness	κ_w	2×10^6	kPa
porosity	n	0.12	
water-saturated permeability	k_w^{sat}	10^{-9}	$m^2/(kPa\,s)$
van Genuchten parameter	a_{vg}	0.05	kPa^{-1}
van Genuchten parameter	n_{vg}	2.3	
residual saturation degree	s_w^{res}	0.1	

of saturated permeability has been chosen to simulate the fissured concrete of an old dam.

Geometry, initial and boundary conditions are depicted in Figure 3.16 a. A uniform initial negative pressure $p_{w0} = -100\,kPa$ is assumed into the dam body in order to simulate nearly dry conditions. A rapid reservoir filling is simulated by instantaneous activation (t=0) of a hydrostatic water pressure distribution on the upstream face and

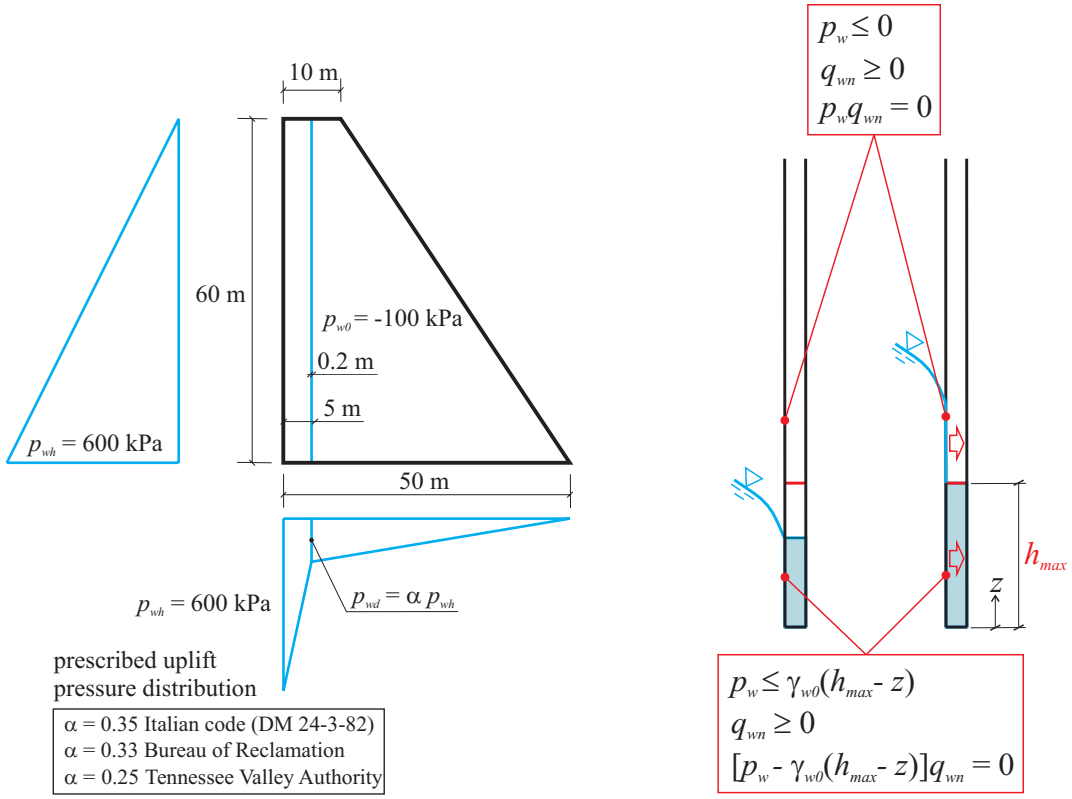

Figure 3.16: Partial saturation of a concrete gravity dam: initial and boundary condition (a) and unilateral constraint on the drainage system (b)

of a uplift pressure distribution at the dam base. Such an uplift distribution is reduced with respect to the triangular shape to simulate the effects of a drainage system [42]. In particular, the uplift pressure under the drainage line is a prescribed fraction of the pressure at the dam heel, i.e. $p_{wd} = \alpha p_{wh}$ (here it is set $\alpha = 0.25$); so, the water level in drains must not exceed the limit value $h_{max} = p_{wd}/\gamma_{w0}$.

As illustrated in Figure 3.16b, in the upstream face of the drainage system, the pressure is constrained by the unilateral condition $p_w \le \gamma_{w0}(h_{max} - z)$ below the maximum water level and by $p_w \le 0$ above it. If the drainage system is effective, when the water table in the upstream part of the dam body is higher than h_{max}, a runoff flow q_{wn} is extracted from the drainage system to keep the water level in the drains below the limit value (Fig. 3.16b). At the downstream face of the drainage system and below the maximum water level, the pore pressure is imposed equal to the upstream value at the same elevation to simulate the impounding of the drains.

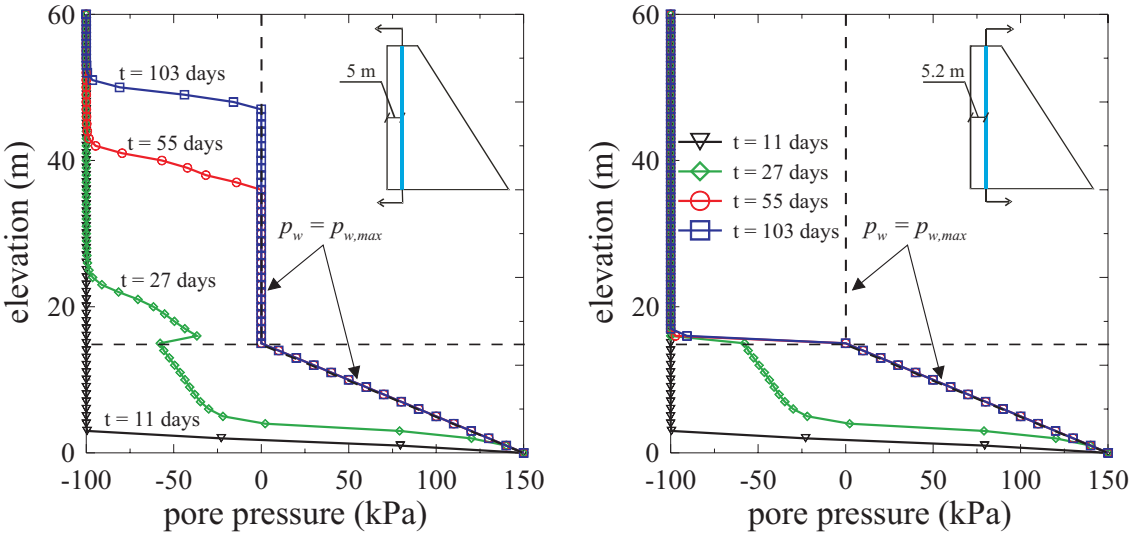

Figure 3.17: Partial saturation of a concrete gravity dam: pore pressure on upstream (a) and downstream face of the drainage system

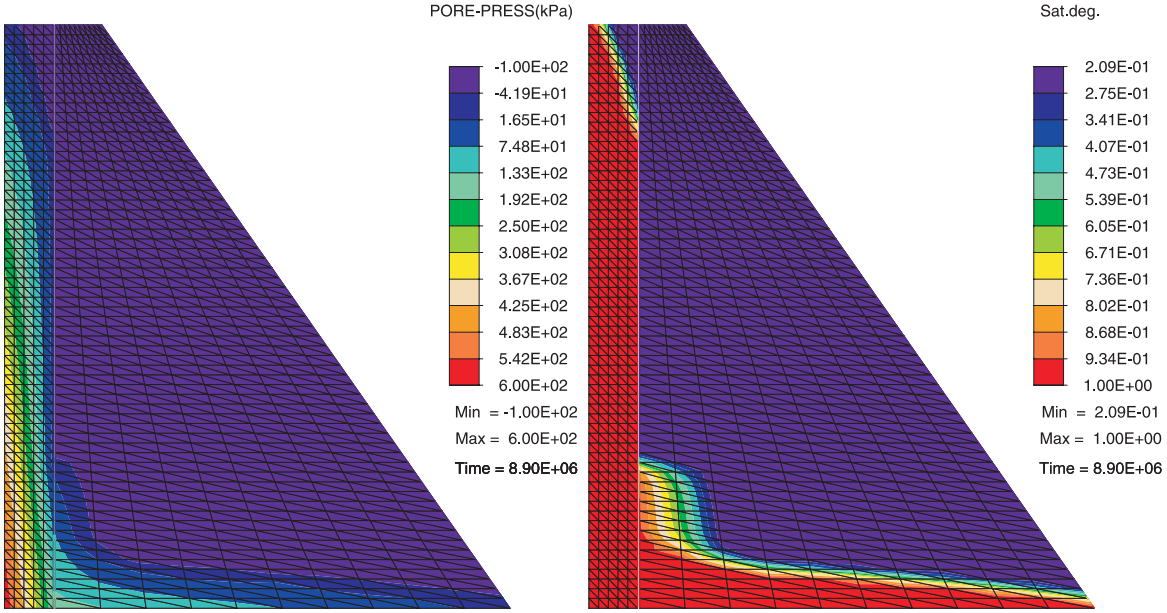

Figure 3.18: Partial saturation of a concrete gravity dam: pore pressure (a) and saturation degree (b) 103 days after the (instantaneous) reservoir filling

Above h_{max}, the downstream face of the drainage system is modelled as impervious. Pressure distributions on both faces of the drainage system are shown in Figure 3.17. In particular, the unilateral condition applied on the upstream face is apparent in Figure 3.17a. The final distributions of pore pressure and saturation degree are plotted in

Figure 3.18. It can be noted how the main hydraulic effect of the drainage system in the dam body is that the portion located upstream the drains is almost fully saturated, while the downstream portion is practically dry, except for the portion close to dam foundation (Fig. 3.18b).

4

Strong discontinuities in multiphase solids

4.1 Introduction

In multiphase porous media, deformations are often characterized by concentration of strains in narrow bands. Propagation of these bands can lead to failure phenomena localized in sliding or fracture surfaces. Moreover, the presence of fluid flow fields strongly affects evolution of these failure mechanisms, as shown for collapse of foundations and for stability of excavations, slopes and tunnels [27, 33, 34, 66].

It is well known that standard finite element methods are not suitable for localization analysis, as they show great difficulties in reproducing the concentration of strains. We denote as "standard" the finite element formulations implementing rate-independent plasticity models of the local continuum. In particular, localized solutions obtained with these conventional methods are unacceptably dependent on the adopted discretization in terms of mesh size and alignment [107, 144]. Such a pathological mesh dependence is due to the lack of a characteristic length in the constitutive model [79, 105, 113, 139], leading to an ill-posed problem in presence of softening and/or non associated evolution laws.

In order to circumvent these drawbacks, a number of non-standard techniques has

been proposed, like viscous [100], high-gradient [50], non-local [17] and Cosserat [61] models. A common feature of some of these approaches is the introduction of small-scale lengths that are able to objectively characterize localized dissipative mechanisms along shear bands.

Small-scale effects can be effectively incorporated in a classical local continuum framework by the strong discontinuity approach [129], a non-standard numerical technique that allows to model the appearance of discontinuous displacement fields and that can be viewed in the more general context of assumed strain enhanced finite element methods [130]. This approach has been employed in problems involving fully saturated porous continua [9, 33, 34].

In this chapter, we present a numerical analysis of strain localization in multiphase porous solids, generalizing the results presented in the last references to the partially saturated case. The analysis considers discontinuous displacement fields and corresponding singular distributions of strain, as well as singular distributions of fluid contents corresponding to discontinuous flows of gaseous and liquid phases, modelling their accumulation and/or drainage in the localized failures of interest. Pore pressure fields are continuous in the proposed approach, in contrast with strong discontinuity analyses presented in [91, 112] for the coupled case, where pore pressure fields are assumed to be discontinuous.

The constitutive model presented in Chapter 1 provides the proper framework for a generalization of the multi-scale approach presented in [34] for the fully saturated case. In particular, a simplified version of the hyperelastic laws presented in Chapter 1 is extended to irreversible phenomena in the general framework of additive elasto-plastic decompositions of strains and fluid mass contents. Therefore, we obtain a simple expression for the Clausius-Duhem inequality, which can be easily employed in the multi-scale approach to strain localization, thus extending the procedure proposed by Armero [8] for purely mechanical problems. A crucial task of this framework is the distinction between the large-scale problem, exhibiting the standard regularity requirements, and the small-scale one, where displacement and fluid flow fields can be discontinuous. In this framework, the internal contribution to dissipation can be

viewed as a distribution, with regular and singular parts. The singular part allows to objectively take into account localized dissipative mechanisms and to introduce localized softening relations between displacement jumps and effective tractions acting on the discontinuity. The small-scale problem is then connected to the large-scale coupled problem through a weak equilibrium statement between this traction and the stresses in the bulk.

An outline of the rest of the chapter is as follows. In Section 4.2, we develop kinematics of the aforementioned multi-scale framework. In particular, the large-scale problem exhibiting standard regularity requirements is described in Section 4.2.1, with Section 4.2.2 introducing strong discontinuities in the small scale. Small and large-scale problems are then connected in Section 4.2.3 by means of the same approach introduced in [6] for purely mechanical problems.

Section 4.3 focuses on the multi-scale poro-plastic constitutive model. The continuum poro-plastic model is developed in Section 4.3.1 in the context of the maximum plastic dissipation principle. The condition for the appearance of a strong discontinuity, as well as a localized softening law are introduced in Section 4.3.2, following arguments similar to the ones employed in [33]. Localized dissipative mechanisms are then introduced in the multi-scale framework adopted herein. In this context, in Section 4.3.3, we consider a particular model example represented by a dilatant poro-plastic cohesive-frictional law.

The enhanced finite element formulation of the proposed multi-scale model is presented in Section 4.4. Singular fields of strain and fluid contents are included as local enhancements and are kept at the element level, thus allowing their static condensation. As a consequence, the numerical implementation in the general finite element code FEAP [138] is relatively simple.

Finally, numerical simulations of different plain strain compression tests on a partially saturated porous solid are presented in Section 4.5. The obtained results illustrate the range of application of developed models and the performance of new finite element methods in simulating localized failure phenomena in multiphase continua.

The main results reported in the present chapter are also presented by Callari,

Armero and Abati [37].

4.2 Discontinuous solutions in multiphase porous continua

In this section the equations governing deformations and fluid mass content rates in a multiphase porous solid exhibiting discontinuous displacement and fluid flow fields are presented; the arguments employed herein are the same ones considered in [33] for the fully saturated case, where the approach presented in [6, 8] for the uncoupled mechanical problem has been adopted. In this framework localized dissipative mechanisms developing in shear bands are incorporated in the large-scale problem, defined by the classical governing equations with the usual regularity requirements, by the strong discontinuity concept. The equations describing large and small-scale problems in the infinitesimal range are briefly summarized in Sections 4.2.1 and 4.2.2, respectively: these two independently introduced problems are connected in Section 4.2.3, where the approach introduced in [6] is considered.

4.2.1 Mechanical and fluid flow problems at the large scale

Due to the infinitesimal deformation assumption, reference and current configurations of the multiphase porous solid are coincident with the domain $\Omega \subset \mathbb{R}^{n_{\text{dim}}}$, with $n_{\text{dim}} = 1, 2$ or 3 the spatial dimension of the problem. The large-scale deformation of the porus solid can be written in terms of the solid skeleton displacement $\mathbf{u}$ as

$$\boldsymbol{\varepsilon} = \nabla^s \mathbf{u} \tag{4.1}$$

being $\nabla^s(\cdot)$ the symmetric part of the gradient operator $\nabla(\cdot)$, and where the large-scale $\mathbf{u}$ is characterized by the standard regularity requirements.

The quasi-static equilibrium of the solid can be expressed in terms of the total stress tensor $\boldsymbol{\sigma}$ by the principle of virtual work as

$$\int_\Omega \boldsymbol{\sigma} : \nabla^s \boldsymbol{\eta} \, d\Omega = \int_\Omega \mathbf{f} \cdot \boldsymbol{\eta} \, d\Omega + \int_{\partial_t \Omega} \bar{\mathbf{t}} \cdot \boldsymbol{\eta} \, dA \tag{4.2}$$

with $\mathbf{f}$ and $\bar{\mathbf{t}}$ imposed volumetric body forces and tractions acting on the boundary portion $\partial_t\Omega \subset \partial\Omega$, respectively. Equation (4.2) must hold for all admissible variations $\boldsymbol{\eta} \in \mathcal{V}_u$ satisfying the aforementioned regularity conditions, where

$$\mathcal{V}_u = \{\boldsymbol{\eta} : \Omega \to \mathbb{R}^{n_{\text{dim}}} \ : \boldsymbol{\eta} = \mathbf{0} \quad \text{on} \quad \partial_u\Omega\} \tag{4.3}$$

for the part of the boundary $\partial_u\Omega \subset \partial\Omega$ with imposed displacements $\mathbf{u} = \bar{\mathbf{u}}$. In the model considered herein, the total stress field $\boldsymbol{\sigma}$ in the weak balance (4.2) depends not only on the large-scale strain field $\boldsymbol{\varepsilon}$ but also on other effects that are introduced at the small scale in Section 4.2.2.

In a similar way, introducing M_α, the large-scale mass content of the fluid α, the mass balance law with no volumetric fluid source reads:

$$\dot{M}_\alpha = -\text{div}\, \mathbf{q}_\alpha \qquad \text{for} \quad \alpha = w, g \tag{4.4}$$

where the large-scale fluid flow $\mathbf{q}_\alpha$ can be defined by a generalized Darcy law:

$$\mathbf{q}_\alpha = -\rho_\alpha \mathbf{k}_\alpha (\nabla p_\alpha - \rho_\alpha \mathbf{g}) \tag{4.5}$$

where p_α, ρ_α and $\mathbf{k}_\alpha$ are the pressure, the density and the permeability tensor of the fluid α respectively and $\mathbf{g}$ is the gravity acceleration vector. The weak form of fluid mass balance (4.4) is:

$$\int_\Omega \dot{M}_\alpha w_\alpha \, d\Omega = \int_\Omega \mathbf{q}_\alpha \cdot \nabla w_\alpha \, d\Omega - \int_{\partial_{q_\alpha}\Omega} \bar{q}_{\alpha n} w_\alpha \, dA \tag{4.6}$$

for all admissible variations $w \in \mathcal{V}_p$ of the pore pressure field, with

$$\mathcal{V}_p = \{w : \Omega \to \mathbb{R} \ : w = 0 \quad \text{on} \quad \partial_p\Omega\} \tag{4.7}$$

where $\partial_p\Omega \subset \partial\Omega$ is the part of the boundary with an imposed pore pressure $p_\alpha = \bar{p}_\alpha$ and $\partial_q\Omega \subset \partial\Omega$ is the part of the boundary with imposed normal component of the fluid flow $\mathbf{q}_\alpha \cdot \mathbf{n} =: q_{\alpha n} = \bar{q}_{wn}$, for the outward unit normal $\mathbf{n}$ to the domain boundary. Similarly to the mechanical problem, the classical regularity conditions are assumed to be satisfied by the large-scale fluid flow problem and localized small-scale effects are introduced independently in Section 4.2.2.

4.2.2 Mechanical and fluid flow problems at the small scale

In the previous section only solutions satisfying standard regularity conditions have been presented: it is well known how such regular fields are not able to correctly capture non-smooth localized dissipative mechanism. In this section, singular fields arising from discontinuous solutions are introduced in the problem at the small scale, following the very same arguments employed in [33] for the saturated case.

In a local neighborhood $\Omega_x \subset \Omega$ of a material point $\mathbf{x} \in \Omega$ (Fig. 4.1) crossed by a surface Γ_x with unit normal $\mathbf{n}$, the discontinuous small-scale displacement field $\mathbf{u}_\mu$ takes the form

$$\mathbf{u}_\mu = \mathbf{u} + \boldsymbol{\zeta}\, \Psi^u_\Gamma \qquad \text{in} \quad \Omega_x \tag{4.8}$$

where the displacement jump across Γ_x is denoted by $\boldsymbol{\zeta} : \Omega_x \times [0,T] \to \mathbb{R}^{n_{\text{dim}}}$ and is parametrized by the function $\Psi^u_\Gamma : \Omega_x \to \mathbb{R}$ given by

$$\Psi^u_\Gamma = H_\Gamma - N^u_\Gamma \quad \text{in} \quad \Omega_x \tag{4.9}$$

where H_Γ is the Heaviside step function across Γ_x and N^u_Γ is a smooth function N^u_Γ, so the function Ψ^u_Γ exhibits a unit jump $[\![\Psi^u_\Gamma]\!] = 1$ across Γ_x.

Infinitesimal strains relative to the non-smooth small-scale displacement field $\mathbf{u}_\mu$ may be introduced in the distributional sense [133] as

$$\boldsymbol{\varepsilon}_\mu := \nabla^s \mathbf{u}_\mu = \underbrace{\boldsymbol{\varepsilon}(\mathbf{u}) + \Psi^u_\Gamma\, \nabla^s \boldsymbol{\zeta} - (\boldsymbol{\zeta} \otimes \nabla N^u_\Gamma)^s}_{\text{regular distribution}} + \underbrace{(\boldsymbol{\zeta} \otimes \mathbf{n})^s\, \delta_\Gamma}_{\text{singular distribution}} \tag{4.10}$$

for the Dirac delta distribution δ_Γ across Γ_x. The strain components

$$\boldsymbol{\varepsilon}_{unr} = \boldsymbol{\varepsilon}_\mu - \boldsymbol{\varepsilon}(\mathbf{u}) \tag{4.11}$$

are defined *unresolved* because large-scale strains $\boldsymbol{\varepsilon}(\mathbf{u})$ are not capable to capture them in the large-scale model: unresolved strains $\boldsymbol{\varepsilon}_{unr}$ characterize the model response at the small-scale in Ω_x by means of the localized dissipative mechanisms introduced in Sections 4.3.2 and 4.3.3.

As in [33], a discontinuous small-scale flow field for the generic fluid α is written in the form

$$\mathbf{q}_{\alpha_\mu} = \mathbf{q}_\alpha + \boldsymbol{v}_\alpha \Psi^q_\Gamma \qquad \text{for} \quad \alpha = w, g \tag{4.12}$$

where Ψ^q_Γ is defined as

$$\Psi^q_\Gamma = H_\Gamma - N^q_\Gamma \quad \text{in} \quad \Omega_x \tag{4.13}$$

for the general smooth function $N^q_\Gamma : \Omega_x \to \mathbb{R}$ and the fluid jump $\boldsymbol{v}_\alpha = [\![\mathbf{q}_{\alpha_\mu}]\!]$ across Γ_x. By applying the divergence operator to (4.12) and with argument similar to the ones used to obtain small-scale deformation $\boldsymbol{\varepsilon}_\mu$ in (4.10), it can be written:

$$\operatorname{div} \mathbf{q}_{\alpha_\mu} = \operatorname{div} \mathbf{q}_\alpha + \Psi^q_\Gamma \nabla \boldsymbol{v}_\alpha : \mathbf{1} - \boldsymbol{v}_\alpha \cdot \nabla N^q_\Gamma + \boldsymbol{v}_\alpha \cdot \mathbf{n} \delta_\Gamma \tag{4.14}$$

which, in turn, is substituted in the following strong form of the small-scale fluid mass balance

$$\dot{M}_{\alpha_\mu} = -\operatorname{div} \mathbf{q}_{\alpha_\mu} \tag{4.15}$$

leading to

$$\dot{M}_{\alpha_\mu} = \underbrace{\dot{M}_\alpha - \Psi^q_\Gamma \nabla \boldsymbol{v}_\alpha : \mathbf{1} + \boldsymbol{v}_\alpha \cdot \nabla N^q_\Gamma}_{\text{regular distribution}} \quad \underbrace{- \boldsymbol{v}_\alpha \cdot \mathbf{n} \delta_\Gamma}_{\text{singular distribution}} \tag{4.16}$$

where large-scale balance (4.4) has been employed. Fluid mass contents can be also written as

$$M_{\alpha_\mu} = \bar{M}_{\alpha_\mu} + \tilde{M}_{\alpha_\mu} \delta_\Gamma \tag{4.17}$$

where $\tilde{M}_{\alpha_\mu}$ is the localized fluid content on Γ_x. Continuum and localized mass-balance equations are given by the regular and the singular parts of (4.16), that is, respectively:

$$\begin{aligned} \dot{\bar{M}}_{\alpha_\mu} &= -\operatorname{div} \left[\mathbf{q}_{\alpha_\mu}\right]\big|_{\Omega_x \setminus \Gamma_x} = \\ &= -\operatorname{div} \mathbf{q}_\alpha - \Psi^q_\Gamma \nabla \boldsymbol{v}_\alpha : \mathbf{1} + \boldsymbol{v}_\alpha \cdot \nabla N^q_\Gamma \qquad \text{in} \quad \Omega_x \setminus \Gamma_x \end{aligned} \tag{4.18}$$

and

$$\dot{\tilde{M}}_{\alpha_\mu} = -[\![\mathbf{q}_{\alpha_\mu}]\!] \cdot \mathbf{n} = -\boldsymbol{v}_\alpha \cdot \mathbf{n} \quad \text{on} \quad \Gamma_x \tag{4.19}$$

The employed approach is different by the one adopted in the saturated case in [91, 134] where discontinuous pore pressure fields are assumed: in fact, discontinuous pressure profiles are physically meaningless, as experimental evidences show [148]: only pressure "kinks", due to concentrated deformations along shear bands and modelled by the present approach, as it can be shown in the numerical results presented in Section 4.5.1, have been observed.

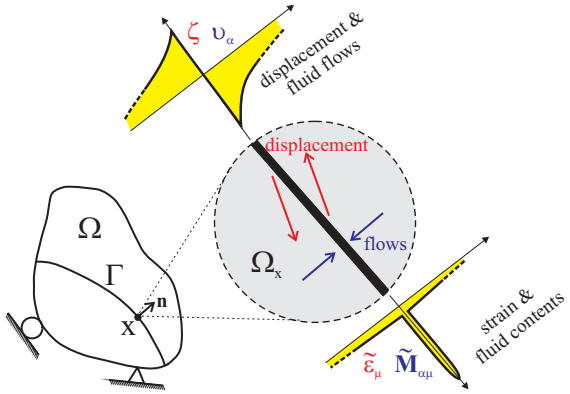

Figure 4.1: Small-scale displacement $\boldsymbol{\zeta}$ and fluid flow $\boldsymbol{\upsilon}_\alpha$ jumps and relative singular distributions of deformation $\tilde{\boldsymbol{\varepsilon}}_\mu$ and fluid mass content $\tilde{M}_{\alpha_\mu}$ [35, 36]

4.2.3 Connection between large and small-scale problems

In Sections 4.2.1 and 4.2.2 large and small-scale displacement and fluid flow fields have been introduced independently. The main goal of this section is to introduce the small-scale effects in the large-scale problem preserving the local continuum character: this implies that no length scale parameter has to be introduced in the final problem. Therefore, in order to construct a well-posed local continuum formulation, the approach introduced in [6, 8] is considered herein. It is well known how the weak form of linear momentum balance at the large scale (4.2) implies regularity of tractions on a given surface of normal unit $\mathbf{n}$ [51]; in particular, the local equilibrium condition

$$\mathbf{t}_\Gamma = \boldsymbol{\sigma}\mathbf{n}|_{\Gamma_x} \tag{4.20}$$

must hold between the (total) traction vector $\mathbf{t}_\Gamma$ acting on Γ_x and the (total) stress $\boldsymbol{\sigma}$ in Ω_x. In [6] it is shown how this condition can be written in a local weak form as

$$-\frac{1}{measure(\Omega_x)}\int_{\Omega_x}\boldsymbol{\gamma}\cdot\boldsymbol{\sigma}\mathbf{n}\,d\Omega+\frac{1}{measure(\Gamma_x)}\int_{\Gamma_x}\boldsymbol{\gamma}\cdot\mathbf{t}_\Gamma\,d\Gamma_x=0 \tag{4.21}$$

for all the variations $\boldsymbol{\gamma}$ of local displacement jumps $\boldsymbol{\zeta}$: therefore, the stress field $\boldsymbol{\sigma}$, depending on large scale displacements $\mathbf{u}$ by the large scale constitutive model described in Section 4.3.1 is connected to displacement jumps $\boldsymbol{\zeta}$ by the traction vector $\mathbf{t}_\Gamma$, that is given as a function of the jumps $\boldsymbol{\zeta}$ by the localized dissipative mechanisms introduced in Sections 4.3.2 and 4.3.3. Therefore, equation (4.21), coupled with the large scale

linear momentum balance (4.2), allows us to solve the mechanical problem in terms of the kinematic variables $\mathbf{u}$ and $\boldsymbol{\zeta}$.

The local equilibrium condition (4.20) is obtained from the weak balance (4.21) in the limit $h_x := measure(\Omega_x)/measure(\Gamma_x) \to 0$, i.e. in the large scale, thus avoiding the introduction of a length scale parameters and preserving the local character of the formulation. An equivalent approach is the "equi-dissipation bridge" introduced in [8], where, by means of equalization of dissipations at large and small scales, the orthogonality of the unresolved strains with the stress field is obtained: for the same limit $h_x := measure(\Omega_x)/measure(\Gamma_x) \to 0$ such a condition, that allows us to think at the unresolved strains as an enhancing of the large-scale ones, leads to the local equilibrium condition (4.20).

In a similar way fluid flow jumps $\boldsymbol{\upsilon}_\alpha$ are related to the large scale fluid flows $\mathbf{q}_\alpha$ by means of equations (4.18) and (4.19): in particular, large-scale flows are related to pore pressures p_α by the generalized Darcy flow laws (4.5) and fluid flow jumps are obtained in terms of displacement jumps $\boldsymbol{\zeta}$ by the localized dissipative response described in Section 4.3.2.

4.3 Constitutive equations for strong discontinuities in multiphase media

In this section the constitutive equations relating deformations and pore pressure fields to stresses and fluid mass contents in the quasi-static problem are outlined. The case of infinitesimal deformations for multiphase poro-elastoplastic solids is considered herein. A constitutive equation set developed in Chapter 1 in a macroscopic thermodynamic framework based on the Biot work [18, 54] for the hyperelastic response of multiphase porous solids, is generalized to take into account dissipative mechanisms in the bulk response at the small-scale $\Omega_x \setminus \Gamma_x$ in Section 4.3.1 as well as on the discontinuity Γ_x in Section 4.3.2.

4.3.1 Continuum poro-elastoplastic model

The characterization of the bulk response is introduced in this section at the small-scale in the general framework of additive elasto-plastic decompositions of strain and fluid mass contents:

$$\boldsymbol{\varepsilon}_\mu = \boldsymbol{\varepsilon}^e_\mu + \boldsymbol{\varepsilon}^p_\mu \qquad\qquad M_{\alpha_\mu} = M^e_{\alpha_\mu} + M^p_{\alpha_\mu} \tag{4.22}$$

Elastic components in (4.22) are related to stresses $\boldsymbol{\sigma}$ and pore pressures p_w and p_g by hyperelastic relations considered in Chapter 1: in the considered formulation, consistently with a "Biot type" macroscopic thermodynamic approach, the poro-elastic continuum is considered as an open system exchanging fluid with the environment, thus leading to a simple expression for the dissipation in the local neighborhood Ω_x. In particular, the contribution due to internal processes takes the form

$$D_{int_\mu} := \boldsymbol{\sigma} : \dot{\boldsymbol{\varepsilon}}_\mu + \sum_{\alpha=w,g} \mu_\alpha \, \dot{M}_{\alpha_\mu} - \dot{\psi} \geq 0 \tag{4.23}$$

with the fluid free enthalpies μ_α, $\alpha = w, g$ and the rate of the Helmholtz free energy $\psi = \hat{\psi}(\boldsymbol{\varepsilon}_\mu, M_{w_\mu}, M_{g_\mu}, \boldsymbol{\alpha}_\mu)$. The general strain-like internal variable vector introduced in the elasto-plastic case has been indicated as $\boldsymbol{\alpha}_\mu$.

Following a very common simplifying assumption, saturation degrees s_α are considered to depend only on the capillary pressure p_c, defined as

$$p_c := p_g - p_w \tag{4.24}$$

Moreover, if the porous space is assumed to be filled by two immiscible barotropic fluids and it is further supposed that these fluids are characterized by infinitesimal deformations, by the use of the standard Coleman and Noll procedure [52], the following simple form of hyperelastic rate equations is proved to be consistent with the dissipation inequality (4.23):

$$\begin{cases} \dot{\boldsymbol{\sigma}} &= \underbrace{\mathbb{C}_{sk}\dot{\boldsymbol{\varepsilon}}^e_\mu}_{=:\,\dot{\boldsymbol{\sigma}}'} - \mathbf{b} \sum_{\gamma=w,g} s_\gamma \dot{p}_\gamma \\ \dfrac{\dot{M}^e_{\alpha_\mu}}{\rho_{\alpha 0}} &= s_\alpha \mathbf{b} : \dot{\boldsymbol{\varepsilon}}^e_\mu + \sum_{\gamma=w,g} C_{\alpha\gamma}\dot{p}_\gamma \qquad \text{for} \quad \alpha = w, g \end{cases} \tag{4.25}$$

for the so-called "drained" elastic tangent tensor $\mathbb{C}_{sk}$ and the Biot coupling tensor $\mathbf{b}$. For the generic anisotropic case, the latter tensor takes the form:

$$\mathbf{b} = \mathbf{1} - \frac{1}{3\kappa_s}\mathbb{C}_{sk}\mathbf{1} \tag{4.26}$$

with κ_s the volumetric stiffness modulus of solid phase.

Denoting by n_0 and n initial and current values of porosity, respectively, tangent storage modulus appearing in $(4.25)_2$ are defined as:

$$C_{\alpha\beta} = \frac{s_\alpha s_\beta}{3\kappa_s}(\mathbf{b} - n_0\mathbf{1}) : \mathbf{1} + \frac{\theta_{\alpha 0}}{\kappa_\alpha}\delta_{\alpha\beta} + n^e s'_\alpha \frac{\partial p_c}{\partial p_\beta} \quad \text{for} \quad \alpha, \beta = w, g \tag{4.27}$$

for the initial volumetric fluid content $\theta_{\alpha 0} = (n s_\alpha)_0$, the stiffness modulus of fluid κ_α, the Kronecker delta $\delta_{\alpha\beta}$, the derivative of saturation degree

$$s'_\alpha := \frac{ds_\alpha}{dp_c} \tag{4.28}$$

and the component n^e of current porosity due to elastic processes, which is in turn evaluated by means of the following rate equation in terms of primary variables:

$$\dot{n}^e = \mathbf{b} : \dot{\boldsymbol{\varepsilon}}^e_\mu + \frac{1}{3\kappa_s}(\mathbf{b} - n_0\mathbf{1}) : \mathbf{1} \sum_{\alpha=w,g} s_\alpha \dot{p}_\alpha \tag{4.29}$$

The aforementioned expressions for poro-elastic tangent operators as well as the elastic porosity model (4.29) are a simplified form of the constitutive model obtained in Chapter 1 by means of typical arguments of mixture theories and averaging techniques, where the consistency of the constitutive equation set has been assessed by means of symmetry requirements and Maxwell conditions obtained in the aforementioned macroscopic thermodynamic framework.

An isotropic hardening/softening regulated by a single scalar strain-like internal variable α_μ with a conjugate stress-like variable q is assumed therein for the sake of simplicity. In the associated case, the evolution of plastic internal variables $\boldsymbol{\varepsilon}^p_\mu$, $M^p_{\alpha_\mu}$ and α_μ is given by rate equations:

$$\begin{cases} \dot{\boldsymbol{\varepsilon}}^p_\mu = \lambda\, \partial_{\boldsymbol{\sigma}} f \\ \dot{\alpha}_\mu = \lambda\, \partial_q f \\ \dot{M}^p_{\alpha_\mu} = \lambda\, \rho_{\alpha 0} \partial_{p_\alpha} f \end{cases} \tag{4.30}$$

in terms of the yield function $f(\boldsymbol{\sigma}, p_w, p_g, q)$, where the plastic consistency parameter λ is determined by the Kuhn-Tucker loading/unloading conditions and the consistency conditions

$$f \leq 0, \quad \lambda \geq 0, \quad \lambda f = 0, \quad \text{and} \quad \lambda \dot{f} = 0 \tag{4.31}$$

Following arguments typically employed in mixture theory thermodynamics, the yield condition can be written in terms of effective stresses $\boldsymbol{\sigma}'$, internal stress-like variable q and capillary pressure p_c, i.e. $f(\boldsymbol{\sigma}, p_w, p_g, q) = f_{sk}(\boldsymbol{\sigma}', p_c, q)$: this model is able to predict some experimental evidences, such as a structural collapse during wetting in collapsible soils and the hysteresis typically observed in retention curves during wetting and drying cycles (e.g. see [5, 22, 85, 117, 126]). However, if the contribution of a capillary pressure reduction to the unrecoverable strain $\boldsymbol{\varepsilon}_\mu^p$ can be neglected and, as commonly assumed in practice, a unique expression of the saturation degree in terms of the capillary pressure is considered both for drying and wetting paths, the yield function can be written only in terms of the effective stress and the internal stress-like variables, i.e. $f(\boldsymbol{\sigma}, p_w, p_g, q) = f_{sk}(\boldsymbol{\sigma}', q)$. From effective stress equation $(4.25)_1$, the following relations are then obtained:

$$\partial_{\boldsymbol{\sigma}} f = \partial_{\boldsymbol{\sigma}'} f_{sk} \quad \text{and} \quad \partial_{p_\alpha} f = s_\alpha \mathbf{b} : \partial_{\boldsymbol{\sigma}'} f_{sk} \tag{4.32}$$

which, in turn, are substituted in $(4.30)_1$ and $(4.30)_3$, leading to the following expression for the rate of plastic fluid content:

$$\dot{M}^p_{\alpha_\mu} = \rho_{\alpha 0} s_\alpha \mathbf{b} : \dot{\boldsymbol{\varepsilon}}^p_\mu \tag{4.33}$$

Therefore, from additive decomposition (4.22), hyperelastic relation $(4.25)_2$ and equation (4.33), the fluid mass content rate can be written as

$$\dot{M}_{\alpha_\mu} = \rho_{\alpha 0} s_\alpha \mathbf{b} : \dot{\boldsymbol{\varepsilon}}_\mu + \sum_{\gamma=w,g} \rho_{\alpha 0} C_{\alpha\gamma} \dot{p}_\gamma \tag{4.34}$$

Remark 4.1 *Expression (4.34) for the (total) fluid mass content rate is to be contrasted with the one obtained by means of mixture theories for the unrecoverable part too. Within this framework, the fluid mass content rate can be written as*

$$\dot{M}_{\alpha_\mu} = \rho_{\alpha 0} s_\alpha \mathbf{b} : \dot{\boldsymbol{\varepsilon}}_\mu + \sum_{\gamma=w,g} \rho_{\alpha 0} C^*_{\alpha\gamma} \dot{p}_\gamma \tag{4.35}$$

with:

$$C^*_{\alpha\beta} = \frac{s_\alpha s_\beta}{3\kappa_s}(\mathbf{b} - n_0\mathbf{1}) : \mathbf{1} + \frac{\theta_{\alpha 0}}{\kappa_\alpha}\delta_{\alpha\beta} + n s'_\alpha \frac{\partial p_c}{\partial p_\beta} \tag{4.36}$$

Therefore expression (4.36) differs from (4.27), where only the elastic part of current porosity is considered. The simplification $n \simeq n^e$ introduced in (4.27) allows to decompose the fluid mass content rate by an additive decomposition. On the contrary, equation (4.35) is characterized by an elasto-plastic coupling, thus leading to significant modifications required not only to ensure thermodynamic consistency of the continuum model, but also to extend strain localization analysis by the strong discontinuity approach to the elasto-plastic coupled case. Such an approximation of the third term of tangent operator (4.36) can be considered acceptable, since the component of porosity change due to plastic strain is normally negligible with respect to s'_α variation, with the latter one typically exhibiting a very wide range in standard multiphase problems.

4.3.2 Formation of strong discontinuities in multiphase media

Because of the yield condition is assumed here to be only a function of the effective stress and the internal stress-like variable, the localization condition as well as the localized softening relation between stress and displacement jump are coincident with those one presented in [9] and are only briefly summarized in this section. In particular, a localized poro-plastic form

$$\lambda = \tilde{\lambda}\delta_\Gamma \tag{4.37}$$

is assumed, consistently with the hypothesis made in [129] for the solid problem. Therefore, the softening modulus can be viewed only in a distributional framework, i.e.

$$\mathcal{H}^{-1}\dot{q} := -\dot{\alpha}_\mu = -\tilde{\lambda}\partial_q f \ \delta_\Gamma \quad \Longrightarrow \quad \mathcal{H}^{-1} = \tilde{\mathcal{H}}^{-1} \ \delta_\Gamma \tag{4.38}$$

that, together with the consistency condition $\dot{f}_{sk} = 0$, after some manipulations, leads to the localized equation

$$\|\dot{\boldsymbol{\zeta}}\| = \frac{1}{\tilde{\mathcal{H}} \ \Xi_{sk}} \partial_{\boldsymbol{\sigma}'} f_{sk} : \dot{\boldsymbol{\sigma}}' \tag{4.39}$$

with

$$\Xi_{sk} = \frac{(\partial_q f_{sk})^2}{\partial_{\boldsymbol{\sigma}'} f_{sk} : \mathbb{C}_{sk} \partial_{\boldsymbol{\sigma}'} f_{sk}} \ \mathbb{C}_{sk}\partial_{\boldsymbol{\sigma}'} f_{sk} : (\mathbf{m} \otimes \mathbf{n}) \tag{4.40}$$

providing the displacement jump rate magnitude $\|\dot{\boldsymbol{\zeta}}\|$ in terms of the normal to the discontinuity $\mathbf{n}$ and of the direction of the displacement jump rate $\mathbf{m}$, which in turn is given imposing the regular character of the traction rate $\dot{\mathbf{t}} = \dot{\boldsymbol{\sigma}}\mathbf{n}$, thus leading to the condition

$$\mathbf{Q}^{ep}_{sk}\mathbf{m} = \mathbf{0} \quad \text{where} \quad \mathbf{Q}^{ep}_{sk} = \mathbf{n} \cdot \left[\mathbb{C}_{sk} - \frac{1}{\partial_{\boldsymbol{\sigma}'} f_{sk} : \mathbb{C}_{sk} \partial_{\boldsymbol{\sigma}'} f_{sk}} \mathbb{C}_{sk} \partial_{\boldsymbol{\sigma}'} f_{sk} \otimes \mathbb{C}_{sk} \partial_{\boldsymbol{\sigma}'} f_{sk} \right] \cdot \mathbf{n} \tag{4.41}$$

necessary to the strain localization, with $\mathbf{Q}^{ep}_{sk}$ the "drained" elastic perfectly plastic acoustic tensor. By means of equation (4.41) also the normal to the discontinuity $\mathbf{n}$ can be obtained: in fact, equation $(4.41)_1$ has a solution if and only if

$$\det(\mathbf{Q}^{ep}_{sk}) = 0 \tag{4.42}$$

which provides the normal to discontinuity $\mathbf{n}$.

Substitution of small-scale strain field (4.10) in (4.34) leads to the following expression for the rate of small-scale fluid content:

$$\dot{M}_{\alpha_\mu} = \underbrace{\dot{M}_\alpha + \rho_{\alpha 0} s_\alpha \mathbf{b} : \left[\Psi^u_\Gamma \, \nabla\dot{\boldsymbol{\zeta}} - \dot{\boldsymbol{\zeta}} \otimes \nabla N^u_\Gamma \right]}_{\text{regular distribution}} + \underbrace{\rho_{\alpha 0} s_\alpha \mathbf{b}\, \dot{\boldsymbol{\zeta}} \cdot \mathbf{n} \; \delta_\Gamma}_{\text{singular distribution}} \tag{4.43}$$

where the large-scale fluid content rate $\dot{M}_\alpha = \dot{M}_\alpha(\mathbf{u})$ is given by (4.34) for the large-scale strain $\boldsymbol{\varepsilon}(\mathbf{u})$ and the pore pressure fields p_α. Comparing equation (4.43) with (4.17), the following expressions for the singular and regular parts of unresolved fluid content, respectively can be obtained:

$$\dot{\tilde{M}}_{\alpha_\mu} = -\boldsymbol{v}_\alpha \cdot \mathbf{n} = \rho_{\alpha 0} \, s_\alpha \mathbf{b}\, \dot{\boldsymbol{\zeta}} \cdot \mathbf{n} \qquad \text{on} \quad \Gamma_x \tag{4.44}$$

and

$$\begin{aligned} \dot{\bar{M}}_{\alpha_{unr}} &= -\Psi^{q_\alpha}_\Gamma \nabla \boldsymbol{v}_\alpha : \mathbf{1} + \boldsymbol{v}_\alpha \cdot \nabla N^{q_\alpha}_\Gamma \\ &= \rho_{\alpha 0} s_\alpha \mathbf{b} : \left[\Psi^u_\Gamma \, \nabla\dot{\boldsymbol{\zeta}} - \dot{\boldsymbol{\zeta}} \otimes \nabla N^u_\Gamma \right] \\ &= \rho_{\alpha 0} s_\alpha \mathbf{b} : \dot{\bar{\boldsymbol{\varepsilon}}}_{unr} \end{aligned} \tag{4.45}$$

for regular $\bar{\boldsymbol{\varepsilon}}_{unr}$ and singular $\tilde{\boldsymbol{\varepsilon}}_{unr}$ parts, respectively, of unresolved strains. A comparison between equations (4.44) and (4.45) allows to assume

$$N^u_\Gamma = N^q_\Gamma \qquad \Longrightarrow \qquad \Psi^u_\Gamma = \Psi^q_\Gamma \qquad \text{in} \quad \Omega_x \tag{4.46}$$

as considered in the finite element methods developed in Section 4.4.

4.3.3 Localized multiphase dissipative model

In the previous section the localized softening law (4.39) has been obtained directly by the large-scale model in terms of the yield function characterizing the large-scale dissipation. Therefore, it seems that the post-localization response has to be determined by the pre-localization one. However, in a multi-scale thermodynamic framework developed in [6] in the context of purely mechanical theories, the localized dissipative mechanism can be modelled independently by the continuum one, thus leading to a possible localized softening law different from equation (4.39).

The aforementioned multi-scale approach has been extended to coupled fully saturated porous solids in [34] in the finite strain range. The generalization to the case of multiphase porous solids is straightforward; the internal contribution to the dissipation in the small scale D_{int_μ} defined in (4.23) can be decomposed as

$$D_{int_\mu} = \bar{D}_{int_\mu} + \tilde{D}_{int_\mu}\delta_\Gamma \tag{4.47}$$

where $\bar{D}_{int_\mu}$ takes into account bulk dissipation and $\tilde{D}_{int_\mu}$ is the contribution due to localized dissipative mechanisms. If a decomposition into regular and singular parts is assumed for the Helmholtz free energy too, i.e.

$$\psi(\boldsymbol{\varepsilon}_\mu, M_{w_\mu}, M_{g_\mu}, \alpha_\mu) = \bar{\psi}(\bar{\boldsymbol{\varepsilon}}_\mu, \bar{M}_{w_\mu}, \bar{M}_{g_\mu}, \bar{\alpha}_\mu) + \tilde{\psi}(\tilde{\boldsymbol{\varepsilon}}_\mu, \tilde{M}_{w_\mu}, \tilde{M}_{g_\mu}, \tilde{\alpha}_\mu)\delta_\Gamma \tag{4.48}$$

regular and singular parts of the internal dissipation take the form

$$\begin{aligned} \bar{D}_{int_\mu} &= \boldsymbol{\sigma} : \dot{\bar{\boldsymbol{\varepsilon}}}_\mu + \sum_{\alpha=w,g} \mu_\alpha \dot{\bar{M}}_{\alpha_\mu} - \dot{\bar{\psi}} \\ &= \boldsymbol{\sigma} : \dot{\bar{\boldsymbol{\varepsilon}}}^p_\mu + \sum_{\alpha=w,g} \mu_\alpha \dot{\bar{M}}^p_{\alpha_\mu} + q\dot{\bar{\alpha}}_\mu \end{aligned} \tag{4.49}$$

and

$$\begin{aligned} \tilde{D}_{int_\mu} &= \boldsymbol{\sigma} : \dot{\tilde{\boldsymbol{\varepsilon}}}_\mu + \sum_{\alpha=w,g} \mu_\alpha \dot{\tilde{M}}_{\alpha_\mu} - \dot{\tilde{\psi}} \\ &= \boldsymbol{\sigma} : \dot{\tilde{\boldsymbol{\varepsilon}}}^p_\mu + \sum_{\alpha=w,g} \mu_\alpha \dot{\tilde{M}}^p_{\alpha_\mu} + q\dot{\tilde{\alpha}}_\mu \end{aligned} \tag{4.50}$$

respectively, where the standard Coleman and Noll procedure [52] has been employed to obtain dissipation expressions in terms of irreversible strain-like variables. The total dissipation in a local neighborhood Ω_x can be computed as

$$\int_{\Omega_x} D_{int_\mu}\, d\Omega_x = \int_{\Omega_x} \bar{D}_{int_\mu}\, d\Omega_x + \int_{\Gamma_x} \tilde{D}_{int_\mu}\, d\Gamma_x \tag{4.51}$$

where the second term on the right side takes into account in an objective way localized dissipative mechanisms. In particular, the singular contribution, in view of (4.50), can be rewritten as

$$\begin{aligned} \tilde{D}_{int_\mu} &= \mathbf{t}_\Gamma \cdot \dot{\boldsymbol{\zeta}} + \sum_{\alpha=w,g} \mu_{\alpha_\Gamma}\, \dot{\tilde{M}}_{\alpha_\mu} - \dot{\tilde{\psi}} \\ &= \mathbf{t}_\Gamma \cdot \dot{\boldsymbol{\zeta}}^p + \sum_{\alpha=w,g} \mu_{\alpha_\Gamma}\, \dot{\tilde{M}}^p_{\alpha_\mu} + q_\Gamma \dot{\tilde{\alpha}}_\mu \end{aligned} \tag{4.52}$$

where the classical result of distribution theory [133]

$$\int_{\Omega_x} \boldsymbol{\sigma} : (\boldsymbol{\gamma} \otimes \mathbf{n})^s\, d\Omega_x = \int_{\Gamma_x} \mathbf{t}_\Gamma \cdot \boldsymbol{\gamma}\, d\Gamma_x \tag{4.53}$$

for all the variation $\boldsymbol{\gamma}$ of the displacement jumps $\boldsymbol{\zeta}$, has been used together with the small-scale deformation definition (4.10) (second term on the right side) and with $\boldsymbol{\zeta}^p$ and $\tilde{M}^p_{\alpha_\mu}$ the plastic parts of the displacement jump and fluid mass content, respectively, q_Γ and $\tilde{\alpha}_\mu$ respectively the stress-like and the strain like scalar variables describing a localized isotropic hardening/softening and μ_{α_Γ} the driving enthalpy on the discontinuity.

In the localized dissipation expression (4.52) it has been assumed that the displacement jump field $\boldsymbol{\zeta}$ is generally given by sum of an elastic part $\boldsymbol{\zeta}^e$ and a plastic part $\boldsymbol{\zeta}^p$ as in [8]. Therefore, reversible and dissipative phenomena on the discontinuity can be modelled in a thermodynamically coherent framework by means of (4.52). However, in this work we assume a rigid-plastic response in the post-localization range along the discontinuity. Therefore, the displacement jump is fully irreversible, i.e. $\boldsymbol{\zeta} = \boldsymbol{\zeta}^p$, and, due to expression (4.44), also the elastic singular part of the fluid mass content is null, i.e. $\tilde{M}_{\alpha_\mu} = \tilde{M}^p_{\alpha_\mu}$. Hence the localized contribution to the internal dissipation takes the form

$$\tilde{D}_{int_\mu} = \mathbf{t}_\Gamma \cdot \dot{\boldsymbol{\zeta}} + \sum_{\alpha=w,g} \mu_{\alpha_\Gamma} \dot{\tilde{M}}_{\alpha_\mu} + q_\Gamma \dot{\tilde{\alpha}}_\mu \tag{4.54}$$

and, in this context, localized dissipative mechanisms on the discontinuity can be described by the yield function

$$\tilde{f}(\mathbf{t}_\Gamma, \mu_{w_\Gamma}, \mu_{g_\Gamma}, q_\Gamma) = \tilde{f}_{sk}(\mathbf{t}'_\Gamma, q_\Gamma) \tag{4.55}$$

with the effective stress vector $\mathbf{t}'_\Gamma := \boldsymbol{\sigma}'\mathbf{n}|_{\Gamma_x}$ acting on the discontinuity. Therefore, it can be assumed that the pre-localization small-scale dissipative response is governed by the bulk dissipation $\bar{D}_{int_\mu}$. In this context, a yield function $f_{sk}(\boldsymbol{\sigma}', q)$ has been introduced in Section 4.3.2. The bulk response is also able to capture the localization condition, given by equation (4.41) in terms of the bulk yield function. In the post-localization range, localized dissipative mechanisms along the discontinuity are described by the singular part $\tilde{D}_{int_\mu}$ and hence the localized softening law (4.39) can be described in terms of the localized yield function $\tilde{f}_{sk}(\mathbf{t}'_\Gamma, q_\Gamma)$.

In this work it is assumed for the bulk dissipative response an associated elasto-plastic Drucker-Prager model, with a yield function written in terms of effective stresses as

$$f_{sk}\left(\boldsymbol{\sigma}', q\right) = \|\mathbf{s}\| + \beta\frac{1}{3}\,\boldsymbol{\sigma}' : \mathbf{1} + \sqrt{\frac{2}{3}}\,q \tag{4.56}$$

with $\mathbf{s} := \mathrm{dev}(\boldsymbol{\sigma}')$ the deviatoric part of the effective stress tensor, and the pressure coefficient β. Denoting by σ'_1, σ'_2 the in-plane principal effective stresses ($\sigma'_1 \geq \sigma'_2$) and by s_3 the out-of-plane principal deviatoric stress, the localization condition (4.41) is satisfied for

$$\frac{\|\mathbf{s}\|}{r} = \sqrt{\frac{2}{1-\beta^2/6}} \qquad \text{with} \qquad r = \frac{\sigma'_1 - \sigma'_2}{2} \tag{4.57}$$

or, equivalently

$$s_3 + \frac{1}{3}\,\beta = 0 \tag{4.58}$$

As previously done in [33] and [39] for fully saturated and purely mechanical problems, respectively, a dilatant perfectly plastic model describing the localized dissipation is assumed consistently with the continuum model. Therefore, the same yield function (4.56) is considered for the post-localization response. Denoting by $\mathbf{t}$ the unit tangent to Γ_x, the *localized* dilatancy is defined under the assumption of plane strain as the

ratio

$$\Phi := \frac{\dot{\zeta}_n}{\left|\dot{\zeta}_t\right|} \qquad \text{where} \quad \zeta_n := \boldsymbol{\zeta} \cdot \mathbf{n} \quad \text{and} \quad \zeta_t := \boldsymbol{\zeta} \cdot \mathbf{t} \tag{4.59}$$

are the normal and the tangential components of displacement jump, respectively. For the considered associated Drucker-Prager model, the appearance of the localized plastic flow (4.37) leads to the expression for the localized dilatancy and of the discontinuity orientation, respectively

$$\Phi = \frac{\sqrt{2}\,\beta}{2\sqrt{1-2\beta^2/3}} \quad \text{and} \quad \theta = \frac{1}{2}\arctan\left[\frac{\operatorname{sign}(\dot{\zeta}_t)}{\Phi}\right] \tag{4.60}$$

where θ is the angle between $\mathbf{n}$ and the major (in-plane) principal stress direction.

Futhermore, the localized relation (4.39) between the stress and the displacement jump rates reads in this case

$$\dot{\tau}_\Gamma \operatorname{sign}(\dot{\zeta}_t) + \Phi\ \dot{\sigma}'_\Gamma = \frac{\tilde{\mathcal{H}}}{3-2\beta^2}|\dot{\zeta}_t| \quad \text{where} \quad \tau_\Gamma := \mathbf{t}'_\Gamma \cdot \mathbf{t} \quad \sigma'_\Gamma := \mathbf{t}'_\Gamma \cdot \mathbf{n} \tag{4.61}$$

are the tangential and the normal components of effective traction vector on Γ_x. In this section the equations describing the localization triggering as well as the localized softening are only briefly summarized: more details can be found in [39].

4.4 Enhanced finite element formulation

The finite element method of the localized coupled poro-plastic model described in the previous sections is developed here in the context of the enhanced finite element method as formulated in [130]. In particular, the developments presented for the fully saturated case in [33, 34] are extended in the partially saturation range.

4.4.1 Finite element interpolations

Standard isoparametric interpolations of the general form

$$\mathbf{u}_e(\mathbf{x}) = \mathbf{N}^u_e(\mathbf{x})\,\mathbf{d}_e \tag{4.62}$$

are considered to approximate the large-scale displacement field $\mathbf{u}$, where $\mathbf{N}_e^u(\mathbf{x})$ and $\mathbf{d}_e$ are shape functions and nodal displacements, respectively; in the following, a regular partition of the domain of interest $\Omega = \cup_{e=1}^{n_{\text{el}}} \Omega_e$ in n_{el} 6-node quadratic triangle is assumed.

The multi-scale framework developed in previous sections is implemented in the proposed finite element method by identifying the local neighborhood Ω_x with the element $\Omega_{e,loc} \subset \Omega$ where localization is detected. In particular, the function Ψ_Γ^u in (4.9) is approximated by

$$\Psi_{\Gamma_e}(\mathbf{x}) = H_\Gamma(\mathbf{x}) - N_\Gamma^{(i)}(\mathbf{x}) \qquad \text{where} \qquad N_\Gamma^{(i)}(\mathbf{x}) = 1 - \frac{(\mathbf{x}^{(i)} - \mathbf{x}) \cdot \mathbf{n}^{(i)}}{h^{(i)}} \tag{4.63}$$

is the linear shape function associated to node (i) sustaining the discontinuity line Γ_e, assumed piece-wise straight at the different elements. The element size $h^{(i)}$ in (4.63) is defined in Figure 4.2, together with the unit normal $\mathbf{n}^{(i)}$ to the side opposite to node (i). As pointed out in [11, 98], the use of the discontinuous function $\Psi_{\Gamma e}$ instead of the Heaviside function H_Γ alone, allows to satisfy the condition $\Psi_{\Gamma e}|_{\partial\Omega} = 0$ thus leading to a compatible strain enhancement, i.e. Dirichlet boundary conditions involve only the large-scale displacement $\mathbf{u}_e$.

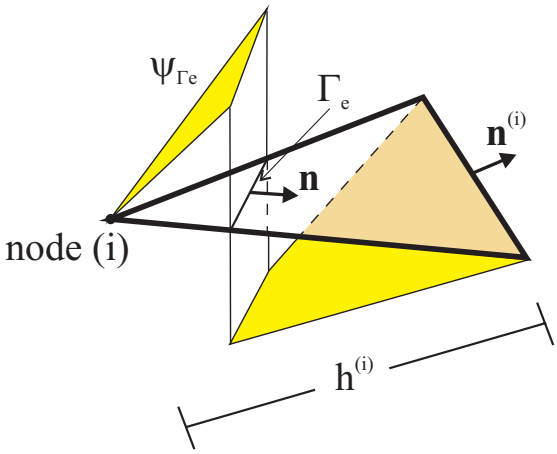

Figure 4.2: Displacement and fluid flow discontinuous interpolation function Ψ_{Γ_e} [35, 36]

Having in mind that $\nabla N^{(i)} = \mathbf{n}^{(i)}/h^{(i)}$, the assumed enhanced strain field takes the

form

$$\boldsymbol{\varepsilon}_e = \underbrace{\mathbf{B}_e^u \mathbf{d}_e}_{\text{conforming}} \quad \underbrace{- \mathbf{G}_e\, \mathbf{z}_e + \mathbf{P}_e\, \mathbf{z}_e\, \delta_\Gamma}_{\text{enhanced}} \tag{4.64}$$

for the standard strain matrix $\mathbf{B}_e^u := \nabla \mathbf{N}_e^u(\mathbf{x})$ associated with the conforming part of the displacements (the large-scale strain field), and for the enhanced strain operators

$$\mathbf{G}_e = \left[\frac{1}{h^{(i)}} (\mathbf{n} \otimes \mathbf{n}^{(i)})^s \qquad \frac{1}{h^{(i)}} (\mathbf{t} \otimes \mathbf{n}^{(i)})^s \right] \quad \mathbf{P}_e = [\mathbf{n} \otimes \mathbf{n} \qquad (\mathbf{t} \otimes \mathbf{n})^s] \tag{4.65}$$

where it has been assumed a constant approximation over the element of the displacement jump vector $\boldsymbol{\zeta}_e = [\mathbf{n} \quad \mathbf{t}]\, \mathbf{z}_e$ and with a vector $\mathbf{z}_e$ of normal and tangential displacement jump taking the form

$$\mathbf{z}_e = \begin{bmatrix} \zeta_{n_e} \\ \zeta_{t_e} \end{bmatrix} \tag{4.66}$$

Fluid flow fields in the porous space are approximated in a very similar way. Pore pressures can be written in terms of nodal values $\mathbf{p}_{\alpha,e}$ by the isoparametric interpolations

$$p_{\alpha,e}(\mathbf{x}) = \mathbf{N}_{\alpha,e}^p(\mathbf{x})\, \mathbf{p}_e \tag{4.67}$$

for the shape functions $\mathbf{N}_e^p(\mathbf{x})$. In the notation of Section 4.2.1, the large-scale fluid flow fields are given by

$$\mathbf{q}_\alpha = -\rho_{\alpha 0} \mathbf{k}_\alpha \left(\mathbf{B}_e^p \mathbf{p}_{\alpha,e} - \rho_{\alpha 0} \mathbf{g} \right) \tag{4.68}$$

for the conforming gradient operator $\mathbf{B}_e^p := \nabla \mathbf{N}_e^p(\mathbf{x})$. In a localized element $\Omega_{e,loc}$, the small-scale flow fields are approximated through the enhanced interpolation

$$\mathbf{q}_{\alpha_\mu}(\mathbf{x}) = \underbrace{- \rho_{\alpha 0} \mathbf{k}_\alpha \left(\mathbf{B}_e^p \mathbf{p}_{\alpha,e} - \rho_{\alpha 0} \mathbf{g} \right)}_{\text{conforming}} + \underbrace{\boldsymbol{\upsilon}_{\alpha,e}\, \Psi_{\Gamma e}(\mathbf{x})}_{\text{enhanced}} \tag{4.69}$$

for the constant approximation over the element of the fluid flow jump vectors $\boldsymbol{\upsilon}_{\alpha,e}$. The use of the same discontinuous interpolation function Ψ_{Γ_e}, given by (4.63) for the displacement field, is consistent with expression (4.44) for the unresolvable fluid mass content rate obtained in Section 4.3.2.

Remark 4.2 *The conforming part of the small-scale deformation in equation (4.64) can be generalized by the use of a general strain operator* $\bar{\mathbf{B}}_e^u$ *due to mixed assumed strain finite element methods [81]: forthcoming developments are the same for a mixed assumed strain operator* $\bar{\mathbf{B}}_e^u$ *as well as for the general strain operator* $\mathbf{B}_e^u$*; then, without loss of generality, the finite element formulation will be developed for the basic displacement method.*

4.4.2 Finite element equations

The nodal values of displacement $\mathbf{d}$, pore pressure $\mathbf{p}$ and enhanced parameters $\boldsymbol{\zeta}_e$ in the elements where localization is detected, are determined by the solution of discretized counterparts of large-scale linear momentum equilibrium (4.2), small-scale local equilibrium (4.21) and large-scale fluid balance equation (4.6). These finite element equations are derived in the following sections.

The large-scale mechanical conforming equations

The introduction of the finite element interpolations (4.62) and (4.64) into the weak form of the linear momentum balance (4.2) leads, after standard algebraic manipulations, to the residual equation

$$\mathbf{r}_m = \mathbf{f}^{ext} - \mathop{\mathbf{A}}_{e=1}^{n_{\rm el}} \int_{\Omega_e} \mathbf{B}_e^{uT} \boldsymbol{\sigma} \, d\Omega = \mathbf{0} \tag{4.70}$$

for the nodal external force vector $\mathbf{f}^{ext}$, (including any imposed boundary displacements). A standard quadrature rule is employed to evaluate the integral in (4.70). The symbol $\mathbf{A}$ used in (4.70) denotes the assembly of all the n_{elem} element contributions. Total stresses $\boldsymbol{\sigma}$ are obtained in terms of effective stresses $\boldsymbol{\sigma}'$ and pore pressures $p_{\alpha,e}$, given by (4.67), by the constitutive equation $(4.25)_1$; by the same constitutive equation, effective stresses are obtained in terms of the regular part $\bar{\boldsymbol{\varepsilon}}_e := \mathbf{B}_e^u \mathbf{d}_e - \mathbf{G}_e \, \mathbf{z}_e$ of the enhanced strain field (4.64).

The enhanced mechanical equations: connection of large and small-scale multiphase discretized problems

Enhanced strain parameters $\boldsymbol{\zeta}_e$ are obtained in terms of large-scale displacement $\mathbf{u}_e$ by the weak form (4.21) of the (total) traction continuity along the discontinuity. In finite element formulations of the multi-scale approach, the local neighborhood Ω_x is identified with the element $\Omega_{e,loc}$ depicted in Figure 4.3 where localization is detected. Therefore, denoting by A_e the area of $\Omega_{e,loc}$ and by l_e the length of discontinuity approximation $\boldsymbol{\gamma}_e$ in $\Omega_{e,loc}$, the finite element discretization of equation (4.21) is

$$-\frac{1}{A_e}\int_{\Omega_{e,loc}} \boldsymbol{\gamma}_e \cdot \boldsymbol{\sigma}\mathbf{n}\, d\Omega + \frac{1}{l_e}\int_{\Gamma_e} \boldsymbol{\gamma}_e \cdot \mathbf{t}_\Gamma\, d\Gamma = 0 \tag{4.71}$$

for all (approximated) variations $\boldsymbol{\gamma}_e$ of displacement jumps across the discontinuity.

In the equation (4.71), total stress and traction vector can be written in terms of effective stress $\boldsymbol{\sigma}'$ and average pore pressure p_f by means of the following stress decompositions:

$$\begin{aligned} \boldsymbol{\sigma} &= \boldsymbol{\sigma}'(\mathbf{u}_e, \boldsymbol{\zeta}_e) - p_f \mathbf{b} \\ \mathbf{t}_\Gamma &= \mathbf{t}'_\Gamma(\boldsymbol{\zeta}_e) - p_{f_\Gamma}\mathbf{b}\mathbf{n} \end{aligned} \tag{4.72}$$

Accordingly with the localized constitutive law (4.39) in Section 4.3.2, the effective traction vector $\mathbf{t}'_\Gamma$ is given as a function of the displacement jump $\boldsymbol{\zeta}_e$, which, in turn, is approximated as constant on Γ_e. As a consequence, the effective traction vector is obtained as constant on the discontinuity and also a constant approximation of average pore pressure p_{f_Γ} is to be consistently considered on Γ_e. For example, a driving value p_{f_Γ} can be taken as coincident with the average value of p_f on the discontinuity, that is,

$$p_{f_\Gamma} = \frac{1}{l_e}\int_{\Gamma_e} p_f\, d\Gamma \tag{4.73}$$

Substitution of stress equations (4.72) allows to rewrite the weak balance (4.71) in terms of effective stresses and effective tractions, i.e.

$$-\frac{1}{A_e}\int_{\Omega_{e,loc}} \boldsymbol{\gamma}_e \cdot \boldsymbol{\sigma}'\mathbf{n}\, d\Omega + \frac{1}{l_e}\int_{\Gamma_e} \boldsymbol{\gamma}_e \cdot \mathbf{t}'_\Gamma\, d\Gamma = 0 \tag{4.74}$$

if the weak equation

$$\frac{1}{A_e}\int_{\Omega_{e,loc}} \boldsymbol{\gamma}_e \cdot p_f\mathbf{b}\mathbf{n}\, d\Omega - \frac{1}{l_e}\int_{\Gamma_e} \boldsymbol{\gamma}_e \cdot p_f\mathbf{b}\mathbf{n}\, d\Gamma = 0 \tag{4.75}$$

holds for all variations $\boldsymbol{\gamma}_e$ of the local displacement jump approximation. As a consequence of the piecewise constant approximation of the jump field and of the straight segment line Γ_e used to approximate the discontinuity in the element $\Omega_{e,loc}$, equation (4.75), in view of arbitrariness of $\boldsymbol{\gamma}_e$ and of the definition (4.73), yields:

$$p_{f_\Gamma} = \frac{1}{A_e} \int_{\Omega_{e,loc}} p_f \, d\Omega \tag{4.76}$$

The effects of this assumption on the definition of driving values of single fluid pressures (p_w, p_g) and saturation degrees (s_w, s_g) on the discontinuity are now investigated.

In the effective stress equation $(4.25)_1$, an approximated average pore pressure rate $\dot{\breve{p}}_f$ of equation $p_f = \sum_{\alpha=w,g} s_\alpha p_\alpha$ is considered, such that

$$\dot{\breve{p}}_f = \sum_{\alpha=w,g} s_\alpha \dot{p}_\alpha \tag{4.77}$$

In view of the constraint on saturation degrees

$$\sum_{\alpha=w,g} s_\alpha = 1 \tag{4.78}$$

and using definition (1.51) of the capillary pressure, equation (4.77) can be rewritten as

$$\dot{\breve{p}}_f = \dot{p}_\alpha + s_\beta \dot{p}_c \frac{\partial p_c}{\partial p_\beta} \qquad \text{for} \qquad \alpha, \beta = w, g \qquad \text{and} \qquad \alpha \neq \beta \tag{4.79}$$

To ensure consistency between large and small scales, equations (4.77) and (4.79) must hold also on the discontinuity. For example, equation (4.79) could be written in terms of values assumed constant on Γ_e for single-fluid pressures and saturation degrees, that is,

$$\dot{\breve{p}}_{f_\Gamma} = \dot{p}_{\alpha_\Gamma} + s_{\beta_\Gamma} \dot{p}_{c_\Gamma} \frac{\partial p_{c_\Gamma}}{\partial p_{\beta_\Gamma}} \qquad \text{for} \qquad \alpha, \beta = w, g \qquad \text{and} \qquad \alpha \neq \beta \tag{4.80}$$

In view of assumption (4.76) on the average pore pressure driving value and of continuum relation (4.79), equation (4.80) reads:

$$\dot{p}_{\alpha_\Gamma} + s_{\beta_\Gamma} \dot{p}_{c_\Gamma} \frac{\partial p_{c_\Gamma}}{\partial p_{\beta_\Gamma}} = \frac{1}{A_e} \int_{\Omega_{e,loc}} \dot{p}_\alpha \, d\Omega + \frac{1}{A_e} \int_{\Omega_{e,loc}} s_\beta \dot{p}_c \frac{\partial p_c}{\partial p_\beta} \, d\Omega \tag{4.81}$$

for $\alpha, \beta = w, g$ and $\alpha \neq \beta$. Consistently with assumption (4.76) on the average pore pressure, single fluid pressures on the discontinuity are assumed to satisfy the following

relation:

$$p_{\alpha_\Gamma} = \frac{1}{A_e} \int_{\Omega_{e,loc}} p_\alpha \, d\Omega \tag{4.82}$$

whose rate forms are introduced in equation (4.81), leading to:

$$s_{\alpha_\Gamma} \dot{p}_{c_\Gamma} = \frac{1}{A_e} \int_{\Omega_{e,loc}} s_\alpha \dot{p}_c \, d\Omega \qquad \text{for} \qquad \alpha = w, g \tag{4.83}$$

An other consistency requirement for the multi-scale approach is the satisfaction on the discontinuity of the constraint (4.78). Such a condition can be written in terms of values s_{α_Γ} assumed constant on Γ, that is,

$$\sum_{\alpha=w,g} s_{\alpha_\Gamma} = 1 \tag{4.84}$$

Time integration of equation resulting from combination of (4.83) with (4.84) leads to the following expression for the driving value of capillary pressure on the discontinuity

$$p_{c_\Gamma} = \frac{1}{A_e} \int_{\Omega_{e,loc}} p_c \, d\Omega \tag{4.85}$$

which is consistent with definition (1.51) of the capillary pressure in the continuum, as shown by substitution of such a definition in the right side of equation (4.85) and application of (4.82), leading to $p_{c_\Gamma} = p_{g_\Gamma} - p_{w_\Gamma}$.

Finally, the following value of the saturation degree on the discontinuity is obtained from substitution of the rate form of the driving capillary pressure (4.85) in relation (4.83):

$$s_{\alpha_\Gamma} = \frac{\displaystyle\int_{\Omega_{e,loc}} s_\alpha \dot{p}_c \, d\Omega}{\displaystyle\int_{\Omega_{e,loc}} \dot{p}_c \, d\Omega} \qquad \text{for} \qquad \alpha = w, g \tag{4.86}$$

that is, the $\dot{p}_c$-weighted average value of s_α in the continuum: it can be noted how, with the driving quantities defined above, the case of a porous solid saturated by a single fluid phase is fully recovered.

The consideration of the driving quantities described before, due to a piecewise constant approximation for displacement jumps and, consequently, of effective tractions, allow to numerically solve the local equilibrium by the following discretized form of the

weak balance (4.74):

$$\hat{\mathbf{r}}_{enh_e} = -\frac{1}{A_e}\int_{\Omega_{e,loc}} \mathbf{P}_e^T \boldsymbol{\sigma}' \, d\Omega \; + \; \mathbf{t}'_\Gamma = \mathbf{0} \tag{4.87}$$

As a consequence of the dilatant model considered in Section 4.3.3 for the localized response, the enhanced equation (4.87) can be rewritten in terms of a single enhanced strain parameter ζ_{t_e} in the following scalar form

$$r_{enh_e} = -\frac{1}{A_e}\mathbf{D}\int_{\Omega_{e,loc}} \mathbf{P}_e^T \boldsymbol{\sigma}' \, d\Omega \; + \; s'_\Gamma = 0 \tag{4.88}$$

where $\mathbf{D} := \begin{bmatrix} \text{sign}(\dot{\zeta}_{t_e})\Phi & 1 \end{bmatrix}$ denotes the projection operator [39], with Φ the localized dilatancy defined by $(4.60)_1$, and s'_Γ is the projected traction, defined as

$$s'_\Gamma := \mathbf{D}\mathbf{t}'_\Gamma = \tau_\Gamma \; + \; \text{sign}(\dot{\zeta}_{t_e}) \, \Phi \, \sigma'_\Gamma \; . \tag{4.89}$$

and given by integrating the localized softening law

$$\dot{\hat{s}}'_\Gamma(\zeta_{t_e}) = \frac{\tilde{\mathcal{H}}}{3 - 2\beta^2}\dot{\zeta}_{t_e} \tag{4.90}$$

In the evaluation of the integral in the equation (4.88), a standard quadrature rule is employed.

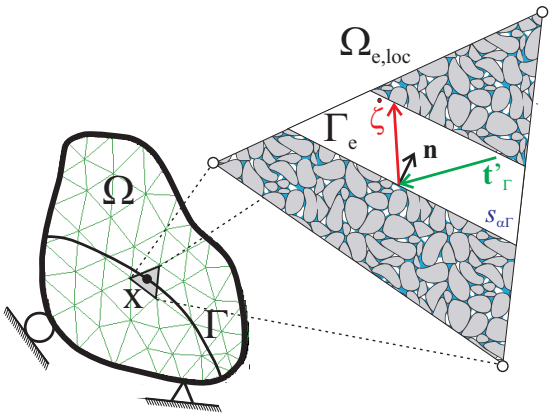

Figure 4.3: Driving effective traction and saturation degree along the discontinuity [35, 36]

The fluid flow finite element equation

The coupled fluid problem is determined by the weak fluid flow balances (4.6) in the large-scale. By means of interpolation of fluid pore pressures $\mathbf{N}_e^p$ and of fluid flows $\mathbf{B}_e^p$ considered in Section 4.4.2, the following residual equation is written for the generic fluid $\alpha = w, g$:

$$\mathbf{r}_\alpha = \mathbf{f}_\alpha^{ext} + \mathbf{f}_{\alpha,c} - \mathop{\mathbf{A}}_{e=1}^{n_{\text{el}}} \left[\int_{\Omega_e} \mathbf{N}_e^{pT} \dot{M}_\alpha \, d\Omega \; - \int_{\Omega_e} \mathbf{B}_e^{pT} \mathbf{q}_\alpha \, d\Omega \right] = \mathbf{0} \tag{4.91}$$

with $\mathbf{f}_\alpha^{ext}$ being the vector taking into account external nodal sources and prescribed boundary conditions for the fluid $\alpha = w, g$; the constitutive equation for the large-scale fluid mass content rate $\dot{M}_\alpha$ can be derived by the conforming part of its small-scale counterpart $(4.25)_2$. In the residual equation (4.91) the vector $\mathbf{f}_{\alpha,c}$ arises from unilateral boundary conditions prescribed on the flow of the fluid $\alpha = w, g$ along the boundary portion $\partial_c\Omega_e = \partial_c\Omega \cap \partial\Omega_e$ and introduced in Chapter 3: in the present work, such a contribution can be evaluated by a penalty method, i.e.

$$\mathbf{f}_{\alpha,c} = -\kappa \mathop{\mathbf{A}}_{e=1}^{n_{\text{el}}} \int_{\partial_c\Omega_e} \mathbf{N}_e^{pT} \langle g_\alpha \rangle \, dA \tag{4.92}$$

with the penalty coefficient κ, the gap $g_\alpha = p_\alpha - p_{\alpha,max}$ and the classical Macaulay operator $\langle \cdot \rangle$ returning the positive part of $(\cdot)$.

4.4.3 Solution of the finite element system

The coupled discretized problem in the unknowns $\mathbf{d}$, $\boldsymbol{\zeta}_e$ and $\mathbf{p}_\alpha$ can be solved by equations (4.70), (4.88) and (4.91). In particular, a standard backward-Euler approximation of the fluid balance (4.91) may be considered, where, in a typical time step $[t_n, t_{n+1}]$ (with $\Delta t = t_{n+1} - t_n$), rate terms are approximated as $\dot{(\cdot)} = [(\cdot)_{n+1} - (\cdot)_n]/\Delta t$ and all the other terms are evaluated at t_{n+1}. A standard closest-point projection return mapping [128] is employed for the bulk elastoplastic model [39] to evaluate the effective stress $\boldsymbol{\sigma}'_{n+1}$ at each quadrature point. A similar procedure is used for the localized softening model: the details of the algorithm can be found in [10, 11].

The resulting coupled solving system is highly non-linear due to the bulk elastoplastic constitutive model, to the localized softening law and to the partial saturation

assumption: assuming the solution known at t_n, a standard Newton-Raphson iterative procedure is employed to achieve the solution at t_{n+1}. The details of the linearization process are omitted here: the interested reader is referred to [33] for the treatment of mechanical non-linearities and to Chapters 2 and 3 for the fluid part; in the forthcoming developments the sub-index $(\cdot)_{n+1}$ will be omitted to simplify the notation. The linearized algebraic solving system takes the form

$$\left\{ \begin{array}{rcl} \mathbf{r}_m^{(k)} & = & \mathbf{K}^{(k)} \Delta \mathbf{d} - \displaystyle\sum_{\gamma=w,g} \mathbf{Q}_{m\gamma}^{(k)} \Delta \mathbf{p}_\gamma - \mathop{\mathbf{A}}_{e=1}^{n_{\mathrm{el}}} \mathcal{L}_{G_e} \, \Delta \zeta_{t_e} \\ \mathbf{r}_\alpha^{(k)} & = & \left(\dfrac{\mathbf{Q}_{\alpha m}}{\Delta t} \right)^{(k)} \Delta \mathbf{d} + \displaystyle\sum_{\gamma=w,g} \left(\dfrac{\mathbf{S}_{\alpha\gamma}}{\Delta t} - \mathbf{G}_{\alpha\gamma} + \mathbf{H}_\alpha \delta_{\alpha\gamma} + \mathbf{P}_\alpha \delta_{\alpha\gamma} \right)^{(k)} \Delta \mathbf{p}_\gamma \end{array} \right. \tag{4.93}$$

for $\alpha = w, g$, with the enhanced parameters $\Delta\zeta_{t_e}$ obtained at the elemental level by the linearized form of equation (4.88)

$$r_{enh_e}^{(k)} - \mathcal{L}_{P_e}^T \, \Delta \mathbf{d}_e + \mathcal{H}_e \, \Delta \zeta_{t_e} = 0 \tag{4.94}$$

Linearized equations (4.93) and (4.94) are to be solved in the increments $\Delta(\cdot) = (\cdot)_{n+1}^{k+1} - (\cdot)_{n+1}^{k}$, where indexes (k) and $(k+1)$ denote the solution at the previous iteration and the newly obtained solution estimate, respectively.

The global coupled solving system (4.93) is written in terms of global matrices of stiffness $\mathbf{K}$, storage $\mathbf{S}_{\alpha\beta}$, fluid-mechanical coupling $\mathbf{Q}_{m\alpha}, \mathbf{Q}_{\alpha m}$ and permeability $\mathbf{H}_\alpha$, defined as:

$$\mathbf{K} = \mathop{\mathbf{A}}_{e=1}^{n_{\mathrm{el}}} \int_{\Omega_e} \mathbf{B}_e^{uT} \frac{\partial \boldsymbol{\sigma}}{\partial \boldsymbol{\varepsilon}} \mathbf{B}_e^u \, d\Omega \tag{4.95}$$

$$\mathbf{S}_{\alpha\beta} = \mathop{\mathbf{A}}_{e=1}^{n_{\mathrm{el}}} \int_{\Omega_e} \mathbf{N}_e^{pT} \frac{\partial M_\alpha}{\partial p_\beta} \mathbf{N}_e^p \, d\Omega \qquad \text{for} \quad \alpha, \beta = w, g \tag{4.96}$$

$$\left. \begin{array}{rcl} \mathbf{Q}_{m\alpha} & = & \displaystyle\mathop{\mathbf{A}}_{e=1}^{n_{\mathrm{el}}} \int_{\Omega_e} \mathbf{B}_e^{uT} \frac{\partial \boldsymbol{\sigma}}{\partial p_\alpha} \mathbf{N}_e^p \, d\Omega \\ \mathbf{Q}_{\alpha m} & = & \displaystyle\mathop{\mathbf{A}}_{e=1}^{n_{\mathrm{el}}} \int_{\Omega_e} \mathbf{N}_e^{pT} \frac{\partial M_\alpha}{\partial \boldsymbol{\varepsilon}} \mathbf{B}_e^u \, d\Omega \end{array} \right\} \qquad \text{for} \quad \alpha = w, g \tag{4.97}$$

$$\mathbf{H}_\alpha = \mathop{\mathbf{A}}_{e=1}^{n_{\mathrm{el}}} \int_{\Omega_e} \rho_{\alpha 0} \mathbf{B}_e^{pT} \mathbf{k}_\alpha \mathbf{B}_e^p \, d\Omega \qquad \text{for} \quad \alpha = w, g \tag{4.98}$$

Remaining matrices $\mathbf{G}_{\alpha\beta}$, $\mathbf{P}_\alpha$ and $\mathcal{L}_{G_e}$ appearing in (4.93) are linearizing operators due to the dependence of the permeability $\mathbf{k}_\alpha$ on the pore pressure p_β in the partially saturated range, to the unilateral boundary condition on the fluid α and to localized enhancement ζ_{t_e}, respectively:

$$\begin{aligned} \mathbf{G}_{\alpha\beta} &= \mathop{\mathbf{A}}_{e=1}^{n_{el}} \int_{\Omega_e} \mathbf{B}_e^{pT} \frac{\partial \mathbf{k}_\alpha}{\partial p_\beta} \mathbf{q}_\alpha^{uni} \mathbf{N}_e^p \, d\Omega \\ \mathbf{P}_\alpha &= \kappa \mathop{\mathbf{A}}_{e=1}^{n_{\rm el}} \int_{\partial_c \Omega_e} \rho_{\alpha 0} H(g_\alpha) \mathbf{N}_e^{pT} \mathbf{N}_e^p \, d\Omega \\ \mathcal{L}_{G_e} &= \mathbf{L}_{G_e} \mathbf{D}^T \end{aligned} \tag{4.99}$$

with the standard Heaviside function $H(\cdot)$ and

$$\mathbf{q}_\alpha^{uni} := -\rho_{\alpha 0}(\mathbf{B}_e^p \mathbf{p}_{\alpha_e} - \rho_{\alpha 0}\mathbf{g}) \quad \text{and} \quad \mathbf{L}_{G_e} = \int_{\Omega_{e,loc}} \mathbf{B}_e^{uT} \mathbb{C}_{sk} \, \mathbf{G}_e \, d\Omega \tag{4.100}$$

In a similar way the operators in the enhanced equation (4.94) can be determined as:

$$\mathcal{L}_{P_e} = \frac{1}{A_e} \int_{\Omega_{e,loc}} \mathbf{B}_e^{uT} \mathbb{C}_{sk} \, \mathcal{P}_e \, d\Omega \qquad \mathcal{H}_e = \frac{1}{A_e} \int_{\Omega_{e,loc}} \mathcal{P}_e^T \mathbb{C}_{sk} \, \mathcal{G}_e \, d\Omega + \frac{ds'_\Gamma}{d\zeta_{t_e}} \tag{4.101}$$

with $\mathcal{P}_e = \mathbf{P}_e \mathbf{D}^T$ and $\mathcal{G}_e = \mathbf{G}_e \mathbf{D}^T$. Because of no continuity requirements are prescribed for the local enhancement ζ_{t_e} and then no assembly operation is requested for enhanced equations (4.94), a staggered static condensation strategy proposed in [129, 130] and employed, for instance, in [33, 39], is considered: firstly, the enhanced equation (4.94) is iteratively solved for fixed value of $\mathbf{d}^{(k)}$ and $\mathbf{p}_\alpha^{(k)}$ and then such values are iteratively updated in the solution of the global problem (4.93), after static condensation of the mechanical part $(4.93)_1$; further details are omitted for the sake of brevity. The use of unregularized discontinuity and of static condensation allows to avoid the use of non-standard quadrature rules: this is to be contrasted with alternative approaches based on numerical regularization of the discontinuity [104].

4.5 Representative numerical simulations

In this section the results of numerical tests are presented to assess the performance of the finite element formulation proposed in Section 4.4. A plane strain compression

test is presented in Section 4.5.1, where the effects of mesh size and alignment on the solution are investigated, as done for the same test in [33] and [34] for fully saturated porous media subjected to infinitesimal and finite deformations, respectively. Moreover, results obtained with the proposed formulation are contrasted with the ones obtained with a standard finite element formulation of the multiphase problem, where "standard" stands for the classical continuum strain softening implemented with the conventional Galerkin interpolations, with no enhancement of the strain field. Finally, we analyze differences between the results obtained in partially and in fully saturated conditions. Furthermore, two different boundary conditions are considered to model top and bottom surfaces of the sample: a prescribed null liquid pressure and the unilateral constraint described in Chapter 3.

In the numerical simulations the pressure of the gaseous phase is constantly hold equal to the atmospheric value, i.e. $p_g = 0$.

The enhanced finite element method developed in previous sections is implemented over the mixed triangle with quadratic interpolation of the displacement and linear interpolation of volumetric strain and stress, that is, the so called P2/P1 six noded triangle; quadratic interpolations are also used for the pore pressure field. The same finite element, but with no strain enhancement, is used to perform computations in the standard finite element framework for a comparison with the response obtained by the enhanced finite element.

As in [33], the enhanced fields are added after propagation of the discontinuity through the use of the localization condition (4.57), evaluated with a tolerance of 1.0×10^{-3}. After the localization is detected, the localized linear softening law

$$\tilde{q}(\alpha_\mu) = -\sigma_y - \tilde{\mathcal{H}}\alpha_\mu \tag{4.102}$$

is used, with $\tilde{\mathcal{H}}$ and σ_y the localized softening modulus and the yield stress, respectively. A linear isotropic response is considered to model the hyperelastic part of the solid skeleton constitutive law, with drained Young modulus E_{sk} and Poisson coefficient ν_{sk}, as well as the flow law, with a saturated permeability matrix $\mathbf{k}_{sat} = k_{sat}\,\mathbf{1}$.

4.5.1 Plane strain compression test

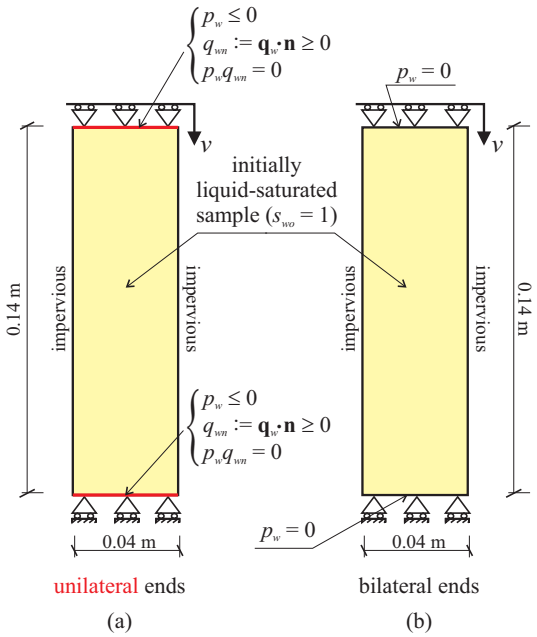

Figure 4.4: Plane strain compression test. Configuration of the problem and assumed boundary conditions with unilateral (a) and bilateral (b) ends

In this section the numerical simulation of a plain strain compression test is considered, with geometry and boundary conditions illustrated in Figure 4.4, where a constant vertical displacement rate $v = 5.0 \times 10^{-6}\ m/s$ is applied at the top of an initially fully saturated sample ($s_{w0} = 1$). In particular, two different kinds of boundary conditions have been considered to model the sample bases.

Free-drainage conditions can be imposed to both ends by a prescribed constant null value of the pore pressure as depicted in Figure 4.4b, thus leading to the so-called globally "drained" test: this boundary condition simulates a continuous water supply through the bases, that flows into the specimen center due to the negative pore pressure concentration developing along the dilatant discontinuity. However, it could be argued that, starting from fully saturated conditions, if lateral surfaces are impervious (to liquid and gaseous phases) and both ends are constantly saturated due to the boundary condition, the air can not enter into the specimen from the outside and partially saturated conditions can be attained only with cavitation [116, 121]. Because

Table 4.1: Material parameters considered in numerical simulations of the plane strain compression test

solid-skeleton bulk modulus	κ_{sk}	13300	kPa
solid-skeleton shear modulus	μ_{sk}	8000	kPa
Drucker-Prager pressure coefficient	β	0.56	
initial yield stress	σ_y	63.41	kPa
localized softening modulus	$\tilde{\mathcal{H}}$	-25000	kPa/m
continuum softening modulus	$\mathcal{H}$	0	kPa
Biot coefficient	b	1.0	
liquid-saturated permeability	k_{sat}	10^{-8}	$m^2/(kPa\,s)$
initial porosity	n_0	0.423	
van Genuchten parameter	a_{vg}	0.04	$1/kPa$
van Genuchten parameter	n_{vg}	3.3	
residual liquid saturation degree	$s_{w,res}$	0.1	
solid phase volumetric stiffness	κ_s	$1.0 \cdot 10^9$	kPa
liquid phase volumetric stiffness	κ_w	$1.42 \cdot 10^6$	kPa
liquid density	ρ_w	$1.0 \cdot 10^3$	kg/m^3
initial liquid pressure	p_{w0}	0	kPa

of this phenomenon is not considered in the present multiphase model, a different desaturation mechanism is considered herein.

In particular we assume that no water supply is provided at the bases and the porous solid is in contact with the atmosphere. When in the compression early stages a pore pressure positive distribution arises in the specimen, a null pressure value is prescribed at the bases and a positive outflow takes place. As the pore pressure distribution becomes negative, the bases become impervious to the water flow and a desaturation process takes place at sample bases. This boundary condition is depicted in Figure 4.4a and is dealt herein by the unilateral interfaces introduced in Chapter 3.

Parameters assumed for solid skeleton, porous solid, solid and fluid phases are

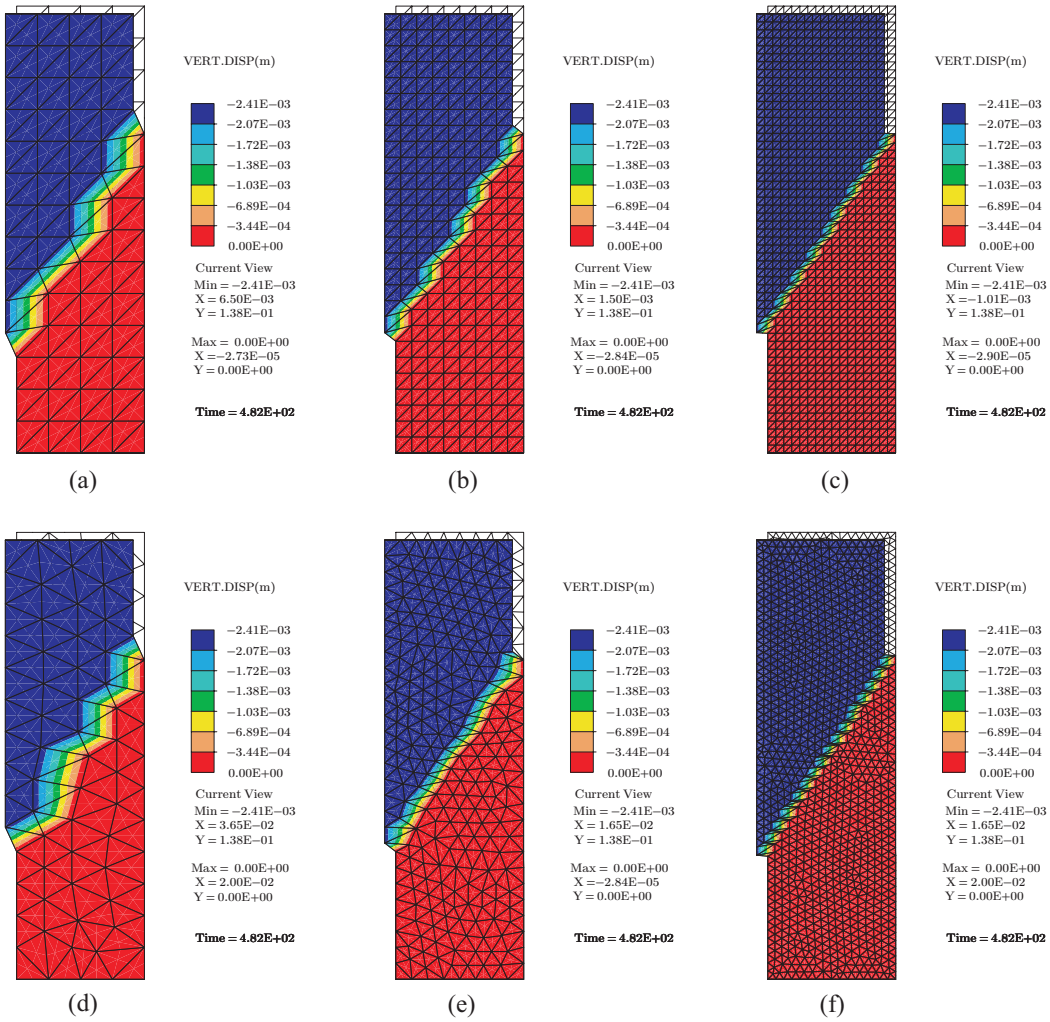

Figure 4.5: Plane strain compression test: enhanced finite elements with strong discontinuities. Contours of vertical displacements on deformed meshes obtained at indicated time with structured finite element meshes of 2×4×14 (a), 2×8×28 (b) and 2×16×56 (c) elements, and with unstructured meshes of 110 (d), 478 (e) and 1964 (f) elements, respectively

reported in Table 4.1: it can be noted that the obtained hydraulic liquid-saturated permeability is $k_{h,sat} = \rho_{w0}|\mathbf{g}|k_{sat} = 1.0 \cdot 10^{-7}\ m/s$ and that, according to (4.27), the Biot modulus relative to the fully saturated case is $Q = 3.33 \cdot 10^{6}\ kPa$. Furthermore, expressions introduced in [147] for saturation degree s_w and relative permeability coefficient k_w^{rel} are considered:

$$\begin{cases} S_w(p_c) = \left[\dfrac{1}{1+(a_{vg}\,p_c)^{n_{vg}}}\right]^{m_{vg}} & \text{with} \quad S_w := \dfrac{s_w - s_w^{res}}{1 - s_w^{res}} \\ k_w^{rel}(s_w) = S_w^{1/2}\left[1-\left(1-S_w^{1/m_{vg}}\right)^{m_{vg}}\right]^2 & \text{with} \quad m_{vg} = 1 - 1/n_{vg} \end{cases} \tag{4.103}$$

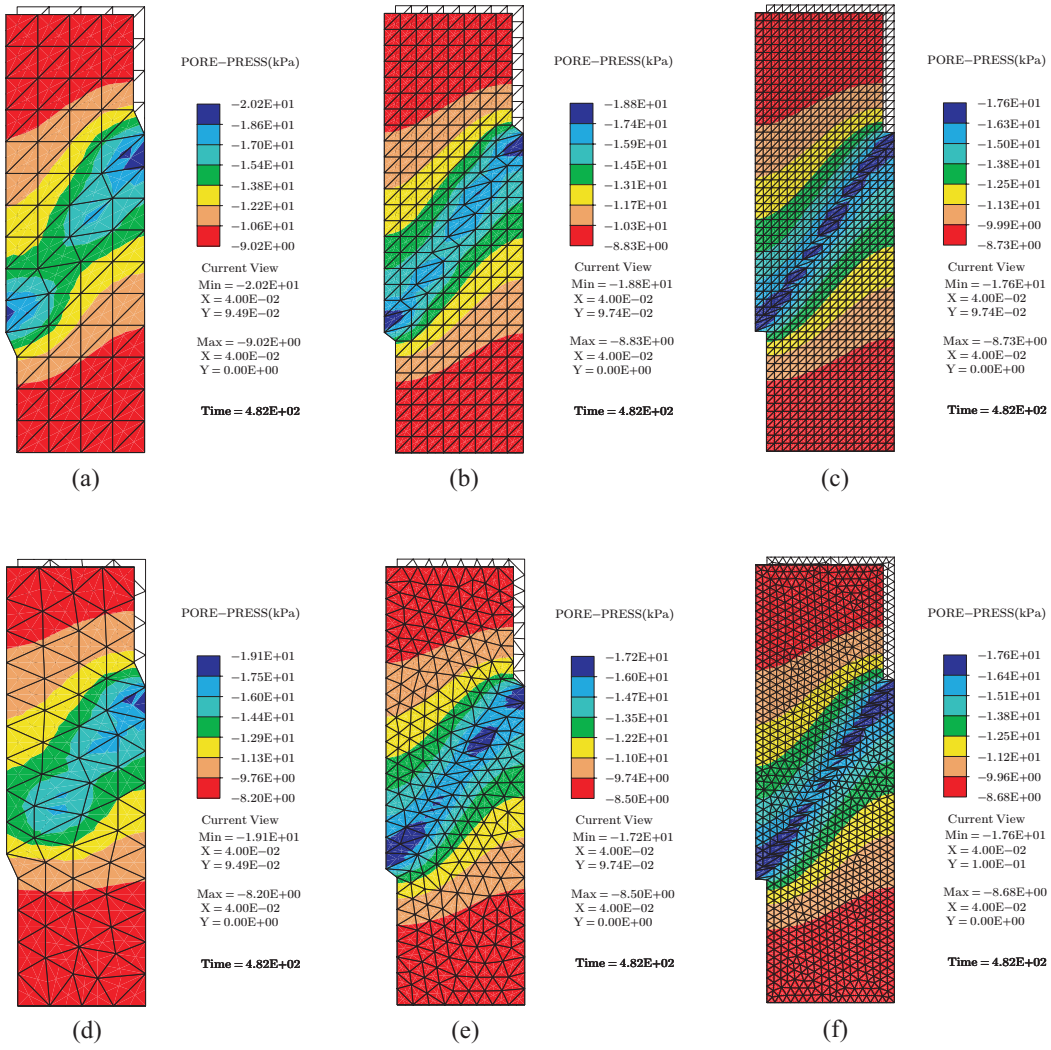

Figure 4.6: Plane strain compression test: enhanced finite elements with strong discontinuities. Contours of pore liquid pressure on deformed meshes obtained at indicated time with structured finite element meshes of 2×4×14 (a), 2×8×28 (b) and 2×16×56 (c) elements, and with unstructured meshes of 110 (d), 478 (e) and 1964 (f) elements, respectively

The test is performed employing six different finite element discretizations of the sample (Fig. 4.5): three structured meshes consisting of 2×4×14 (a), 2×6×22 (b) and 2×8×28 (c) elements, as well as three unstructured meshes consisting of 110 (d), 272 (e) and 478 (f) elements, respectively. The obtained solutions are all practically coincident, both in terms of vertical reaction (Fig. 4.9a) and of pore liquid pressure (Fig. 4.6 and Fig. 4.9b), thus showing the objectivity of the described method with respect to the mesh size and alignment. Largest differences can be noted for the saturation degree

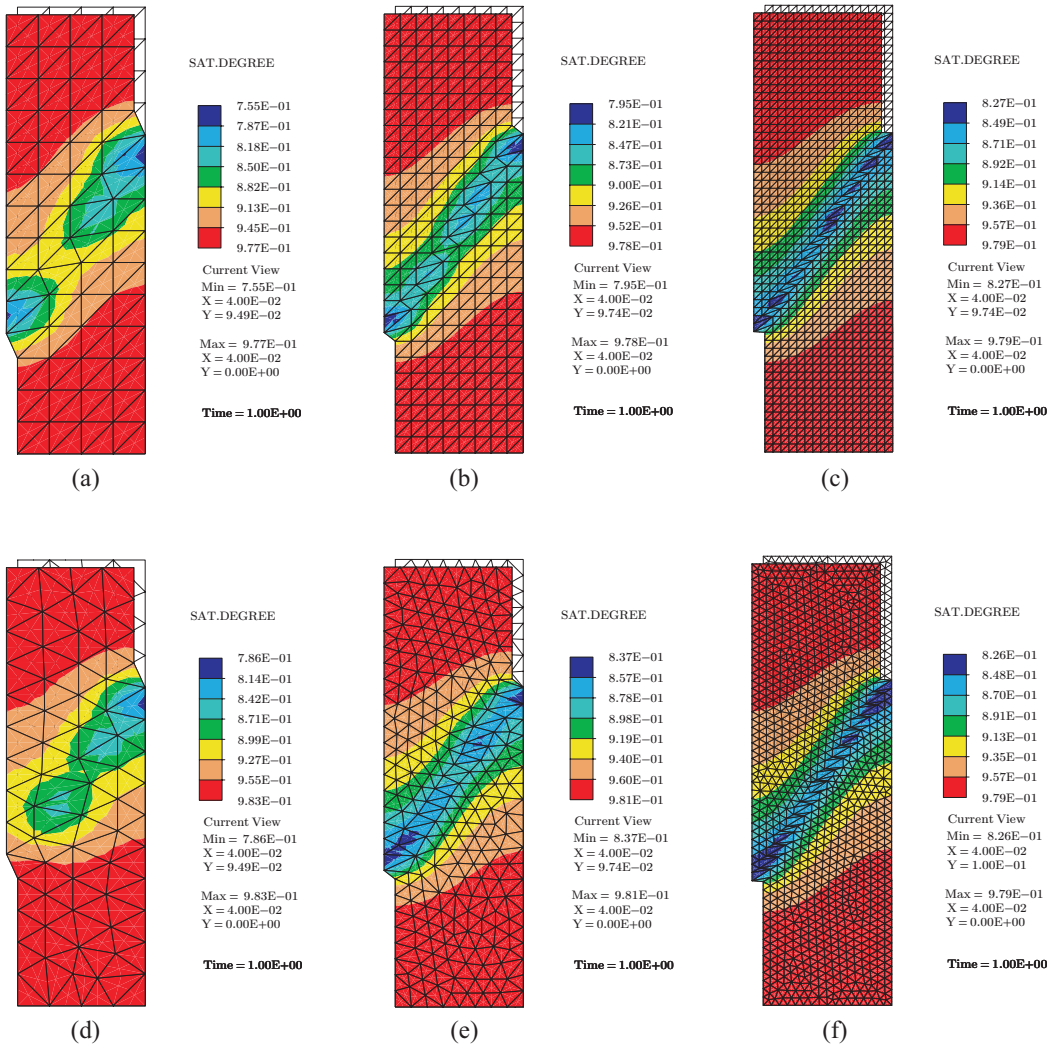

Figure 4.7: Plane strain compression test: enhanced finite elements with strong discontinuities. Contours of saturation degree on deformed meshes obtained at indicated time with structured finite element meshes of 2×4×14 (a), 2×8×28 (b) and 2×16×56 (c) elements, and with unstructured meshes of 110 (d), 478 (e) and 1964 (f) elements, respectively

(Fig. 4.7 and Fig. 4.10a) and for the relative permeability coefficient (Fig. 4.10b): this is mainly due to the employed retention model (4.103), whose analytical form strongly amplifies the observed small differences in pore liquid pressures.

The effectiveness of the method in capturing discontinuity propagation across the sample is shown in Figure 4.5, where the localized elements are clearly highlighted by contours of vertical displacements and by the deformed configuration of the mesh. We remark that no displacement amplification is employed in the representation of the

deformed meshes reported herein. We also remark that no imperfection is introduced

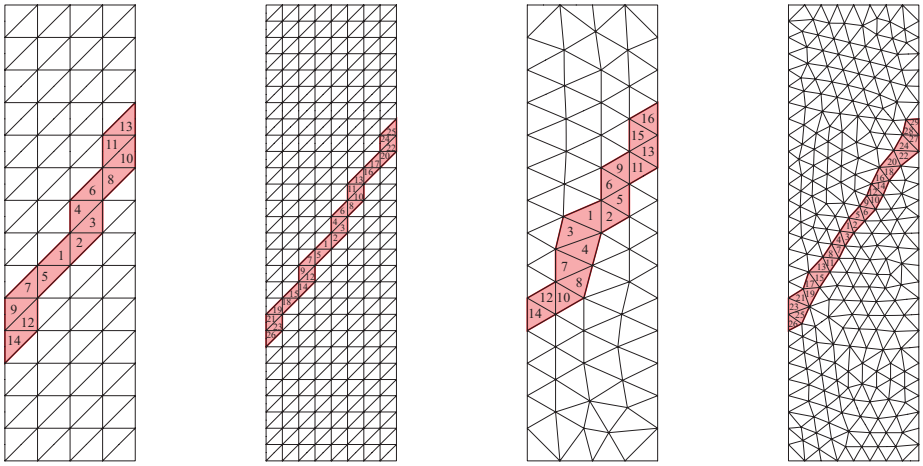

Figure 4.8: Plane strain compression test. Elements crossed by discontinuity, numbered to show the time sequence of discontinuity activation. Results obtained with structured finite element meshes of 2×4×14 (a) and 2×8×28 (b), and with unstructured meshes of 110 (c) and 478 (d) elements, respectively

to trigger the onset of localization. On the contrary, condition (4.57) for discontinuity activation is satisfied by the heterogeneous effective stress state induced by fluid flow coupling since the early stages of the test. In Figure 4.8, elements crossed by strong discontinuities are highlighted and numbered to show the time sequence of discontinuity activation. It can be observed that practically the same propagation history is obtained for the employed meshes. In particular, discontinuity is firstly activated in the central part of the sample and antisymmetrically propagates towards the lateral boundaries. The instants corresponding to first and last localization registered in finite elements are marked on curves plotted in Figures 4.9 and 4.10.

The same test is also simulated by means of the standard finite element formulation, setting $\mathcal{H} = -200\ kPa$ for the continuum strain-softening modulus. Conventional finite elements show difficulties in capturing localization in an objective way, as demonstrated by the structured deformed mesh reported in Figure 4.11. A considerable mesh-size dependence is exhibited by the standard finite element solution, both in terms of vertical reaction (Fig. 4.13a) and pore liquid pressure (Fig. 4.12 and Fig. 4.13b).

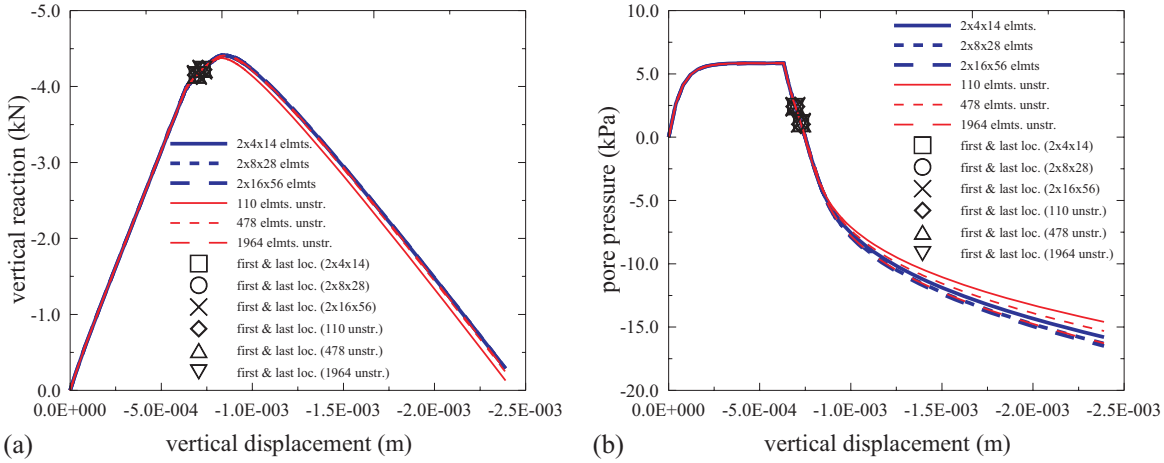

Figure 4.9: Plane strain compression test: enhanced finite elements with strong discontinuities. Results corresponding to structured meshes with 2×4×14, 2×8×28, 2×16×56, and unstructured meshes with 110, 478 and 1964 elements: vertical reaction (a) and pore liquid pressure (b) at sample center, both versus the imposed vertical displacement

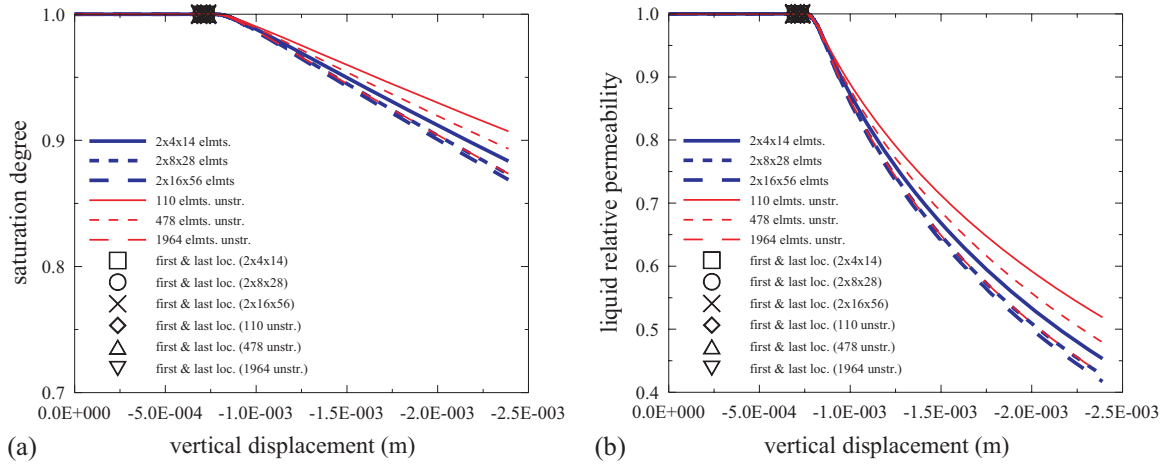

Figure 4.10: Plane strain compression test: enhanced finite elements with strong discontinuities. Results corresponding to structured meshes with 2×4×14, 2×8×28, 2×16×56, and unstructured meshes with 110, 478 and 1964 elements: liquid phase saturation degree (a) and relative permeability (b) at sample center, both versus the imposed vertical displacement

Due to the draining action of the dilatant discontinuity and to subsequent negative pore liquid pressures (Fig. 4.6 and Fig. 4.9b), conditions of partial saturation are calculated in the proximity of the strong discontinuity ($s_w < 1$ in Fig. 4.10), as expected. Moreover, the main effect of the unilateral constraint on both ends is that partially saturated conditions are attained not only on the discontinuity but also in

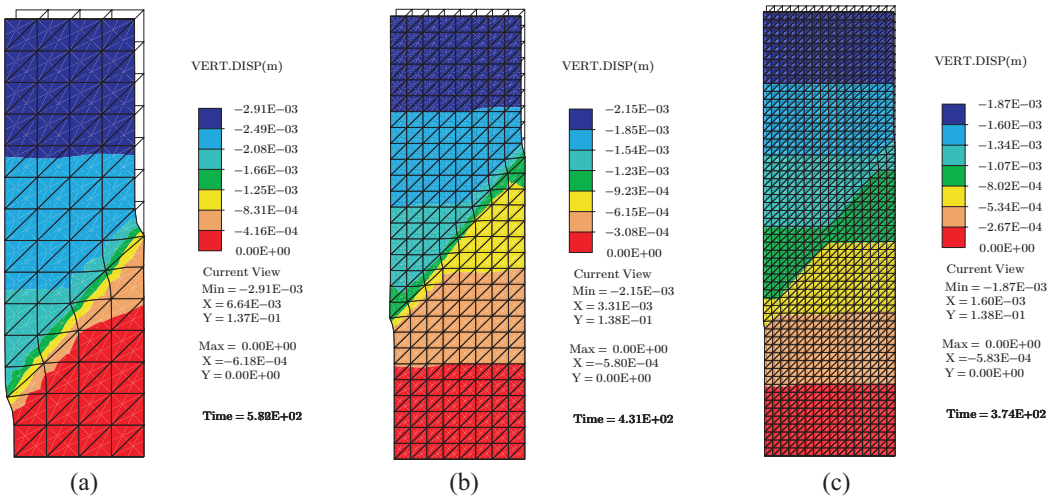

Figure 4.11: Plane strain compression test: standard coupled finite element formulation (Galerkin formulation with no strong discontinuities). Contours of vertical displacements on deformed configuration obtained at the indicated time with structured mesh of 2×4×14 (a), 2×8×28 (b) and 2×16×56 (c) elements, respectively

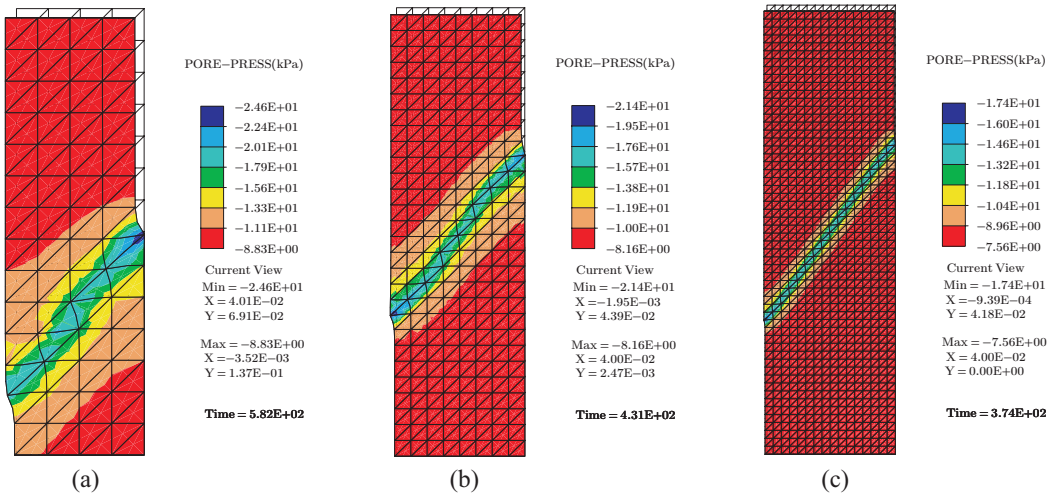

Figure 4.12: Plane strain compression test: standard coupled finite element formulation (Galerkin formulation with no strong discontinuities). Contours of pore liquid pressure on deformed configuration obtained at the indicated time with structured mesh of 2×4×14 (a), 2×8×28 (b) and 2×16×56 (c) elements, respectively

the whole specimen. In fact, as it can be noted in Figure 4.14, as the discontinuity is completely formed and begins to drain the specimen, the pore liquid pressure begins to drop instantaneously in the whole sample, but with increasing velocity near the discontinuity. Therefore, the specimen begins to desaturate at the same time in its whole length, but, as air has entered in the domain from the outside, the saturation

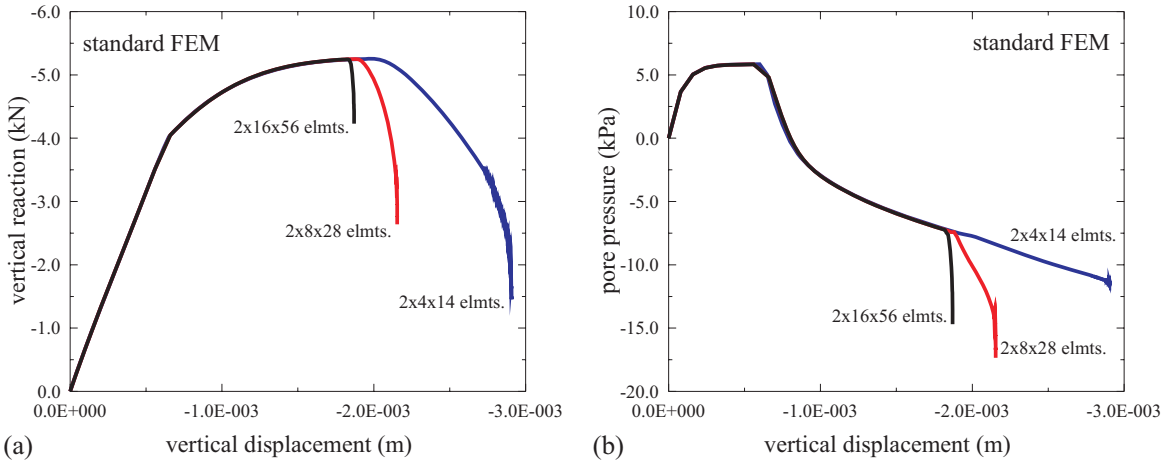

Figure 4.13: Plane strain compression test: standard coupled finite element formulation. Results corresponding to structured meshes with 2×4×14, 2×8×28, 2×16×56 elements: vertical reaction (a) and pore liquid pressure (b) at sample center, both versus the imposed vertical displacement

degree decreases more rapidly near the dilatant discontinuity.

The response calculated with the formulation proposed herein is compared in Figure 4.15 with the response obtained assuming the porous solid as constantly fully saturated by the liquid phase. Differences between the vertical reactions calculated with the two

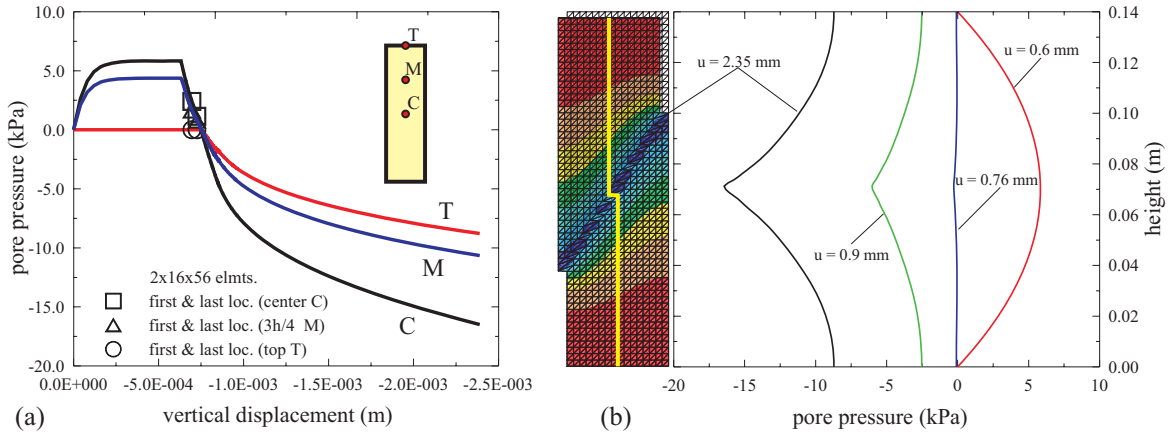

Figure 4.14: Plane strain compression test: enhanced finite elements with strong discontinuities (structured mesh with 2×16×56 elements). Desaturation process in terms of pore pressure evolution in three points (a) and in terms of pore pressure distribution at different instants

formulations are apparent in the post-localization response (Fig. 4.15a), due to the

development of negative pore pressures (Fig. 4.15b). With respect to the case of variable liquid saturation, the assumption of full saturation together with unilateral boundary conditions, leads to difficulties in capturing a post-localization softening branch. In fact, when a negative pore liquid pressure distribution arises in the whole sample, globally "undrained" conditions are attained and a softening branch can be obtained only if partial saturation effects are taken into account.

A different behavior can be noted if pore liquid pressure is constantly kept equal to the null value at the sample ends, as in [33, 34]. In this case, the full saturation assumption implies an overestimation of negative pore pressures (Fig. 4.16b) with the related strengthening effects (Fig. 4.16a), due to underestimation of storage modulus in fluid content equation (4.34) and to overestimation of the role played by liquid phase in stress equation $(4.25)_1$.

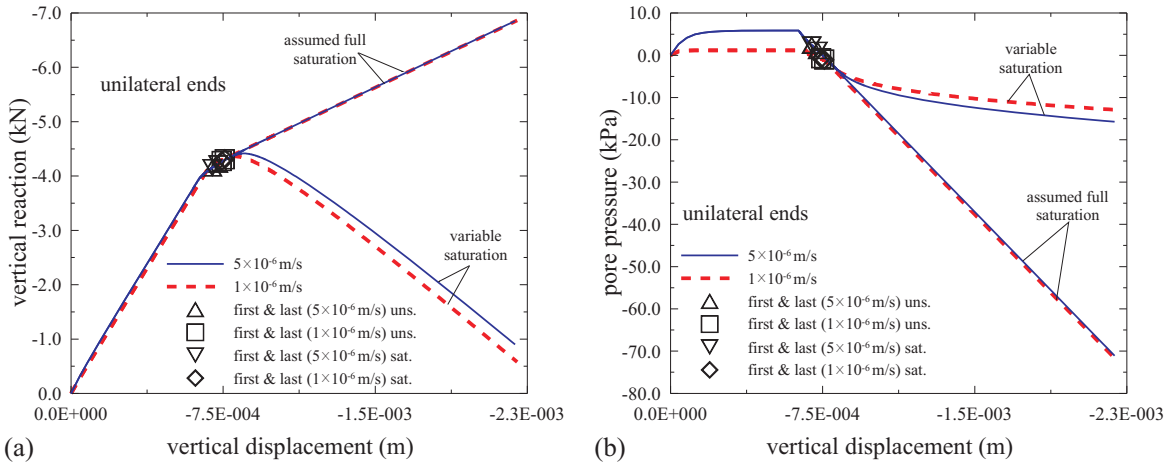

Figure 4.15: Plane strain compression test: enhanced finite elements with strong discontinuities (structured mesh with 2×16×56 elements). Response obtained with formulations assuming variably saturated and fully saturated conditions and with unilateral ends, both for the displacement rates $v = 1.00 \cdot 10^{-6}\ m/s$ and $v = 5.00 \cdot 10^{-6}\ m/s$. Vertical reaction (a) and pore liquid pressure at sample center (b) vs. vertical imposed displacement

The test is also simulated for a slower vertical displacement rate ($v = 1.00 \cdot 10^{-6}\ m/s$). With respect to the assumed fully saturated case and consistently with the above considerations, rate effects are less apparent if variable liquid saturation is taken into account (Fig. 4.16a). For the slower displacement rate, results obtained

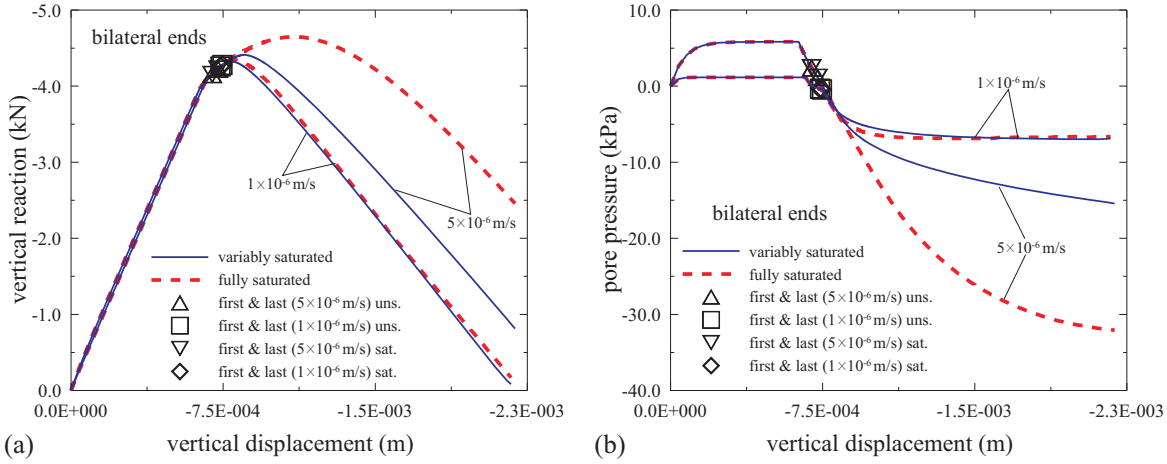

Figure 4.16: Plane strain compression test: enhanced finite elements with strong discontinuities (structured mesh with 2×16×56 elements). Response obtained with formulations assuming variably saturated and fully saturated conditions and with bilateral ends, both for the displacement rates $v = 1.00 \cdot 10^{-6}\ m/s$ and $v = 5.00 \cdot 10^{-6}\ m/s$. Vertical reaction (a) and pore liquid pressure at sample center (b) vs. vertical imposed displacement

with the two formulations are practically coincident, due to the small magnitude of post-localization negative pore pressures (Fig. 4.16b).

The strengthening effect due to more rapid vertical displacement rates can be observed, for the partially saturated case, also when unilateral constraints are employed to model sample ends (Fig. 4.15a). However, this difference is less remarkable with respect to the case of globally "drained" conditions. It can also be shown how, in the saturated case, no coupling effects arise from the application of a different displacement velocity when no inflow is allowed at the sample bases, because globally "undrained" conditions hold as negative pore liquid pressures are attained in the whole length.

Finally, for slower rates, as already observed in [33], pre-localization excess pore pressures are practically negligible and the corresponding effective stress state is not "heterogeneous enough" to avoid the numerical sensitivity of the localization onset. So, to trigger the localization onset in this computation, a 1% yield stress imperfection is introduced in the element marked with "1" in Figure 4.8.

Conclusions

In this thesis we have presented a constitutive theory for multiphase porous solids developed in a macroscopic thermodynamic framework. Numerical formulations of this model in the framework of non-standard finite element methods have been also considered to model strain localization phenomena in multiphase continua.

As a first step, a general form of hyperelastic rate equations has been provided for a three-phase porous continuum in terms of tangent operators (solid skeleton elastic tensor, coupling tensors, storage modulus). Particular forms for these operators have been obtained by means of tools typically employed in mixture theories. The compatibility of the so-obtained operators with the aforementioned macroscopic thermodynamical theory has been investigated by employing symmetry and Maxwell conditions. The aforementioned constitutive model is also presented by Callari and Abati [31].

A finite element formulation of the proposed hyperelastic laws for porous media has been developed for quasi-static problems in the infinitesimal deformation range and is presented by Callari and Abati [32]. The highly non-linear solving system resulting from discretization in space and time domains has been solved by a standard Newton-Raphson iterative procedure, focusing the attention on the linearization process. Numerical examples have been also presented to assess the effectiveness of the numerical formulation. In particular, benchmark problems involving the desaturation of a sand column [96] and the propagation of a saturation front in an initially dry solid [106] have been simulated. The formulation has been also applied to analyze a problem of interest for dam engineering, namely the analysis of the effects of rapid drawdown on a reservoir bank.

We have also considered the theoretical treatment and the numerical formulation of boundary conditions commuting between "imposed pressure" and "imposed flow" types, depending on the system response evolution. This kind of boundary conditions effectively models interfaces between porous solid and atmosphere in many situations of practical interest where the geometric locus of zero pore pressure intersects the boundary in contact with atmosphere. In this thesis these boundary conditions have been formulated in the general framework of unilateral constraints. Penalty and augmented Lagrangian numerical techniques have been introduced to treat fluid-flow unilateral boundaries in the finite element formulation for multiphase porous solids presented in Chapter 2. The performance of such regularization techniques has been investigated by representative numerical examples. Firstly, simple one-dimensional problems have been considered, where both the numerical and formal analogies between seepage problems with unilateral constraints and frictionless contact problems have been pointed out. Further situations of practical interest have been numerically simulated, as the propagation of a saturation front in a soil sample during a rainfall event and the partial saturation of a concrete gravity dam. The numerical formulation of unilateral boundary conditions on fluid flow, as well as applications to representative examples, is also presented by Abati and Callari [3].

The extension to irreversible phenomena of a simplified form of the aforementioned hyperelestic model has been presented in the general framework of additive elasto-plastic decompositions of strains and fluid mass contents. This constitutive theory has led to a simple expression for the Clausius-Duhem inequality, which has been employed in a multi-scale approach to strain localization [8] in multiphase continua. In particular, we have extended to partially saturated conditions the analysis of strong discontinuities presented in [33, 34] for fully saturated porous solids. With this aim, we have considered discontinuous displacement fields and corresponding singular distributions of strain, as well as singular distributions of fluid contents corresponding to discontinuous flows of gaseous and liquid phases, modelling their accumulation and/or drainage in the localized failures of interest. In the multi-scale context employed herein, the small-scale problem has been defined by the localized mass balances of liquid and gas contents,

both related to singular dilatancy of the discontinuity, besides the mechanical response driven by the assumed effective traction. The localized dissipative mechanism has been modelled by an associated Drucker-Prager criterion [39], thus leading to particular forms for the localization condition and the localized softening law relating effective traction on the discontinuity surface to the displacement jump. Pore pressures and saturation degrees on the discontinuity have been properly defined to connecte small and large-scale problems through a weak equilibrium statement between traction acting on the discontinuity surface and stresses in the bulk. The governing equations have been approximated by finite elements enhanced with singular fields of strain and fluid contents. These enhancements have been kept local at the element level, allowing the static condensation of the different enhanced parameters. The aforementioned theoretical and numerical formulation of localization analysis in multiphase porous media is also presented by Callari, Armero and Abati in [37], together with numerical representative examples.

Finally, results of the numerical simulation of a plain strain compression test on a partially saturated porous solid have been presented. The effects of mesh size and alignment on the solution have been investigated. The obtained results have shown the effectiveness of the proposed method in capturing discontinuity propagation across the sample in terms of displacements, pore pressures, saturation degree and propagation history of the discontinuity. These results have been contrasted with the ones obtained with a standard finite element formulation of the multiphase problem. The so-obtained results have shown the difficulties of conventional finite elements in capturing localization in an objective way. Finally, results obtained in variably saturated conditions are contrasted with the ones obtained in the fully saturated case. Moreover, two different boundary conditions have been considered on top and bottom surfaces: a prescribed null liquid pressure value and the aforementioned unilateral boundary conditions. In the latter case, we have simulated the localization-induced desaturation of a porous sample in contact with the atmosphere.

The numerical simulations presented in this work show how the proposed model and the relative non-standard finite element formulation are able to effectively cap-

ture strain localization phenomena in multiphase continua. Differences from solutions obtained by assuming different boundary conditions occurring in the variably saturated case have been also analyzed. Moreover, we have pointed out the lack of any pathological mesh size dependence as well as an efficient solution of the highly oriented deformation patterns, independent of the mesh alignment. This situation has been contrasted with standard finite element treatments of the problem at hand.

Appendix A

Relations between porosity and volumetric strains

In this Appendix, relations between porosity and volumetric strains of solid skeleton, solid phase and void space are obtained by imposition of mass balance for solid phase. Such a balance is expressed in terms of solid mass content, defined as

$$M_s := J\rho_{sk} = J(1-n)\rho_s \tag{A.1}$$

where ρ_s is the solid "intrinsic" density, that is, the mass of unit current volume of the solid phase. The material time derivative of (A.1) is

$$\dot{M}_s = J\rho_s[(1-n)d_v - (1-n)\dot{e}_s - \dot{n}] \tag{A.2}$$

for $\dot{e}_s = -\dot{\rho}_s/\rho_s$ the rate of logarithmic volumetric strain e_s of solid phase. The mass balance for the solid phase ($\dot{M}_s = 0$) leads to the following rate relation for porosity

$$\dot{n} = (1-n)(d_v - \dot{e}_s) \tag{A.3}$$

in terms of the difference between the volumetric strain rates of solid skeleton and solid phase, respectively.

A straightforward calculation based only on porosity definition shows that the porosity increment rate can be in general related to the logarithmic volumetric strain e_{vd} of void space according to:

$$\dot{n} = n(\dot{e}_{vd} - d_v) \tag{A.4}$$

Therefore, combination of (A.3) with (A.4) leads to the following relation between the aforementioned volumetric strain rates:

$$d_v = n\,\dot{e}_{vd} + (1-n)\,\dot{e}_s \tag{A.5}$$

Assuming infinitesimal deformations for solid skeleton, solid phase and void space, we have:

$$d_v \simeq \dot{\varepsilon}_v \qquad \dot{e}_s \simeq \dot{\varepsilon}_s \qquad \dot{e}_{vd} \simeq \dot{\varepsilon}_{vd} \tag{A.6}$$

for the traces ε_v, ε_s and ε_{vd} of infinitesimal strain tensors associated to deformation of solid skeleton, solid phase and void space, respectively. Furthermore, the porosity rate can be expressed as a linear combination of $\dot{\varepsilon}_v$ and $\dot{\varepsilon}_s$ or $\dot{\varepsilon}_v$ and $\dot{\varepsilon}_{vd}$. In other words, we neglect nonlinear geometric effects in rate relations (A.3) and (A.4), respectively:

$$\dot{n} \simeq (1-n_0)(\dot{\varepsilon}_v - \dot{\varepsilon}_s) \tag{A.7}$$

and

$$\dot{n} \simeq n_0(\dot{\varepsilon}_{vd} - \dot{\varepsilon}_v) \tag{A.8}$$

for the initial porosity value n_0. Therefore, the linearized form of relation (A.5) among volumetric strain rates is

$$\dot{\varepsilon}_v = n_0\,\dot{\varepsilon}_{vd} + (1-n_0)\,\dot{\varepsilon}_s \tag{A.9}$$

Finally, by means of a time integration of (A.7) we obtain:

$$n \simeq n_0 + (1-n_0)(\varepsilon_v - \varepsilon_s) \simeq n_0 + \varepsilon_v - \varepsilon_s \tag{A.10}$$

where we employed the approximations $1 \mp \varepsilon_v \simeq 1$ and $1 \mp \varepsilon_s \simeq 1$.

Appendix B

Thermodynamic consistency of poro-elastic model

B.1 Strain-independent retention laws

In this Appendix, we employ Maxwell relations (1.35) to assess the thermodynamic admissibility of the simplified model represented by system (1.40) with tangent operators (1.107) and porosity law (1.92) for $p_f = \check{p}_f$ obtained from integration of (1.110).

Maxwell condition $(1.35)_1$ can be easily verified keeping in mind that the elastic tensor $\mathbb{C}_{sk}$ is assumed as constant. In view of relation (1.108), also Maxwell condition $(1.35)_2$ is satisfied, as shown by the following equation:

$$\frac{\partial}{\partial \mu_\beta}(\rho_\alpha \mathbf{b}_\alpha) = \rho_\alpha \rho_\beta \left(\frac{s_\alpha}{\kappa_\alpha}\delta_{\alpha\beta} + \check{s}'_\alpha \frac{\partial p_c}{\partial p_\beta} \right) \mathbf{b} \qquad \text{for} \qquad \alpha, \beta = w, g \tag{B.1}$$

which is a consequence of $(1.107)_2$ as well as of the considered retention model $(1.102)_2$ and of the assumed barotropic behaviour (1.38,1.84).

As a consequence of barotropy and of expression $(1.107)_3$ as well as of the assumed strain-independency of the retention model, the right side of Maxwell condition $(1.35)_3$ can be calculated as:

$$\frac{\partial}{\partial \boldsymbol{\varepsilon}}(\rho_\alpha \rho_\beta C_{\alpha\beta}) = \rho_\alpha \rho_\beta \frac{\partial C_{\alpha\beta}}{\partial n}\frac{\partial n}{\partial \boldsymbol{\varepsilon}} = \rho_\alpha \rho_\beta \left(\frac{s_\alpha}{\kappa_\alpha}\delta_{\alpha\beta} + \check{s}'_\alpha \frac{\partial p_c}{\partial p_\beta} \right) \frac{\partial n}{\partial \boldsymbol{\varepsilon}} \tag{B.2}$$

for $\alpha, \beta = w, g$. Therefore, a direct comparison between (B.1) and (B.2) shows that Maxwell condition $(1.35)_3$ is verified if

$$\frac{\partial n}{\partial \boldsymbol{\varepsilon}} = \mathbf{b} \tag{B.3}$$

which is fully consistent with the porosity model (1.92) employed herein, as shown by $(1.97)_1$ after introduction of $(1.102)_1$.

In view of barotropy (1.38,1.84) of fluid phases, left and right sides of Maxwell condition $(1.35)_4$ can be calculated as, respectively:

$$\frac{\partial}{\partial \mu_\beta}(\rho_\alpha^2 C_{\alpha\alpha}) = \rho_\alpha^2 \rho_\beta \left(\frac{2}{\kappa_\alpha} C_{\alpha\alpha} \delta_{\alpha\beta} + \frac{\partial C_{\alpha\alpha}}{\partial p_\beta} \right) \tag{B.4}$$

$$\frac{\partial}{\partial \mu_\alpha}(\rho_\alpha \rho_\beta C_{\alpha\beta}) = \rho_\alpha^2 \rho_\beta \left(\frac{1+\delta_{\alpha\beta}}{\kappa_\alpha} C_{\alpha\beta} + \frac{\partial C_{\alpha\beta}}{\partial p_\alpha} \right) \tag{B.5}$$

As a consequence of storage modulus expression $(1.107)_3$ and assumed retention model $(1.102)_2$, the derivatives appearing in right sides of (B.4-B.5) can be expressed as, respectively:

$$\begin{aligned} \frac{\partial C_{\alpha\alpha}}{\partial p_\beta} &= \frac{\partial n}{\partial p_\beta} \left(\frac{s_\alpha}{\kappa_\alpha} + \check{s}'_\alpha \frac{\partial p_c}{\partial p_\alpha} \right) + n \left(\frac{\check{s}'_\alpha}{\kappa_\alpha} + \check{s}''_\alpha \frac{\partial p_c}{\partial p_\alpha} \right) \frac{\partial p_c}{\partial p_\beta} + \\ &\quad + 2 s_\alpha \check{s}'_\alpha \frac{\partial p_c}{\partial p_\beta} (\mathbf{b} - n_0 \mathbf{1}) : \frac{\mathbf{1}}{3\kappa_s} \end{aligned} \tag{B.6}$$

$$\begin{aligned} \frac{\partial C_{\alpha\beta}}{\partial p_\alpha} &= \frac{\partial n}{\partial p_\alpha} \left(\frac{s_\alpha}{\kappa_\alpha} \delta_{\alpha\beta} + \check{s}'_\alpha \frac{\partial p_c}{\partial p_\beta} \right) + n \left(\frac{\check{s}'_\alpha}{\kappa_\alpha} \delta_{\alpha\beta} + \check{s}''_\alpha \frac{\partial p_c}{\partial p_\beta} \right) \frac{\partial p_c}{\partial p_\alpha} + \\ &\quad + (\check{s}'_\alpha s_\beta + s_\alpha \check{s}'_\beta) \frac{\partial p_c}{\partial p_\alpha} (\mathbf{b} - n_0 \mathbf{1}) : \frac{\mathbf{1}}{3\kappa_s} \end{aligned} \tag{B.7}$$

with:

$$\check{s}''_\alpha(p_c) := \frac{d\check{s}'_\alpha}{dp_c} \qquad \text{for} \qquad \alpha = w, g \tag{B.8}$$

A consequence of definition (1.51) of capillary pressure is:

$$\frac{\partial p_c}{\partial p_\alpha} \frac{\partial p_c}{\partial p_\beta} = 2\,\delta_{\alpha\beta} - 1 \tag{B.9}$$

and the coincidence between (B.4) and (B.5) can be easily verified for $\alpha = \beta$. For the significant case $\alpha \neq \beta$, after some manipulation employing (1.49), $(1.107)_3$, (1.108-

1.109), it is:

$$\frac{\partial}{\partial\mu_\beta}(\rho_\alpha^2 C_{\alpha\alpha}) - \frac{\partial}{\partial\mu_\alpha}(\rho_\alpha\rho_\beta C_{\alpha\beta}) = \rho_\alpha^2\rho_\beta \left\{ \frac{s_\alpha}{\kappa_\alpha}\left[\frac{\partial n}{\partial p_\beta} - s_\beta(\mathbf{b}-n_0\mathbf{1}):\frac{\mathbf{1}}{3\kappa_s}\right] - \right.$$
$$\left. -\breve{s}'_\alpha\frac{\partial p_c}{\partial p_\beta}\left[\sum_{\gamma=w,g}\frac{\partial n}{\partial p_\gamma} - (\mathbf{b}-n_0\mathbf{1}):\frac{\mathbf{1}}{3\kappa_s}\right]\right\} \tag{B.10}$$

So, also in view of (1.49), satisfaction of Maxwell condition $(1.35)_4$, that is, vanishing of right side of (B.10), is obtained for

$$\frac{\partial n}{\partial p_\alpha} = s_\alpha(\mathbf{b}-n_0\mathbf{1}):\frac{\mathbf{1}}{3\kappa_s} \qquad \text{for} \qquad \alpha = w,g \tag{B.11}$$

which is again fully consistent with assumed porosity model (1.92), as shown by direct comparison between (B.11) and $(1.97)_2$, after the introduction of (1.106).

B.2 Porosity-dependent retention laws

In this Appendix, the full thermodynamic admissibility of the poro-elastic model presented in Section 1.4.3 is assessed by means of Maxwell relations (1.35). We recall that such a model is represented by rate equation system (1.40), with tangent operators given by (1.129). In expressions (1.129), functions n, ω and $\breve{\xi}^*_\alpha$ are given by (1.92), (1.116) and (1.125), respectively.

The developments that follows require the evaluation of partial derivatives of relevant functions with respect to primary variables. For the assumed porosity function, such derivatives are obtained by substitution of (1.115,1.125) and consideration of (1.124) in general expressions (1.95), yielding:

$$\frac{\partial n}{\partial\boldsymbol{\varepsilon}} = \frac{1}{\omega}\frac{\partial\hat{n}}{\partial\boldsymbol{\varepsilon}} \qquad \text{and} \qquad \frac{\partial n}{\partial p_\alpha} = \frac{\breve{\xi}^*_\alpha}{\omega}\frac{\partial\hat{n}}{\partial p_f} \quad \text{for} \quad \alpha = w,g \tag{B.12}$$

Following the same formal arguments employed in the developments leading to (1.115,1.126), partial derivatives of function $\breve{s}'_\alpha(np_c)$ (1.114) can be obtained as:

$$\frac{\partial s'_\alpha}{\partial\boldsymbol{\varepsilon}} = \frac{p_c}{\omega}\breve{s}''_\alpha\frac{\partial\hat{n}}{\partial\boldsymbol{\varepsilon}} \qquad \text{and} \qquad \frac{\partial s'_\alpha}{\partial p_\beta} = \breve{s}''_\alpha\varsigma_\beta \tag{B.13}$$

for $\alpha, \beta = w, g$, with:

$$\breve{s}''_\alpha(np_c) := \frac{d\breve{s}'_\alpha}{d(np_c)} \qquad \text{for} \qquad \alpha = w, g \tag{B.14}$$

It can be observed that a consequence of (1.118) is:

$$\sum_{\alpha=w,g} \breve{s}''_\alpha = 0 \tag{B.15}$$

so, in view of definition (1.51) of capillary pressure, it is:

$$\breve{s}''_\alpha \frac{\partial p_c}{\partial p_\alpha} = \breve{s}''_\beta \frac{\partial p_c}{\partial p_\beta} \qquad \text{for} \quad \alpha, \beta = w, g \tag{B.16}$$

In porosity model (1.92), a linear dependency on strain and average pore pressure is assumed, thus leading to the following expressions for partial derivatives of function ω defined by (1.116):

$$\left.\begin{aligned} \frac{\partial \omega}{\partial \boldsymbol{\varepsilon}} &= -p_c^2 \frac{\partial \hat{n}}{\partial p_f} \frac{\partial s'_\alpha}{\partial \boldsymbol{\varepsilon}} \frac{\partial p_c}{\partial p_\alpha} \\ \frac{\partial \omega}{\partial p_\beta} &= -p_c \frac{\partial \hat{n}}{\partial p_f} \frac{\partial p_c}{\partial p_\alpha} \left(2\breve{s}'_\alpha \frac{\partial p_c}{\partial p_\beta} + p_c \frac{\partial s'_\alpha}{\partial p_\beta} \right) \end{aligned}\right\} \quad \text{for} \quad \alpha, \beta = w, g \tag{B.17}$$

In view of (B.13), these derivative reads:

$$\left.\begin{aligned} \frac{\partial \omega}{\partial \boldsymbol{\varepsilon}} &= -\frac{p_c^3}{\omega} \frac{\partial \hat{n}}{\partial p_f} \breve{s}''_\alpha \frac{\partial p_c}{\partial p_\alpha} \frac{\partial \hat{n}}{\partial \boldsymbol{\varepsilon}} \\ \frac{\partial \omega}{\partial p_\beta} &= -p_c \frac{\partial \hat{n}}{\partial p_f} \frac{\partial p_c}{\partial p_\alpha} \left(2\breve{s}'_\alpha \frac{\partial p_c}{\partial p_\beta} + p_c \breve{s}''_\alpha \varsigma_\beta \right) \end{aligned}\right\} \quad \text{for} \quad \alpha, \beta = w, g \tag{B.18}$$

Similarly, partial derivatives of coupling coefficient $\breve{\xi}^*_\alpha$ are obtained by substitution of (1.115,1.126–1.127,B.12,B.13) in

$$\left.\begin{aligned} \frac{\partial \breve{\xi}^*_\alpha}{\partial \boldsymbol{\varepsilon}} &= \frac{\partial s_\alpha}{\partial \boldsymbol{\varepsilon}} + p_c \breve{s}'_\alpha \frac{\partial n}{\partial \boldsymbol{\varepsilon}} + n p_c \frac{\partial \breve{s}'_\alpha}{\partial \boldsymbol{\varepsilon}} \\ \frac{\partial \breve{\xi}^*_\alpha}{\partial p_\beta} &= \frac{\partial s_\alpha}{\partial p_\beta} + p_c \breve{s}'_\alpha \frac{\partial n}{\partial p_\beta} + n p_c \frac{\partial \breve{s}'_\alpha}{\partial p_\beta} + n \frac{\partial p_c}{\partial p_\beta} \breve{s}'_\alpha \end{aligned}\right\} \quad \text{for} \quad \alpha, \beta = w, g \tag{B.19}$$

leading to:

$$\left.\begin{aligned} \frac{\partial \breve{\xi}^*_\alpha}{\partial \boldsymbol{\varepsilon}} &= \left(2\breve{s}'_\alpha + n p_c \breve{s}''_\alpha\right) \frac{p_c}{\omega} \frac{\partial \hat{n}}{\partial \boldsymbol{\varepsilon}} \\ \frac{\partial \breve{\xi}^*_\alpha}{\partial p_\beta} &= \left(2\breve{s}'_\alpha + n p_c \breve{s}''_\alpha\right) \varsigma_\beta \end{aligned}\right\} \quad \text{for} \quad \alpha, \beta = w, g \tag{B.20}$$

after some simple algebra. Finally, partial derivatives of $\breve{\xi}_w$ and $\breve{\xi}_g$, are evaluated by substitution of equations (B.18) and (B.20) in

$$\left.\begin{aligned} \frac{\partial \breve{\xi}_\alpha}{\partial \boldsymbol{\varepsilon}} &= \frac{1}{\omega^2}\left(\frac{\partial \breve{\xi}^*_\alpha}{\partial \boldsymbol{\varepsilon}}\omega - \breve{\xi}^*_\alpha \frac{\partial \omega}{\partial \boldsymbol{\varepsilon}}\right) \\ \frac{\partial \breve{\xi}_\alpha}{\partial p_\beta} &= \frac{1}{\omega^2}\left(\frac{\partial \breve{\xi}^*_\alpha}{\partial p_\beta}\omega - \breve{\xi}^*_\alpha \frac{\partial \omega}{\partial p_\beta}\right) \end{aligned}\right\} \quad \text{for} \quad \alpha,\beta = w,g \tag{B.21}$$

thus obtaining, after some manipulation employing (1.122) and (1.127):

$$\left.\begin{aligned} \frac{\partial \breve{\xi}_\alpha}{\partial \boldsymbol{\varepsilon}} &= \frac{p_c}{\omega^2}\left(2\breve{s}'_\alpha + p_c \breve{s}''_\alpha \frac{\partial p_c}{\partial p_\alpha}\varsigma_\alpha\right)\frac{\partial \hat{n}}{\partial \boldsymbol{\varepsilon}} \\ \frac{\partial \breve{\xi}_\alpha}{\partial p_\beta} &= \frac{1}{\omega}\left[2\breve{s}'_\alpha \frac{\partial p_c}{\partial p_\beta}\left(\varsigma_\alpha \frac{\partial p_c}{\partial p_\alpha} + \varsigma_\beta \frac{\partial p_c}{\partial p_\beta} - n\right) + p_c \breve{s}''_\alpha \frac{\partial p_c}{\partial p_\alpha}\varsigma_\alpha\varsigma_\beta\right] \end{aligned}\right\} \tag{B.22}$$

for $\alpha,\beta = w,g$. With reference to partial derivatives $(\text{B.22})_2$, it can be observed that:

$$\frac{\partial \breve{\xi}_\alpha}{\partial p_\beta} = \frac{\partial \breve{\xi}_\beta}{\partial p_\alpha} \qquad \text{for} \quad \alpha,\beta = w,g \tag{B.23}$$

as shown by (1.117) and (B.16).

Since elastic tensor $\mathbb{C}_{sk}$ is assumed constant in $(1.129)_1$ and as a consequence of barotropic relation (1.38), the left side of Maxwell condition $(1.35)_1$ can be written as:

$$\begin{aligned} \frac{\partial \tilde{\mathbb{C}}_{sk}}{\partial \mu_\alpha} &= -\rho_\alpha \frac{\partial}{\partial p_\alpha}\left(\frac{p_c^2}{\omega}\breve{s}'_\alpha\right)\frac{\partial p_c}{\partial p_\alpha}\,\mathbf{b}\otimes\mathbf{b} = \\ &= -\rho_\alpha \frac{p_c}{\omega}\left(2\frac{\partial p_c}{\partial p_\alpha}\breve{s}'_\alpha - \frac{p_c}{\omega}\frac{\partial \omega}{\partial p_\alpha}\breve{s}'_\alpha + p_c \frac{\partial \breve{s}'_\alpha}{\partial p_\alpha}\right)\frac{\partial p_c}{\partial p_\alpha}\,\mathbf{b}\otimes\mathbf{b} \end{aligned} \tag{B.24}$$

for $\alpha = w,g$. Substitution of partial derivatives $(\text{B.13})_2$ and $(\text{B.18})_2$ in (B.24) leads to:

$$\frac{\partial \tilde{\mathbb{C}}_{sk}}{\partial \mu_\alpha} = -\rho_\alpha \frac{p_c}{\omega^2}\left(2\breve{s}'_\alpha + p_c \breve{s}''_\alpha \frac{\partial p_c}{\partial p_\alpha}\varsigma_\alpha\right)\mathbf{b}\otimes\mathbf{b} \tag{B.25}$$

after some manipulation employing (1.122,1.124). In view of $(1.129)_2$ and $(\text{B.22})_1$, right side of Maxwell condition $(1.35)_1$ can be calculated as:

$$\begin{aligned} -\frac{\partial}{\partial \boldsymbol{\varepsilon}}(\rho_\alpha \mathbf{b}_\alpha) &= -\rho_\alpha \frac{\partial \breve{\xi}_\alpha}{\partial \boldsymbol{\varepsilon}}\otimes\mathbf{b} = \\ &= -\rho_\alpha \frac{p_c}{\omega^2}\left(2\breve{s}'_\alpha + p_c \breve{s}''_\alpha \frac{\partial p_c}{\partial p_\alpha}\varsigma_\alpha\right)\frac{\partial \hat{n}}{\partial \boldsymbol{\varepsilon}}\otimes\mathbf{b} \end{aligned} \tag{B.26}$$

Maxwell condition $(1.35)_1$ is then satisfied, as shown by a direct comparison between (B.25) and (B.26), recalling relation $(1.96)_1$ for porosity derivative.

Due to relation (B.23), also Maxwell condition $(1.35)_2$ is satisfied, as shown by the following equation:

$$\frac{\partial}{\partial \mu_\beta}(\rho_\alpha \mathbf{b}_\alpha) = \rho_\alpha \rho_\beta \left(\frac{\breve{\xi}_\alpha}{\kappa_\alpha}\delta_{\alpha\beta} + \frac{\partial \breve{\xi}_\alpha}{\partial p_\beta} \right) \mathbf{b} \qquad \text{for} \qquad \alpha, \beta = w, g \tag{B.27}$$

which is obtained considering expression $(1.129)_2$ for coupling operator and barotropic relations (1.38,1.84).

As a consequence of assumed barotropic behavior, intrinsic densities of fluid phases are independent on strain of porous continuum. In view of expression $(1.129)_3$ for the storage modulus and of relation (1.125), right side of Maxwell condition $(1.35)_3$ can be calculated as follows:

$$\begin{aligned} \frac{\partial(\rho_\alpha \rho_\beta C_{\alpha\beta})}{\partial \boldsymbol{\varepsilon}} &= \rho_\alpha \rho_\beta \left[\frac{\partial n}{\partial \boldsymbol{\varepsilon}} \left(\frac{s_\alpha}{\kappa_\alpha}\delta_{\alpha\beta} + 2n\breve{s}'_\alpha \frac{\partial p_c}{\partial p_\beta} \right) + \frac{n}{\kappa_\alpha}\frac{\partial s_\alpha}{\partial \boldsymbol{\varepsilon}}\delta_{\alpha\beta} + n^2 \frac{\partial \breve{s}'_\alpha}{\partial \boldsymbol{\varepsilon}}\frac{\partial p_c}{\partial p_\beta} + \right. \\ &\quad \left. + \left(\frac{\partial \breve{\xi}_\alpha}{\partial \boldsymbol{\varepsilon}}\breve{\xi}^*_\beta + \frac{\partial \breve{\xi}^*_\beta}{\partial \boldsymbol{\varepsilon}}\breve{\xi}_\alpha \right) (\mathbf{b} - n_0 \mathbf{1}) : \frac{\mathbf{1}}{3\kappa_s} \right] \end{aligned} \tag{B.28}$$

In this equation, expressions $(1.115,B.12_1,B.13_1,B.20_1,B.22_1)$ of involved partial derivatives are substituted. The so-obtained equation, after manipulation using relations (1.96,1.117,1.122,1.125,1.127,B.16), reads:

$$\begin{aligned} \frac{\partial}{\partial \boldsymbol{\varepsilon}}(\rho_\alpha \rho_\beta C_{\alpha\beta}) &= \rho_\alpha \rho_\beta \mathbf{b} \left\{ \frac{\breve{\xi}_\alpha}{\kappa_\alpha}\delta_{\alpha\beta} + \right. \\ &\quad \left. + \frac{1}{\omega} \left[2\breve{s}'_\alpha \frac{\partial p_c}{\partial p_\beta} \left(\varsigma_\alpha \frac{\partial p_c}{\partial p_\alpha} + \varsigma_\beta \frac{\partial p_c}{\partial p_\beta} - n \right) + p_c \breve{s}''_\alpha \frac{\partial p_c}{\partial p_\alpha}\varsigma_\alpha \varsigma_\beta \right] \right\} \end{aligned} \tag{B.29}$$

Therefore, Maxwell condition $(1.35)_3$ is shown to be verified by means of a direct comparison between (B.27) and (B.29), taking into account relation $(B.22)_2$.

Left and right sides of Maxwell condition $(1.35)_4$ can be again calculated by means of (B.4) and (B.5), respectively. The derivatives appearing in right sides of (B.4-B.5)

can now be evaluated considering expression $(1.129)_3$ for storage modulus, that is,

$$\frac{\partial C_{\alpha\alpha}}{\partial p_\beta} = \frac{\partial n}{\partial p_\beta}\left(\frac{s_\alpha}{\kappa_\alpha} + 2n\breve{s}'_\alpha\frac{\partial p_c}{\partial p_\alpha}\right) + \frac{n}{\kappa_\alpha}\frac{\partial s_\alpha}{\partial p_\beta} + n^2\frac{\partial \breve{s}'_\alpha}{\partial p_\beta}\frac{\partial p_c}{\partial p_\alpha} + + \left(\frac{\partial \breve{\xi}_\alpha}{\partial p_\beta}\breve{\xi}^*_\alpha + \frac{\partial \breve{\xi}^*_\alpha}{\partial p_\beta}\breve{\xi}_\alpha\right)(\mathbf{b} - n_0\mathbf{1}) : \frac{\mathbf{1}}{3\kappa_s} \tag{B.30}$$

$$\frac{\partial C_{\alpha\beta}}{\partial p_\alpha} = \frac{\partial n}{\partial p_\alpha}\left(\frac{s_\alpha}{\kappa_\alpha}\delta_{\alpha\beta} + 2n\breve{s}'_\alpha\frac{\partial p_c}{\partial p_\beta}\right) + \frac{n}{\kappa_\alpha}\frac{\partial s_\alpha}{\partial p_\alpha}\delta_{\alpha\beta} + n^2\frac{\partial \breve{s}'_\alpha}{\partial p_\alpha}\frac{\partial p_c}{\partial p_\beta} + + \left(\frac{\partial \breve{\xi}_\alpha}{\partial p_\alpha}\breve{\xi}^*_\beta + \frac{\partial \breve{\xi}^*_\beta}{\partial p_\alpha}\breve{\xi}_\alpha\right)(\mathbf{b} - n_0\mathbf{1}) : \frac{\mathbf{1}}{3\kappa_s} \tag{B.31}$$

In these equations, expressions $(1.126,B.12_2,B.13_2,B.20_2,B.22_2)$ of involved derivatives are substituted and some simplification is achieved by applying relations $(1.96_2,1.117,1.122,$ B.16), thus obtaining:

$$\frac{\partial C_{\alpha\alpha}}{\partial p_\beta} = \left(\frac{\partial \hat{n}}{\partial p_f}\frac{s_\alpha\breve{\xi}^*_\beta}{\omega} + n\breve{s}'_\alpha\varsigma_\beta\right)\frac{1}{\kappa_\alpha} + + \frac{2\breve{s}'_\alpha}{\omega}\frac{\partial \hat{n}}{\partial p_f}\left[n\left(\frac{\partial p_c}{\partial p_\alpha}\breve{\xi}^*_\beta - \frac{\partial p_c}{\partial p_\beta}\breve{\xi}^*_\alpha\right) + \frac{\partial p_c}{\partial p_\alpha}\frac{\partial p_c}{\partial p_\beta}\breve{\xi}^*_\alpha\varsigma_\alpha + 2\breve{\xi}^*_\alpha\varsigma_\beta\right] + + \breve{s}''_\alpha\frac{\partial p_c}{\partial p_\alpha}\varsigma_\beta\left[n^2 + \frac{p_c}{\omega}\frac{\partial \hat{n}}{\partial p_f}\breve{\xi}^*_\alpha\left(\varsigma_\alpha + n\frac{\partial p_c}{\partial p_\alpha}\right)\right] \tag{B.32}$$

$$\frac{\partial C_{\alpha\beta}}{\partial p_\alpha} = \left(\frac{\partial \hat{n}}{\partial p_f}\frac{s_\alpha\breve{\xi}^*_\alpha}{\omega} + n\breve{s}'_\alpha\varsigma_\alpha\right)\frac{\delta_{\alpha\beta}}{\kappa_\alpha} + + \frac{2\breve{s}'_\alpha}{\omega}\frac{\partial \hat{n}}{\partial p_f}\left[n\left(\frac{\partial p_c}{\partial p_\beta}\breve{\xi}^*_\alpha - \frac{\partial p_c}{\partial p_\alpha}\breve{\xi}^*_\beta\right) + \frac{\partial p_c}{\partial p_\alpha}\frac{\partial p_c}{\partial p_\beta}\breve{\xi}^*_\alpha\varsigma_\alpha + 2\breve{\xi}^*_\beta\varsigma_\alpha\right] + + \breve{s}''_\alpha\frac{\partial p_c}{\partial p_\beta}\varsigma_\alpha\left[n^2 + \frac{p_c}{\omega}\frac{\partial \hat{n}}{\partial p_f}\left(\frac{\partial p_c}{\partial p_\alpha}\frac{\partial p_c}{\partial p_\beta}\breve{\xi}^*_\beta\varsigma_\alpha + n\frac{\partial p_c}{\partial p_\alpha}\breve{\xi}^*_\alpha\right)\right] \tag{B.33}$$

For the trivial case $\alpha = \beta$, the coincidence between (B.4) and (B.5) is equivalent to the coincidence between equations (B.32) and (B.33), which, in turn, can be easily verified applying (1.122). For the relevant case $\alpha \neq \beta$, further manipulation employing

(1.125),(1.127) and $(1.129)_3$ is required to obtain:

$$\begin{aligned}\frac{\partial}{\partial\mu_\beta}(\rho_\alpha^2 C_{\alpha\alpha}) &- \frac{\partial}{\partial\mu_\alpha}(\rho_\alpha\rho_\beta C_{\alpha\beta}) = \\ &= \rho_\alpha^2\rho_\beta\left(-\frac{1}{\kappa_\alpha}C_{\alpha\beta} + \frac{\partial C_{\alpha\alpha}}{\partial p_\beta} - \frac{\partial C_{\alpha\beta}}{\partial p_\alpha}\right) = \\ &= \rho_\alpha^2\rho_\beta\left[-\frac{1}{\kappa_\alpha}C_{\alpha\beta} + \left(\frac{\partial\hat{n}}{\partial p_f}\frac{s_\alpha\breve{\xi}_\beta^*}{\omega} + n\breve{s}'_\alpha\varsigma_\beta\right)\frac{1}{\kappa_\alpha}\right] = 0 \qquad \text{(B.34)}\end{aligned}$$

Therefore, also Maxwell condition $(1.35)_4$ is satisfied by the class of models presented in Section 1.4.3.

Appendix C

Convex Helmholtz free energy

In this Appendix we prove that conditions (1.36) are sufficient for the Helmholtz free energy ψ to be (strictly) convex. Firstly, in developments that follow it is useful to rewrite rate constitutive equations (1.31) in a more compact form. Therefore we introduce the following vectors and matrices

$$\mathbf{M} := \begin{bmatrix} M_w \\ M_g \end{bmatrix} \qquad \boldsymbol{\mu} := \begin{bmatrix} \mu_w \\ \mu_g \end{bmatrix} \qquad \mathbf{b}_\rho^T := \begin{bmatrix} \rho_w \mathbf{b}_w \\ \rho_g \mathbf{b}_g \end{bmatrix} \qquad \mathbf{C}_\rho := \begin{bmatrix} \rho_w^2 C_{ww} & \rho_w \rho_g C_{wg} \\ \rho_g \rho_w C_{gw} & \rho_g^2 C_{gg} \end{bmatrix} \tag{C.1}$$

thus allowing to rewrite system (1.31) as

$$\begin{bmatrix} \dot{\boldsymbol{\sigma}} \\ \dot{\mathbf{M}} \end{bmatrix} = \begin{bmatrix} \tilde{\mathbb{C}}_{sk} & -\mathbf{b}_\rho \\ \mathbf{b}_\rho^T & \mathbf{C}_\rho \end{bmatrix} \begin{bmatrix} \dot{\boldsymbol{\varepsilon}} \\ \dot{\boldsymbol{\mu}} \end{bmatrix} \tag{C.2}$$

Inversion of the second equation with respect to fluid free enthalpies provides

$$\dot{\boldsymbol{\mu}} = \mathbf{C}_\rho^{-1} \left(\dot{\mathbf{M}} - \mathbf{b}_\rho^T \dot{\boldsymbol{\varepsilon}} \right) \tag{C.3}$$

that, substituted in the first equation of system (C.2), leads to the following "pure stiffness" formulation of rate constitutive equations:

$$\begin{bmatrix} \dot{\boldsymbol{\sigma}} \\ \dot{\boldsymbol{\mu}} \end{bmatrix} = \begin{bmatrix} \mathbb{C}_{undr} & -\mathbf{b}_\rho \mathbf{C}_\rho^{-1} \\ -\mathbf{C}_\rho^{-1} \mathbf{b}_\rho^T & \mathbf{C}_\rho^{-1} \end{bmatrix} \begin{bmatrix} \dot{\boldsymbol{\varepsilon}} \\ \dot{\mathbf{M}} \end{bmatrix} \tag{C.4}$$

where

$$\mathbb{C}_{undr} := \tilde{\mathbb{C}}_{sk} + \mathbf{b}_\rho \mathbf{C}_\rho^{-1} \mathbf{b}_\rho^T \tag{C.5}$$

is the "undrained" elastic tensor providing the reversible response of the porous solid when both the fluid mass content rates are null. Due to hyperelastic equations (1.27), the global coefficient matrix appearing in system (C.4) can be viewed as the Hessian matrix of the Helmholtz free energy ψ. Therefore, this function is (strictly) convex if and only if

$$\begin{aligned} \bar{\psi}(\mathbf{A}, \mathbf{a}) \;\; &:= \;\; \mathbf{A} : \mathbb{C}_{undr}\, \mathbf{A} + \mathbf{a} \cdot \mathbf{C}_\rho^{-1} \mathbf{a} - 2\mathbf{A} : \mathbf{b}_\rho \mathbf{C}_\rho^{-1} \mathbf{a} > 0 \\ &\forall\, (\mathbf{A}, \mathbf{a}) \in Sym \times \mathbb{R}^2 \setminus \{(\mathbf{0}, \mathbf{0})\} \end{aligned} \tag{C.6}$$

In view of definition (C.5) and due to the symmetry of $\mathbf{C}_\rho$, condition (C.6) takes the form

$$\begin{aligned} \bar{\psi}(\mathbf{A}, \mathbf{a}) \;\; &= \;\; \mathbf{A} : \tilde{\mathbb{C}}_{sk}\, \mathbf{A} + \left(\mathbf{b}_\rho^T \mathbf{A} - \mathbf{a}\right) \cdot \mathbf{C}_\rho^{-1} \left(\mathbf{b}_\rho^T \mathbf{A} - \mathbf{a}\right) > 0 \\ &\forall\, (\mathbf{A}, \mathbf{a}) \in Sym \times \mathbb{R}^2 \setminus \{(\mathbf{0}, \mathbf{0})\} \end{aligned} \tag{C.7}$$

Positive definiteness $(1.36)_1$ of the drained elastic tensor implies

$$\bar{\psi}(\mathbf{A}, \mathbf{a}) > \left(\mathbf{b}_\rho^T \mathbf{A} - \mathbf{a}\right) \cdot \mathbf{C}_\rho^{-1} \left(\mathbf{b}_\rho^T \mathbf{A} - \mathbf{a}\right) \qquad \forall\, \mathbf{A} \in Sym \setminus \{\mathbf{0}\} \tag{C.8}$$

Positive definiteness $(1.36)_2$ of the matrix of storage modulus implies the positive definiteness of $\mathbf{C}_\rho^{-1}$, which in turn, together with (C.8), allows to write

$$\begin{aligned} \bar{\psi}(\mathbf{A}, \mathbf{a}) \;\; &> \;\; \left(\mathbf{b}_\rho^T \mathbf{A} - \mathbf{a}\right) \cdot \mathbf{C}_\rho^{-1} \left(\mathbf{b}_\rho^T \mathbf{A} - \mathbf{a}\right) \geq 0 \\ &\forall\, \mathbf{A} \in Sym \setminus \{\mathbf{0}\} \quad \text{and} \quad \forall\, \mathbf{a} \in \mathbb{R}^2 \end{aligned} \tag{C.9}$$

moreover

$$\bar{\psi}(\mathbf{0}, \mathbf{a}) = \mathbf{a} \cdot \mathbf{C}_\rho^{-1} \mathbf{a} = 0 \qquad \Leftrightarrow \qquad \mathbf{a} = \mathbf{0} \tag{C.10}$$

that, together with (C.9), is equivalent to (C.7).

Appendix D

Integrability conditions

In this Appendix we provide necessary and sufficient conditions for a matrix to be the Hessian operator of a scalar function. For the sake of simplicity, we restrict to the three-dimensional case. Therefore, we consider a point $(x_1, x_2, x_3) \in D \subset \mathbb{R}^3$ with D *connected* and $H(x_1, x_2, x_3)$ a matrix of sufficiently smooth functions, at least with continuous derivatives:

$$H(x_1, x_2, x_3) = \begin{bmatrix} H_{11}(x_1, x_2, x_3) & H_{12}(x_1, x_2, x_3) & H_{13}(x_1, x_2, x_3) \\ H_{21}(x_1, x_2, x_3) & H_{22}(x_1, x_2, x_3) & H_{23}(x_1, x_2, x_3) \\ H_{31}(x_1, x_2, x_3) & H_{32}(x_1, x_2, x_3) & H_{33}(x_1, x_2, x_3) \end{bmatrix} \tag{D.1}$$

It is well known that the necessary conditions for H to be the Hessian matrix of a scalar function f, i.e.

$$H(x_1, x_2, x_3) = \nabla^2 f(x_1, x_2, x_3) \tag{D.2}$$

can be written in this way:

$$H(x_1, x_2, x_3) = H^T(x_1, x_2, x_3) \tag{D.3}$$

$$\frac{\partial H_{ij}}{\partial x_k} = \frac{\partial H_{ik}}{\partial x_j} \qquad \text{for} \qquad i, j, k = 1 \dots 3 \tag{D.4}$$

for all $(x_1, x_2, x_3) \in D$.

This lemma, providing necessary conditions for the integrability of a matrix of functions, can be inverted if $D \subset \mathbb{R}^3$ is *simply connected*. In this case, it is well known

that conditions (D.4) are also sufficient for the existence of scalar functions ϕ_i such that

$$H_{ij} = \frac{\partial \phi_i}{\partial x_j} =: \phi_{i,j} \qquad \text{for} \qquad i,j = 1 \ldots 3 \tag{D.5}$$

These functions can be obtained by integrating the i row of (D.1) on an arbitrary path γ in $D \subset \mathbb{R}^3$. For example, we may consider the piecewise linear path

$$\gamma = \gamma_1 \cup \gamma_2 \cup \gamma_3 \tag{D.6}$$

with γ_i being a line connecting points P_{i-1} and P_i, where $P_0 \equiv (0,0,0)$, $P_1 \equiv (x_1,0,0)$, $P_2 \equiv (x_1,x_2,0)$ and $P_3 \equiv (x_1,x_2,x_3)$. Therefore, we may write:

$$\phi_i = \int_{P_{k-1}}^{P_k} H_{ik}\, dx_k \tag{D.7}$$

with summation on the repeated index. Finally, we have to prove the existence of a scalar function f such that

$$\phi_i = \frac{\partial f}{\partial x_i} =: f_{,i} \tag{D.8}$$

This scalar function exists if the following conditions hold in the simply connected set $D \subset \mathbb{R}^3$:

$$\frac{\partial \phi_i}{\partial x_j} = \frac{\partial \phi_j}{\partial x_i} \qquad \text{for} \qquad i,j = 1 \ldots 3 \tag{D.9}$$

These conditions can be easily verified by means of (D.3), (D.4) and (D.7). We may conclude that, for a matrix of functions given in the form (D.1), conditions (D.3) and (D.4) are not only necessary, but also sufficient for the existence of a scalar function such that relation (D.2) holds, providing that the domain is simply connected.

References

[1] Abati, A. and Callari, C., Finite element formulation of a macroscopic theory for three-phase porous media, presentation at *ECCM 06 - 3rd European Conference on Computational Mechanics*, Lisbon, 2006.

[2] Abati, A. and Callari, C., Un modello agli elementi finiti per continui porosi parzialmente saturi, presentation at *GIMC 06 - XVI Convegno Italiano di Meccanica Computazionale*, Bologna, 2006.

[3] Abati, A. and Callari, C., Finite element formulation of unilateral boundary conditions for unsaturated flow in porous continua, to be submitted.

[4] Allen, M. B., Mechanics of multiphase fluid flows in variably saturated porous media, *International Journal of Engineering Science*, 24(3), 1986, 339-351.

[5] Alonso, E.E., Gens, A. and Josa A., A constitutive model for partially saturated soils, *Géotechnique*, 40(3), 1990, 403-430.

[6] Armero, F., Large-scale modeling of localized dissipative mechanisms in a local continuum: applications to the numerical simulation of strain localization in rate-dependent inelastic solids, *Mechanics of Cohesive-Frictional Materials*, 4, 1999, 101-131.

[7] Armero, F., Formulation and finite element implementation of a multiplicative model of poro-plasticity at finite strains under fully saturated conditions, *Computational Methods in Applied Mechanics and Engineering*, 171, 1999, 205-241.

[8] Armero, F., On the characteriaztion of localized solutions in inelastic solids: an analysis of wave propagation in a softening bar, *Computer Methods in Applied Mechanics and Engineering*, 191, 2001, 181-213.

[9] Armero, F. and Callari, C., An analysis of strong discontinuities in a saturated poro-plastic solid, *International Journal for Numerical Methods in Engineering*, 46, 1999, 1673-1698.

[10] Armero, F. and Garikipati, K., Recent advances in the analysis and numerical simulation of strain localization in inelastic solids, in: Owen, D. and Oñate, E. editors, *Computational Plasticity, Proceedings of the 4^{th} International Conference*, Barcelona, 1995, 547-561.

[11] Armero, F. and Garikipati, K., An analysis of strong discontinuities in multiplicative finite strain plasticity and their relation with the numerical simulation of strain localization in solids, *International Journal of Solids and Structures*, 33, 1996, 2863-2885.

[12] Armero, F. and Park, J.G., An analysis of strain localization in a shear layer under thermally coupled dynamic conditions. Part 1: Continuum thermoplastic models, *International Journal for Numrical Methods in Engineering*, 56(14), 2003,2069-2100.

[13] Arrow, K.J., Hurwicz, L. and Uzawa, H., *Studies in Non-Linear Programming*, Stanford University Press, 1958.

[14] Auricchio, F. and Sacco, E., Augmented lagrangian finite-elements for plate contact problems, *International Journal for Numerical Methods in Engineering*, 39(24), 1996, 4141-4158.

[15] Baiocchi, C., Su un problema di frontiera libera connesso a questioni di idraulica, *Annali di Matematica Pura e Applicata*, 92, 1972, 107-127.

[16] Bathe, K.J., Sonnad, V. and Domigan, P., Some experiences using finite element methods for fluid flow problems, *Proceedings of the 4^{th} International Conference on finite Element Methods*, Hannover, 1982, 9.3-9.16.

[17] Bazant, Z.P., Belytschko, T. and Chang, T.P., Continuum theory for strain-softening, *Journal of Engineering Mechanics, ASCE*, 110, 1984, 1666-1691.

[18] Biot, M.A., General theory of three-dimensional consolidation, *Journal of Applied Physics*, 12, 1941, 155-164.

[19] Biot, M.A., Theory of finite deformations of porous solids, *Indiana University Mathematics Journal*, 21, 1972, 597-620.

[20] Biot, M.A. and Willis, D.G., The elastic coefficients of the theory of consolidation, *Journal of Applied Mechanics*, 24, 594-601, 1957.

[21] Bishop, A.W., The principle of effective stress, *Teknisk Ukeblad*, 39, 859-863, 1959.

[22] Bolzon, G., Schrefler, B.A. and Zienkiewicz, O.C., Elastoplastic soil constitutive laws generalized to partially saturated states, *Géotechnique*, 46(2), 1996, 279-289.

[23] Borja, R., On the mechanical energy and effective stress in saturated and unsaturated porous continua, *International Journal of Solids and Structures*, 43, 2006, 1764-1786.

[24] Borja, R.I. and Kishnani, S.S., On the solution of elliptic free boundary problems via Newton's method, *Computer Methods in Applied Mechanics and Engineering*, 88(2), 1991, 341-361.

[25] Brezis, H., Kinderlehrer, D. and Stampacchia, G., Sur une nouvelle formulation due probleme de l'ecoulement a travers une digue, *Comptes Rendus de l'Academie de Sciences Paris, Series A*, 287, 1978, 711-714.

[26] Bruch, J.C., A survey of free boudary value problems in the theory of fluid flow through porous media: variational inequality approach - Part I, *Advances in Water Resources*, 3, 1980, 65-80.

[27] Callari, C., Coupled numerical analysis of strain localization induced by shallow tunnels in saturated soils, *Computers and Geotechnics*, 31, 2004, 193-207.

[28] Callari, C., *Appunti del corso di meccanica dei mezzi porosi*, 2007.

[29] Callari, C. and Abati, A., Effetti tridimensionali delle operazioni di serbatoio in presenza di accoppiamento idro-meccanico, invited presentation at *Accademia dei Lincei - II Convegno Nazionale: Problemi Strutturali nell'Ingegneria delle Dighe*, Roma, 2007.

[30] Callari, C. and Abati, A., Numerical treatment of fluid-flow boundary conditions for partially saturated porous solids, invited presentation at 6^{th} *International Conference on Unilateral Problems in Structural Analysis*, Siracusa, 2007.

[31] Callari, C. and Abati, A., Hyperelastic multiphase porous continua with strain-dependent retention laws, to be submitted.

[32] Callari, C. and Abati, A., Finite element methods for unsaturated porous solids, in preparation.

[33] Callari, C. and Armero, F., Finite element methods for the analysis of strong discontinuities in coupled poro-plastic media, *Computer Methods in Applied Mechanics and Engineering*, 191, 2002, 4371-4400.

[34] Callari, C. and Armero, F., Analysis and numerical simulation of strong discontinuities in finite strain poroplasticity, *Computer Methods in Applied Mechanics and Engineering*, 193, 2004, 2941-2986.

[35] Callari, C., Armero, F. and Abati, A., Strong discontinuities in coupled multiphase poro-plastic media, presentation at *USNCCM 07 - 9th United States National Congress on Computational Mechanics*, San Francisco, 2007.

[36] Callari, C., Armero, F. and Abati, A., Analysis of displacement discontinuties in variably saturated poroplastic solids, invited presentation at *Colloquium Lagrangianum 2007*, Ferme des Vallées - Aufargis, 2007.

[37] Callari, C., Armero, F. and Abati, A., Strong discontinuities in coupled multiphase poro-plastic media, in preparation.

[38] Callari, C., Fois, N. and Cicivelli, R., The role of hydro-mechanical coupling in the behaviour of dam-foundation system, in: Yao, Z.H., Yuan, M.W. and Zhong, W.X. editors, *Proceedings of the 6th Congrees on Computational Mechanics in conjunction with the 2nd Asian-Pacific Congress on Computational Mechanics*, Beijing, 2004.

[39] Callari, C. and Lupoi, A., Localization analysis in dilatant elasto-plastic solids by a strong-discontinuity method, in: Maceri, F. and Frémond, M. editors, *Novel Approaches in Civil Engineering*, Springer Verlag, Berlin, 2004, 121-129.

[40] Caro Vargas, B., Formulazione agli elementi finiti di vincoli unilateri nel problema di filtrazione in mezzi parzialmente saturi, *M.D. thesis*, tutored by: Callari, C. and Abati, A., University of Rome "Tor Vergata" and Ecole Nationale des Ponts et Chaussées, 2005.

[41] Carroll, M.M., An effective stress law for anisotropic elastic deformation, *Journal of Geophysical Research*, 84, 1979, 7510-7512.

[42] Casagrande, A., Control of seepage through foundations and abutments of dams, First Rankine Lecture, *Géotechnique*, 11, 1961, 161-182.

[43] Celia, M.A., Bouloutas, E.T. and Zarba, R.L., A general mass-conservative numerical solution for the unsaturated flow equation, *Water Resources Research*, 26(7), 1990, 1483-1496.

[44] Chateau, X. and Dormieux, L., Micromechanics of saturated and unsaturated porous media, *International Journal for Numerical and Analytical Methods in Geomechanics*, 26, 2002, 831-844.

[45] Cheng, A.H.D., Material coefficients for anisotropic poroelasticity, *International Journal of Rock Mechanics and Mining Sciences*, 34, 1997, 199-205.

[46] Childs, E.C. and Collis-George, N., The permeability of porous materials, *Proceedings of the Royal Society of London, Series A*, 201, 1950, 392-405.

[47] Chung, K.Y. and Kikuchi, N., Adaptive methods to solve free boundary problems of flow through porous media, *International Journal for Numerical and Analytical Methods in Geomechanics*, 11, 1987, 17-31.

[48] Cividini, A. and Gioda, G., On the variable mesh finite element analysis of unconfined seepage problems, *Géotechnique*, 2, 1989, 251-267.

[49] Cocchetti, G. and Maier, G., Shakedown analysis in poroplasticity by linear programming, *International Journal for Numrical Methods in Engineering*, 47, 2000, 141-168.

[50] Coleman, B.D. and Hodgon, M.L., On shear bands in ductile materials, *Archive of Rational Mechanics and Analysis*, 90, 1985, 219-247.

[51] Coleman, B.D. and Gurtin, M., Thermodynamics with internal variables, *Journal of Chemistry and Physics*, 47, 1967, 597-613.

[52] Coleman, B.D. and Noll, W., The thermodynamics of elastic materials with heat conduction and viscosity, *Archives of Rational Mechanics and Analysis*, 13, 1963, 168-178.

[53] Comi, C., Fedele, R. and Perego, U., Un modello chemo-elastico a danneggiamento per il degrado del calcestruzzo da reazione alcali-aggregati, *Proceedings of the XVI Italian Conference of Computational Mechanics*, Bologna, 2006.

[54] Coussy, O. *Mechanics of Porous Continua*, John Wiley & Sons, Chichester, 1995.

[55] Coussy, O., *Poromechanics*, John Wiley & Sons, Chichester, 2004.

[56] Coussy, O., Eymard, R. and Lassabatère, T., Constitutive modeling of unsaturated drying deformable materials, *Journal of Engineering Mechanics*, 124(6), 1998, 658-667.

[57] Cowin S.C., Bone fluid poroelasticity, *Journal of Biomechanics*, 32, 1999, 217-238.

[58] Dalhuijsen, A.J. and Segal, A., Comparison of finite element techniques for solidification problems, *International Journal for Numerical Methods in Engineering*, 23, 1986, 1807-1829.

[59] Dangla, P., Malinsky, L. and Coussy, O., Plasticity and imbibition-drainage curves for unsaturated soils: a unified approach, in: Pande G. and Pietruszczak, S. editors, *Numerical Models in Geomechanics, NUMOG VI*, Balkema, Rotterdam, 1997, 141-146.

[60] de Boer, R., Highlights in the historical developments of the porous media theory: toward a consistent macroscopic theory, *Applied Mechanics Review*, 49(4), 1996, 201-261.

[61] de Borst, R. and Sluys, L.J., Localization in a Cosserat continuum under static and dynamic loading conditions, *Computer Methods in Applied Mechanics and Engineering*, 90, 1991, 805-827.

[62] De Buhan, P. and Dormieux, L., On the validity of the effective stress concept for assessing the strength of saturated porous materials: A homogenization approach, *Journal of the Mechanics and Physics of Solids*, 44(10), 1996, 1649-1667.

[63] Desai, C.S., Finite element residual schemes for unconfined flow, *International Journal for Numerical Methods in Engineering*, 10, 1976, 1415-1418.

[64] Desai, C.S. and Li, G.C., Transient free surface flow through porous media using a residual procedure, *Proceedings of the 4th International Conference on Finite Elements in Fluids*, Tokio, 1982.

[65] Desai, C.S. and Li, G.C., A residual flow procedure and application for free surface in media using, *Advances in Water Resources*, 6(1), 1983, 27-35.

[66] Ehlers, W., Graf, T. and Ammann, M., Deformation and localization analysis of partially saturated soil, *Computer Methods in Applied Mechanics and Engineering*, 193, 2004, 2885-2910.

[67] Faragó, I., Horváth, R. and Korotov, S., Discrete maximum principle for linear parabolic problems solved on hybrid meshes, *Applied Numerical Mathematics*, 53, 2005, 249-264.

[68] France, P.W., Parekh, C.J., Peters, J.C. and Taylor, C., Numerical analysis of free surface seepage problems, *Journal of the Irrigation and Drainage Division, ASCE*, 97(IR1), 1971, 165-179.

[69] Franceschini, G., Bigoni, D., Regitnig, P. and Holzapfel, G.A., Brain tissue deforms similarly to filled elastomers and follows consolidation theory, *Journal of the Mechanics and Physics of Solids*, 54, 2006, 2592-2620.

[70] Fredlund, D.G. and Morgenstern, N.R., Stress state variables and unsaturated soils, *Journal of the Geotechnical Engineering Division, ASCE*, 103, 1977, 447-466.

[71] Gallipoli, D., Wheeler, S.J. and Karstunen, M., Modelling the variation of degree of saturation in a deformable unsaturated soil, *Géotechnique*, 53(1), 2003, 105-112.

[72] Gawin D., Pesavento, F. and Schrefler, B.A., Hygro-thermo-chemo-mechanical modelling of concrete at early ages and beyond. Part II: Shrinkage and creep of concrete, *International Journal For Numerical Methods in Engineering* 67, 2006, 332-363.

[73] Gawin D., Pesavento, F. and Schrefler, B.A., Towards prediction of the thermal spalling risk through a multi-phase porous media model of concrete, *Computer Methods in Applied Mechanics and Engineering* 195, 2006, 5707-5729.

[74] Gens, A., Carol, I. and Alonso, E.E., An interface element formulation for the analysis of soil-reinforcement interaction, *Computers and Geotechnics*, 7, 1988, 133-151.

[75] Gens, A., do N. Guimaraes, L., Garcia-Molina, A. and Alonso, E.E., Factors controlling rock-clay buffer interaction in a radioactive waste repository, *Engineering Geology*, 64, 2002, 297-308.

[76] Gray, W.G. and Schrefler, B.A., Thermodynamic approach to effective stress in partially saturated porous media, *European Journal of Mechanics A/Solids*, 20, 2001, 521-538.

[77] Hassanizadeh, S.M. and Gray, W.G., General conservation equations for multi-phase systems: 3 Constitutive theory for porous media flow, *Advances in Water Resources*, 3, 1980, 25-40.

[78] Hestenes, M.R., Multiplier and gradient methods, *Journal of Optimization, Theory and Applications*, 4, 1969, 303-320.

[79] Hill, R., Acceleration waves in solids, *Journal of the Mechanics and Physics of Solids*, 16, 1962, 1-10.

[80] Houlsby, G.T., The work input to an unsaturated granular material, *Géotechnique*, 47(1), 1997, 193-196.

[81] Hughes, T.J.R., *The Finite Element Method*, Prentice Hall, Englewood Cliffs, 1987.

[82] Hutter, K., Laloui, L. and Vulliet, L., Thermodynamically based mixture models of saturated and unsaturated soils, *Mechanics of Cohesive-Frictional Materials*, 4, 1999, 295-338.

[83] Huyakorn, P.S., Springer, E.P., Guvanasen, V. and Wadsworth, T.D., A three-dimensional finite-element model for simulating water flow in variably saturated porous media, *Water Resources Researh*, 22(13), 1986, 1790-1808.

[84] Jacob, C.E., On the flow of water in an elastic artesian aquifer, *Transactions of the American Geophysical Union*, 22, 1940, 783-787.

[85] Jommi, C., Remarks on the constitutive modelling of unsaturated soils, in: Tarantino, A. and Mancuso, C. editors, *Experimental Evidence and Theoretical Approaches in Unsaturated Soils*, Balkema, Rotterdam, 2000, 139-153.

[86] Kikuchi, N. and Oden, J.T., *Contact Problems in Elasticity: A Study of Variational Inequalities and Finite Element Methods*, SIAM, Philadelphia, 1988.

[87] Kim, J.M., Fully coupled poroelastic governing equations for groundwater flow and solid-skeleton deformation in variably saturated true anisotropic porous geologic media, *Geosciences Journal*, 8, 2004, 291-300.

[88] Lacy, S.J. and Prevost, J.H., Flow through porous media: a procedure for locating the free surface, *Interantional Journal for Numerical and Analytical in Geomechanics*, 11(6), 1987, 585-601.

[89] Lade, P.V. and de Boer, R., The concept of effective stress for soil, concrete and rock, *Géotechnique* 47, 1997, 61-78.

[90] Laloui, L., Klubertanz, G. and Vulliet, L., Solid−liquid−air coupling in multiphase porous media, *International Journal for Numerical and Analytical Methods in Geomechanics*, 27, 2003, 183-206.

[91] Larsson, J. and Larsson, R., Localization analysis of a fluid-saturated elastoplastic porous medium using regularized discontinuities, *Mechanics of Cohesive-Frictional Materials*, 5(7), 2000, 565-582.

[92] Laursen, T.A., *Computational Contact and Impact Mechanics*, Springer, Berlin, 2002.

[93] Lehmann, F. and Ackerer, P., Comparison of iterative methods for improved solutions of the fluid flow equation in partially saturated porous media, *Transport in Porous Media*, 31, 1998, 275-292.

[94] Lewis, R.W. and Schrefler, B.A., A finite element simulation of the subsidence of gas reservoirs undergoing a water drive in, *Finite Element in Fluids*, 4, 1982, 179-199.

[95] Lewis, R.W. and Schrefler, B.A., *The Finite Element Method in the Static and Dynamic Deformation and Consolidation of Porous Media*,2^{nd} edition, John Wiley & Sons, New York, 1998.

[96] Liakopoulos, A.C., Transient flow through unsaturated porous madia, *Ph.D. Thesis*, University of California, Berkeley, 1965.

[97] Loret, B. and Khalili, N., A three-phase model for unsaturated soils, *International Journal for Numerical and Analitical Methods in Geomechanics*, 24, 2000, 893-927.

[98] Mosler, J., On the modeling of highly localized deformations induced by material failure: the strong discontinuity approach, *Archives of Computational Methods in Engineering*, 11(4), 2004, 389-446.

[99] Muskat, M., *Physical Principles of Oil Production*, McGraw-Hill, New York, 1949.

[100] Needleman, A., Material rate dependence and mesh sensitivity in localization problems, *Computational Methods in Applied Mechanics and Engineering*, 67, 1988, 69-85.

[101] Ng, C.W.W. and Pang, Y.W., Influence of stress-state on soil-water characteristics and slope stability, *Journal of Geotechnical and Geoenvironmental Engineering, ASCE*, 126(2), 2000, 157-166.

[102] Nour-Omid, B. and Wriggers, P., A note on the optimum choice for penalty parameters, *Communications in Applied Numerical Methods*, 3, 1987, 581-585.

[103] Nur, A. and Byerlee, J.D., An exact effective stress law for elastic deformation of rock with fluids, *Journal of Geophysical Research*, 76, 1971, 6414-6419.

[104] Oliver, J., Modelling string discontinuities in solid mechanics via strain softening constitutive equations. Part 1: Fundamentals. Part 2: Numerical simulation, *International Journal for Numerical Methods in Engineering*, 39, 1996, 3575-3623.

[105] Ottosen, N.S. and Runesson, K., Properties of discontinuous solutions in elastoplasticity, *International Journal of Solids and Structures*, 27, 1991, 401-421.

[106] Philip, J.R., The theory of infiltration: 1. The infiltration equation and its solution, *Soil Science*, 83, 1957, 435-448.

[107] Pietrszczak, S. and Mróz, Z., Finite Element analysis of deformation of strain-softening materials, *International Journal of Numerical Methods in Engineering*, 17, 1981, 327-334.

[108] Powell, M.J.D., A method for nonlinear constraints in minimization problems, in: Fletcher, R. editor, *Optimization*, Academic Press, New York, 1969.

[109] Quarteroni, A., Sacco, R. and Saleri, F., *Numerical Mathematics*, Springer, New York, 2000.

[110] Rank, E., Katz, C. and Werner, H., On the importance of the discrete maximum principle in transient analysis using finite element methods, *International Journal for Numerical Methods in Engineering*, 19, 1983, 1771-1782.

[111] Raous, M., Quasistatic Signorini problem with Coulomb friction and coupling to adhesion, in: Wriggers, P. and Panagiotopoulos, P. editors, *CISM Courses and Lectures, No. 384*, Springer, Vienna, 1999, 101-178.

[112] Réthoré, J., de Borst, R. and Abellan, M.A., A discrete model for the dynamic propagation of shear bands in a fluid-saturated medium, *International Journal for Numerical Methods in Geomechanics*, 31, 2007, 347-370.

[113] Rice, J., The localization of plastic deformations, in: Koiter, W.T. editor, *Theoretical and Applied Mechanics*, 1976, 207-219.

[114] Rice, J. R., and Cleary, M. P., Some basic stress diffusion solutions for fluid-saturated elastic porous media with compressible constituents, *Reviews of Geophysics and Space Physics*, 14, 1976, 227-241.

[115] Rutqvist, J., Wu, Y.S., Tsang, C.F. and Bodvarsson, G., A modeling approach for analysis of coupled multiphase fluid flow, heat transfer, and deformation in fractured porous rock, *International Journal of Rock Mechanics and Mining Sciences*, 39, 2002, 429-442.

[116] Sanavia, L., Pesavento, F. and Schrefler, B.A., Finite element analysis of non-isothermal multiphase geomaterials with application to strain localization simulation, *Computational Mechanics*, 37(4), 2006, 331-348.

[117] Santagiuliana, R. and Schrefler, B.A., Enhancing the Bolzon-Schrefler-Ziekiewicz constitutive model for partially saturated soil, *Transport in Porous Media*, 65, 2006, 1-30.

[118] Schellekens, J.C.J., and de Borst, R., On the numerical integration of interface elements, *International Journal for Numerical Methods in Engineering*, 36, 1993, 43-66.

[119] Schrefler, B.A., Mechanics and Thermodynamics of Saturated-Unsaturated Porous Materials and Quantitative Solutions, *Applied Mechanics Reviews*, 55(4), 2002, 351-388.

[120] Schrefler, B.A. and Gawin, D., The effective stress principle: incremental or finite form? *International Journal for Numerical and Analytical Methods in Geomechanics*, 20, 1996, 785-814.

[121] Schrefler, B.A., Sanavia, L. and Majorana, C.E., A multiphase medium model for localisation and postlocalisation simulation in geomaterials, *Mechanics of Cohesive-Frictional Materials*, 1, 1996, 95-114.

[122] Schrefler, B.A. and Scotta, R., A fully coupled dynamic model for two-phase fluid flow in deformable porous media, *Computer Methods in Applied Mechanics and Engineering*, 3223, 3223-3246, 2001.

[123] Sewell, M.J., *Maximum and Minimum Principles: a Unified Approach, with Applications*, Cambridge University Press, 1987.

[124] Sheng, D., Sloan, S.W., Gens, A. and Smith, D.W., Finite element formulation and algorithms for unsaturated soils. Part I: Theory, *International Journal for Numerical and analytical Methods in Geomechanics*, 27, 2003, 745-765.

[125] Sheng, D., Smith, D.W., Sloan, S.W. and Gens, A., Finite element formulation and algorithms for unsaturated soils. Part II: Verification and application, *International Journal for Numerical and analytical Methods in Geomechanics*, 27, 2003, 767-790.

[126] D. Sheng, S. W. Sloan, A. Gens, A constitutive model for unsaturated soils: thermomechanical and computational aspects, Computational Mechanics, **33**, 453-465, 2004.

[127] Sillers, W.S., Fredlund, D.G. and Zakerzadeh, N. Mathematical attributes of some soil-water characteristic curve models, *Geotecnical and Geological Engeneering*, 19, 2001, 243-283.

[128] Simo, J.C. and Hughes, T.J.R., *Computational Inelasticity*, Springer, New York, 1998.

[129] Simo, J.C., Oliver, J. and Armero, F., An analysis of strong discontinuities induced by strain-softening in rate-independent inelastic solids, *Computational Mechanics*, 12, 1993, 277-296.

[130] Simo, J.C. and Rifai, S., A class of mixed assumed strain methods and the method of incompatible modes, *International Journal for Numerical Methods in Engineering*, 29, 1990, 1595-1638.

[131] Skempton, A.W., Effective stress in soils, concrete and rocks, *Proceedings of the Conference on Pore Pressure and Suction in Soils*, Butterworths, London, 1961, 4-16.

[132] Snow, D., A Parallel Plate Model of Fracturated Permeable Media, *Ph.D. Thesis*, University of California, Berkeley, 1965.

[133] Stackgold, I., *Green's Functions and Boundary Value Problems*, Wiley, New York, 1979.

[134] Steinmann, P., A finite element formulation for strong disocntinuities in fluid-saturated porous media, *Mechanics of Cohesive-Frictional Materials*, 4(2), 1999, 133-152.

[135] Suklje, L., *Rheological aspects of soil mechanics*, Wiley-Interscience, New York, 1969.

[136] Sukumar, N., Moës, N., Moran, B. and Belytschko, T., Extended finite element method for three-dimensional crack modelling, *International Journal for Numerical Methods in Engineering*, 48, 2000, 1549-1570.

[137] Tamagnini, R. and Pastor, M., A thermodynamically based model for unsaturated soil: a new framework for generalized plasticity, in: Mancuso, C. and

Tarantino, A. editors, *Unsaturated soils. Advances in testing, modelling and engineering applications*, Balkema, Leiden, 2005, 121-134.

[138] Taylor, R.L., *FEAP - A Finite Element Analysis Program: Version 7.5 Theory Manual*, University of California at Berkeley, 2003.

[139] Thomas, T.Y., *Plastic Flow and Fracture in Solids*, Academic Press, New York, 1961.

[140] Thompson, M. and Willis, J.R., A reformulation of the equations of anisotropic poroelasticity, *Journal of Applied Mechanics, ASME*, 58, 1991, 612-616.

[141] Topp, G.C., Soil-water hysteresis measured in a sandy loam and compared with the hysteric domain model, *Soil Science Society American Proceedings*, 33(5), 1969, 645-651.

[142] Torelli, A., Su un problema a frontiera libera di evoluzione, *Bollettino dell'Unione dei Matematici Italiani*, 11, 1975, 559-570.

[143] Tsaparas, I., Rahardjo, H., Toll, D.G. and Leong, E.C., Controlling parameters for rainfall-induced landslides, *Computers and Geotechnics*, 29, 2002, 1-27.

[144] Tvergaard, V., Needleman, A. and Lo, K.K., Flow localization in the plane strain tensile test, *Journal of the Mechanics and Physics of Solids*, 29, 1981, 115-142.

[145] Ulm F.J., Coussy, O., Kefei, L. and Larive, C., Thermo-chemo-mechanics of ASR expansion in concrete structures, Journal of Engineering Mechanics, 126(3), 2000, 233-242.

[146] Vanapalli, S.K., Fredlund, D.G. and Pufahl, D.E., The influence of soil structure and stress history on the soil-water characteristics of a compacted till, *Géotechnique*, 49, 1999, 143-159.

[147] van Genuchten, A closed form equation predicting the hydraulic conductivity of unsaturated soils, *Soil Science Society of America Journal*, 44, 1980, 892-898.

[148] Vardoulakis, I., Deformation of water-saturated sand: I. Uniform undrained deformation and shear banding; II. Effect of pore water flow and shear banding, *Géotechnique*, 46, 1996, 441-472.

[149] Vaunat, J., Gens, A. and Jommi, C., A strategy for numerical analysis for the transition between saturated and unsaturated flow conditions, in: Pietruszczak, S. and Pande, G. editors, *Numerical Models in Geomechanics*, Balkema, Rotterdam, 1997.

[150] Wang, H.F., *Theory of Linear Poroelasticity: with Applications to Geomechanics and Hydrology*, Princeton University Press, 2000.

[151] Wriggers, P., *Computational Contact Mechanics*, John Wiley & Sons, Chichester, 2002.

[152] Wriggers, P., Simo, J. and Taylor, R.L., Penalty and augmented Lagrangian formulations for contact problems, in: Middleton, J. and Pande, G. editors, *Proceedings of NUMETA Conference*, Balkema, Rotterdam, 1985.

[153] Zavarise, G., Wriggers, P. and Schrefler, B.A., On augmented Lagrangian algorithms for thermomechanical contact problems with friction, *International Journal for Numerical Methods in Engineering*, 38(17), 1995, 2929-2949.

[154] Zhang, H.W. and Shrefler, B.A., Uniqueness and localization analysis of elastoplastic saturated porous media, *International Journal For Numerical and Analitical Methods in Geomechanics*, 25(1), 2001, 29-48.

[155] Zheng, H., Liu, D.F., Lee, C.F. and Tham, L.G., A new formulation of Signorini's type for seepage problems with free surfaces, *International Journal for Numerical Methods in Engineering*, 64(1), 2005, 1-16.